Structural characterisation of the Foot-and-Mouth Disease Virus uncoating pathway



Nayab Malik

Trinity College

University of Oxford

A thesis submitted for the degree of

Doctor of Philosophy

Trinity term 2016

Acknowledgements

I would like to acknowledge my supervisors Dave Stuart and Juha Huiskonen for their continuous support through good and bad times, especially Dave, who adopted me after the first part of my PhD ended badly and I had to change labs and projects. Liz Fry and Abhay Kotecha have been instrumental to this thesis; without their tireless help with experiments and manuscripts, this project would never have completed successfully and on time. I also gratefully acknowledge the help from Jingshan Ren. The STRUBI technical and administrative teams have been extremely patient and I'm forever thankful for their support. Thanks also to our collaborators: Sarah, Amin, Toby, Francois and Julian, for not only providing samples but also valuable insights and time. I am also thankful to Kay Grünewald for his mentorship in the first two years and for teaching me that we do not just learn from our successes.

I am also lucky to have found wonderful friends in STRUBI who made my time here memorable. For that I'd like to thank Serban, Max, Eamon, Steinar, Rhys and everyone else for much-needed coffee breaks and pub nights. Thanks also to Lien, Olivia, Nikola and other friends at Trinity College who have been there for me these four years and allowed me to vent or celebrate, as needed.

My two families, the Maliks and the Lückens, have been a constant support for me for as long as I have known them and helped me stay sane through this endeavour.

Lastly, I dedicate this thesis to my fiancé and better-half, Malte Lücken, without whom I would not be where I am now. Thank you.

Abstract

Foot-and-Mouth Disease Virus is a single-stranded RNA virus that belongs to the genus *aphthoviruses*, in the family *Picornaviridae*, and causes disease in cloven-hoofed animals. It is one of the biggest hindrances to the international trade of animals and animal products in the world. The virus capsids readily dissociate into pentamers at acidic pH. While there have been several studies on *enterovirus* uncoating, this process is poorly-understood for *aphthoviruses*, and there are no published structures elucidating how FMDV undergoes this transformation to infect cells. Furthermore, there are no structures available for a dissociated FMDV pentamer. Thus far, there has been only one paper claiming to show, at low resolution, a disassembly intermediate for another *aphthovirus*, Equine Rhinitis A Virus (ERAV).

Here, a 5.2Å-structure of an FMDV assembly formed from acid dissociated pentamers, visualised using cryo-electron microscopy (cryo-EM), is presented. This inside-out assembly of the pentamers highlights the extensive conformational changes in the pentamers that may have lead to the disassembly of the native capsid. Also presented here is a lower-resolution structure of the isolated dissociated pentamer (8.2 Å), enabling a comparison of the differences between native FMDV particles, the dissociated- and the re-assembled pentamers. These analyses elucidate why the pentamers may have been unable to re-assemble properly. Together, these data suggest that the ERAV structure mooted to be a disassembly intermediate may have formed from re-assembled dissociated pentamers. Furthermore, it is concluded that there is still no hard structural evidence that *aphthoviruses* form an intermediate particle during disassembly.

The thesis also includes high-resolution cryo-EM structures of the FMDV serotypes SAT1 and SAT3 (3.8 Å and 3.1 Å respectively), derived from inactivated virus-pellets, thus completing the repository of high-resolution structures for all SAT serotypes. The results provide an insight into the reasons for SAT3 being the most thermally-unstable *picornaviruses*, and also include predictions and comparative analyses with known antigenic sites of other FMDV serotypes.

Contents

1 Introduction **1**

1.1 Chapter summary 1

1.2 *Picornaviridae* family 2

1.2.1 *Picornavirus* genome 4

1.3 Foot and Mouth Disease Virus 5

1.3.1 The virus 5

1.3.2 The capsid 6

1.3.3 Life cycle 8

1.3.4 Immune response 12

1.3.5 Antigenic variation 13

1.3.6 Outbreaks and economic implications 15

1.3.7 Vaccination 16

1.4 Overview and aims 17

2 Electron microscopy **19**

2.1 Chapter summary 19

2.2 Hardware 20

2.2.1 The column and the electron source 20

2.2.2 Lenses and apertures . . . 21
2.2.3 Specimen holder . . . 23
2.2.4 Detectors . . . 24
2.2.4.1 CCD cameras . . . 25
2.2.4.2 Direct electron detectors . . . 26
2.2.4.3 Comparison of electronic detectors . . . 27
2.3 Sample preparation and data collection . . . 28
2.3.1 Negative-stain electron microscopy . . . 29
2.3.2 Plunge-freezing for cryo-electron microscopy . . . 29
2.3.3 Data acquisition . . . 30
2.4 Cryo-EM image processing . . . 32
2.4.1 Frame alignment and motion correction . . . 33
2.4.2 Contrast Transfer Function (CTF) . . . 34
2.4.2.1 Impact of defocus on CTF . . . 35
2.4.2.2 Envelope functions of the CTF . . . 38
2.4.2.3 CTF correction . . . 39
2.4.3 Particle picking and extraction . . . 41
2.4.4 2D classification . . . 42
2.4.5 3D reconstruction for model generation . . . 43
2.4.6 3D classification and refinement . . . 44
2.4.7 Model fitting . . . 46
2.5 Classical vs. cryo-EM . . . 47

3 Native structures for FMDV SAT serotypes 50

3.1 Chapter summary . . . 50

3.2 Methods . . . 52
3.2.1 Virus production . . . 52
3.2.1.1 Virus growth and inactivation . . . 52
3.2.1.2 Virus purification from the inactivated pellet . . . 53
3.3 Results . . . 57
3.3.1 SAT-1 . . . 57
3.3.1.1 Negative-stain electron microscopy . . . 57
3.3.1.2 Cryo-EM data collection . . . 57
3.3.1.3 2D classification . . . 58
3.3.1.4 3D classification and refinement . . . 59
3.3.1.5 Model fitting . . . 63
3.3.2 SAT-3 . . . 68
3.3.2.1 Negative-stained electron microscopy . . . 68
3.3.2.2 CryoEM data collection . . . 68
3.3.2.3 2D classification . . . 69
3.3.2.4 3D classification and refinement . . . 71
3.3.2.5 Model fitting . . . 74
3.4 Discussion . . . 79
3.5 Conclusion and future direction . . . 81

4 SAT3 structure analysis **82**

4.1 Chapter summary . . . 82
4.2 Methods and Results . . . 83
4.2.1 SAT3 vs. serotypes SAT1 and SAT2 . . . 84
4.2.1.1 Thermostability . . . 84

4.2.1.2 RMSD 86
4.2.1.3 PISA 89
4.2.1.4 Electrostatics 91
4.2.1.5 Surface difference 94
4.2.2 SAT3 vs. serotypes SAT1, SAT2, A and O 96
4.2.2.1 Antigenic variation 96
4.2.2.2 ConSurf 98
4.3 Discussion 101
4.3.1 Stability 102
4.3.2 RMSD between SAT serotypes 106
4.3.3 Antigenic variation 108
4.4 Conclusions and future directions 110

5 A mis-assembled FMDV particle 112

5.1 Chapter summary 112
5.2 Methods 113
5.2.1 Virus growth and harvest 113
5.2.2 Low-pH treatment to capture intermediates 114
5.2.3 Enzyme Linked Immunosorbent Assay (ELISA) 114
5.2.4 Scale-up and shipment 116
5.2.5 Desalting and concentration for EM 117
5.3 Results 118
5.3.1 Negative-stain electron microscopy 118
5.3.1.1 Control fraction with untreated virus 119
5.3.1.2 Low-pH treatment in the presence of Formaldehyde 119

5.3.1.3 Low-pH treatment in the absence of Formaldehyde 121
5.3.2 Thermofluor assay . . . 124
5.3.3 Cryo-EM data collection and processing . . . 125
5.3.3.1 2D classification . . . 126
5.3.3.2 3D classification . . . 126
5.3.3.3 Refinement and model fitting . . . 132
5.3.4 Polara vs. Titan Krios . . . 135
5.3.5 A novel FMDV mis-assembly structure . . . 137
5.3.6 Inter-pentameric interfaces of the mis-assembled particle . . 138
5.4 Discussion . . . 145
5.4.1 Native vs. mis-assembled FMDV particles . . . 145
5.4.1.1 Structural changes in VP2 . . . 145
5.4.1.2 Structural changes in VP3 . . . 147
5.4.2 Comparison with other *aphthoviruses* . . . 150
5.5 Conclusion and future direction . . . 155

6 FMDV pentamer structure 158

6.1 Chapter summary . . . 158
6.2 Methods . . . 159
6.2.1 Sample preparation . . . 159
6.2.2 Negative-stain electron microscopy . . . 159
6.2.3 Attempts at cryo-electron microscopy . . . 161
6.2.3.1 1:10 dilution . . . 162
6.2.3.2 1:20 dilution . . . 163
6.2.3.3 1:20 dilution, double-blotted grids . . . 163

6.2.3.4 1:10 dilution with TWEEN-20 . . . 165
6.2.3.5 1:20 dilution with DMNG . . . 165
6.2.3.6 1:20 dilution with NP-40 . . . 166
6.2.3.7 Lacey-carbon support grids . . . 168
6.3 Results . . . 169
6.3.1 Structure determination from negative-stained EM . . . 169
6.3.1.1 2D classification . . . 169
6.3.1.2 3D classification . . . 169
6.3.1.3 Final structure from negative-stained EM . . . 171
6.3.2 Structure determination from cryo-EM . . . 173
6.3.2.1 2D classification: first attempt . . . 174
6.3.2.2 2D classification: second attempt . . . 176
6.3.2.3 3D classification . . . 177
6.3.2.4 Final structure from cryo-EM . . . 178
6.3.2.5 Atomic-model fitting into the EM structure . . . 182
6.4 Discussion . . . 184
6.4.1 Difficulties with sample preparation for pentamers . . . 184
6.4.2 Pentamer from the mis-assembled particle . . . 185
6.4.3 Dissociated vs. pentamers from the native particle . . . 187
6.5 Conclusion and future direction . . . 189

7 Contributions and prospects 190

7.1 A complete SAT structural repository . . . 190
7.2 Insights into FMDV disassembly . . . 191
7.3 Questions about *aphthovirus* intermediates . . . 192

7.4 The first high-resolution standalone pentamer 193
7.5 Concluding remarks 195

A PISA: FMDV mis-assembled particle interface **196**

B ResMap stats **200**

C Multiple sequence alignment **205**

D RMSD between FMDV serotypes **208**

Bibliography **210**

List of Figures

1.1 Picornaviruses 2
1.2 Picornavirus phylogeny 3
1.3 Picornavirus genome 4
1.4 FMDV capsid and capsid proteins 7
1.5 Different thermal stability of all the FMDV serotypes 8
1.6 FMDV life cycle 9
1.7 Native and expanded capsid structure of ERAV 10
1.8 Antigenic sites of FMDV O1K 13
1.9 Antigenic sites listed 14
1.10 Thesis overview schematic 18

2.1 Electron microscope schematic 22
2.2 CCD camera operation mechanism schematic 25
2.3 Comparison of the DQEs of different detectors 28
2.4 Cryo-EM data processing pipeline 32
2.5 Beam-induced drift 33
2.6 Range of defoci imaged leading to different CTF curves 36
2.7 A range of information covered by imaging at a range of defoci . . . 37

2.8 Theoretical vs. observed CTF for astigmatic and good images . . . 40
2.9 3D reconstruction principle . . . 43
2.10 3D classification principle . . . 44
2.11 Atomic model fitting into EM density . . . 46
2.12 Classical vs. cryo-EM . . . 47

3.1 First gradient purification of the virus . . . 54
3.2 Second gradient purification of the virus . . . 54
3.3 SAT1: negative-stained and cryo-EM micrographs . . . 57
3.4 SAT1: 2D classification . . . 58
3.5 SAT1: 3D classification . . . 59
3.6 SAT1: 3D classes in Chimera . . . 60
3.7 SAT1: final structure . . . 61
3.8 SAT1: resolution determination . . . 62
3.9 SAT1: ResMap . . . 63
3.10 SAT1: fitting . . . 64
3.11 SAT1: fitting in stereo . . . 65
3.12 SAT1: Ramachandran plot . . . 66
3.13 SAT3: missing VP4 density . . . 67
3.14 SAT3: negative-stained and cryo-EM micrographs . . . 68
3.15 SAT3: 2D classification . . . 70
3.16 SAT3: 3D classification . . . 71
3.17 SAT3: 3D classes in Chimera . . . 72
3.18 SAT3: final structure . . . 73
3.19 SAT3: ResMap . . . 74

3.20 SAT3: Refinement 75
3.21 SAT3: fitting 77
3.22 SAT3: fitting in stereo 78
3.23 Missing G-H loops 79

4.1 Thermofluor assay for all FMDV serotypes 83
4.2 Sequence alignment of SAT1, 2, and 3 85
4.3 RMSD deviation between SAT1, 2, and 3 87
4.4 Sequence identity between SAT1, 2 and 3 88
4.5 PISA comparison of all SAT inter-pentameric interfaces 90
4.6 PISA stats: trends 91
4.7 Electrostatic surface of FMDV protomers 92
4.8 Surface difference between SAT3 vs SAT1 or SAT2 95
4.9 Antigenic sites from O1K, A10, SAT1 and SAT2 mapped on to SAT3 97
4.10 Conserved residues on the SAT3 protomer 98
4.11 Conserved residues on the SAT3 pentamer 99
4.12 Phylogenetic tree of FMDV serotypes 101
4.13 Melting temperatures of different picornaviruses 102
4.14 VP2-93 comparison of all SATs 103
4.15 Superposition of SAT1 and SAT3 106
4.16 Superposition of SAT2 and SAT3 108

5.1 ELISA profile of FMDV altered particle preparation 115
5.2 Sample preparation and shipment timeline 116
5.3 Negative-stained EM of the control fraction with just the virus capsids 118
5.4 Negative-stained EM of the formaldehyde treated fractions 120

5.5 Negative-stained and cryo-EM images of the first batch of the low-pH treated particles . . . 121
5.6 Negative-stained and cryo-EM images of the second, more concentrated, batch of the low-pH treated particles . . . 123
5.7 Thermofluor assay comparison of the altered vs. native FMDV particles . . . 124
5.8 Altered particle: 2D classification . . . 127
5.9 Altered particle: 3D classification . . . 128
5.10 Altered particle: 3D classes in Chimera . . . 128
5.11 Altered particle: final structure . . . 130
5.12 Altered particle: resolution determination . . . 131
5.13 Altered particle: ResMap results . . . 131
5.14 Altered particle: model fitting . . . 133
5.15 Altered particle: model fitting . . . 134
5.16 Altered particle: refinement statistics . . . 135
5.17 Data collection at the Polara vs. the Titan Krios . . . 136
5.18 Native vs. altered particle . . . 140
5.19 Stereo: altered particle . . . 141
5.20 Native vs. altered particle: pentamers in stereo view . . . 141
5.21 Native vs. altered particle: protein chain comparison . . . 142
5.22 PISA analysis of the native vs. altered particle inter-pentameric interface . . . 143
5.23 Altered particle: stabilising interactions . . . 144
5.24 Native vs. altered particle VP2 . . . 146
5.25 Native vs. altered particle VP3 . . . 147

5.26 Clashes in the altered particle in case of its proper re-assembly . . . 148
5.27 FMDV vs. ERAV altered particle 150
5.28 FMDV vs. ERAV altered particle interface comparison 151
5.29 FMDV vs. ERAV protomer comparison 152
5.30 VP2-Phe116 residues at the altered particle interface 154
5.31 Attempt to generate an FMDV disassembly intermediate 155

6.1 Negative-stained EM of heat-treated capsids to produce pentamers . 160
6.2 1:10 dilution of pentamers 161
6.3 1:20 dilution of pentamers 162
6.4 1:20 diluted pentamers, double blotted onto grids 163
6.5 1:10 dilution of pentamers, with Tween-20 164
6.6 1:20 dilution of pentamers, on grids soaked in 0.003% DMNG . . . 165
6.7 1:20 dilution of pentamers, with NP-40 167
6.8 1:30 dilution of pentamers, on lacey-carbon grids 167
6.9 FMDV dissociated pentamers: 2D classification 170
6.10 FMDV dissociated pentamers: 3D classification 171
6.11 FMDV dissociated pentamers: 3D classes in Chimera 172
6.12 FMDV dissociated pentamers: Final structure from negative-stained EM 173
6.13 FMDV dissociated pentamers: cryo-EM 2D classes from the first sample 174
6.14 FMDV dissociated pentamers: second sample for cryo-EM 175
6.15 FMDV dissociated pentamers: 2D classes from the second sample . 176
6.16 FMDV dissociated pentamers: 3D classification 177

6.17 FMDV dissociated pentamers: Resolution determination 178
6.18 FMDV dissociated pentamers: Final structure at 8.2 Å 179
6.19 Dissociated pentamer: ResMap analysis 179
6.20 Dissociated pentamer: orientation sampling 180
6.21 FMDV dissociated pentamers: fitting in stereo 181
6.22 FMDV dissociated pentamers: atomic model fitting 183
6.23 Segmentation in Chimera 185
6.24 Fitting the mis-assembled pentamer into dissociated pentamer map 186
6.25 Mis-assembled pentamer vs. native pentamer atomic model 188

7.1 FMDV disassembly overview 191

A.1 Mis-assembled particle PISA statistics 197
A.2 VP2 Lys64 and VP3 Asp70 interaction 198
A.3 VP2 Phe65 and VP3 Arg67 interaction 198
A.4 VP2 Tyr200 and VP3 Asp69 interaction 199
A.5 VP2 Lys198 and VP3 Glu196 interaction 199

B.1 ResMap stats for SAT1 201
B.2 ResMap stats for SAT3 202
B.3 ResMap stats for A10 particle 203
B.4 ResMap stats for the standalone pentamer 204

D.1 RMSD between FMDV serotypes 209
D.2 Evolutionary distances between FMDV serotypes 209

Abbreviations

ATP ..... Adenosine tri-hosphate

BEI ..... Binary ethyleneimine

CCD ..... Charge-coupled device

CMOS ..... Complementary metal-oxide-semiconductor

CTF ..... Contrast transfer function

Cryo-EM ..... Cryo-electron microscopy

DMNG ..... Decyl maltose neopentyl glycol

DNA ..... Deoxyribonucleic acid

DQE ..... Detector quantum efficiency

EFTEM ..... Energy filtered transmission electron microscopy

ELISA ..... Enzyme linked immunosorbent assay

ERAV ..... Equine rhinitis A virus

FA ..... Formaldehyde

FMDV ..... Foot-and-mouth disease virus

FSC ..... Fourier shell correlation

HS ..... Heparan sulfate

MAb ..... Monoclonal antibody

ML ..... Maximum likelihood

MWCO ..... Molecular weight cut-off

PSF ..... Point spread function

RMSD ..... Root mean square deviation

RNA ..... Ribonucleic acid

SAT ..... South african territories

SOP ..... Standard operating protocol

TEM ..... Transmission electron microscopy

UTR ..... Untranslated region

VP ..... Viral protein

WRL ..... World reference laboratory

Chapter 1

Introduction

1.1 Chapter summary

All the work in this thesis was performed on foot-and-mouth disease virus (FMDV), which belongs to the family of non-enveloped RNA viruses known as *Picornaviridae*. This chapter explains the basic features common to all the viruses in this family and their life cycle. It also introduces the details of the virus uncoating stage of the life cycle, and introduces what is already known about it. This background is important to understand the model organism used for this study and for the later chapters that cover its disassembly. This chapter aims to introduce the said model organism; the primary method used for structure determination, electron microscopy, and its theory is covered separately in the next chapter. Specific methods, results, and discussion will be covered in each respective chapter.

Genus	Species	Disease	Host
Aphthovirus	Foot-and-mouth disease virus	Foot and mouth disease	Livestock
	Equine rhinitis A virus	Respiratory disease	Horses
Enterovirus	Coxsackieviruses, Enteroviruses, Echoviruses, Human Polioviruses	Hand foot and mouth disease, meningitis, myocarditis, paralysis, polio	Human
	Rhinoviruses	Common cold	
Cardiovirus	Encephalomyocarditis virus	Encephalitis, myocarditis	Mouse
Erbovirus	Equine rhinitis B viruses	Respiratory disease	Horse
Hepatovirus	Hepatitis A virus	Hepatitis	Human
Kobuvirus	Aichi viruses	Gastroenteritis	Human, cattle, pig
Parechovirus	Human parecho virus, Ljungan virus	Respiratory disease, Gastroenteritis	Human
Teschovirus	Porcine teschovirus	Encephalomyelitis	Pig
Sapelovirus	Porcine, Avian and Simian Seploviruses	Often subclinical but can cause neurological problems	Pigs, ducks, monkeys
Senecavirus	Seneca Valley virus	Vesicular disease	Pig
Tremovirus	Avian encephalomyelitis virus	Epidemic tremor	Chicken

Figure 1.1: Some major *picornaviruses*, their example species and the disease they cause in the given hosts.

1.2 *Picornaviridae* family

The *Picornaviridae* is a family of small, non-enveloped, icosahedral, single-strand positive-sense RNA viruses. They include various pathogens that cause a range of human and animal diseases as mild as the common cold (rhinoviruses) and as serious as poliomyelitis (poliovirus), as shown in Figure 1.1. The main genera [2], and some representative species, are shown in Figure 1.1. The evolutionary relationship between these major genera, and some provisional ones, is shown in Figure 1.2 [1]. Capsid proteins VP1 - 3 and replicase proteins 2C, 3C and 3D are conserved in the *picornaviridae* [1, 3], and were used to derive the phylogenetic tree shown here.

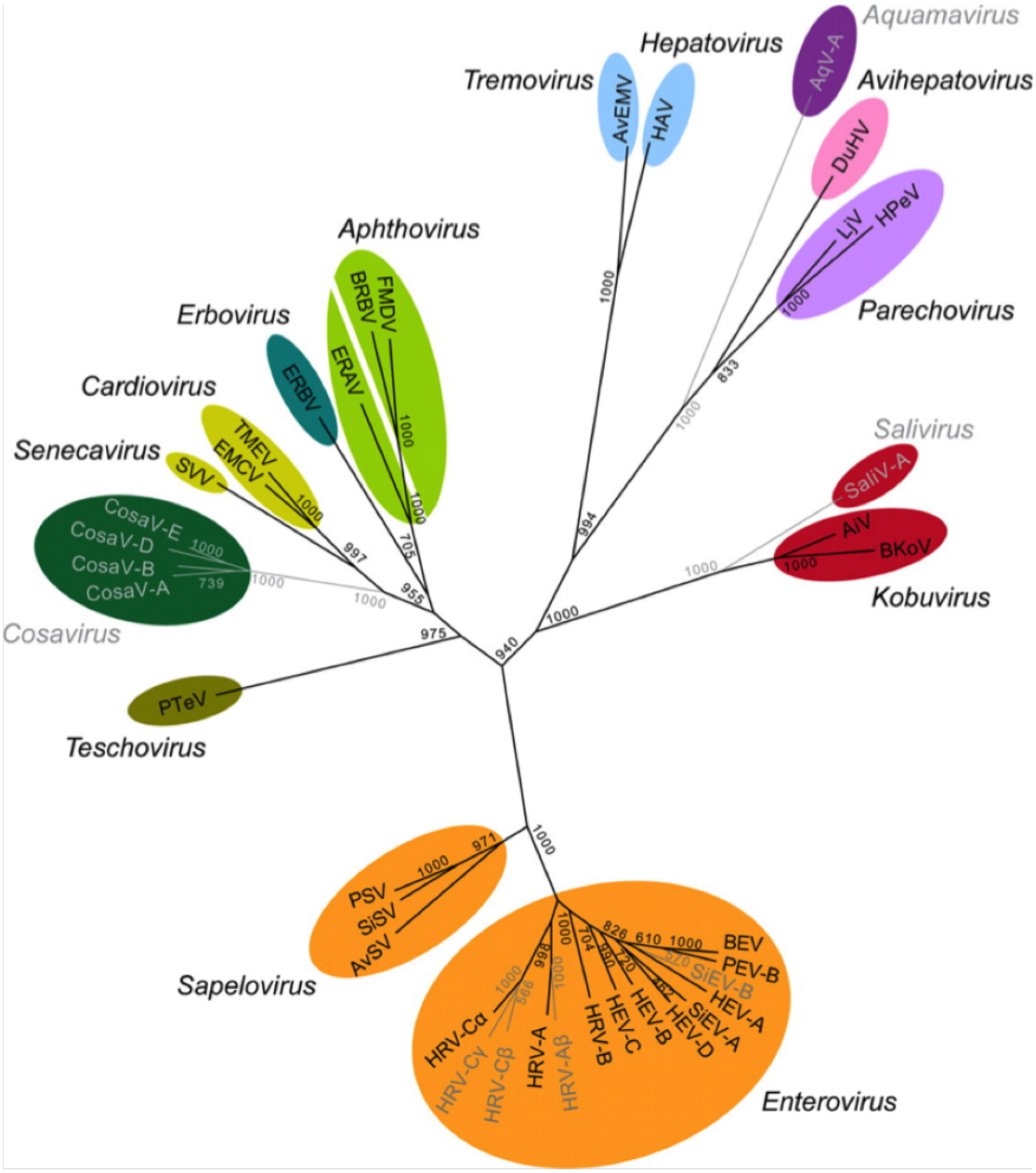


Figure 1.2: A phylogenetic tree depicting the maximum-likelihood based evolutionary relationship between the major (black lines) and provisional (grey lines) taxa in the *picornaviridae*, based on the conserved structural proteins VP1-3 and non-structural proteins 2C, 3C and 3D. Taken from Lauber et al., [1].

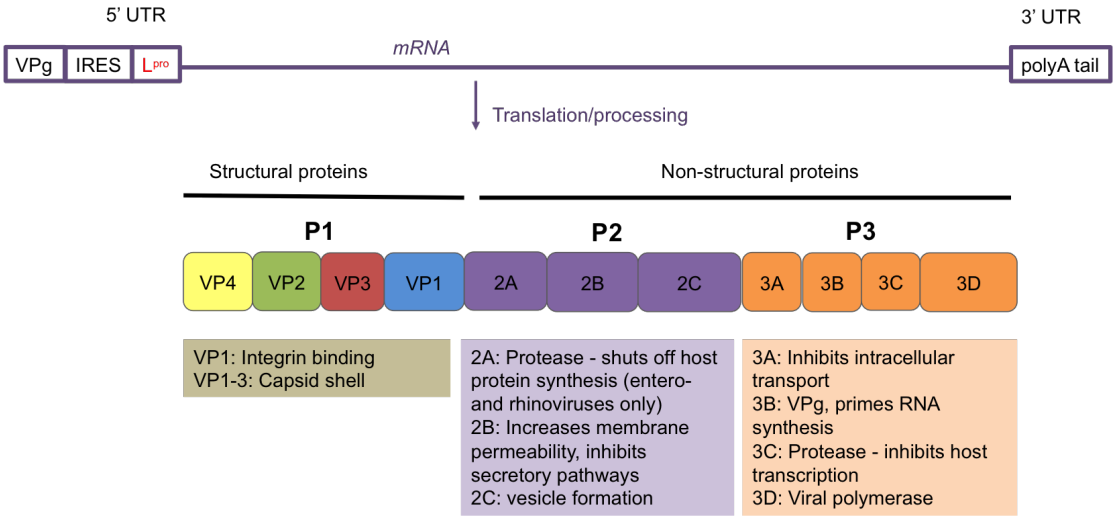


Figure 1.3: The genome organisation and respective functions of structural and non-structural proteins in FMDV. Based on a review by Whitton et al., 2005 [4].

1.2.1 *Picornavirus* genome

The picornavirus genome (Figure 1.3), is between 6,500 and 9000 nucleotides in length; most of it encodes for a single polyprotein which results in the formation of 11 - 13 mature proteins post-cleavage [1, 5]. It is translated as a single long open reading frame (ORF) into a polyprotein. One third of the polyprotein codes for structural, and the remainder for non-structural proteins. The cleavage of this polyprotein by viral proteases (such as L(pro) and 3C) generates these structural and non-structural proteins [6–8]. The 5' and 3' untranslated regions or UTRs also play a role in viral replication. These regions have several parts that play a role in translation and viral replication. Attached to the 5' end of the genome is the genome-linked protein (VPg), which performs a role in acting as a primer for RNA synthesis. Next comes an untranslated region which acts as an internal ribosome entry site (IRES), by forming a landing site for the ribosome, which assists in translation, and the cis-activating replicative element (*cre*) which helps

in genome replication [9–13]. The 3' end has a poly-adenine tail which serves as a site for the negative-strand RNA replication complex to bind to, stabilises the viral RNA and plays an important role in replication [14–18].

In the case of *aphthoviruses*, the polyprotein has an additional protein, the leader or the L-region, at the amino terminus, preceding the P1(capsid) region, which is also responsible for encoding the two AUG initiation codons [7, 19]. This is followed by P1, which encodes the structural proteins VP0, VP1 and VP3, that self-assemble to form a capsid. VP0 cleaves into VP2 and VP4 upon the maturation of the capsid; VP2 forms part of the capsid together with VP1 and VP3, and VP4 is internal. The subsequent P2 and P3 regions encode the Non-Structural (NS) proteins. The functions of these proteins, which include specific proteases and the viral RNA-dependent RNA polymerase, are shown in Figure 1.3 [20–22].

1.3 Foot and Mouth Disease Virus

1.3.1 The virus

Foot-and-mouth disease virus (FMDV) belongs to *aphthovirus* genus (Figures 1.1 and 1.2). It was the very first animal virus identified, by Loeffler and Frosch, in 1897 [23] and is a highly contagious pathogen that infects cloven-hoofed animals such as cattle, sheep, swine and goats. There exist seven known serotypes of FMDV, namely South African Terrorities (SAT)1, SAT2, SAT3, Asia1, A, O and C, and each have several sub-serotypes. The symptoms of an FMDV infection are fever, lesions and blisters in the mouth and on the hooves, which may

burst and often lead to lameness in the infected animals. The disease is not usually fatal in adult animals, however it is economically important since it causes reduced milk production, weight loss, reduced draught power and can kill young animals [24]. The virus is spread mostly through the infection of the respiratory tract via aerosols but can also be spread indirectly by contaminated vehicles, equipment, clothes, shoes and skin. Some animals may act as carriers of the virus, transmitting it to more susceptible animals [25, 26]. As a result, FMDV is one of the most important economical constraints to international trade in animals and animal goods [24, 27]. The last major outbreak in the UK in 2001, that affected 23 european countries, was a reminder of the severe economic consequences of FMDV [28, 29]. Due to its potential biological danger, FMDV is a Biosafety-level 4 pathogen and can only be studied in highly secure laboratories, under strict containment conditions.

1.3.2 The capsid

Like many other *picornaviruses*, FMDV particles are roughly spherical, icosahedral, non-enveloped protein shells, around 30 nm in diameter. Several FMDV capsid structures have been determined using X-ray crystallography and electron microscopy [31–35]. Each FMDV pentamer consists of 5 copies of the protomer subunit consisting of one copy each, of the capsid proteins VP1 (32kDa), VP2 (28kDa), VP3 (27kDa), and VP4 (8kDa, buried within the capsid). Twelve such pentamers form an icosahedral arrangement in the capsid structure. This is a T:1 icosahedral structure; however, VP1-3 are broadly similar to each other and are arranged such that the capsid has a pseudo T:3 quasi-symmetry. The capsid

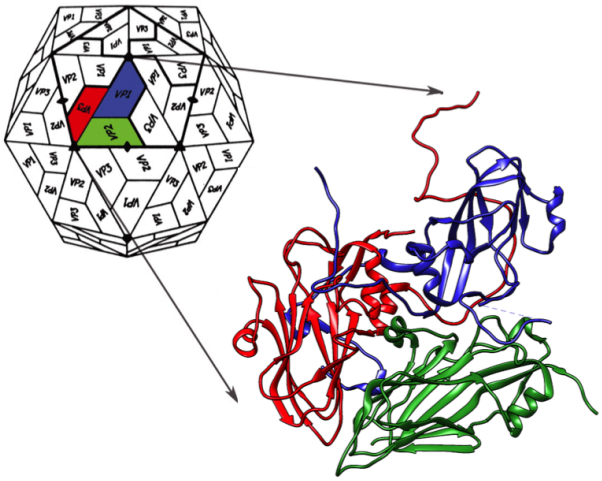


Figure 1.4: A schematic figure showing the arrangement of the viral proteins in a capsid and the location of the biological protomer forming the FMDV capsid. The 5-fold symmetric pentamer is highlighted with a dark black outline. An enlarged cartoon representation of the secondary structure of the biological protomer comprising VP1 (blue), VP2 (green) and VP3 (red) is also shown. Modified from Fry et al., 2005 [30].

organisation is such that the five VP1 proteins in each pentamer interact at the five-fold axis of the pentamer and the VP2 and VP3 proteins alternate at the inter-pentamer interfaces. Figure 1.4 shows how the different proteins are arranged in a capsid and also highlights the individual biological protomer comprising of VP1, VP2 and VP3; as VP4 is internal to the capsid, it is not displayed here.

There are extensive interactions within each pentamer, especially through VP4 and the N-terminal extensions of VP1-3, making these assemblies rather robust. The capsids are then held together by weak hydrophobic, electrostatic and hydrogen-bond interactions between the pentamers [31]. They are extremely sensitive to elevated temperature [36] and low pH [37, 38]. Under these conditions, the capsid readily dissociates into pentamers. The low-pH sensitivity presumably facilitates the release of the virus genome inside the cells, in the acidic compartments of

Virus serotype	Inactivated virus	Untreated virus
	50 percent reduction time (min)	
SAT1 (Bot 1/68)	2.5	2.5
SAT2 (Bot 3/77)	2.5	7
SAT3 (Bec 1/65)	5	7
O (BFS 1860)	4	16
C (Noville)	6	40
Asia1 (Iran 1/73)	36	315
A (Cruziero)	100	340

Figure 1.5: Table showing the different thermal stabilities of the seven FMDV serotypes, based on Doel et al [36]. All serotypes were heated at 49 °C and the time observed for the live virus particles to be halved, using spectrophotometry, was noted.

the cell such as the endosomes, and it is proposed that this occurs due to the acidification of the histidine residues at the inter-pentameric interfaces [39, 40]. The sensitivity to high temperature varies between the different FMDV serotypes, and between the native untreated and inactivated capsids of the virus as well, as shown in Figure 1.5 [36]. The SAT serotype viruses are the most unstable, as indicated by their rapid disintegration (Figure 1.5), and therefore present the greatest difficulties in vaccine development. The results presented in later chapters indicate that different FMDV strains, even within the same serotype, may have very different thermal stability. This may be due to different selection pressures on the virus in different outbreaks, leading to variation in the protein sequences. Our SAT3 strain (SAR/02/06) was much more unstable than SAT1 or SAT2, unlike the results shown in Figure 1.5.

1.3.3 Life cycle

Figure 1.6 highlights the different stages in the replication cycle of FMDV. The replication cycle is short, taking about four hours from the point of infection. The

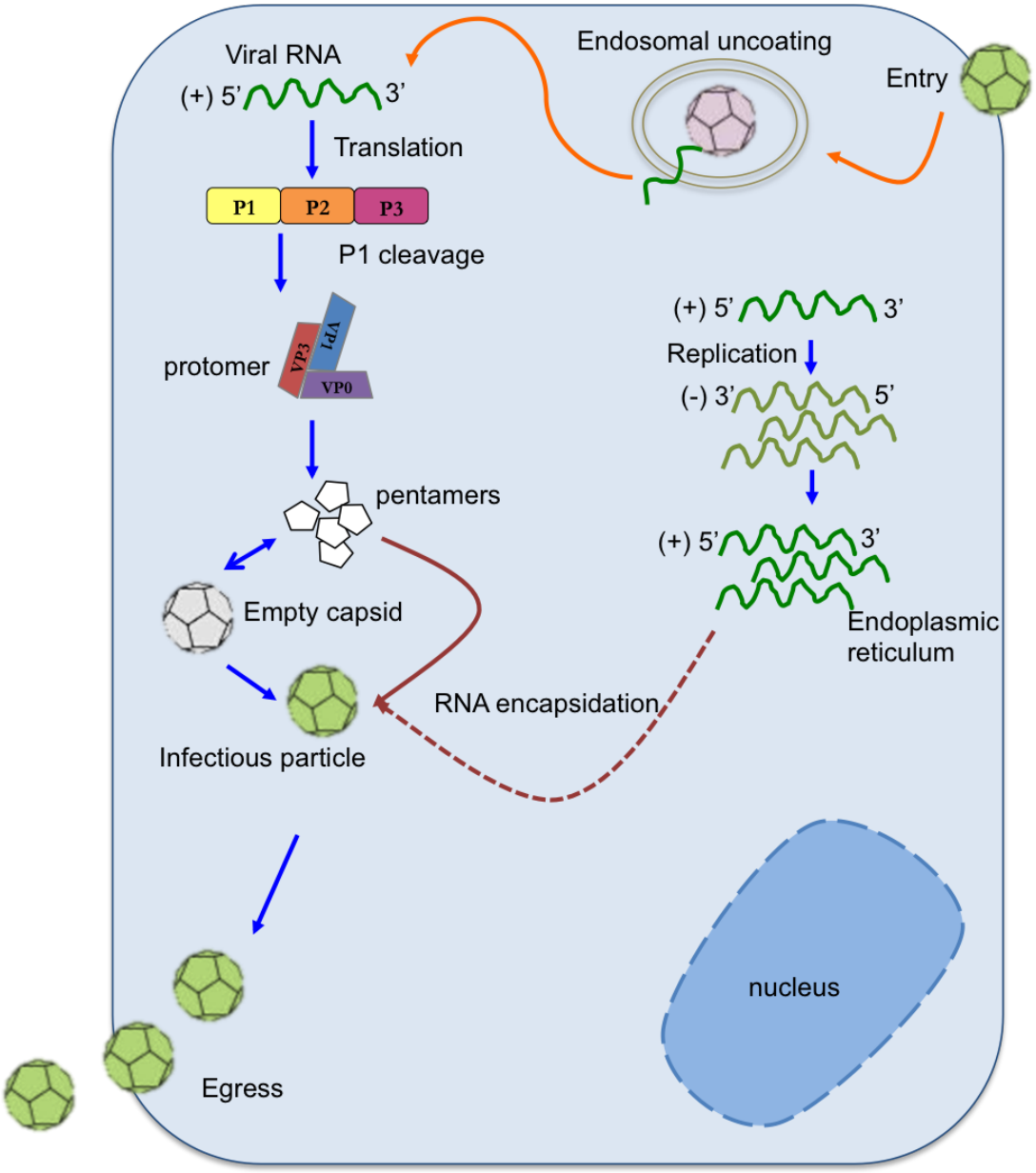


Figure 1.6: Illustrating the main steps of the infectious cycle of the foot-and-mouth disease virus. Based on Hogle et al., 2002 [41].

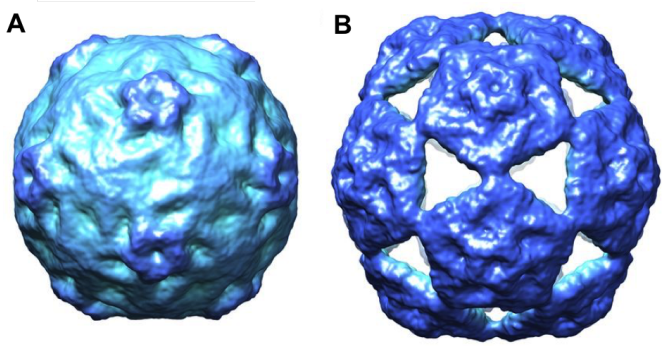


Figure 1.7: Structures of (A) native and (B) the claimed disassembly intermediate of ERAV at 16.9 Å and 17.4 Å respectively. Modified from Bakker et al., 2014 [42].

virus capsids attach to the host cells' integrin receptors using a flexible VP1 loop called the βG-βH (or GH) loop (roughly residues 135-160). This immunogenic GH loop has been shown to have a highly-conserved Arg-Gly-Asp (RGD) motif, that acts as the integrin receptor binding site [43–45]. The GH loop has not been shown to have the same immunogenicity in the case of dissociated capsids, potentially because it might be in a different conformation in the capsid vs. the standalone pentamer. Three RGD-specific integrins have been reported as FMDV receptors so far: αvβ1, αvβ3 and αvβ6 [45–51]. If this sequence is deleted by mutagenesis, the virus loses the ability to infect and cause disease in animals [52–54]. Tissue-culture adapted FMDV capsids may also bind to the Heparan Sulphate (HS) receptor [55, 56].

After uptake into the cells via endosomes the acidic environment causes the capsid to break down into its pentameric units and release the RNA [37, 57, 58]. This disassembly process in the endosomes is not well-understood for FMDV and it is unclear if there are any intermediate stages in FMDV disassembly; there are no structural studies thus far on the dissociated pentamers either, which might

help elucidate the dissociation mechanism for FMDV. VP4 and the N-terminus of VP1 are believed to play a role in membrane penetration so as to allow the viral genome to traverse the membrane of the cell's acidic compartments in order to enter the cytoplasm. This is the case for *enteroviruses*, where they are shown missing from the disassembly intermediates [59–62], but no structural evidence for this mechanism exists for *aphthoviruses* yet.

There have been several studies on *picornavirus* disassembly intermediates [42, 59, 61–66]. For enteroviruses such as human enterovirus 71, coxsackievirus A16 or poliovirus, it was demonstrated that they form an expanded or "breathing" particle, as an intermediate stage of virus uncoating, where VP1 N-terminus is transiently exposed and could even be visualised [64,67]. Thus far there have been no such structures showing an FMDV disassembly intermediate and there is no evidence to prove that such an intermediate exists. The closest structure mooted to be a potential disassembly intermediate of another *aphthovirus* is that of the equine rhinitis A virus (ERAV) [42], for which an intermediate particle formation has previously been proposed [63]. As shown in Figure 1.7, Bakker and colleagues claim that this expanded particle (Figure 1.7 (B)) has huge structural rearrangements compared to the native (Figure 1.7 (A)) and large gaps through which the genome is proposed to be released. The solved structures are low-resolution, which hinders detailed analyses. Furthermore, taking our results in subsequent chapters into account, this proposed disassembly intermediate might not necessarily be such, but rather a result of the mis-assembly of dissociated pentamers.

Once released in the cytoplasm of the host cell, the virus genome is subsequently

translated and replicated, as depicted in Figure 1.6. Protein synthesis results in a single polypeptide, which undergoes cleavage into structural and non-structural proteins by different proteases [7, 68–73]. In particular, the P1 section of the polypeptide is cleaved into VP0, VP1 and VP3, the capsid-forming protomer.

Meanwhile, during the replication of the genome for re-packaging into new progeny capsids, the minus-strand RNA molecule acts as a template for the formation of several plus-strand RNA molecules [74]. These reactions are catalysed by the FMDV RNA-dependent RNA polymerase encoded by 3D region of the polyprotein (Figure 1.3). The newly assembled plus-strand viral RNA is encapsidated to form immature capsids, 12 pentamers each, and contain five biological protomers consisting of VP0, VP1 and VP3. The maturation of the capsid is triggered by an autocatalytic cleavage of VP0 to VP2 and VP4, once the RNA is packaged [75–77], as it is essential to the formation of infectious virus particles [78–80]. VP4 is also implicated in the stabilisation of the virus particles, by forming stabilising interactions with the N-termini of the capsid proteins [75], and therefore plays a crucial role in the maturation of the virus. FMDV is a cytocidal virus and kills the cell as the new progeny virus bursts out of it at the end of the replication cycle.

1.3.4 Immune response

Once infected, the host responds by producing protective antibodies against the virus. However, a good antibody response takes between 7 and 14 days to become apparent. As a result of the infection, the T-cell count in the host decreases over the first four days [81]. This suggests a lowering of the host's defences by the

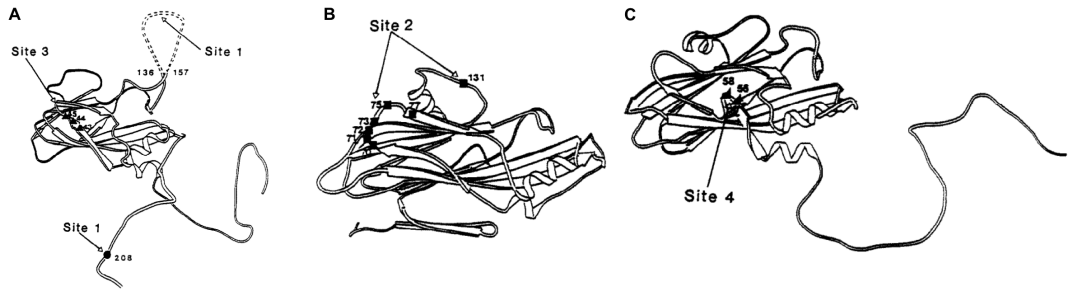


Figure 1.8: Figure showing the locations of the four antigenic sites determined in the FMDV serotype O1K, that are analogous to the ones in A10. The three capsid proteins are separated in panels showing (A) VP1, (B) VP2 and (C) VP3. Modified from Kitson et. al, 1990 [86].

virus to help the infection spread. The FMDV infection also generates a dominant B-cell response to help fight the spreading virus.

The FMDV genome, by virtue of FMDV being an RNA virus, has a high rate of mutation [82,83]. This high frequency of mutation, especially with no error correction mechanism in the polymerase, affects the capsid proteins as they are exposed to the environment and thus have to evade the host cells' immune system [84]. As a consequence, there is a large antigenic variation between the different serotypes and sub-serotypes of FMDV, which in turn has consequences for vaccine efficacy. Escape-mutant studies are often used to characterise the antigenic sites for the different strains of FMDV [85].

1.3.5 Antigenic variation

As mentioned, FMDV is a rapidly mutating RNA virus. Its surface residues face selection pressure due to their exposure to the host cells during infection, and therefore mutate in order to evade the immune response from the host [87,88]. The mutations in the surface epitopes recognised by the antibodies to evade the host's

	O	A	SAT1	SAT2
Site 1	1144-1149, 1154, 1208	1142-1153, 3175-3178	1146, 1148, 1154-1157	1154, 1210
Site 2	2070-2077, 2131-2134	2080, 2196	2072	2072
Site 3	1043-1048	1169	1048	
Site 4	3056-3058	3058-3061, 3069-3070, 3136, 3139, 3195,	3071, 3076, 3135	
Site 6			1135, 1175, 1179, 1181	
Site 7			1181	
Site 8			1111	

Figure 1.9: A list of the antigenic sites known from different FMDV serotypes, mined from several studies that performed escape-mutant studies [85, 86, 89–91]. Syntax: first digit represents the viral protein (VP) and the last three quote the residue number.

immune system result in a large sequence variation between the serotypes. There are significant variations even within the sub-types of the same serotype. Studies determining the antigenic sites on the surface are thus crucial to the vaccine-development efforts in the field, as these mutations result in the vaccines directed against one serotype ineffective against the others. Several groups have aimed to characterise the specific epitopes recognised by the MAb (monoclonal antibodies) in order to better characterise the antigenic sites for different serotypes of the virus, using MAb resistant (MAR) or escape-mutants [86, 89–92].

Figure 1.9 lists the residues implicated in antigenicity in serotypes O, A, SAT1 and SAT2 [85, 86, 89–91]. The locations of the four major antigenic sites (from O1K) are marked on individual capsid proteins VP1-3 in Figure 1.8 to show their location on the structure [86]. The mapping of antigenic sites must be performed for each serotype, as they might differ due to high inter- and intra-serotype sequence vari-

ability (the mean sequence identity between SAT3 and the four serotypes shown here was 44% - Appendix C).

1.3.6 Outbreaks and economic implications

Since the beginning of the 20th century, FMDV outbreaks have lead to the culling of millions of animals and huge economic losses. A number of specialised institutes were created to respond to the outbreaks of this highly infectious virus, for instance Insel Riems in Germany in 1909, The Pirbright Institute in the UK in 1924, Lindholm Island in Denmark in 1925, Centro Panamericano de Fiebre Aftosa in Brazil in 1951 and the Plum Island Animal Disease Center in the US in 1953 [93].

Looking at the history of the virus shows that the 1930s saw the invention of the first inactivated vaccine, which was obtained by infecting animals, slaughtering them and obtaining their epithelium and vesicular fluids [93]. This method could not produce large amounts of vaccine doses which were required in case of outbreaks. It was only after Frenkel and co-workers discovered that viruses could be produced by infecting the epithelium of a bovine tongue, obtained after healthy animals were slaughtered, that the commercialisation of the FMDV vaccines really started [94]. The current method of growing virus in culture, harvesting and inactivating it to vaccinate animals is based on these early experiments. This lead to a dramatic reduction in the incidences of FMDV in Europe. About a billion doses of FMDV vaccines were being produced annually worldwide in the 1990s, but as there were no outbreaks after 1989, in 1992 the EU adopted a no-vaccination policy [95, 96].

After some minor outbreaks, it was in 1997, in Taiwan, that the virus re-emerged to international significance. After 68 years of being FMDV-free, Taiwan had an outbreak of O/Taw/97 strain, which spread enough in 3 weeks to cause 38% of the entire population of pigs (roughly 4 million) to be slaughtered and cost billions of dollars in economic losses [97]. In late 1999 and 2000 a series of outbreaks occurred in East Asia, South Africa and the UK and Europe, caused by the O PanAsia serotype [28]. This was the first outbreak in the UK since 1981 and went unnoticed for 3 weeks, during which it spread to 16 of the 23 countries affected in the outbreak [29]. It lead to the slaughter of 6.5 million animals and the losses were estimated to be between US $12.3 - $13.8 billion [29]. It was only in 2002 that the UK regained it's no-vaccination FMDV-free status [29].

1.3.7 Vaccination

Developing or underdeveloped countries cannot realistically adopt the strategy of culling all potentially infected animals in the case of an outbreak, yet they are the ones hit the hardest by such outbreaks [85]. This highlights the need for a good vaccination strategy, and more crucially the development of better vaccines. Due to the high antigenic variation between different serotypes, current FMDV vaccines do not offer cross-protection. This also poses the challenge of the possibility of mutations during the virus production process, as the virus needs to be passaged several times in cell culture during vaccine production in the current methods. These methods require working with the live virus in expensively maintained high containment facilities, but nevertheless runs the risk of introducing

the live virus in the animal population in case of leaks from vaccine-production facilities [98]. Such an incident occurred in the UK in 2007 when a drainage pipe from the Pirbright facility leaked [99]. Furthermore, as the immune response takes several days to kick in, the animals are still susceptible to infection several days post-vaccination, in case of an outbreak.

As a result of these challenges, FMDV vaccine development is an actively researched topic [100]. There have been efforts in preparing peptide-based vaccines that do not depend on work with the live virus. Furthermore, there have been recent studies attempting to create thermally stable vaccine candidates and also ones using recombinant capsids instead of the live virus [101–103]. The question of generating chimeric vaccines that offer cross-protection against several serotypes of FMDV still remains unresolved.

1.4 Overview and aims

This thesis aims to cover structural characterisation of the FMDV disassembly products. The main question to address was: could we capture a disassembly intermediate for this *picornavirus*. Particles observed after acid treatment of the virus were investigated to understand if they were disassembly intermediates or whether they were formed by re-assembly of dissociated pentamers. This concept is illustrated in Figure 1.10.

Chapter 2 is a methods section covering the details of electron microscopy, the technique used in all the projects herein. Both the theory and the practical steps

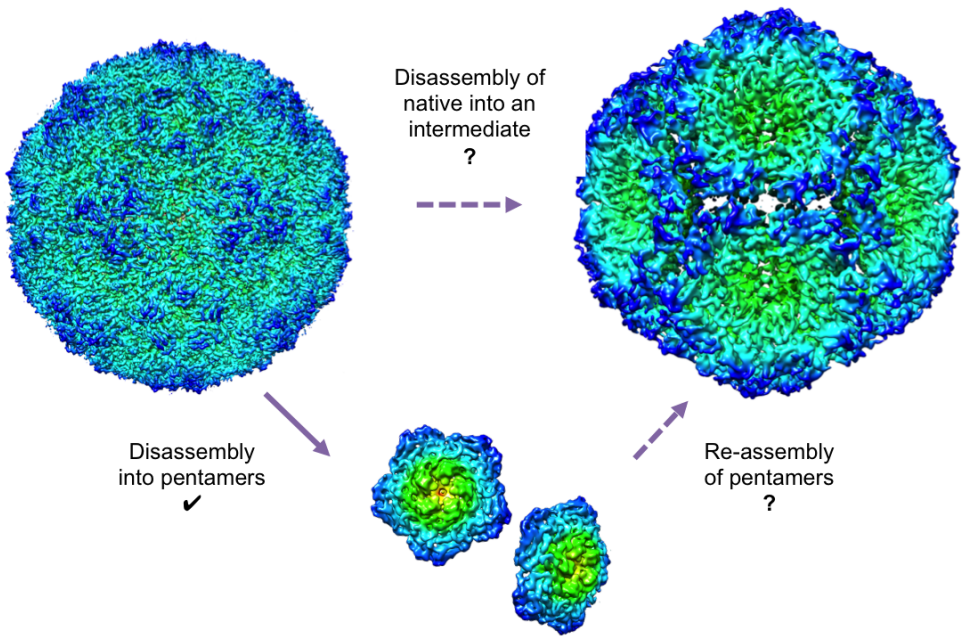


Figure 1.10: Project overview: The different theories to explain the FMDV intermediate structure illustrated.

are explained in detail. Chapter 3 focuses on the structure determination of the native FMDV serotypes, SAT1 and SAT3. SAT3 had no known structure published previously; therefore the next chapter, Chapter 4, focuses on the comparison of SAT3 to other SAT serotypes and subsequently also to other major serotypes: A and O. Chapter 5 then proceeds to cover the results of our studies to understand the uncoating intermediate of FMDV and Chapter 6 provides the results on the dissociated pentamers, the end-product of the virus disassembly during infection. Lastly, Chapter 7 concludes the thesis with future outlooks.

Please note that there are stereo-viewing glasses attached at the end of this thesis, for 3D-viewing the structures presented here in a "wall-eyed stereo" representation.

Chapter 2

Electron microscopy

2.1 Chapter summary

All the projects in this thesis rely on electron microscopy (EM). Therefore, to avoid repetition, this chapter will focus on the electron microscopy methods used in the different parts of the projects, and the theoretical background behind them. The specific results from each of the processing steps will be included in the respective chapters later.

Electron microscopes have existed since 1931, when Ernst Ruska and Max Knoll built the first one in Berlin, expanding on the principles of Louis de Broglie from 1924. De Broglie had shown that material particles had wave-like properties and this could be exploited using fast-moving electrons, in an electron microscope, to surpass the resolution limit of light microscopy [104].

The basic structure of an electron microscope remains the same to date, with

a column under high vacuum and an electron source at the top, a camera or an electron detector at the bottom. The following sections provide a summary of how the microscope hardware, combined with image detection and reconstruction methods produces the high-resolution images of biological specimens that are now possible.

2.2 Hardware

2.2.1 The column and the electron source

The electron emission source at the top of the TEM column is responsible for emitting coherent, fast moving electrons, that are used for imaging the specimen. A strong current (for thermionic emission in case of Tungsten filaments or LaB6 crystals) or a strong magnetic field (in case of Field Emission Guns or FEGs) is applied to the electron source, to cause electron emission. These electrons are accelerated through the column, due to a strong electric field generated by having a plate at 0 V at the bottom, and therefore have extremely high speeds and a small wavelength for high-resolution imaging. For example, the 300kV electrons used for single-particle analysis here have a wavelength of about 0.02 Å.

In this study, several different microscopes were used with different electron sources. Field Emission Guns (FEGs) produce the brightest and the most spatially (all electrons coming from the same direction) and temporally (all electrons having the same speed) coherent electrons, which results in sharper images due to better focusing by the lenses. This coherence is a result of the field surrounding the

filament, pulling out the electrons, instead of electrons escaping at random. Therefore the higher end microscopes used for high resolution cryo- electron microscopy, the Technai F30, the Polara and the Titan-Krios (FEI Company), all have FEGs, whereas the low-voltage microscopes used for negative-stained electron microscopy have a LaB6 crystal as the electron source.

Electrons are prone to strong interactions with matter. Therefore, to ensure that they are not scattered by anything other than the specimen, the microscope column is kept under high vacuum (typically around 10^{-5} Pa). The maintenance of a high vacuum is achieved by several pumps, to prevent sample contamination and ensure a long, free path for the electrons to accelerate through.

2.2.2 Lenses and apertures

Electromagnetic lenses are used to focus the electrons in an electron microscope. They work using the principle that current passing through a coiled wire produces a magnetic field, which can be used to focus electrons. Lenses in an electron microscope are essentially copper coils with current flowing through them, generating a magnetic field. Changing the current through the coils can change the strength of the magnetic field and therefore the focusing power of the lenses.

In a typical electron microscope, the electrons from the source first pass through an accelerator stack which has a high voltage difference across it, and serves to accelerate the electrons to very high velocities. The electron beam then passes through the condenser lens system, that focuses the beam onto the specimen. Af-

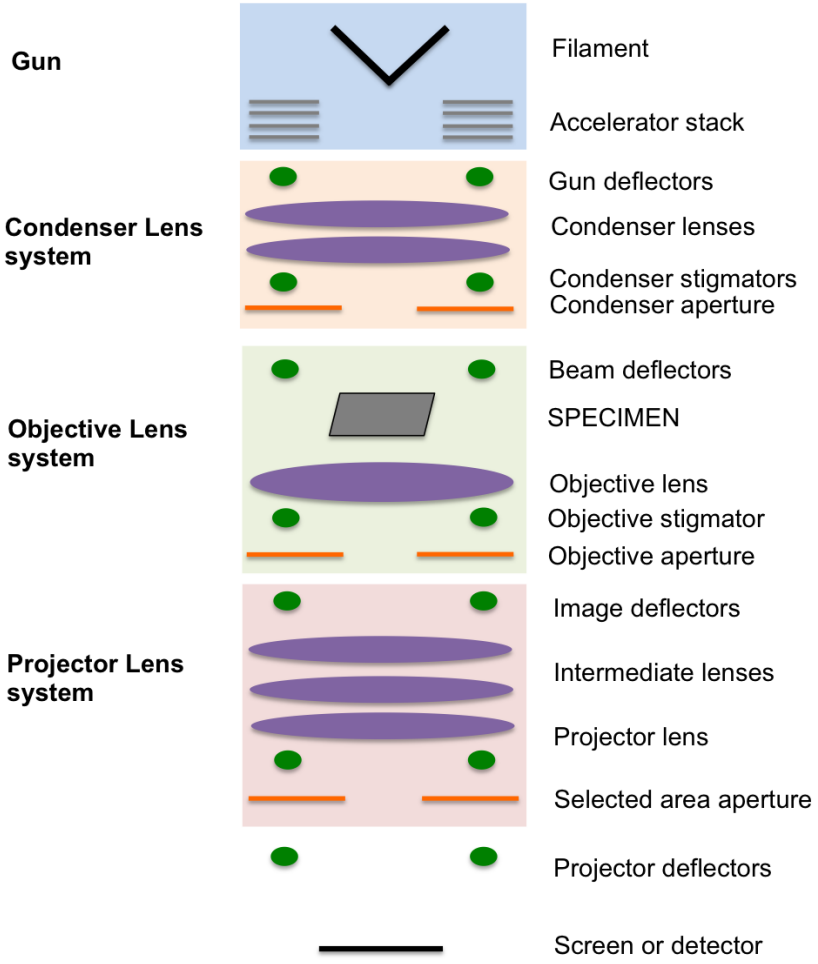


Figure 2.1: Schematic depiction of the main components of a typical electron microscope (after Grant Jensen's Caltech lecture series).

ter passing through the specimen, the electrons pass through the objective lens, which in turn deflects the electrons in a manner such as to produce a magnified image. This electron beam from the sample is subsequently further magnified by the projector lens system onto the detector at the end, generating the final image.

The different lens systems can be modified to produce a range of magnifications by altering the current flowing through them. Each lens system has deflectors, to change the course of the electron beam if necessary, and stigmators, to produce or correct the magnetic field to alter the beam path if it deviates from the axis. The electron beam also has to pass through the condensor and the selected-area apertures, that remove different parts of the beam or the image by removing the inelastically scattered electrons for instance, to reduce the interference and increase the amplitude contrast [105, 106]. An energy-slit may be introduced to filter out the inelastically scattered electrons, that contribute noise to the high-resolution images, for imaging in the EFTEM (Energy Filtered Transmission Electron Microscopy) mode. The lenses and apertures have to be extremely well-aligned to produce a sharp, in-focus image.

A schematic diagram illustrating the main lens components of the electron microscope can be seen in Figure 2.1.

2.2.3 Specimen holder

The sample is applied to the EM grid and vitrified beforehand (explained in the later sections). Vitrified grids are clipped into insertion rods of various kinds under

liquid nitrogen. The mechanism of insertion varies depending on the microscope in use. Side entry holders, e.g. for the Tecnai T12 and TF30 microscopes (FEI Company), have a small dewar attached to the insertion rod, to maintain the sample at a low temperature. They only allow loading of one sample at a time and are not ideal for imaging over a long duration. The Polara and Titan-Krios microscopes (FEI Company) have multi-specimen rods, allowing loading of several samples at once, which can later be selected one by one by the insertion rod for insertion into the column. This loading mechanism is much more stable and better suited for high throughput data collection over several hours, even days at a time. The grid, once inserted into the column, stays at ultra-low (below $-170\,^{\circ}\mathrm{C}$) temperature for imaging in the vacuum.

2.2.4 Detectors

Detectors may be electronic or chemical (i.e. the photographic film), but the latter were not used in this study. While photographic film does allow high-resolution imaging, it has to be developed and digitised before use. Due to the very slow response time of this process, digitisation is performed at the end of the session, after collecting the entire data set. This is not ideal for screening difficult samples or tweaking microscope settings to optimise the imaging, as the data are not easily and immediately accessible. At the Division of Structural Biology (STRUBI) at Oxford, the use of film has now stopped due to it being time consuming, tedious and causing contamination problems. The two kinds of electronic detectors used for this study are introduced below.

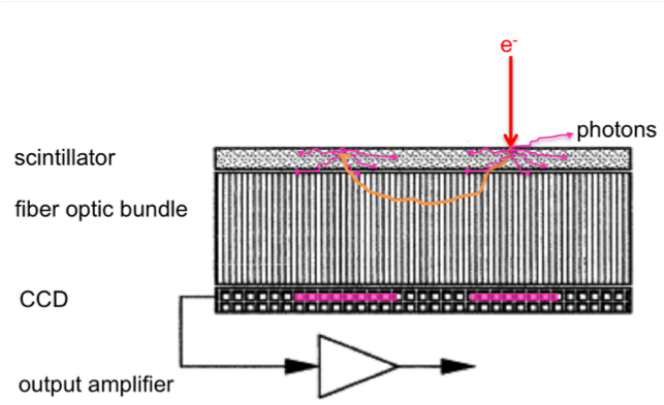


Figure 2.2: Schematic depiction of how a CCD camera operates. Incident electrons from the column (red) on the scintillator cause the emission of photons (pink), which are transmitted by the fibre optic bundle to the respective CCD pixels, where the photons are converted into counts. The CCD chip is read out at the end of the exposure to produce a digital image. The electron might be scattered several times within the scintillator, producing photons upon each scattering event and thus resulting in several counts on the CCD detector, looking like a large spot. If the electron is scattered to quite some distance away (orange path) from where it was incident, the same incident electron might produce two separate spots on the CCD detector, as shown. Modified from Downing et al., 1999. [107]

2.2.4.1 CCD cameras

Charge-coupled device (CCD) cameras, invented in 1969 [108] largely replaced photographic film over the last decade. The top layer of the CCD detector is a scintillator. The electrons from the column hit the scintillator, producing photons. These photons are transferred by a fibre-optic bundle to the CCD pixels, where they are converted to electron counts. After each exposure of the specimen to the electrons, the electrons counts on each pixel on the CCD detector are read out to produce a digital image, in a matter of seconds [107]. CCD cameras thus allow for quick and automatic data collection.

However, the CCD camera also has some limitations. The incident electron may be scattered several times inside the scintillator and produce photons each time

that happens [107]. As a result, several photons would be counted by a group of pixels in the CCD detector for each electron contributing to the image. This results in a diffused, large spot on the detector, as shown in Figure 2.2 by the colouring of several pixels in the CCD detector as pink and the quality of data collection at high resolution suffers. There might also be noise in the image if an electron is scattered to a large distance away from the incident position and re-enters the scintillator, thus producing photons in the second incident position as well. The CCD detector would read counts from the second spot as well as the first in this case, generating two spots for a single electron, producing noise in the image. Overall the result is that the CCD cameras have a substantial point-spread function and an effective efficiency less than the film, but a much faster read-out.

2.2.4.2 Direct electron detectors

The latest breakthrough in imaging technology used in cryo-EM came in the form of direct electron detectors, resulting in the recent *resolution revolution* or the *quantum leap* in cryo-EM data collection [109, 110]. In this case, the incident electrons are detected directly by a complementary metal-oxide-semiconductor (CMOS) chip and converted to charge [111]. Thus the counts produced by individual electrons are much less spread out and there is also a dramatically reduced back-scattering of electrons. This results in preservation of high-resolution information in the image, even at low electron dose, reduced noise and much better contrast [112]. The detectors are read out several hundred times per second, resulting in a much faster read out, which is key in single-electron counting and acquiring high-resolution images. The direct detectors record a series of frames, several per second, to produce movies instead of single-projection images. This

feature allows the computer to keep track of any sample drift due to beam-induced motion and later motion-correct it to further reduce the blurring of the image [113].

2.2.4.3 Comparison of electronic detectors

Perhaps the single most important characteristic of a detector for cryo-EM is the Detector Quantum Efficiency (DQE). It is essentially a measure of the noise added to the images by the detector and is defined by the ratio of the square of the signal-to-noise ratio (SNR) of the output, to that of the input [114].
Effectively:

$$DQE = \frac{SNR(output)^2}{SNR(input)^2} \tag{2.1}$$

and it varies as a function of spatial frequency (in the case of an imaging detector, this corresponds to resolution or a fraction of Nyqvist; where the Nyqvist limit is the minimum discreet sampling that faithfully reproduces the information in the original signal). An ideal detector would not add extra noise to the output and therefore have a DQE of 1, but in reality all detectors have a DQE of less than 1. This especially affects cryo-EM, where the signal-to-noise ratio in the data is already low.

A comparative analysis of the DQEs of different electronic and chemical detectors is shown in Figure 2.3. As the figure shows, direct electron detectors consistently outperform the photographic film (grey line, panel (A)) and the CCD cameras (brown line for CCD camera US4000, panel (B)). The detector used for the data collection in this thesis, K2 Summit (Gatan Inc.), is widely regarded as the most competent detector currently available, as confirmed by the results in Figure 2.3.

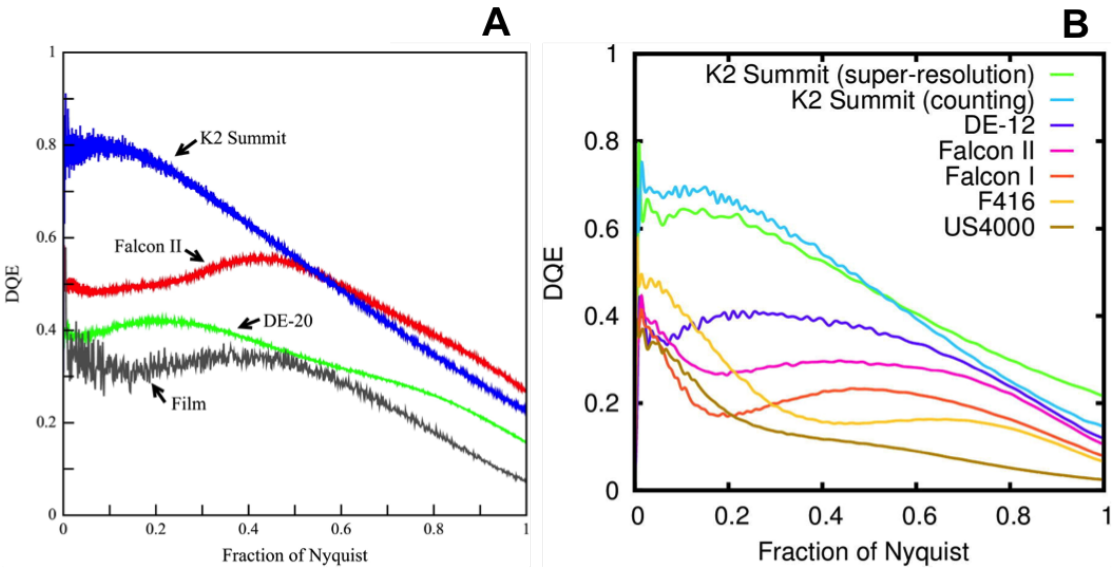


Figure 2.3: A comparison of the DQEs of (A) film vs. three direct electron detectors and (B) US4000 CCD camera vs. several other modes of direct electron detectors. Modified from McMullan et al. and Ruskin et al., [115, 116].

2.3 Sample preparation and data collection

Biological samples have to be preserved in some form to be studied using Transmission Electron Microscopy (TEM), as they are subjected to a high vacuum and thus cannot be imaged live and unprotected [117]. Classical electron microscopy (EM) methods used here involve staining the sample with heavy-metal salts, such as uranyl acetate or uranyl formate, to provide high amplitude contrast [118]. The stain deposits on top of and around the sample on the carbon-coated support surface of the grid and produces a strong signal detected on each exposure. While this method is the most common method used for TEM, it does not allow the imaging of the specimen in physiological conditions. The latest advances in EM data collection involve plunge-freezing or vitrifying the biological sample and imaging it in vitreous ice in a frozen-hydrated form [119, 120]. The methods, along

with the advantages and disadvantages of each are explained below.

2.3.1 Negative-stain electron microscopy

Formvar/carbon-coated grids (Electron Microscopy Sciences) were glow-discharged in a plasma cleaner to make the surface charged before applying the sample, so as to allow better adhering. Subsequently, an aliquot of 3 - 5 μL was applied to the grid and allowed to adhere for 30 - 60 seconds, before the excess liquid was blotted away. The grid was washed twice, by swirling it around in a droplet of de-ionised water, and blotted to remove the liquid each time, ensuring that the un-adsorbed sample and any contaminants were removed. Care was taken to not allow the grid to dry between these steps. Finally, a drop of 1% uranyl acetate or uranyl formate was added on top of the sample, allowed to settle for a minute, and blotted dry. The stain settles around the particles, which appear light against the dark background of the stain, thereby giving the technique its name.

2.3.2 Plunge-freezing for cryo-electron microscopy

All the cryo-EM grids for this study were prepared in a Vitrobot (FEI). The Vitrobot provides a humidity-controlled environment to prevent the grids from drying out during the blotting and plunging process. 4 μL of the sample were applied to glow-discharged holey carbon-coated C-flat grids (C-flat, CF-2/1-2C, Protochips), in a chamber kept at 90% humidity. After a 30-second incubation the grids were blotted to remove excess liquid and plunged in liquid-nitrogen-cooled ethane, for rapid heat transfer from the specimen [121]. This rapid-cooling ensures that the water in the specimen is vitrified, not crystallised. The grids were stored

in cryo-grid boxes under liquid-nitrogen until imaging time was available.

2.3.3 Data acquisition

All cryo-EM grid handling was performed under liquid nitrogen in special transfer stations. The grids were placed in a side-entry holder or a multi-specimen rod, depending on the microscope used, and kept cooled during insertion into the column. The column was allowed time to recover after each insertion. Low-dose settings were used for all cryo-EM data collection. After centring the beam and checking the microscope alignments, the specimen was brought to eucentric height. This was done by adjusting the position of the sample on the z-axis, to ensure that there was no translational movement of the sample when it was rotated around the specimen-holder axis. The grid was scanned in Search mode in SerialEM [122] at low-magnification to identify areas of interest, which were then marked for data collection. The beam was focussed using Autofocus in SerialEM or manual-focus, depending on the microscope, before data collection using Record.

The negative-stained grids were used for sample screening and optimisation and checked using the Tecnai T12 (FEI Company) microscope at 120 kV. Data were acquired on a 4k x 4k FEI Eagle CCD-camera at a magnification of 67,000x, corresponding to a pixel size of 1.68 Å/pixel.

The cryo-EM grids were mostly imaged using a direct electron detector (K2 Summit, Gatan Inc.) at the Tecnai F30 Polara electron microscope (FEI), operating at 300 kV and equipped with an energy filter (GIF Quantum, Gatan) operated in

zero-loss mode (0-20 eV energy slit). 25 frames were recorded per movie, where each frame lasted 0.2s, at a defocus of 1.5 - 3.5 μm. This was performed using SerialEM with the detector operating in counting-mode at a nominal magnification of 37,027x with a resultant pixel size of 1.35 Å/pixel, and an electron dose of 25 electrons per Å^2.

The data collection at the Titan-Krios at the Diamond Light Source was also performed using the 400Hz K2 direct electron detector (Gatan Inc.), equipped with an Energy filter (0-20 eV slit), using an automated data acquisition software suite, EPU (FEI Company), at an effective magnification of 62,500x with a resulting pixel size of 0.8 Å/pixel. The electron dose in this case was 30 electrons per Å^2.

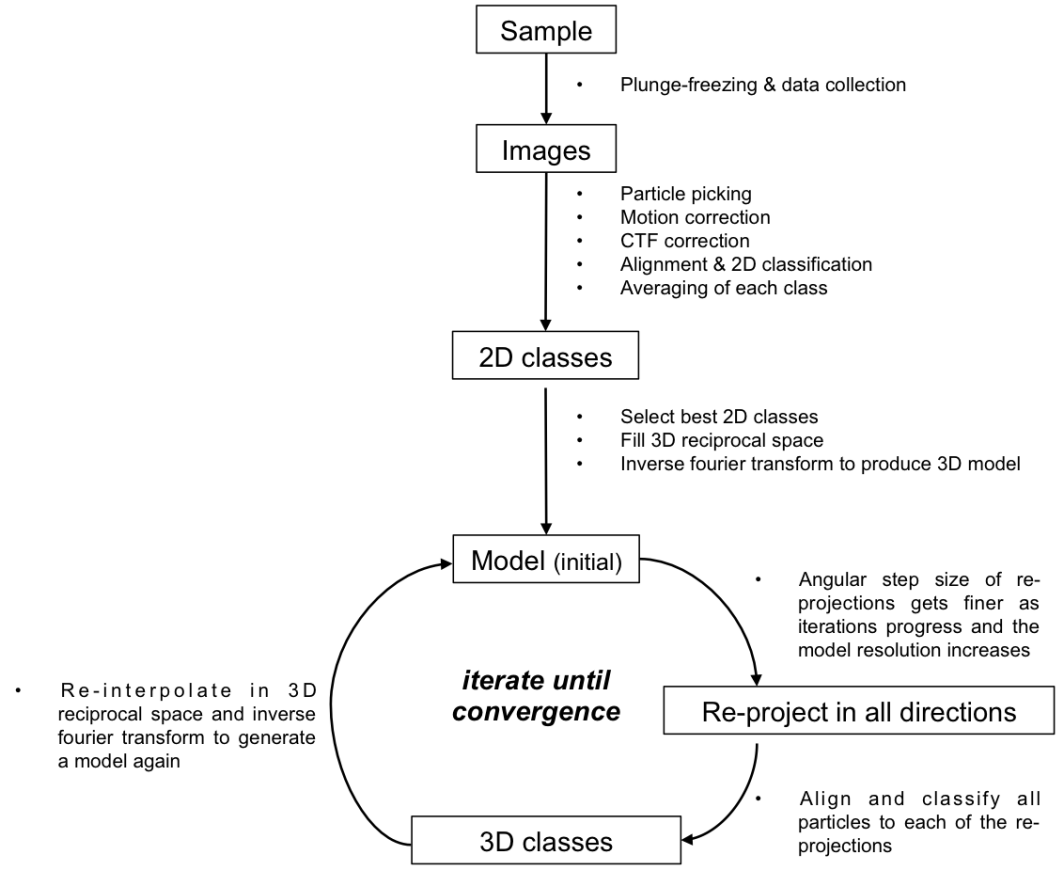


Figure 2.4: Flowchart showing the main steps in the image-processing pipeline for cryo-EM data. After Grant Jensen's Caltech lecture series.

2.4 Cryo-EM image processing

Image processing for cryo-EM data may take several weeks or even months. The flowchart in Figure 2.4 outlines the main steps involved. This section aims to explain these steps and the principles behind them in detail.

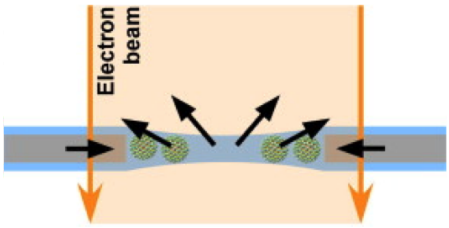


Figure 2.5: Schematic depiction of beam-induced drift of the particles (green) in vitreous ice (blue). Carbon-support layer (grey) deformation caused by the electron beam (orange) results in the shrinking of the hole and radiation damage of the specimen. This leads to rotational and translational movements of the particles, resulting in slight changes in location, charging and orientation of the particles. This leads to blurring and poor image quality. Modified from Brilot et al., 2012 [113].

2.4.1 Frame alignment and motion correction

The electrons interacting with the specimen cause sample drift. The carbon support film and the vitreous-ice layer suspended in between the support, deform by a small amount on several electron exposures, changing the size of the holes that contain the sample embedded in vitreous ice. This, combined with the radiation damage of the specimen itself, results in small rotational and translational movements of the particles within the vitreous-ice layer and contributes to a blurring effect (Figure 2.5). Tracking the movement of the particles during each movie collection by cross-correlation and motion-correcting for this sample drift results in a much improved image quality [113, 123].

The cryo-EM data sets here comprised movies, acquired by the direct electron detector, for each exposure. The first two and the last frame from each movie were excluded from the average, to exclude the effects of beam-induced drift from the initial exposure and the radiation damage from the last frame. The remaining frames were averaged and motion-corrected using MotionCorr [123] to produce

high quality micrographs. Micrographs with significant astigmatism and large drift were also removed from subsequent analyses (explained in detail in the following sections).

2.4.2 Contrast Transfer Function (CTF)

To understand the theory behind the contrast transfer function (CTF), it is essential to remember the wave-particle duality of electrons. Consider each electron is an electron-wave that it is scattered into its Fourier components upon interaction with the sample. Some components of the electron-wave pass through unscattered [124], but most are scattered, and these contain information about the specimen. Each component has a spatial frequency (low- or high-frequency proportional to low or high scattering angles and thus resolution), and an amplitude. All these components have the same wavelength (about 2 picometres for a 300kV emission) coming from the same electron-wave, but are phase-shifted due to the scattering. The scattered waves from the specimen travel a different path length than the unscattered ones, leading to an additional phase shift. After being focused by the lens onto a point on the image plane, the different components interfere and the detector records the resultant electron wave. Some wave components interfere constructively and contribute more to the resultant signal than other components, which might interfere destructively. If the components cancel each other out, some spatial frequencies might not contribute any contrast to the final image. Plotting a function of contrast vs. spatial frequencies to depict this gives the contrast transfer function or the CTF of the electron, thus showing how each spatial frequency contributes to the resultant signal from that electron-wave.

The CTF of the entire image is a sum of the CTF of each electron-wave that contributed to it. In simple terms, the CTF represents how much contrast from each Fourier component of each electron is transferred to the final image. This information can be depicted using a *power spectrum* of the image: a set of concentric Thon rings showing the alternating pattern of the presence (the maxima in a CTF function) and absence of signal (the zeros in the CTF function) for the entire exposure that produced the image. The centre of the spectrum represents low-resolution information and the increasingly further out circles depict the high-resolution details.

The CTF depends on several factors, some of which are considered in the calculation of the theoretical value of the CTF for correction. These include the spherical aberration of the objective lens, the voltage and magnification used to collect the images, the spatial and temporal coherence of the electron source and the defocus of the image, and are discussed in subsequent sections.

2.4.2.1 Impact of defocus on CTF

Subjecting the electrons to a defocus, i.e. changing where the different components of the electron are focussed, changes the path lengths of each of the scattered components along with the scattering angles, which results in changed phases. What this means for the CTF and thus the image is that different spatial frequencies now contribute to the image. Thus, the CTF is different for different defocus values. By imaging a specimen at a range of defocus values, a different range of contributing spatial frequencies is recorded at each defocus. Through this, the whole range of spatial frequencies can be recorded and the missing spatial frequencies from

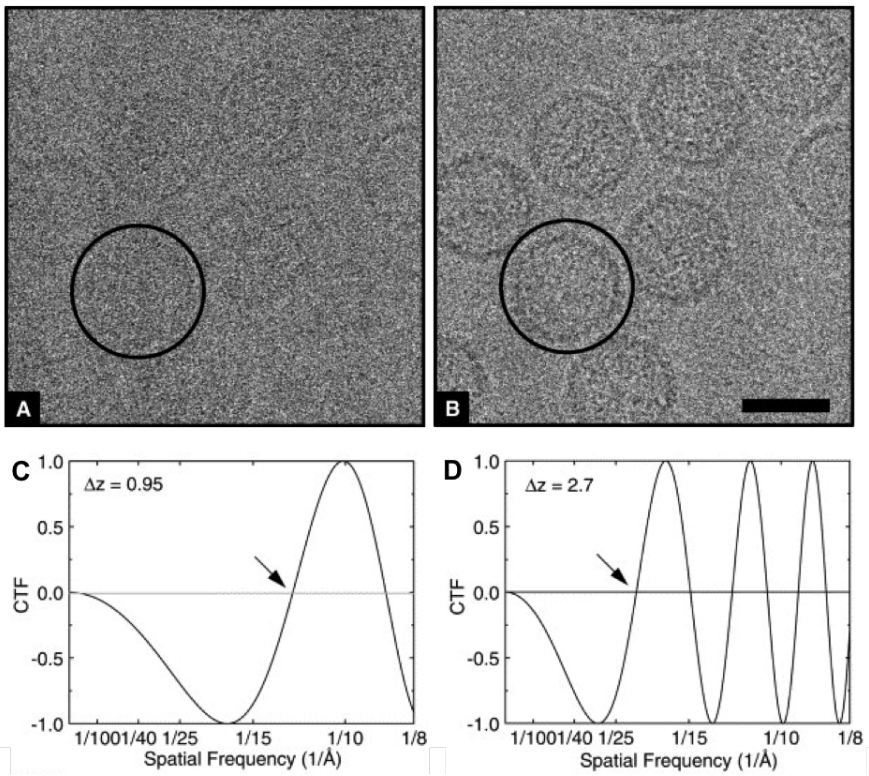


Figure 2.6: An example illustrating the different CTF curves obtained by imaging at different defocus values. (A) Close-to-focus micrograph of bacteriophage-22 procapsids at a defocus of 0.95 μm. (B) Far-from-focus micrograph of the procapsids at a defocus of 2.7 μm, with better contrast. Scale bar = 500 $\mathring{A}$. (C) CTF curve corresponding to A showing presence of more high-resolution frequencies contributing to the final function. (D) CTF curve corresponding to B, showing faster oscillation and thus more true-zeros of the CTF, where no information is transferred to the final image. Modified from Thuman-Commike et al., 2000 [125].

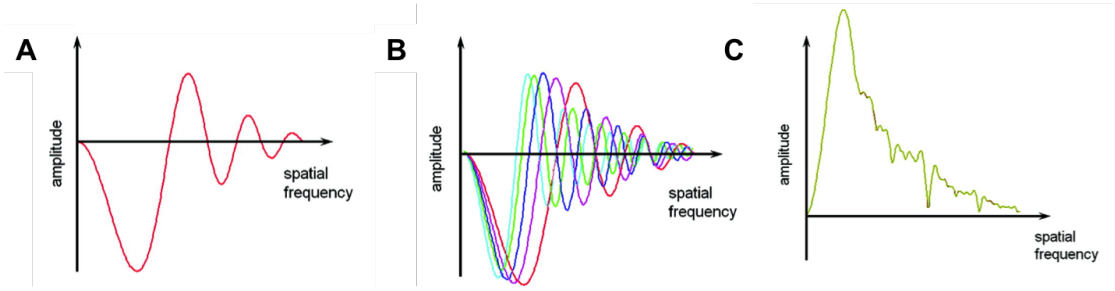


Figure 2.7: CTF curves showing the effect of collecting data at a range of defocus values. (A) CTF curve for one defocus value. (B) CTF curves for multiple defoci. The red curve is at a lowest defocus and thus oscillates the slowest. Cyan/green curves correspond to the highest defoci. (C) Summed CTF for overall transfer for spatial frequency components in the image. Modified from Orlova et al, 2011 [124].

each CTF compensated for. Figure 2.6 shows how imaging at a high defocus value enhances the signal contribution from lower frequencies but dampens the higher frequencies. At higher defocus, the CTF oscillates faster. This results in more true-zeros of the function, showing that a lot of high frequencies do not contribute to the final image. It is, therefore, easier to locate the particles in panel B due to high-contrast, but it comes at an expense of the high-resolution information. As the number of true-zeros increases (at higher defoci), more information is missing from the image and the harder it becomes to perform a reliable CTF correction.

Collecting data at several defocus values and combining it to produce the final structure ensures that both low and high resolution features from the sample are imaged for the final structure [124, 126]. Figure 2.7 shows how information from different CTF curves when summed, makes up for the lack of information from the zeros of the individual contrast transfer functions and leads to a much higher transfer of spatial frequencies in the final image than from a single CTF obtained at a single defocus value.

2.4.2.2 Envelope functions of the CTF

The CTF function is dampened by an envelope function at higher frequencies. This may be the result of different electrons from the electron source being produced at slightly different angles, known as the partial *spatial* coherence of the electron source. The images resulting from each of these electrons are, therefore, formed slightly shifted from each other, resulting in the blurring of the net image produced by all the electrons interacting with the sample. The blurring affects the higher-resolution much more than the lower-resolution information, which is reflected in the dampening of the CTF of the image at higher spatial frequencies.

Dampening may also be a result of different electrons being produced with different energies. This is known as the partial *temporal* coherence of the source. Electrons with different energies are focussed on different image planes and thus produce the resultant images at these planes accordingly. The net image is therefore a sum of all the images contributed by each electron. As they are in different focal planes, and consequently have different contrast transfer functions (CTFs) which are out of phase with each other, summing them results in dampening of the higher frequencies.

There might be several other factors affecting the image resolution at high frequencies, such as the lack of proper alignment of the lenses in the microscope, heterogeneity in the particles, spherical aberrations of the lenses, inaccurate calculation of the defocus and the magnification values used etc. The net envelope function is, thus, the product of all these individual envelope functions [127]. The

dampening effect can also be represented by the *point spread function* or the *PSF* of the image, which is essentially the real space version of the CTF. Therefore, the final image is a convolution of the specimen with the point spread function.

2.4.2.3 CTF correction

In the following equations that show the relation between the CTF and the specimen, I = Image, O = Object (specimen), PSF = Point Spread Function, CTF = contrast transfer function, $*$ = convolution:

$$I = O * PSF \tag{2.2}$$

$$\mathcal{F}\{I\} = \mathcal{F}\{O * PSF\} \tag{2.3}$$

$$\mathcal{F}\{I\} = \mathcal{F}\{O\} \times \mathcal{F}\{PSF\} \tag{2.4}$$

$$\mathcal{F}\{I\} = \mathcal{F}\{O\} \times CTF \tag{2.5}$$

$$I = \mathcal{F}^{-1}\{\mathcal{F}\{O\} \times CTF\} \tag{2.6}$$

$$\mathcal{F}\{O\} = \frac{\mathcal{F}\{I\}}{CTF} \tag{2.7}$$

$$O = \mathcal{F}^{-1}\{\frac{\mathcal{F}\{I\}}{CTF}\} \tag{2.8}$$

Following from the explanation of how certain frequencies from the specimen are degraded by the point spread function, as the CTF is never perfect, it can be concluded that not all frequencies from the specimen are recorded in the final image. The image (I) is a result of the convolution of the point spread function (PSF) with the object (O) (equation 2.2). In other words it is the inverse Fourier

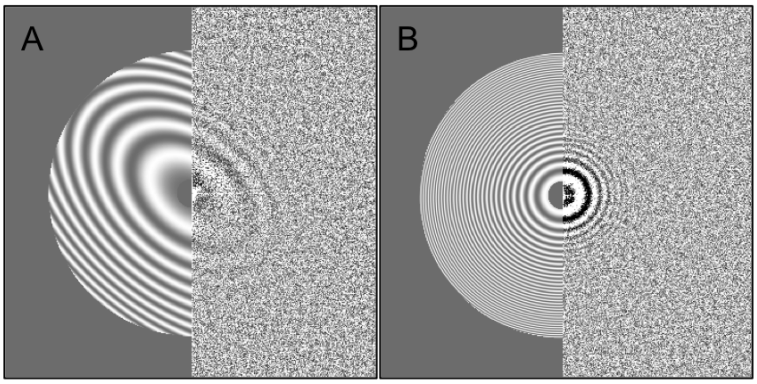


Figure 2.8: Power spectra showing the theoretical CTF (left half of the images) fitted to observed CTF (right half of the images) of two example micrographs using Relion. (A) CTF shows astigmatism and such micrographs were removed from the data set. (B) A good fitting of the theoretical CTF to the observed signal ensures better CTF correction.

transform of the Fourier transform of the object times the CTF formed on the back focal plane of the microscope. Therefore, in simplistic terms, the Fourier transform of the image may be divided by the theoretical CTF and inverse Fourier transformed to perform CTF correction (equation 2.7). When performed for all the pixels in the image, this results in *phase flipping* of the values contributing negatively to the amplitude of CTF. This process, known as CTF correction, gives us an image closer to the true specimen. The mathematical justification of this is shown in equations 2.1 - 2.7.

For all the data used in structure determination in this thesis, the Relion software suite [128] was used to perform the CTF correction. Relion uses the CTFFIND algorithm to match the theoretical CTF to the experimental values for CTF correction [129]. The power spectra of the micrographs were manually inspected to remove any micrographs with astigmatism, large drifts or strange diffraction patterns due to large ice crystal contamination, such as the one shown in panel (A) of

Figure 2.8. Out of the remaining micrographs, only those with a well-fitted CTF, such as the one in panel (B) of Figure 2.8, were included in subsequent processing steps.

2.4.3 Particle picking and extraction

For subsequent processing, individual particles were extracted from the micrographs. The particle picking was performed using e2boxer.py from the EMAN2 software suite [130]. Micrographs were displayed using e2boxer.py, the particles picked manually and their coordinates saved as .box files. These coordinates were fed into the Relion software suite [128], which extracted the particles in a given box size.

Particles were picked automatically, using pattern matching, for the SAT project (Chapter 3) as they were regular in shape. The sample was extremely concentrated and picking tens of thousands of particles manually would have proven too time-consuming [131]. In this case, picking was performed by providing a spherical radius of the particles which EMAN could use to search for the particles in the micrographs. The automatically picked particles were manually screened to ensure no deformed particles or contaminants were included in the subsequent processing. For the A10 intermediate project (Chapter 5), manual picking was used, as there were only a few particles per micrograph. Lastly, the pentamers (Chapter 6) were mostly found in side views in cryo-EM and did not have an isometric shape so manual picking was performed in their case as well.

2.4.4 2D classification

The sample on the grid might contain single particles in several orientations, different conformational states or with partial ligand binding [132–134]. A variety of available views of the particles is crucial for structure determination as we need to image the object we are interested in from all angles. These different views of the particle in different images are combined to produce the final structure. After picking all the individual particles from the micrograph, it is essential to sort them out into different classes, each containing a homogenous population of views or conformations. This is done to remove any damaged particles that might have been picked accidentally, or in case of automatic picking, to remove contaminants or ice crystals that were picked by the program because they matched the particle size and shape. The particles are aligned by being allowed x- and y-shifts as well as in-plane rotations while being separated into homogenous 2D classes and subsequently averaged to boost the signal to noise ratio in the class averages [135,136].

There are several methods to generate the 2D classes. Here, Relion [128] was used for classification, which makes use of the Maximum Likelihood (ML) approach. In this, all images are assigned into a given number of classes, such that the probability of all images in all possible orientations is iteratively calculated and the images are x- and y-shifted and in-plane rotated until the particles are aligned into homogeneously-oriented classes in 2D. For each iteration, this leads to a probability-weighted average of all the particles in all different orientations, for each class, to go into the next iteration. The iterative process continues until it converges and the particles are sorted into homogenous classes. The final classes

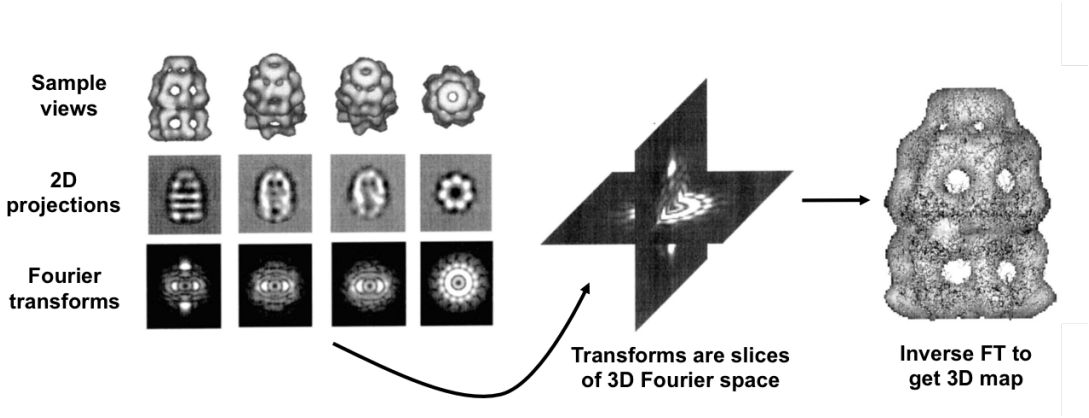


Figure 2.9: Figure showing the principle of 3D reconstruction from 2D projection images. Each particle is imaged to give 2D projection images, which can be Fourier transformed and used to populate a Fourier space, representing the actual specimen. Modified from Saibil H., 2000 [118].

are screened manually, by visual inspection and based on the angular-rotation accuracy obtained from the model.star file in Relion.

2.4.5 3D reconstruction for model generation

The images obtained from the microscope are 2D projection images of the specimen. Reconstructing them into a 3D structure after sorting them into homogenous populations, requires the use of computer algorithms that employ the *projection slice theorem*, also known as the *Fourier slice theorem* to build a model [137, 138]. This approach relies on the principle that the Fourier transform of each 2D projection is a centre-slice of the Fourier transform of the 3D structure of the specimen, and taking the inverse Fourier transform generates the 2D-projection of the respective 3D density perpendicular to the slice in Fourier space [118, 124, 137, 139]. Therefore, each 2D projection image contributes to the 3D representation of the specimen in Fourier space and the more 2D projections of the sample acquired, the finer the 3D Fourier space sampled and the better the final 3D reconstruction.

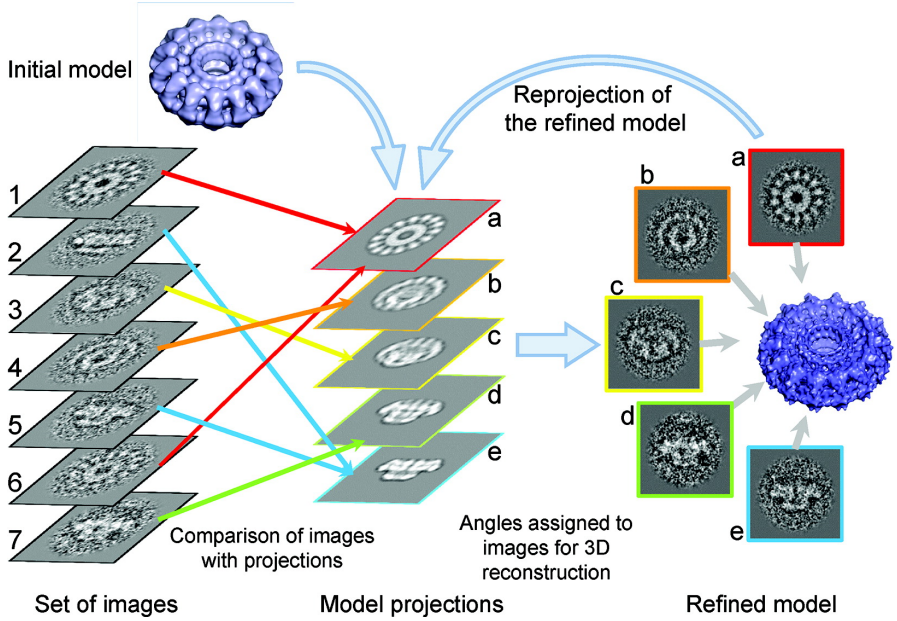


Figure 2.10: Figure showing the principle of 3D classification. 2D re-projection images are matched to the re-projections of the template during classification. Class averages of each template projection are calculated at the end of the iterative process. From Orlova et al, 2011 [124].

Figure 2.9 depicts the projection slice theorem.

To generate the initial model to start this iterative process, the best approach is to provide a low-resolution (around 50 Å in our case, so as to include no high-resolution features) starting model of a similar structure as a template. It is critical that the template is very low-resolution, so as not to reference-bias the resulting structure. The model generation then fills in the high-resolution details in the Fourier space.

2.4.6 3D classification and refinement

Once a 3D model has been generated, it is re-projected to create reference 2D projections. The 2D projection images of the particles from the specimen are then

cross-correlated to each of the template 2D projections, using Relion, and the angles required to match them to each template projection are assigned accordingly. These assigned angles determine how each image in the dataset contributes to the final refined image in each iteration. Essentially, the underlying principle as in 2D classification is that, each particle has a probability of being matched to each template projection of the model with an in-plane rotation and an x-, y-shift, which is used to create a weighted estimate of the model of the particle iteratively.

Each iteration thus generates a new and progressively better model and the iterative process continues until it converges on a consensus 3D model of the structure. This process is illustrated in Figure 2.10 from a review by Orlova and Saibil [124]. For novel structures, it is important to repeat the 3D classification a few times, with different starting models or different number of classes, so as to make sure that the starting template does not introduce reference-bias in the final structure.

For the resolution calculation of the final structure, Fourier shell correlation (FSC) is used [140]. To this end, the entire dataset is split into two halves and the 3D structural refinement performed for each half independently [141]. Subsequently, the reconstruction from each half is Fourier transformed and correlated against the reconstruction from the other half. The correlation is plotted against resolution to see how far it matches between the two halves. The resolution of the final structure is reported at the Fourier shell correlation (FSC) cut off of 0.143, the empirically-determined gold-standard in the field [141, 142].

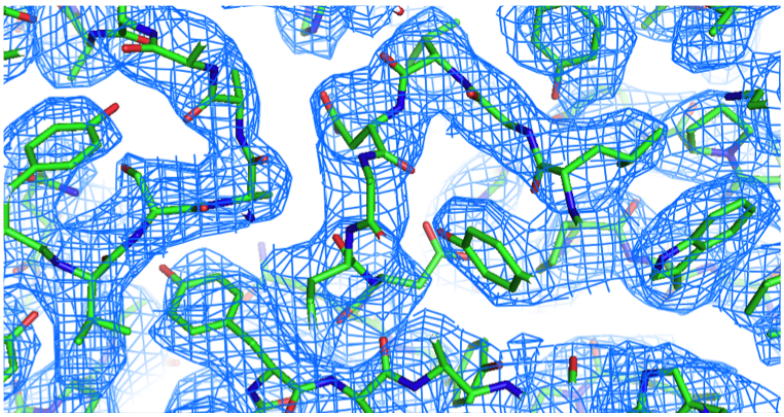


Figure 2.11: An example of an atomic model (green) fitting into a cryo-EM map (blue mesh). Here, FMDV SAT3 cryo-EM map at 3.1 Å is shown with a model fitted in (discussed in a later chapter). Figure rendered in Pymol [143].

2.4.7 Model fitting

Once a cryo-EM density map has been obtained, atomic models can be *de novo* built or fitted into it via density correlation [144,145]. These may be obtained from a known crystal structure of the specimen imaged, or from a crystal structure of a related structure. Model fitting can be a tricky process for low-resolution density maps and care must be taken to avoid over-fitting and over-interpretation of structural data. Sometimes the cryo-EM maps can be at a high enough resolution to unambiguously fit even the side chains. An example from the FMDV SAT3 structure fitting can be seen in Figure 2.11. In this case, a model from a closely related virus, SAT2, was fitted into the density and checked residue by residue to mutate the sequence to the SAT3 sequence.

Rigid body fitting was used for the lower resolution maps in this thesis, such as the A10 altered particle map (5.19 Å) in Chapter 5 or the pentamer map (8.2 Å) in Chapter 6, to dock the crystal structure in the map without allowing any flexibility

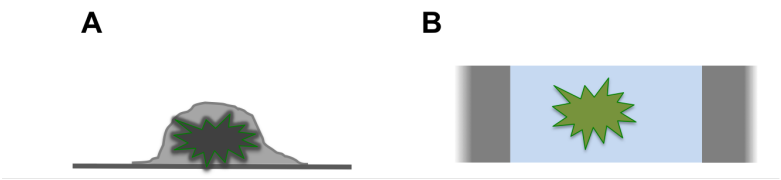


Figure 2.12: Cartoon depiction of side views of biological specimen, (A) covered with heavy-metal salt stain on a grid or (B) embedded frozen-hydrated in vitreous ice (blue).

of the secondary structure. The fitting was manually checked in COOT [146] and tweaked to allow better fitting of the protein backbone into the density. Loops often had too little density to unambiguously fit the crystal structure to the density map, which is why rigid body fitting was crucial, so as not to modify the basic chemistry of the structure based on unclear density. Phenix [147] was ultimately used to correct rotamer and Ramachandran outliers and to refine the structure in real-space.

2.5 Classical vs. cryo-EM

Classical EM methods using negative-staining allow rapid and easy sample preparation. The staining also provides high contrast, making it easier to find the objects of interest. Negative-staining is, however, not suitable for making reliable conclusions about how objects might look under physiological conditions, as most stains have an acidic pH and can interfere with the biological specimens. The stain and the drying out process can be disruptive to the sample and the analysis might be difficult due to the stain filling the empty cavities in the structure or not covering the specimen uniformly. Furthermore, the layer of stain on top of the sample might mask the high-resolution information. The signal is further dampened by the additional background scattering of the continuous carbon support

film. This technique is nevertheless quite useful for getting information about the distribution of the particles on the grid, their heterogeneity and a general estimate of their size and shape. It is also used to get information about small structures (less than 200kDa), which are too difficult to accurately detect in cryo-EM.

Vitrification allows samples to be embedded in vitreous ice, which has a density close to that of liquid water, in a frozen-hydrated state. It was first developed by Dubochet and colleagues in the 1980s [119, 148], and allows for imaging of biological specimens in close-to-native conditions. The sample has to be rapidly frozen and kept under $-140\,^{\circ}\mathrm{C}$ to prevent formation of crystalline ice. Therefore, the signal collected for each image corresponds directly to biological information from the specimen, as there is no staining involved and the samples are dispersed in holes on the grids, preventing interference of the signal coming from the specimen and that from the grid support. Figure 2.12 depicts how a frozen-hydrated biological sample, snap-frozen in liquid ethane (B), is preserved better than a negative-stained one (A).

There are also challenges in working with plunge-frozen samples. As there is no staining involved and the biological material and the vitreous ice scatter electrons similarly, the contrast in the resultant images is very low. This can be overcome by working a few microns away from focus, thus artificially enhancing contrast by introducing a phase shift between unscattered electrons and electrons scattered by the sample. Biological samples are also sensitive to radiation damage and therefore can only be exposed once, at low electron-dose, to preserve structural integrity. The low temperatures used in cryo-EM do, however, reduce radiation damage to

the sample. Another problem that might arise in working with cryo-EM is that some specimens have a preferred orientation in vitreous ice. This might result in uneven sampling of the Fourier space and lead to anisotropic resolution across the reconstruction [149]. In such cases, better experimental conditions need to be investigated, under which the samples have several different orientations in vitreous ice, allowing imaging of the specimen from all angles. The sample may also be tilted and imaged from different angles, as in cryo-electron tomography [150, 151]. For all the projects in this thesis, single-particle cryo-EM was used.

Chapter 3

Native structures for FMDV SAT serotypes

3.1 Chapter summary

As introduced before, foot-and-mouth disease virus has seven serotypes. South African Territories (SAT) form three of the seven, namely SAT1, SAT2 and SAT3. The serotypes vary antigenically, which is a major problem in vaccination against FMDV; vaccines against one serotype are not cross-protective against another [32, 103]. Even different strains within a serotype may not respond to the same vaccination. To add to the complexity of developing a cross-reactive vaccine, FMDV, like all RNA viruses, has a high rate of mutation. It is crucial to identify which specific strain of a serotype is responsible for an outbreak, for effective vaccination. The structure of each virus serotype is different, based on antigenic variation. There have been several structural studies performed on different FMDV virus capsids and capsid proteins [31,33,34,45,152–155], in an effort

to understand the structure-function relationship across different serotypes.

In this chapter, high-resolution cryo-EM structures of SAT3 (low-passage strain SAR/2/06) and SAT1 (high-passage strain ZIM) are presented. The structure of SAT3 had not been determined before by crystallography or electron microscopy, in part due to its very low thermostability. A PDB entry for a SAT1 crystal structure does exist (2WZR), but there had not been any thorough structural characterisation, comparison of its structure against other FMDV structures or any EM studies on it thus far. Completing the repository of SAT structures facilitates structural comparison of these serotypes. Comparative structural studies of virus capsids may be important in developing chimeric, cross-protective vaccines, that may be effective against several serotypes, and give an insight into what makes the capsids more stable for one serotype versus the others.

3.2 Methods

The production of FMDV on an industrial scale started with the discovery in the 1940s that virulent FMDV could be grown in epithelial tissue from a bovine tongue [94]. The model of FMDV production used today, that is in baby hamster kidney (BHK-21) cells, was first used in 1965 by Capstick and coworkers [156] and is described below. Live FMDV is a Bio-Safety Level (BSL) 4 pathogen and can only be handled under strict containment conditions. For this reason, the live virus growth in cultures was performed by our collaborators at the Pirbright Insitute (SAT3) or MSD (Merck Sharp & Dohme GmbH) (SAT1). The sections below describe how that was performed. All purification and subsequent imaging and analyses were performed on the inactivated virus at The Division of Structural Biology (STRUBI), University of Oxford, in containment suites operating at BSL-2.

3.2.1 Virus production

3.2.1.1 Virus growth and inactivation

BHK-21 cells were grown in Glasgow Minimum Essential Medium (GMEM, Sigma) with 10% Fetal Calf Serum (FCS) until they were confluent. They were then infected with FMDV and the cell culture medium containing the virus was harvested when complete cytopathic effect (CPE) was observed (usually after overnight incubation).

The cell culture medium was inactivated using binary ethyleneimine (BEI) inactivation standard operating protocols (SOPs) [157]. This involved removing the

dead cell debris from the medium, by centrifugation at roughly 2000xg for 30 minutes at 4 °C. The supernatant, which contained the released virus, was then inactivated by the addition of 10ml, 0.1M BEI solution per litre of virus supernatant, producing a final concentration of 0.001M BEI. The solution was then incubated at 37 °C for 24 hours and mixed with intermittent inversions. After this process was performed twice, the World Reference Laboratory (WRL) confirmed the success of the inactivation process through innocuity testing. Bovine thyroid cells (BTY), together with ELISA assays, were used to detect if any infectious virus was still present in the supernatant. Once the samples were cleared by WRL, they were transported to Oxford in a frozen form for subsequent analyses, and stored at −20 °C until further steps. All subsequent steps in the following sections describe how the virus was purified for both SAT1 and SAT3 experiments. The purification protocol was kept consistent between the serotypes.

3.2.1.2 Virus purification from the inactivated pellet

The frozen cell lysates of SAT1 and SAT3 from Pirbright were thawed on ice and then cleared of cell-debris by a low-speed centrifugation at 3500xg for 10 min at 4 °C. Virus particles were then precipitated by adding 8% weight/volume (8g per 100mL) polyethylene glycol 6000 (PEG-6000) and incubated at 4 °C overnight. The virus precipitate was spun down at 3500xg for 1 hour and thoroughly re-suspended in an NP40 detergent buffer (50mM Hepes, 400mM NaCl, 1% NP40, pH 8.0), leading to a final volume of 1.5mL. Care was taken to ensure that the pellet was completely broken down, so as to release all the virus in the buffer supernatant. The supernatant was again clarified, to remove any remaining insoluble clumps, by centrifugation at 3500xg for 20 min at 4 °C. The clarified supernatant

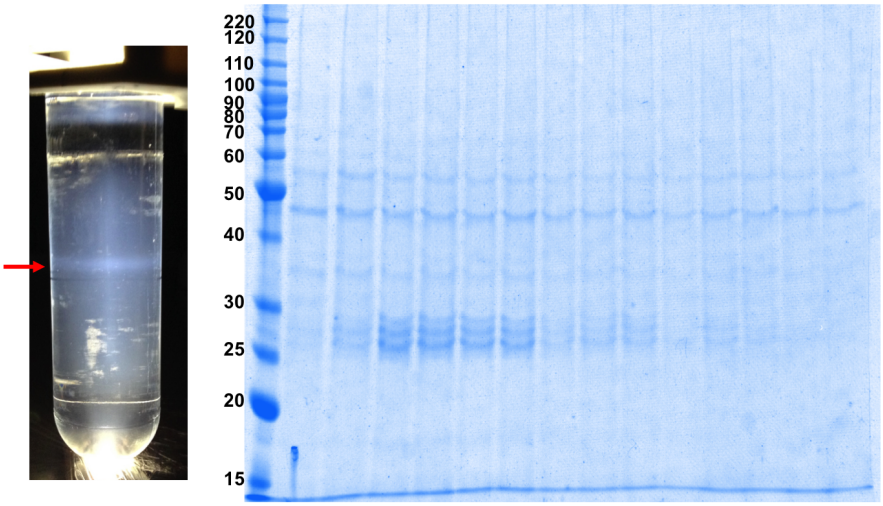


Figure 3.1: The first gradient purification (left) of the solubilised virus pellet, resulting in a band (red arrow) indicating the virus particles. Several 1-mL fractions were harvested around the light-scattering band on the gradient and checked on a Coomassie-stained 12% SDS-PAGE gel (right) for the presence of capsid proteins (between 20 - 30 kDa markers) .

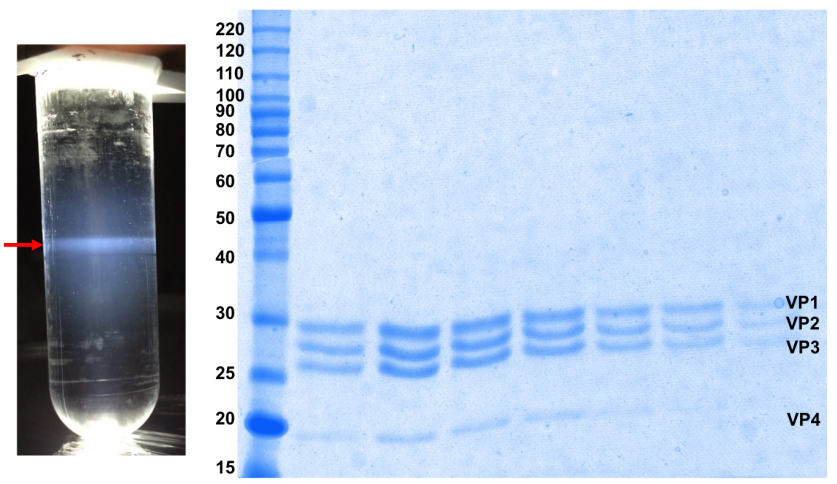


Figure 3.2: The second gradient purification (left) of the solubilised virus pellet, resulting in a much more defined band (red arrow), indicating a more purified virus preparation. Several 1-mL fractions were again harvested around the light scattering band on the gradient and checked on a Coomassie-stained 12% SDS-PAGE gel for a reduction in impurities (right).

containing the virus was subjected to ultra-centrifugation at 105,000xg for 3 hours at 4 °C, to pellet the virus particles through a 2 mL 30% sucrose cushion. The virus pellet was left to soften overnight in the NP40 buffer. It was thoroughly solubilised the next day, taking care to avoid the introduction of air bubbles which might damage the virus particles, in a total volume of 3 mL. To ensure that this volume contained only solubilised virus, the solubilised pellet was centrifuged at 16000xg in a table-top centrifuge for 20 min at 4 °C to remove any remaining clumps. The clarified solution containing the virus was gently layered on top of a 15 - 45% linear sucrose gradient. This was prepared using a gradient maker (Biocomp) and carefully balanced after the sample was loaded on top of it. The virus solution was thus fractionated on the sucrose gradient by ultra-centrifugation at 105,000xg for 3 hours at 4 °C. Figure 3.1 (left) shows the resulting band (red arrow) on this first gradient. In total, 14 1-mL bands from the gradient were collected in the region around the light scattering band (red arrow, Figure 3.1) by pipetting out a series of 1mL fractions, as the sample might have diffused over a larger area than was visible by eye. These bands were run on an SDS-PAGE gel and stained using Coomassie blue stain; the results are shown in Figure 3.1, on the right side. As shown, the four capsid proteins were present in all the fractions (between 20 - 30 kDa markers) but several contaminants were also present.

Bands 3 - 12 were pooled, as there was not much material present in the others, and further purified as follows. First, 7 kDa Molecular weight cut off (MWCO) spin-desalting columns (Zeba, Thermoscientific) were used to remove the sucrose from the collected gradient fractions. After desalting at 1000xg for 2 min at 4 °C, the samples were concentrated, using a 100 kDa MWCO concentrator, to bring

the volume down to 3 mL. The concentrated virus-containing sample was applied to another 15 - 45% linear sucrose gradient and ultra-centrifuged as before at 105,000xg for 3 hours at 4 °C. The resulting gradient fractionation is shown in Figure 3.2, where the red arrow shows a much clearer and more defined band containing highly-purified viruses. A few 1-mL fractions around the band were carefully collected, ensuring the liquid did not stir inside the tube, and checked on an SDS-PAGE gel to verify the purity of the virus preparation (Figure 3.2, right). All fractions were again pooled, desalted and concentrated as before. The final volume of the samples this time was much lower; they were concentrated to roughly 2 mg/mL for electron microscopy. The subsequent sections present the steps followed for structure determination of each serotype separately.

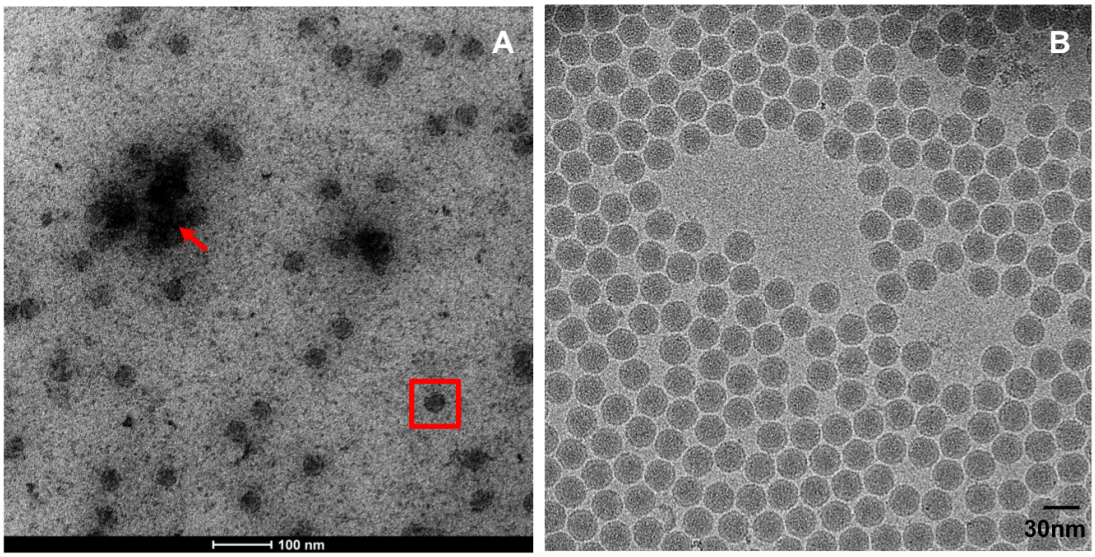


Figure 3.3: Electron micrographs showing SAT1 particles in (A) negative-stained EM and (B) cryo-EM. Red square in panel (A) shows an individual virus particle and the red arrow points to an aggregate of virus particles.

3.3 Results

3.3.1 SAT-1

3.3.1.1 Negative-stain electron microscopy

The virus was first checked for optimal concentration and quality control in negative-stained EM. To this end, the purified virus was diluted 1:10 and checked using negative-staining by uranyl formate. Figure 3.3 (A) shows the results. As seen, there were some aggregates of virus particles present, but most of the particles were nicely distributed and intact.

3.3.1.2 Cryo-EM data collection

Once the quality of the preparation was verified in negative-stained EM, the sample was diluted to 0.6 - 0.7 μg/μL, to give a good particle density on the plunge-

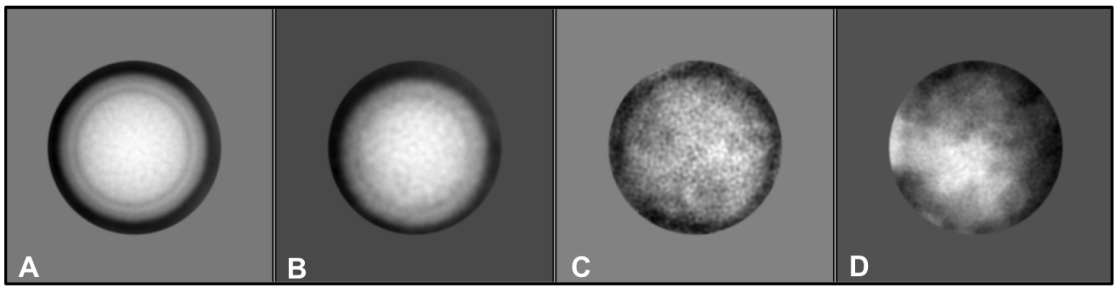


Figure 3.4: SAT1 particles sorted into 2D classes in the Relion processing pipeline. Here shown in reverse-sorted order by class distribution, i.e.: A is the most populous and and D the least.

frozen grids. This value was empirically determined for FMDV grid preparations. After plunge-freezing, the virus particles were imaged in cryo-EM, on a Polara microscope (FEI), as described in Chapter 2. Figure 3.3 (B) is a representative micrograph showing the quality of the data collected. After CTF correction and automatic particle picking, the data was cleaned to remove any damaged particles or contaminants. Roughly 20,000 particles were subsequently classified into 2D classes.

3.3.1.3 2D classification

Relion [128] was used to sort the particles into 20 2D classes iteratively. However, it was observed that the particles were predominantly classified in only two different 2D classes (Figure 3.4, A and B) and only 4 classes were populated by the 2D projections. This could potentially mean that the 2D classification did not work properly and converged into a local minimum. Figure 3.4 shows the classes obtained, in decreasing order of particles per class (reverse-sorted by class occupancy). Class A had 17030 particles, Class B 2949 and Class C and D had 3 and 1 particle(s) respectively. Classes A and B were combined and 3D classified, which meant that almost all the picked particles were put through 3D classifica-

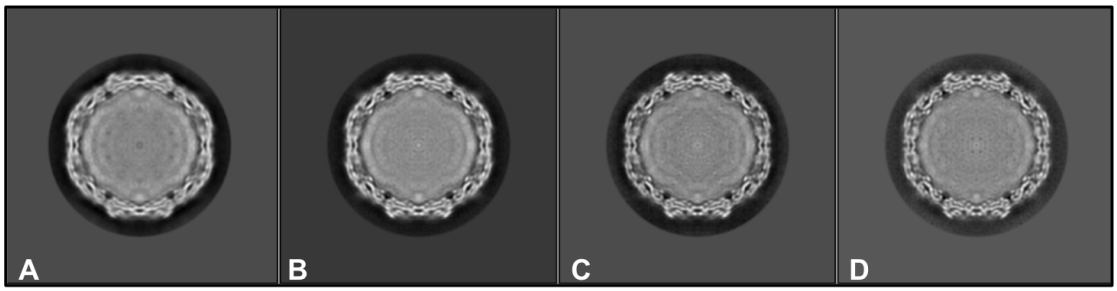


Figure 3.5: SAT1 particles sorted into 3D classes in the Relion processing pipeline. Central section through the 3D class averages shown in reverse-sorted order by class distribution.

tion in the next step. Since the data were put through 3D classification after this, we were confident that any remaining bad particles would be removed in the 3D sorting of data. Furthermore, the picked particles had been manually screened after automatic picking to remove any ice or obviously damaged particles.

3.3.1.4 3D classification and refinement

The particles were then classified in 3D into 4 classes, using a known FMDV structure as template, after it was filtered to a very low resolution (50 Å) so as not to bias the final structure. The Bsoft software suite [158] was used to ensure that the template had the same pixel and box size as the picked particles. Once the 3D classification had converged, Relion [128] also provided the angular accuracy of rotation for the determination of each 3D class-average. This was the measure used in the end, together with manual inspection of the classes to determine which 3D classes looked the best and were to be further refined to give the final structure. Figure 3.5 shows the 2D central slice through each of the 3D classes obtained for SAT-1 particles. Class A had 7941, class B 6614, class C 3349 and class D 2075 particles. The 2D projections of the 3D classes looked quite similar, therefore the angular accuracies of 3D reconstruction of each class were checked. The rotational

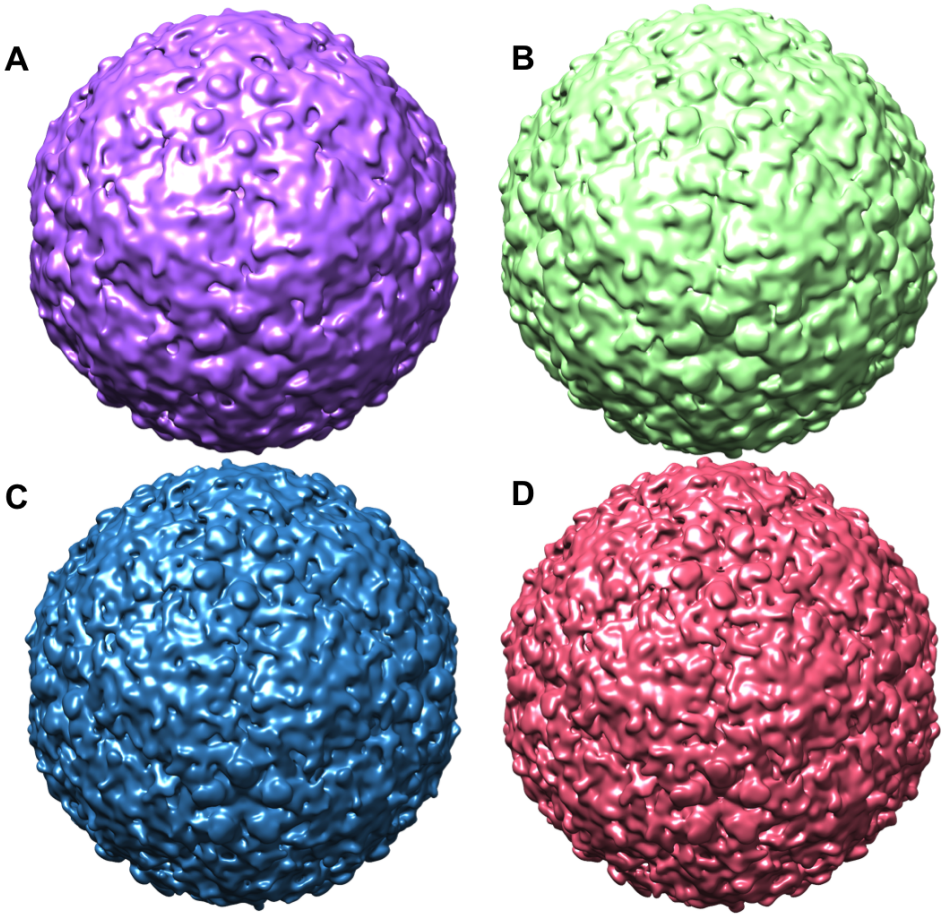


Figure 3.6: SAT1 particles sorted into 3D classes in the Relion processing pipeline. 3D class averages displayed in Chimera with the same level of thresholding for all classes, in the same order as shown in Figure 3.5.

angular accuracy of classes C and D was better (0.5 and 0.4 degrees respectively) than that of classes A and B (0.9 and 0.7 degrees respectively), as shown in the model.star file generated by Relion's 3D classification.

3D structures of each class were also displayed in Chimera [159], as shown in Figure 3.6. This confirmed that Classes C and D displayed higher-resolution features more clearly and were subsequently selected for further structural refinement. This

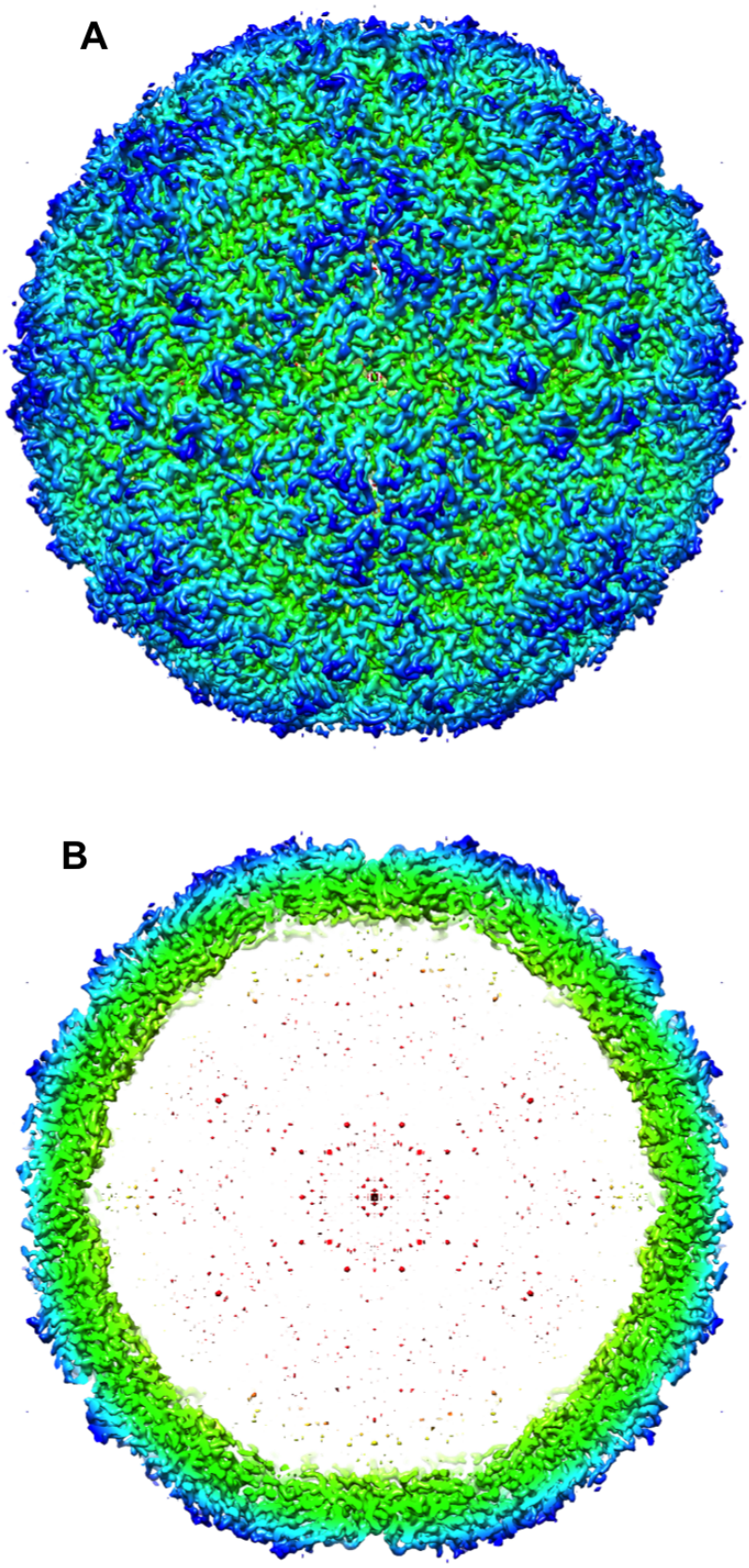


Figure 3.7: Final structure of SAT1 at 3.8 Å, as displayed in Chimera. (A) Full density, coloured by radius. and (B) the centre slice of the particle.

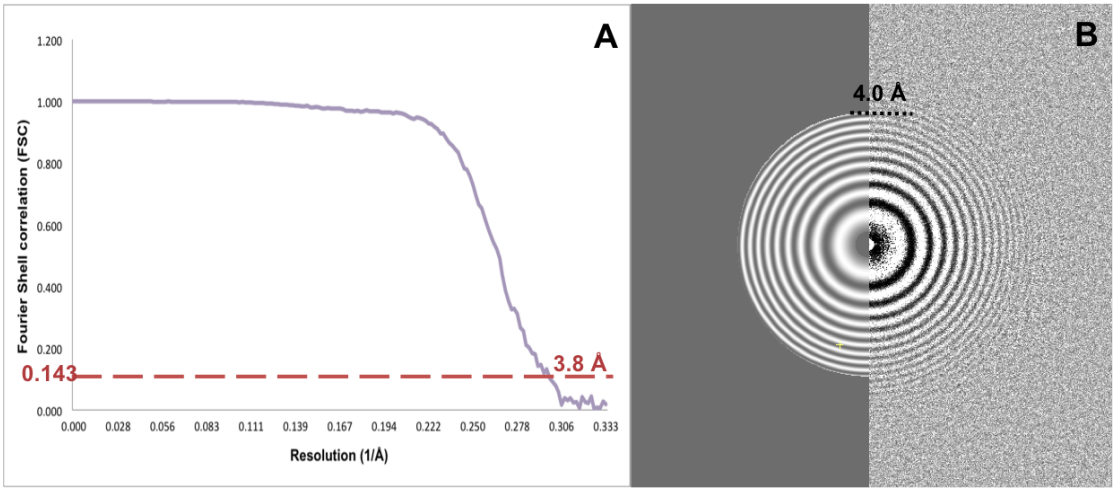


Figure 3.8: (A) Resolution determination of the cryo-EM structure at the FSC cut-off of 0.143 and (B) the power spectrum from the CTF of an example micrograph showing the extent of meaningful information in the images.

meant that roughly 5400 particles contributed to the final structure. 3D structural refinement converged at a resolution of 3.8 Å, which was determined at a Fourier shell correlation (FSC) of 0.143. Figure 3.7 shows the final structure (A) after refinement along with a slice through the centre of the particle (B), displayed in Chimera. The red speckles in the centre of the particle represent density from the genome, at this threshold. Figure 3.9 shows the inside of the capsid at a different threshold, showing the layered structure of the RNA genome within.

Figure 3.8 shows the graph from the gold-standard resolution determination procedure using an FSC cut-off of 0.143 (A), and the CTF (B) of an example micrograph showing that the meaningful information in some images extended beyond the theoretically estimated CTF at 4.0 Å.

Furthermore, ResMap [160] was used to visualise the regions of the structure with

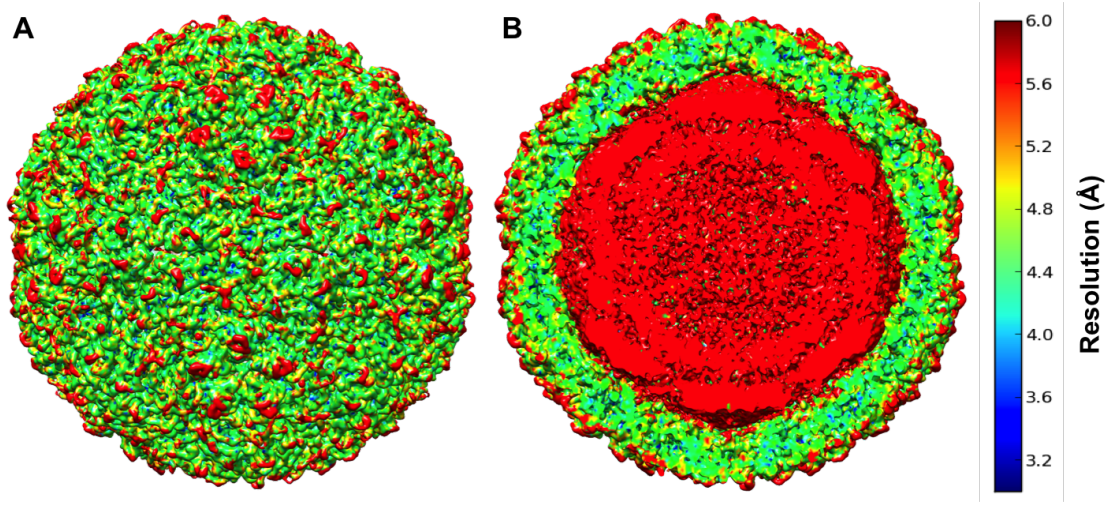


Figure 3.9: SAT1 structure colour-coded as shown in ResMap to show (A) the outer surface and (B) the inside of the capsid, containing the genome.

the highest and the lowest resolution, to give further indication of the resolution of the core capsid structure and highlight the more flexible outer regions. Figure 3.9 shows that the majority of the capsid shell was close to the resolution of 4.0 Å (Figure B.1, Appendix B for additional statistics), but the regions closer to the surface were determined to a lower resolution.

3.3.1.5 Model fitting

Once the final 3.8Å-structure was obtained, the atomic model could be fitted for further analyses. A 3.0Å-crystal structure from a different strain of SAT-1 was available (PDB ID: 2WZR), and used for this purpose. The sequence was not modified as the full protein sequence of SAT1-ZIM was not yet available from MSD. Thus, 2WZR-crystal structure was docked into the density using Coot [146] and manually checked for fitting errors to fix any rotamer or Ramachandran outliers. Phenix [147] was subsequently used for real-space refinement. The correlation between the map unit cell and the atomic model was over 70%, whereas

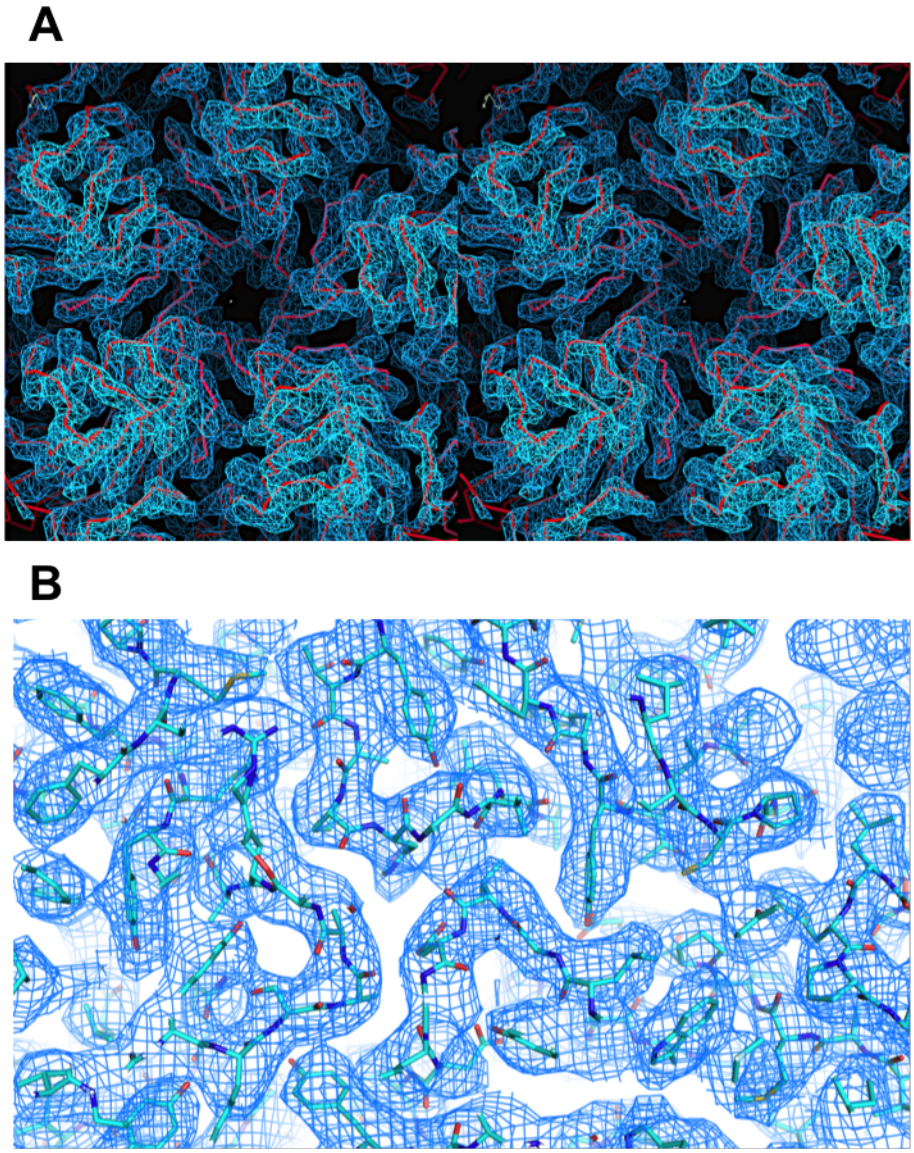


Figure 3.10: The fitting of the atomic model from 2WZR into the EM density (mesh, sigma level 2.5 RMSD) of SAT1 shown (A) at the five-fold axis in wall-eye stereo for overview and (B) zoomed in on a representative area to show the quality of fitting (not in stereo).

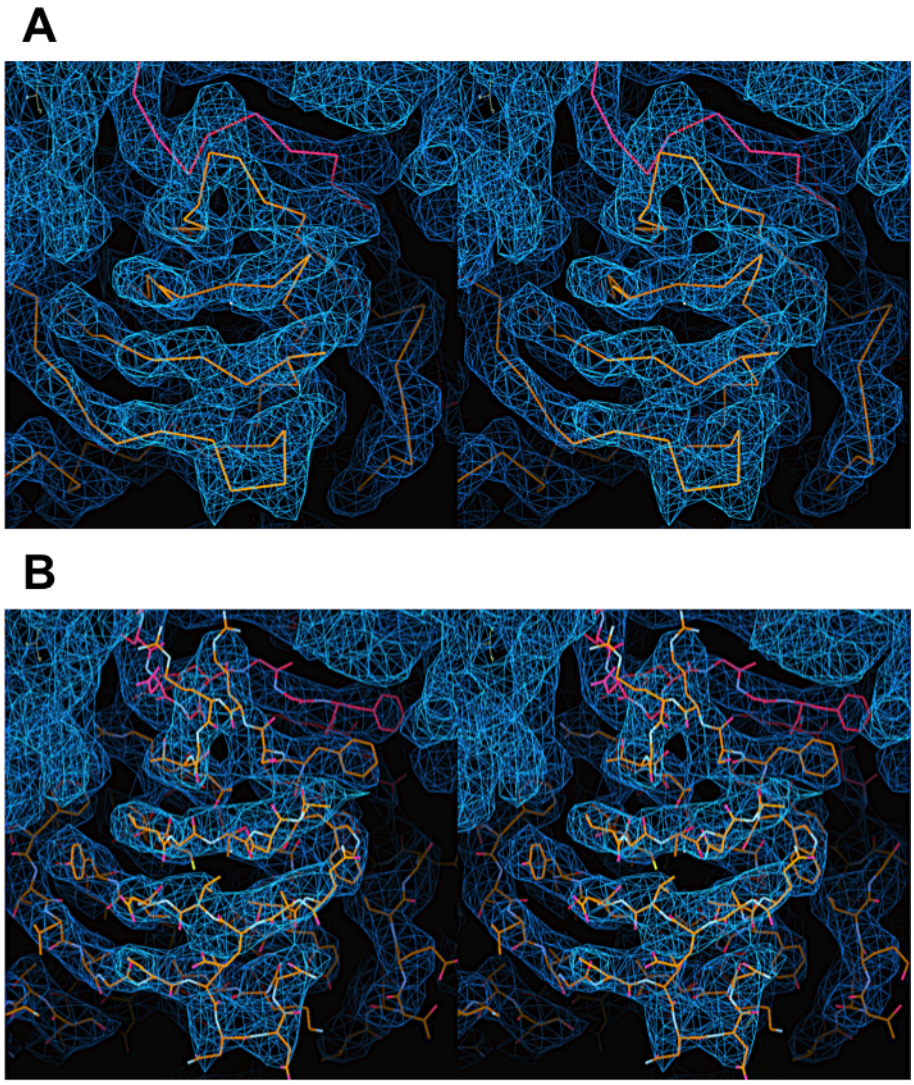


Figure 3.11: The fitting of the atomic model from 2WZR (sticks) into the EM density (mesh) (at sigma level 2.4 RMSD) of SAT1 shown in wall-eye stereo (A) as protein backbones and (B) the atomic model using the same region.

SAT1 refinement measure	Final figures
Map cross-correlation (whole unit cell)	70.8%
Map cross-correlation (around atoms)	84.9%
All-atom clash score	12.42
Ramachandran outliers	0.30%
Ramachandran allowed	14.11%
Ramachandran preferred	85.58%
Rotamer outliers	0.00%
C-beta deviations	0

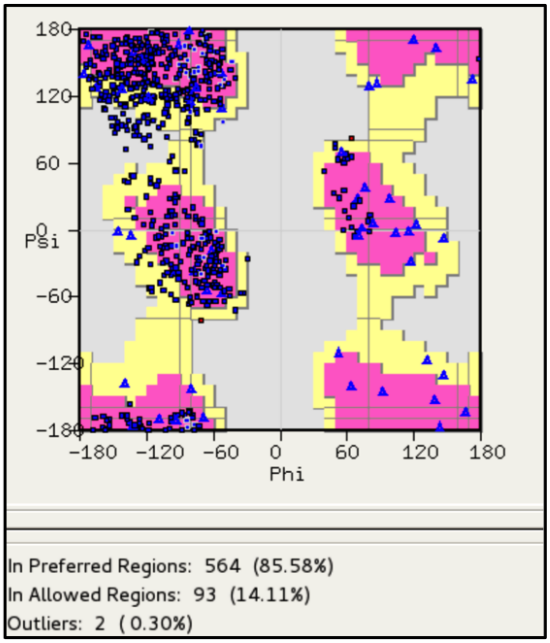


Figure 3.12: Refinement statistics and the Ramachandran plot of the final SAT1 structure.

the correlation between the map and the model around the atoms reached 84.9%. The fitting process was iteratively repeated until there were no rotamer outliers, roughly 86% of the residues were in the favoured and 14% were in the allowed region of the Ramachandran plot. Figures 3.10 and 3.11 show the quality of the fitting of the model into the EM map and Figure 3.12 shows the Ramachandran plot for the final SAT1 structure, along with the final refinement statistics.

The final structure had missing EM density for the capsid protein VP1 between residues 140 and 162 (inclusive), known to be the highly flexible and antigenic G-H loop in FMDV. The EM density at the N-terminus of VP2 (residues 1 - 12) and two regions of VP4 (residues 1 - 14 and 40 - 64) were also not well-resolved. Therefore, these residues were removed from the atomic model, so as to accurately represent which residues could be seen without a doubt in the EM density. Figure 3.13

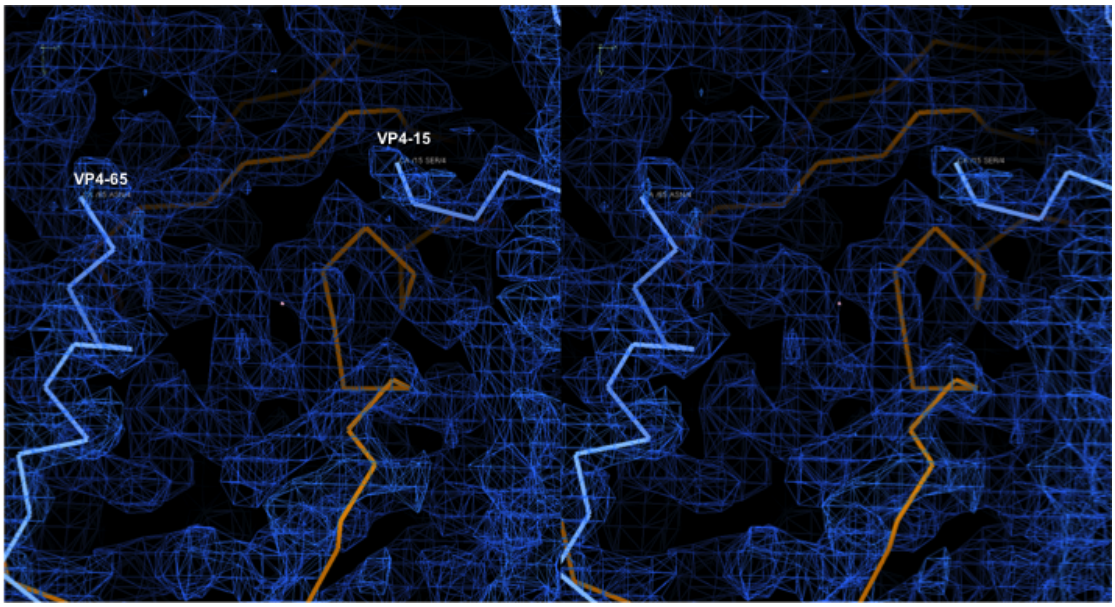


Figure 3.13: Missing VP4 in SAT3 showing missing cryo-EM density (blue mesh), in stereo, between residues 39 - 65 of VP4 and the N-terminal residues 1-14 (blue line) to justify removal of these residues from the final fitted atomic model. VP1 (yellow) can be seen in the background.

shows an example regions to highlight such areas with missing cryo-EM density in VP4.

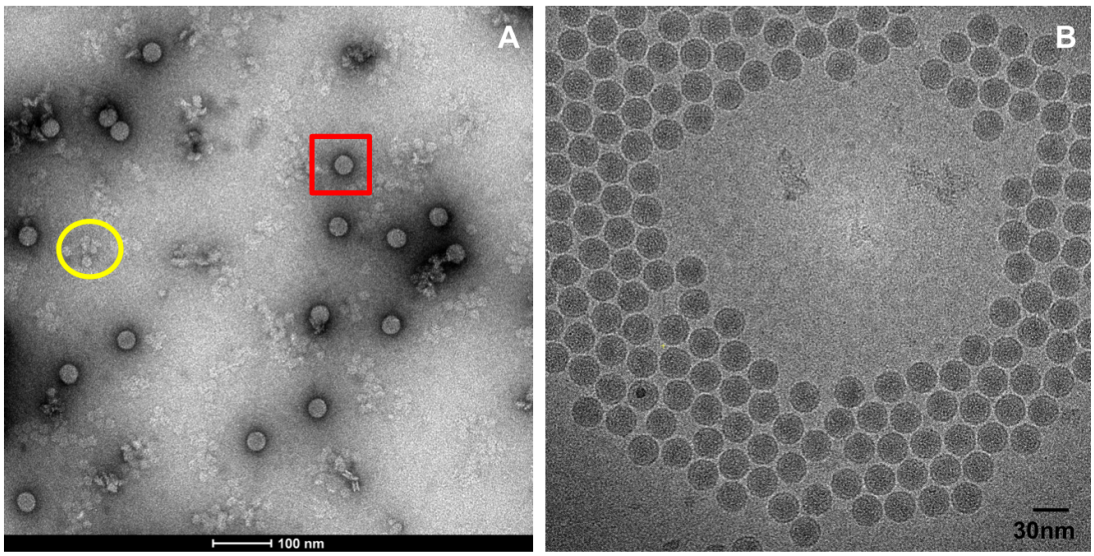


Figure 3.14: Electron micrographs showing SAT3 particles in (A) negative-stained EM and (B) cryo-EM. The red square in panel (A) shows an intact virus particle, as evident by the exclusion of stain from it and the yellow circle shows a group of pentamers from the dissociated particles.

3.3.2 SAT-3

3.3.2.1 Negative-stained electron microscopy

As in the case of SAT1, the quality of the virus purification was checked in negative-stained EM before the sample was plunge-frozen. Figure 3.14 (A) shows that the particles were not aggregated, and even though some particles had dissociated into pentamers, there were plenty of intact virus particles present even in a diluted sample.

3.3.2.2 CryoEM data collection

After ensuring that the virus purification protocol had been successful, the sample was diluted down to 0.6 μg/μL and plunge-frozen for cryo-EM data collection. A sample micrograph is shown in Figure 3.14 (B). The cryo-EM data were collected

at the Polara microscope (FEI) and after motion-correction, alignment and CTF correction, about 71,000 particles were picked for further processing.

3.3.2.3 2D classification

Similar parameters as in the case of SAT1 were used for the 2D classification of the SAT3 dataset, with the addition of the *–only_flip_phases* option in Relion. This option seemed to correct the problem initially seen with SAT1, where all the 2D-classes were not being populated. Using this option ensured that the amplitudes of the CTF function were not modified in the CTF corrected version of the particles. Under normal CTF correction parameters, Relion evens out the amplitudes of the CTF function (except at true zeros of the function). When only phases are flipped and the amplitudes are not modified, the lower-resolution information from the particles is emphasised more than the higher-resolution information. This makes it easier for Relion to classify large particles, such as viruses, into 2D classes based on low-resolution features. The 2D classes obtained are shown in Figure 3.15. All the classes represent the different views of the virus particle. There were no glaringly bad particles in the 2D classes (as shown in Figure 3.15) and the angular accuracy of rotation for all the classes ranged from 0.46 - 1.42 degrees in the model.star file. Often, particles in close proximity to each other lead to poorer angular alignment due to smearing (second in the top row, Figure 3.15), but these low-resolution details of the viral particles may still be important; therefore all the particles were combined for 3D classification.

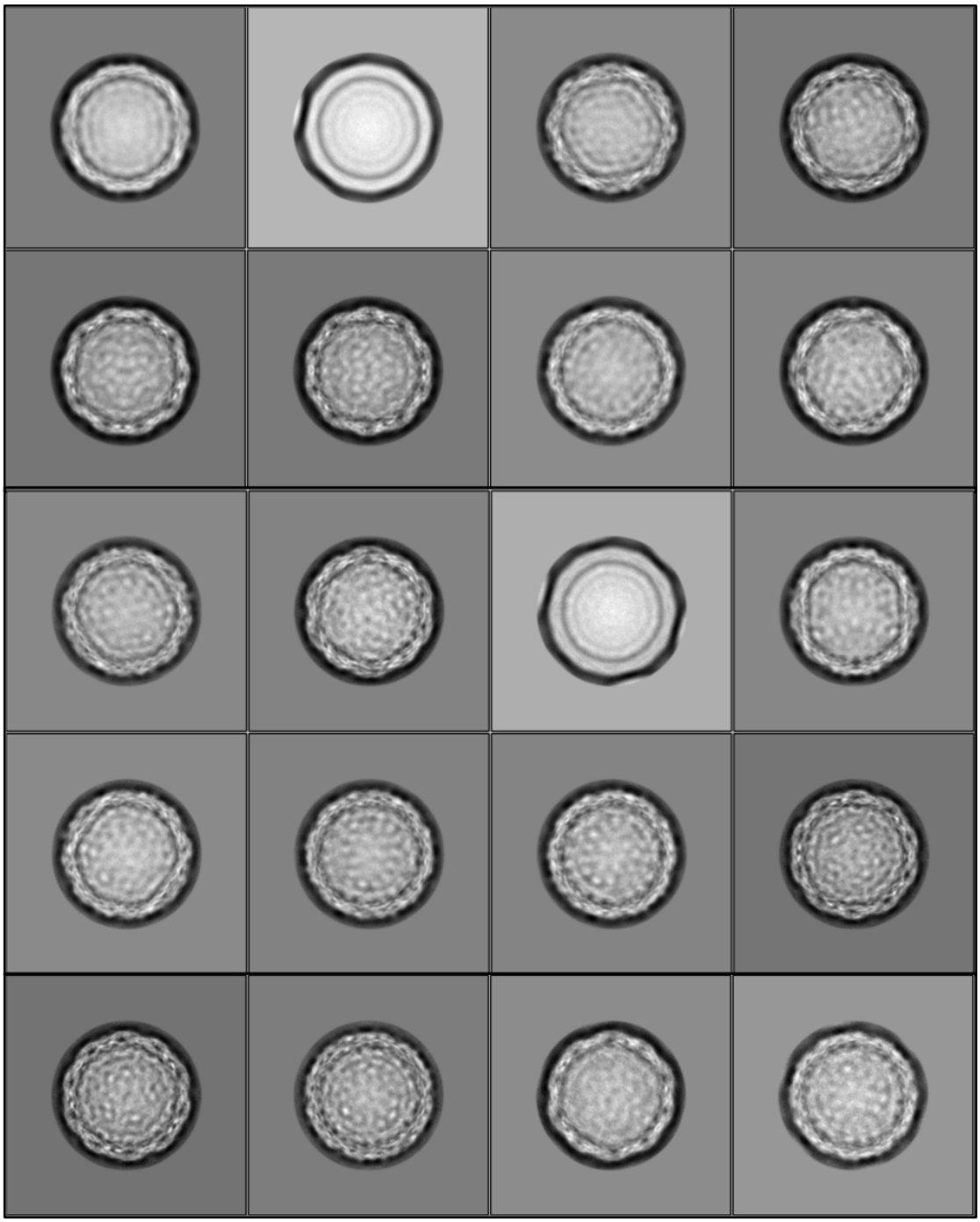


Figure 3.15: About 71,000 SAT3 particles sorted into twenty 2D classes. Here shown in reverse-sorted order by class distribution. The number of particles per class were 11493, 5635, 4822, 4477, 4107, 3823, 3685, 3232, 3174, 2944, 2938, 2910, 2903, 2781, 2633, 2416, 2352, 1872, 1597 and 847 respectively, and they were re-combined for 3D classification.

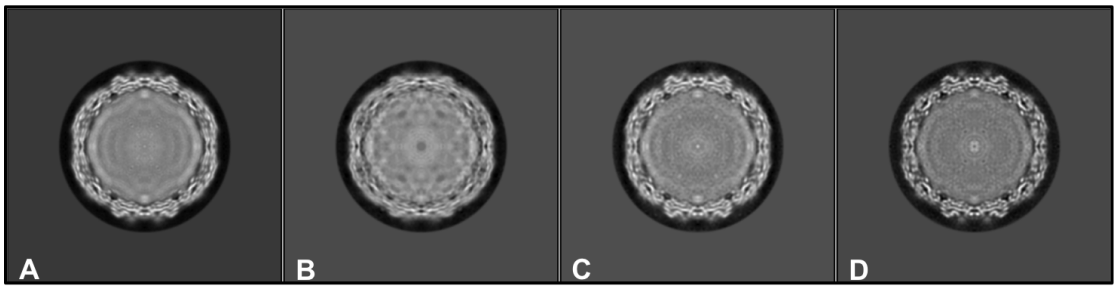


Figure 3.16: SAT3 particles sorted into 3D classes in Relion, shown in reverse-sorted order by class distribution, where Class A had the most and Class D the least number of particles.

3.3.2.4 3D classification and refinement

The 3D reconstruction of the virus particle, obtained from the 2D class averages, was re-projected and 3D classified by the iterative process of 3D classification (as explained in the EM methods chapter). To this end, as with SAT1, an existing FMDV map, low-pass filtered to 50 Å, was used as the initial model. Figure 3.16 shows the 2D projections of each of the 3D class averages obtained after the iterative classification procedure converged on a consensus structure in each case. Class A had roughly 41000, class B 25000, class C 2800 and class D 1800 particles; their 3D depictions are shown in Figure 3.17.

The angular accuracies of the four classes did not differ significantly (from Class A - D: 0.47, 0.66, 0.58, 0.37 degrees respectively). Therefore, the classes with the most particles (A and B as shown here) were combined to produce the final structure. This resulted in roughly 66,000 particles contributing to the final structure of SAT3, which is shown in Figure 3.18 along with a centre-slice through the particle density. The resolution of the final structure was calculated at the Fourier shell correlation (FSC) of 0.143, and determined to be 3.1 Å (Figure 3.20 (A)).

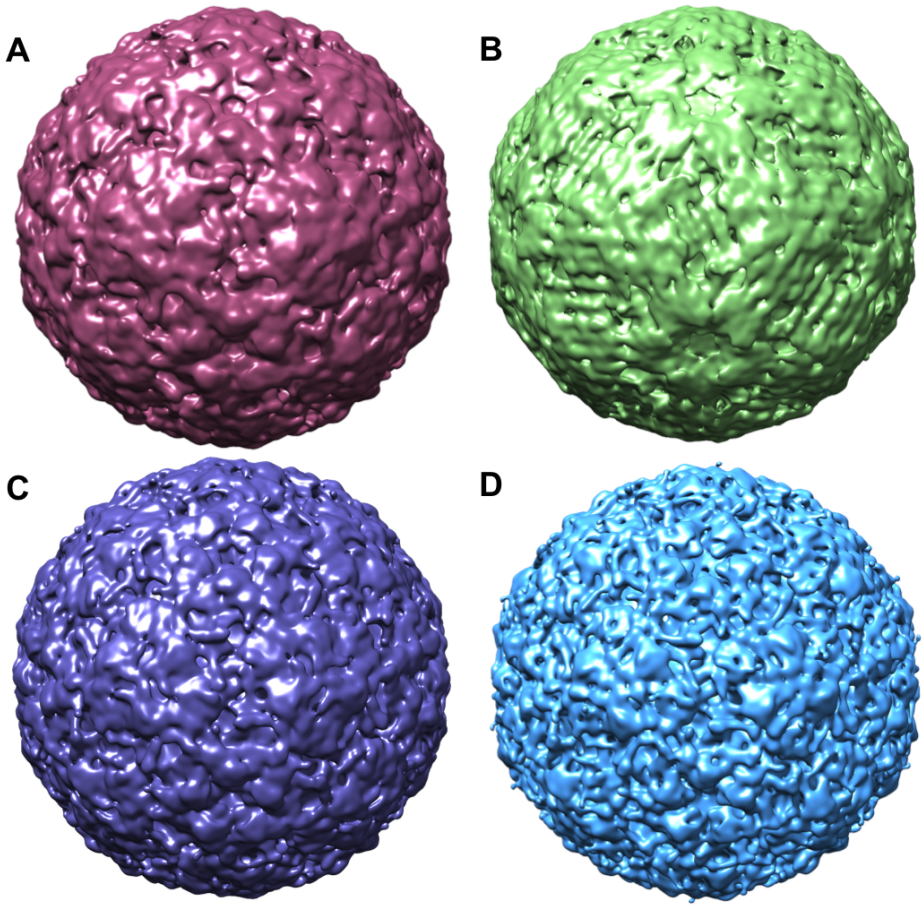


Figure 3.17: SAT3 particles in 3D classes in the Relion processing pipeline. 3D class averages displayed in Chimera with the same level of thresholding for all classes, in the corresponding order to that of Figure 3.16.

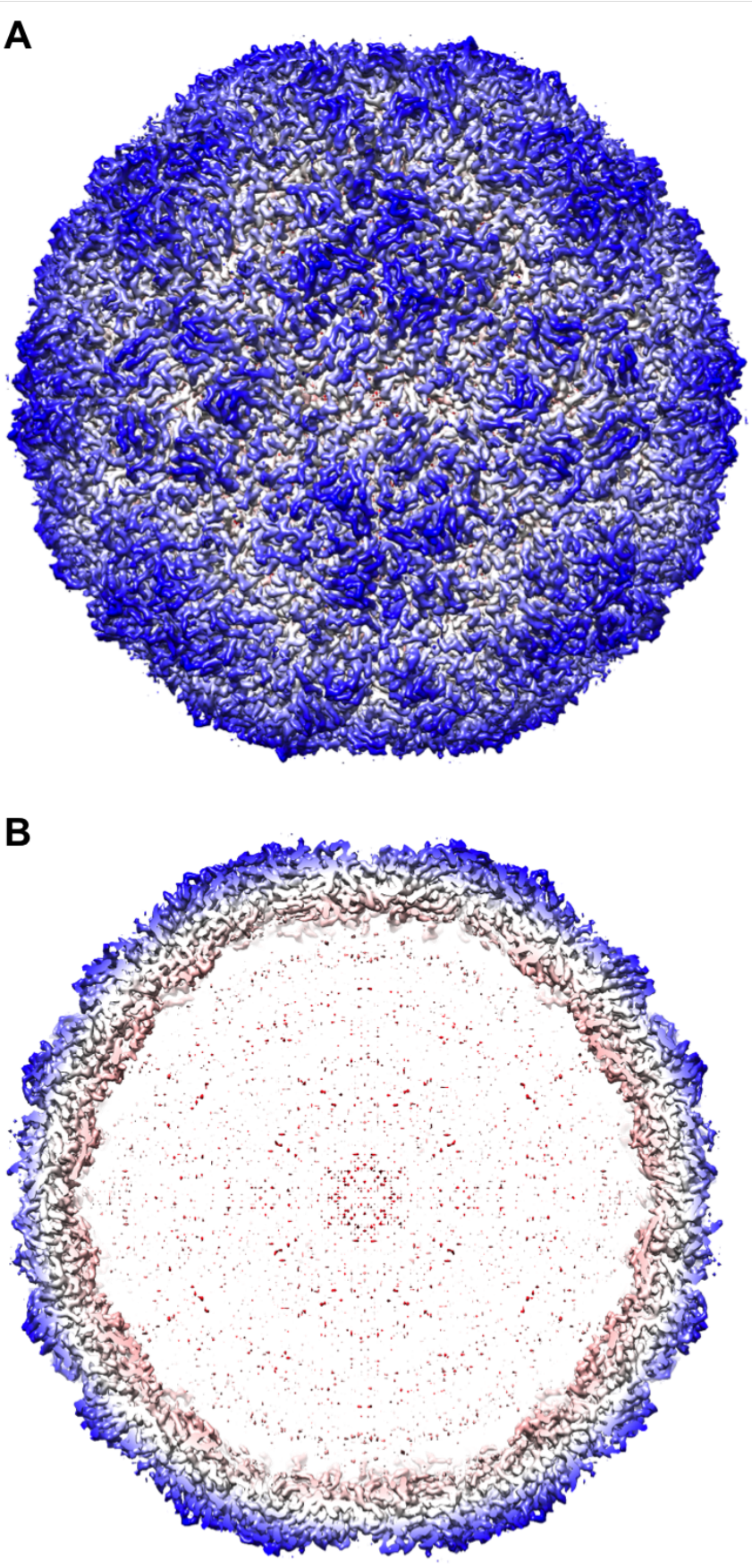


Figure 3.18: Final structure of SAT3 at 3.1 Å, as displayed in Chimera. (A) Full density, coloured by radius and (B) the centre slice of the particle.

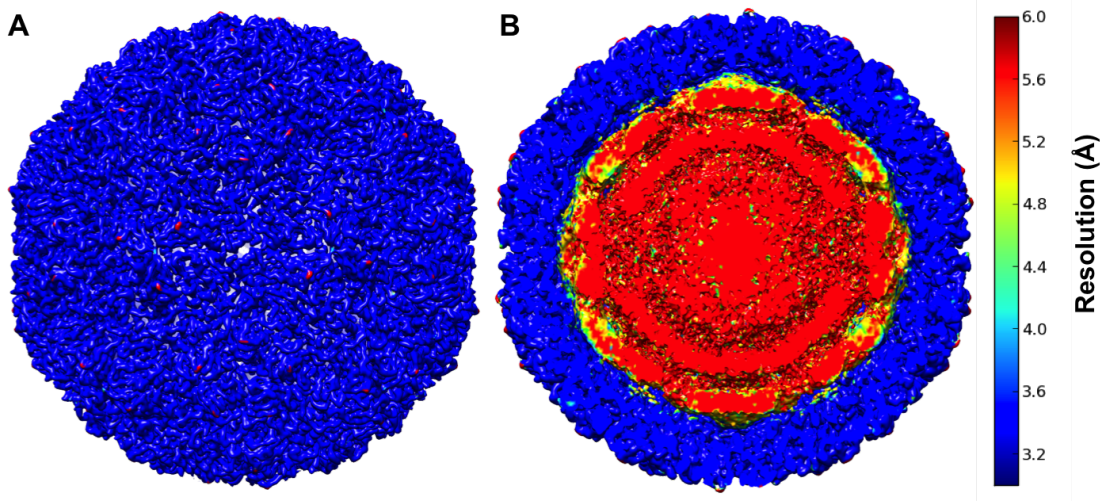
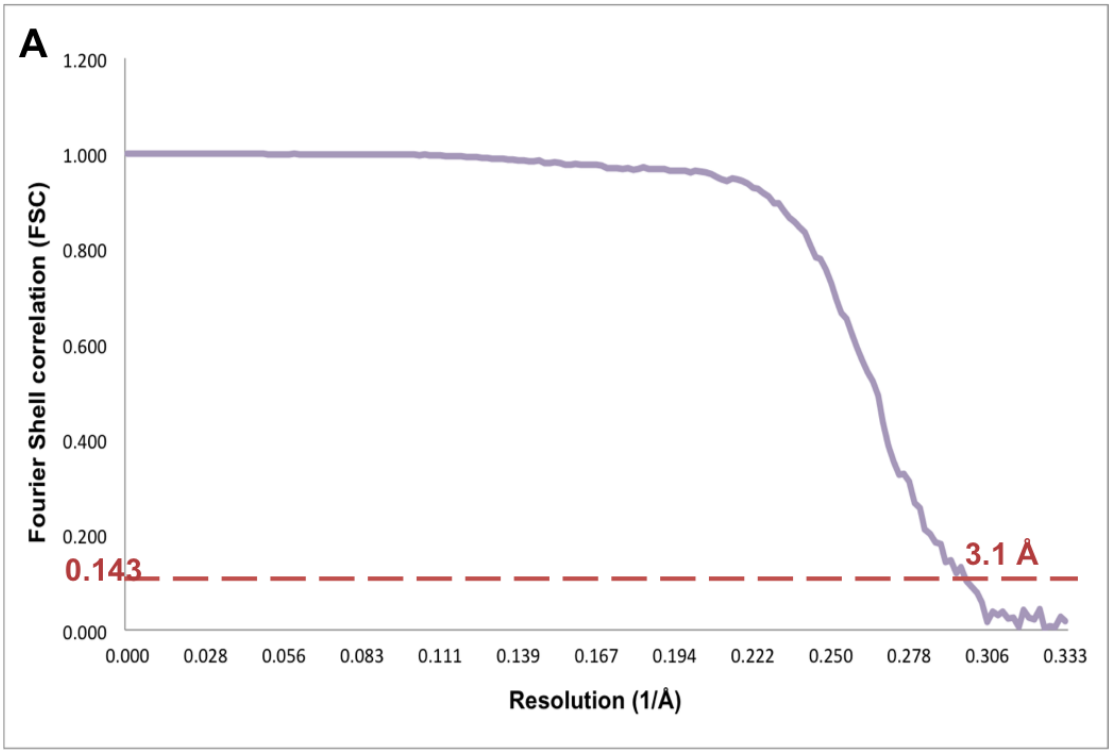


Figure 3.19: SAT3 structure colour-coded as shown in ResMap to show (A) the outer surface and (B) the inside of the capsid, containing the genome.

As in the case of SAT1, ResMap [160] was used to visualise the highest- and the lowest-resolution regions of the SAT3 capsid. Figure 3.19 shows that the majority of the capsid shell was close to the resolution of 3.0 Å (Figure B.2, Appendix B for additional statistics), and very few areas, close to the outer edges (beside the inside of the capsid, showing the genome) of the structure, were at a significantly low resolution. This was expected, as a lot more particles contributed to the SAT3 than the SAT1 structure, leading to a much better resolution determination. Compared to SAT1, a slightly more layered structure of the RNA genome inside the capsids could also be seen.

3.3.2.5 Model fitting

As there are no known structures of SAT3, the atomic model of SAT2 (PDB ID 5ACA [103]) was docked into the final cryo-EM density map of SAT3, using Coot [146] (Figure 3.21 and 3.22). The sequence was then manually checked, and mutated residue by residue, to match that of SAT3. The viral sequence of



B

SAT3 refinement measure	Final figures
Map cross-correlation (whole unit cell)	71.7%
Map cross-correlation (around atoms)	84.7%
All-atom clash score	12.93
Ramachandran outliers	0.47%
Ramachandran allowed	13.29%
Ramachandran preferred	86.23%
Rotamer outliers	0.00%
C-beta deviations	0

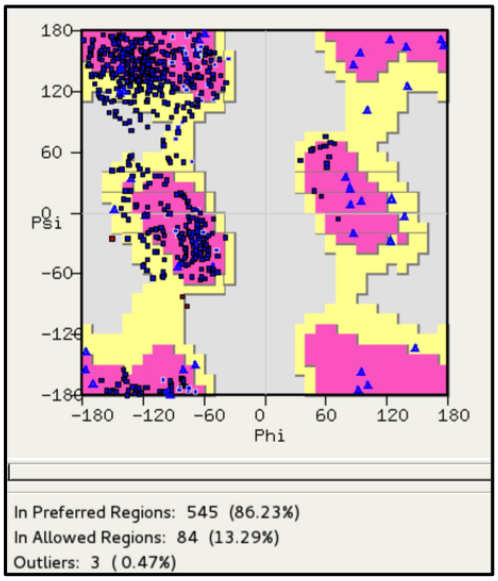


Figure 3.20: (A) Gold-standard resolution determination, at the FSC cut-off of 0.143, of the SAT3 structure. (B) The refinement statics and the Ramachandran plot of the final structure is also shown.

SAR/1/06 SAT3 strain was provided by our collaborator Francois Maree's lab in South Africa, and used for the atomic model building of VP2, VP3 and VP4, as the sequence of SAR/2/06 available at the time only included VP1. As both the sequences had been obtained from the same strain and the same outbreak, just two different animals, the sequence of SAR/1/06 was considered adequate for model building. A sequence comparison of all SATs is included in the following chapter along with more detailed structural comparison.

The docked model was manually refined to ensure the residues fitted well into the density. Phenix [147] was then used for real-space refinement and the structure manually checked again to fix any rotamer or Ramachandran outliers. After a few iterations, a cross-correlation between the atomic model and the EM map unit cell of over 70% was achieved; the cross-correlation around the atoms was even higher (about 85%). There were no rotamer outliers, roughly 86% of the residues were in favoured region of the Ramachandran plot and 14% in the allowed region. Figure 3.21 shows the overview of the atomic model fitting into the EM density at the five-fold axis (in wall-eye stereo view). A close-up of the fitting around the atoms is also shown. Figure 3.20 shows the Ramachandran plot for the final SAT3 structure along with the refinement statistics. Almost all of the side chains could be fitted into the EM density with high confidence, as shown by Figure 3.22.

As with almost all FMDV capsid EM structures, the flexible VP1 antigenic G-H loop, was not seen in the EM density (residues 134 - 155). The N-terminus of VP2 (residues 1 - 11) and two regions of VP4 (residues 1 - 14 and 39 - 64) were not well resolved either, and therefore cut out of the final fitted atomic model, to

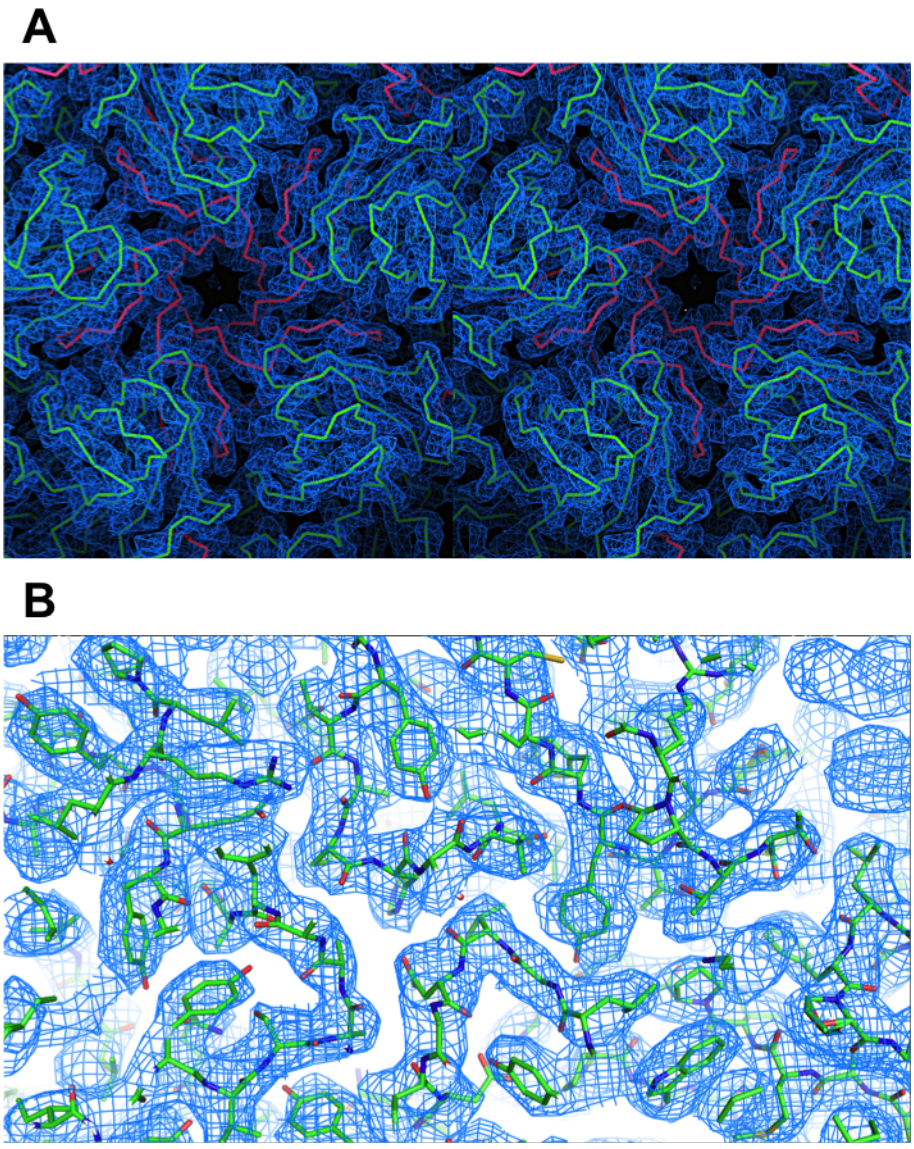


Figure 3.21: The fitting of the atomic model from 5ACA (sticks) into the EM density (mesh, sigma level 2.4 RMSD) of SAT3 shown (A) at the five-fold axis in wall-eye stereo for overview and (B) zoomed in on a representative area to show the quality of fitting in Pymol (not in stereo).

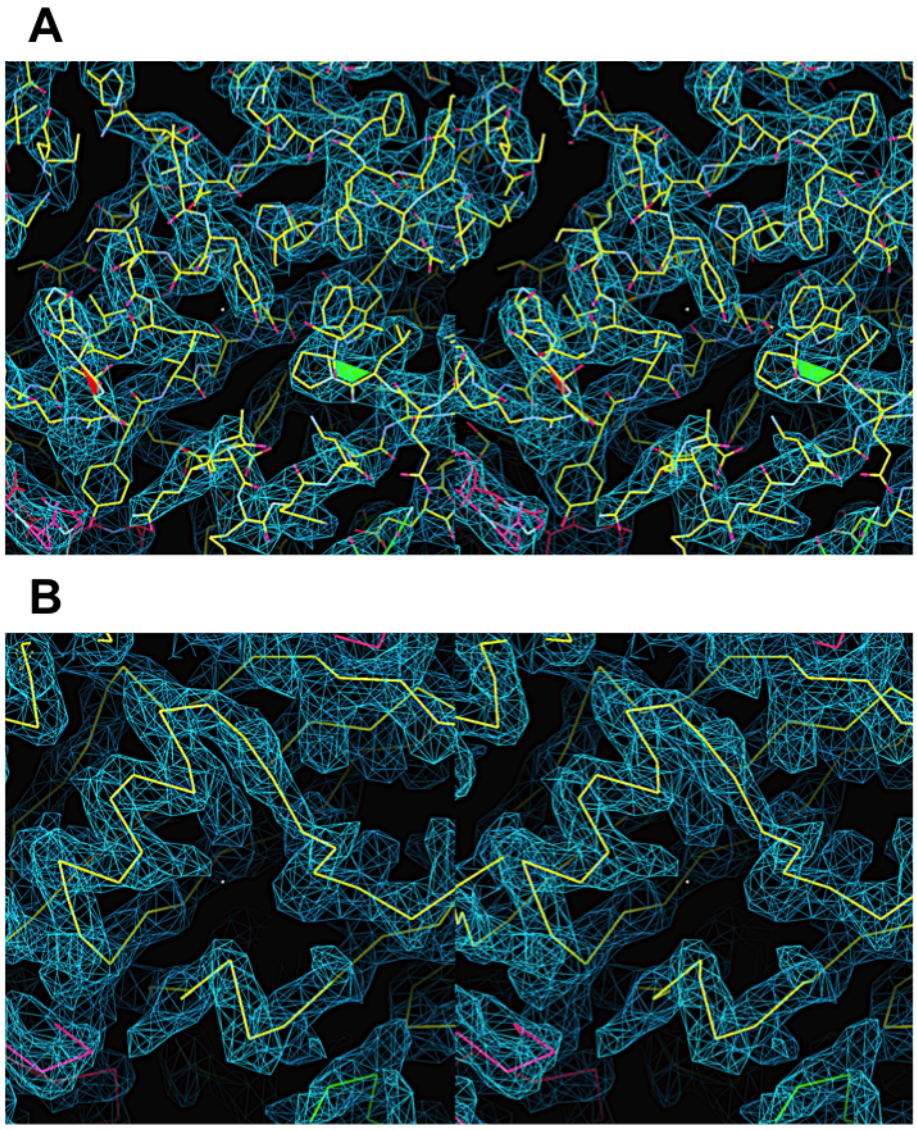


Figure 3.22: Another example area showing the fitting of the atomic model into the EM density (mesh) (sigma level 2.3 RMSD)of SAT3 shown in wall-eye stereo view (A) as the atomic model and (B) the protein backbone using the same region. The loop shown spans residues 89-97 of VP2 (yellow line).

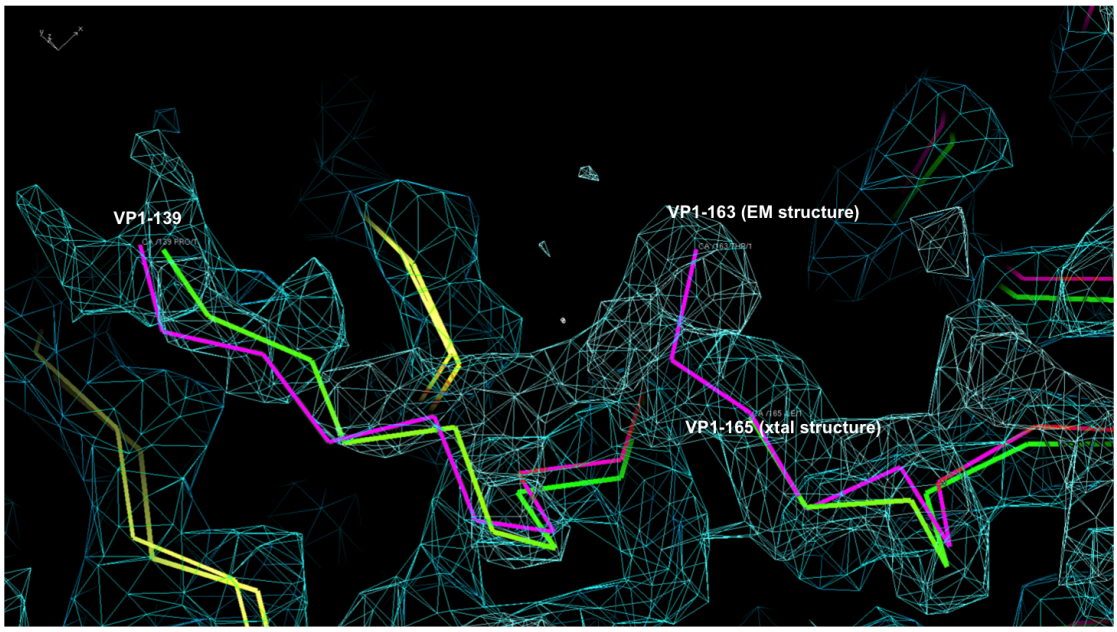


Figure 3.23: Showing the missing G-H loop from SAT1, between residues 139 and 163 of VP1. The atomic model (pink) has been removed where EM density (mesh) (sigma level = 2.3 RMSD) could not be observed. The difference between the atomic model from the crystal structure (2WZR) (green) and the EM structure (pink) is also highlighted, where the crystal structure is missing residues 163-164 in addition to the G-H loop mentioned before. VP4 can be seen in the background in yellow.

accurately represent the structure density seen by cryo-EM.

3.4 Discussion

Cryo-EM is becoming an increasingly powerful tool for structure determination of large and complex biological machineries. Viruses can be ideal samples for the single-particle cryo-EM approaches, especially in the cases where they offer icosahedral symmetry. The time spent in possibly lengthy crystallisation attempts to determine a high-resolution structure may be saved if the samples prove amenable to vitrification. Furthermore, the advent of direct electron detectors has pushed the resolution boundaries possible for structure determination using cryo-EM. The

need to pick hundreds of thousands of particles from cryo-EM samples has also been reduced. These structural studies have the potential to assist in vaccine design, a crucial effort in the field, for a virus that has the potential to cause severe economic problems in several parts of the world.

The structures presented in this chapter complete the database for SAT serotype structures. 5400 particles were used to determine the structure of SAT1 at 3.8 Å, whereas the structure of SAT3 was determined using roughly 66,000 particles, demonstrating that the resolution gain in cryo-EM is not linearly dependent on the number of particles and the resolution reaches a plateau after a certain number of particles. The 3.0Å-SAT1 crystal structure, that had previously been deposited in the PDB (2WZR) but not explained in detail in literature, has now been put into a native context in the cryo-EM maps. The novel SAT3 structure at a resolution of around 3 Å allowed unambiguous fitting of an atomic model into the map.

As expected, the flexible VP1 G-H loop was missing from both the structures, along with the N-terminus of VP1. The regions of the G-H loop that were disordered were slightly different between SAT1 (VP1 residues 140-162) and SAT3 (VP1 residues 134-155) . Figure 3.23 shows the disordered region from SAT1 as a representative example, with missing cryo-EM density between VP1 residues 139-163. Furthermore, the crystal structure of SAT1 (2WZR) (shown in green) had a slightly more disordered G-H loop, compared to the atomic model fitted into the cryo-EM density (shown in pink).

A comparison of the structural stability of these two and other FMDV serotypes

is covered in the following chapter.

3.5 Conclusion and future direction

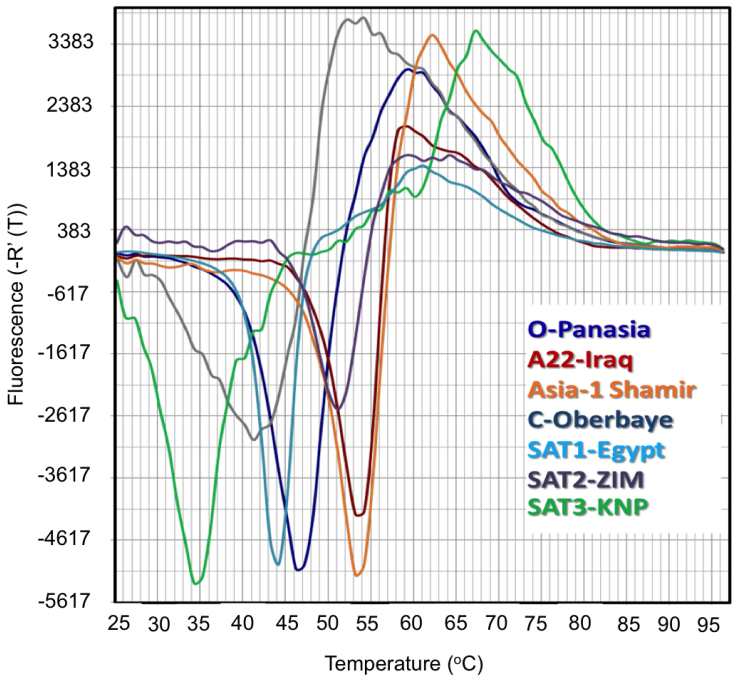
The results in this part of the study comprised of a high-resolution, novel, structure of the FMDV serotype SAT3, determined by cryo-EM in a close-to-native state. A high-resolution cryo-EM structure of SAT1 was also presented, complementing the crystal structure published previously, thus also completing the repository of SAT serotype EM structures. As FMDV must always be handled in high-containment biosafety level-4 facilities, performing structural studies on it is always a challenge. With the help of our collaborators at the Pirbright Institute and the MSD, we were able to get inactivated FMDV SAT1 and SAT3 samples for cryo-EM studies. We hope that these high-resolution structures may benefit further computational and experimental work on FMDV around the world, especially in labs that do not have access to high-containment laboratories or high-end electron microscopes, by providing a high-resolution structure for studies such as those involving antigen-mapping, MD simulations or vaccine design.

Chapter 4

SAT3 structure analysis

4.1 Chapter summary

The SAT2 cryo-EM structure has been published previously (5ACA), with a stabilising mutation at VP2-residue 93 [103]. Once the high-resolution SAT1 and SAT3 cryo-EM structures with fitted atomic models were determined, a comparison to understand the structural variability among the three SATs was performed. The novel SAT3 structure was also compared to serotypes O and A, for antigenic properties, as it is a novel structure with no antigenic data available for it. Using these comparisons, some speculations of the antigenic properties of SAT3 were made and are presented here.



Serotype	Melting temp (°C)
O-Panasia	46.2
A22-Iraq	53.2
Asia-1 Shamir	53.2
C-Oberbayern	42.2
SAT1-Egypt	44.2
SAT2-Zim	51.0
SAT3-KNP	34.3

Figure 4.1: PaSTRy assay showing thermal stability of different FMDV serotypes (from Abhay Kotecha) [32] .

4.2 Methods and Results

The FMDV serotypes vary in their thermostability considerably, as shown by the results in this section. Subsequently, computational approaches were used to compare the SAT3 structure to other serotypes in order to explain this difference in structural stability and speculate on its antigenic consequences. Each method and its results are presented in separate sections and explained in the Discussion section.

4.2.1 SAT3 vs. serotypes SAT1 and SAT2

4.2.1.1 Thermostability

Thermal stability is a crucial factor for the research or design of vaccine candidates [102, 103, 161]. How thermally stable the vaccines are determines how long a shelf life they might have, or how susceptible to fluctuation of temperature in the cold chain they might be. The stability of the capsids is important, because the more structurally intact the particles in the vaccines, the better the antigenic immune response generated [36]. FMDV capsids dissociate at low pH or high temperatures into non-potent pentamers; the temperature at which this happens varies between different serotypes [36]. Inactivation protocols further reduce the stability of the capsids [32, 36, 162]. FMDV SAT serotypes are prevalent in sub-Saharan Africa, where the warm weather puts even higher demands on the cold chain in storage and handling. The vaccines, especially in such cases, have a much higher chance of success if they are thermally stable. Therefore, when solving a novel FMDV structure, it was of interest to know how stable it was in comparison to the other FMDV serotypes.

To check the thermostability of the FMDV capsids, the thermofluor assay PaSTRy (Particle Stability Thermal Release Assay), was used [32, 163]. The assay relies on the virus dissociating (melting) at high temperatures and exposing the RNA in the process. The genome then becomes accessible to the fluorophore, and their binding is detected by the release of a fluorescent signal. For the results shown in Figure 4.1, 0.4 μg of each virus serotype was used. The dye used was SYTO9 (Molecular Probes, Invitrogen, final dilution 1:100) and the plates were read out

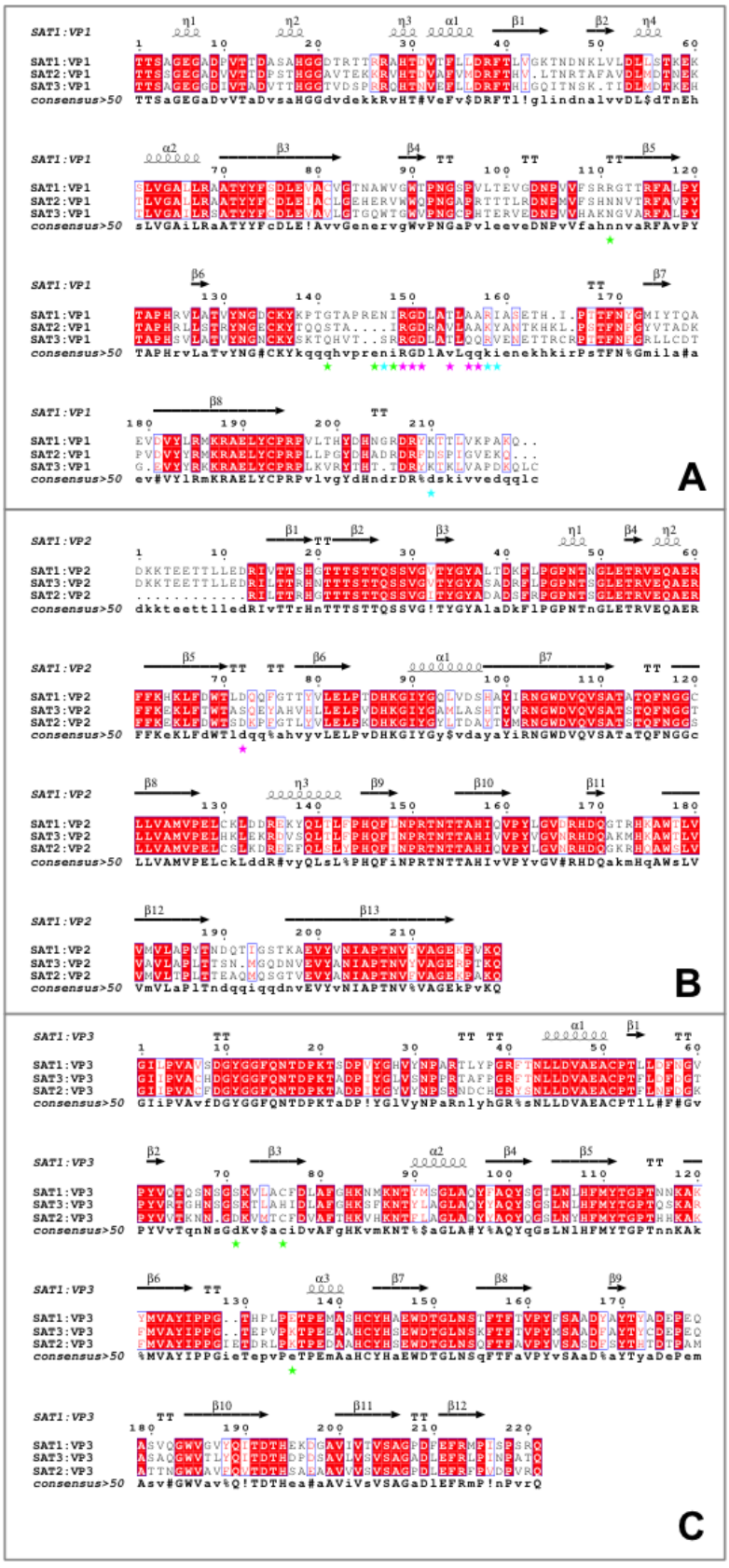


Figure 4.2: Multiple sequence alignment of SAT1, 2 and 3. (A) VP1, (B) VP2 and (C) VP3 proteins were aligned against the secondary structure of SAT1 (2WZR) to check for consensus. VP4, almost entirely conserved between the three serotypes, is not shown here. Green stars represent the experimentally determined antigenic sites for SAT1, blue stars SAT2, and pink stars the sites that were shown to be antigenic in both SAT1 and SAT2 [91].

using an Agilent MX3005 PCR machine. The temperature was increased from 25 °C to 94 °C with a step size of 0.5 °C every 10 seconds, and fluorescence was read at the wavelength of 490 nm for excitation and 516 nm for emission. The data obtained were visualised in MxPro software (Strategene, UK) and the minima of the negative first derivative of the fluorescence curves were taken to be the RNA-release temperatures in each case.

Figure 4.1 shows that the SAT serotypes were relatively more unstable compared to the other FMDV serotypes. The SAT2 strain used here had a stabilising mutation at VP2 residue 93 (from Serine to Tyrosine) [103], which rendered it much more thermally stable (discussed in the next section). Native SAT2 has a lower melting temperature of 46.3 °C [32], which is nevertheless higher than the melting temperature of SAT1 (44.2 °C). SAT3 SAR/2/06 is the most unstable SAT serotype as confirmed by the lowest melting temperature of 34.3 °C.

4.2.1.2 RMSD

SAT1, 2 and 3 have a sequence-identity of over 60% in the capsid proteins (Figure 4.2), yet there is still a difference in their structural stability as shown by the thermal stability results in Figure 4.1. The differences in sequences can be considerable between the three capsid proteins, as shown by Figure 4.4; VP4 is largely conserved (over 95% sequence identity between the three serotypes), as it faces the inside of the capsid and does not encounter selection pressure. SAT1 and SAT3 structures were expected to be the most similar, based on their highest sequence similarity.

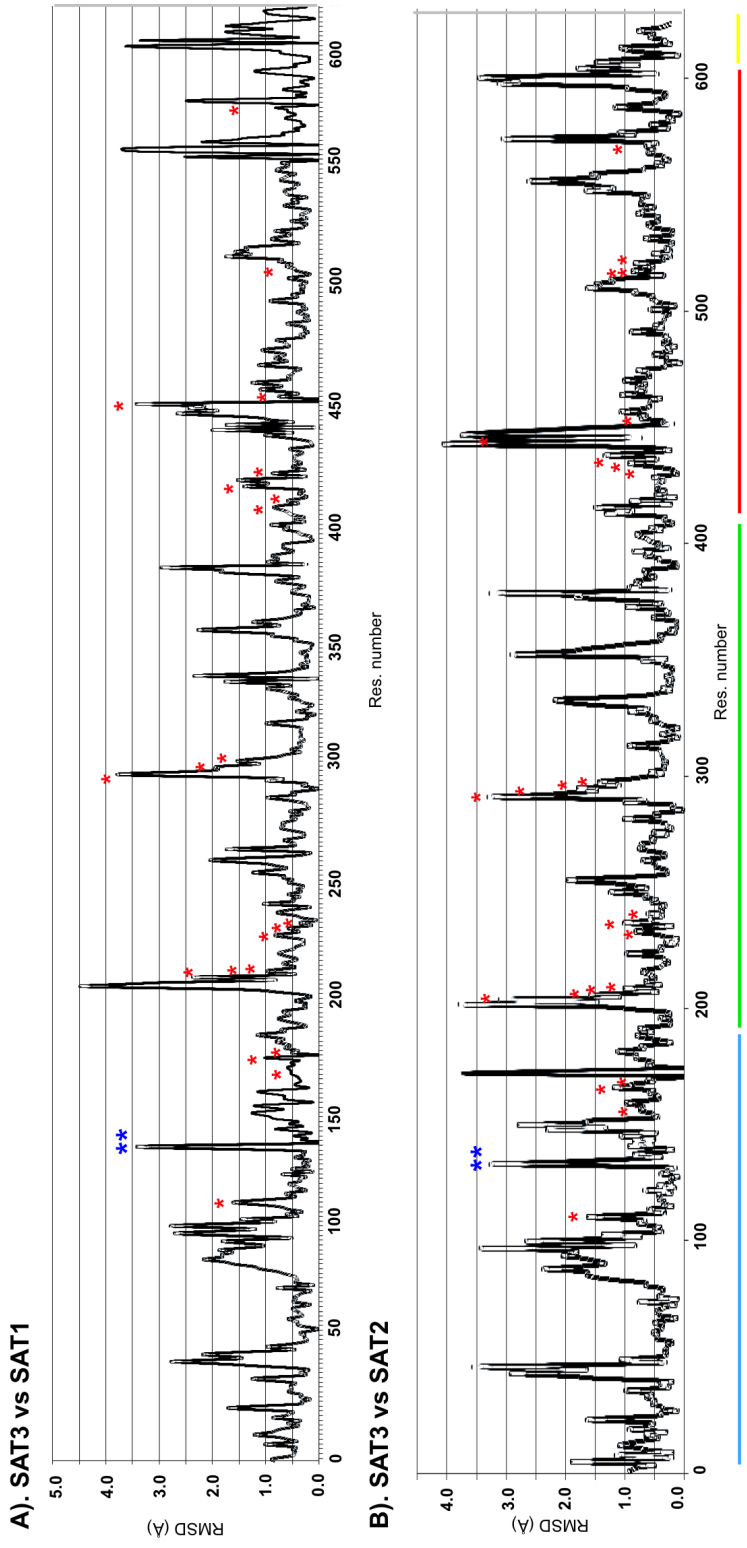


Figure 4.3: RMSD deviation curves between (A) SAT3 and SAT1 and (B) SAT3 and SAT2. Residues 1-172 represent VP1, 173-379 VP2, 380-600 VP3, and 601-624 VP4 overlay respectively; marked at the bottom by blue, green, red and yellow lines respectively. Residues shown to be antigenic (Figure 1.9) in other serotypes are marked with a red asterisk. The two blue asterisks mark the peak at the site near the missing GH loop.

VP1	SAT1	SAT2	SAT3
SAT1	-	57.8%	59.4%
SAT2	57.8%	-	53.1%
SAT3	59.4%	53.1%	-

VP2	SAT1	SAT2	SAT3
SAT1	-	73.0%	75.7%
SAT2	73.0%	-	75.2%
SAT3	75.7%	75.2%	-

VP3	SAT1	SAT2	SAT3
SAT1	-	66.8%	76.0%
SAT2	66.8%	-	70.9%
SAT3	76.0%	70.9%	-

Figure 4.4: ClustalW [164] was used to compare the sequence identity of the three viral proteins (VP1-3) between SAT1, SAT2 and SAT3, shown in a tabular form here.

It is worth bearing in mind that even small structural changes and point mutations may lead to dramatically different stability and antigenic variation. Figure 4.2 shows the antigenic sites for SAT1 (marked with green stars) and SAT2 (marked with blue stars) that were determined experimentally, via escape-mutant studies, by Grazioli et al., 2006 [85, 91]. There were some sites that were common between the two serotypes (marked with pink stars), and are possibly conserved in SAT serotypes. The antigenic properties are covered in greater detail in a separate section.

The structure of SAT3 was completely novel, therefore as the first comparison, its core structure was superposed, in Coot (and verified with SHP), on to SAT1 and SAT2 respectively. This showed a sequence identity of about 68% and 65% respectively. A pair-wise RMSD plot was generated to see where the two structures differed most significantly; Figure 4.3 shows the results. The overall RMSD

between the pairs of structures were not structurally significant, except in the vicinity of the disordered regions, confirming that the core structures of the three serotypes were almost identical. The average RMSD between SAT3 vs. SAT1 and SAT2 was roughly 1.3 Å and 1.6 Å respectively, which did not indicate large structural differences. However, where the residue-wise RMSD plots showed that there were a few pairs where the RMSD exceeded 4 Å (VP2-131 for SAT1 and VP2-130, VP3-64 and VP3-193 for SAT2), the overlaid structures were inspected manually to see whether the secondary structure folds might be different at these positions, leading to different structural properties. These results are discussed in the Discussion section.

4.2.1.3 PISA

The inter-protomer interface for each SAT serotype was analysed in PISA [165]. As PISA detects and analyses interactions between each chain recognised in the PDB file supplied, the interfacing proteins (VP2 and VP3) for each protomer were re-labeled to a single chain using a python script, such that the final file contained only two chain labels (one for each protomer) instead of four. Figure 4.5 (B) shows the structure after re-labelling the chains, that was input into PISA. The interactions between adjacent protomers were thus analysed in terms of hydrogen-bonding and interacting surface area. The interacting surface area (Interface Area highlighted in Figure 4.5 (A)) was shown as roughly the same between the three serotypes; this may be expected, as the secondary structure is widely conserved in the SAT serotypes. Whereas, the hydrogen-bonding (N_{HB} highlighted in Figure 4.5 (A)) varied significantly between the three serotypes, with SAT1 having the most extensive hydrogen bonding of the three SAT serotypes, and SAT3 the least.

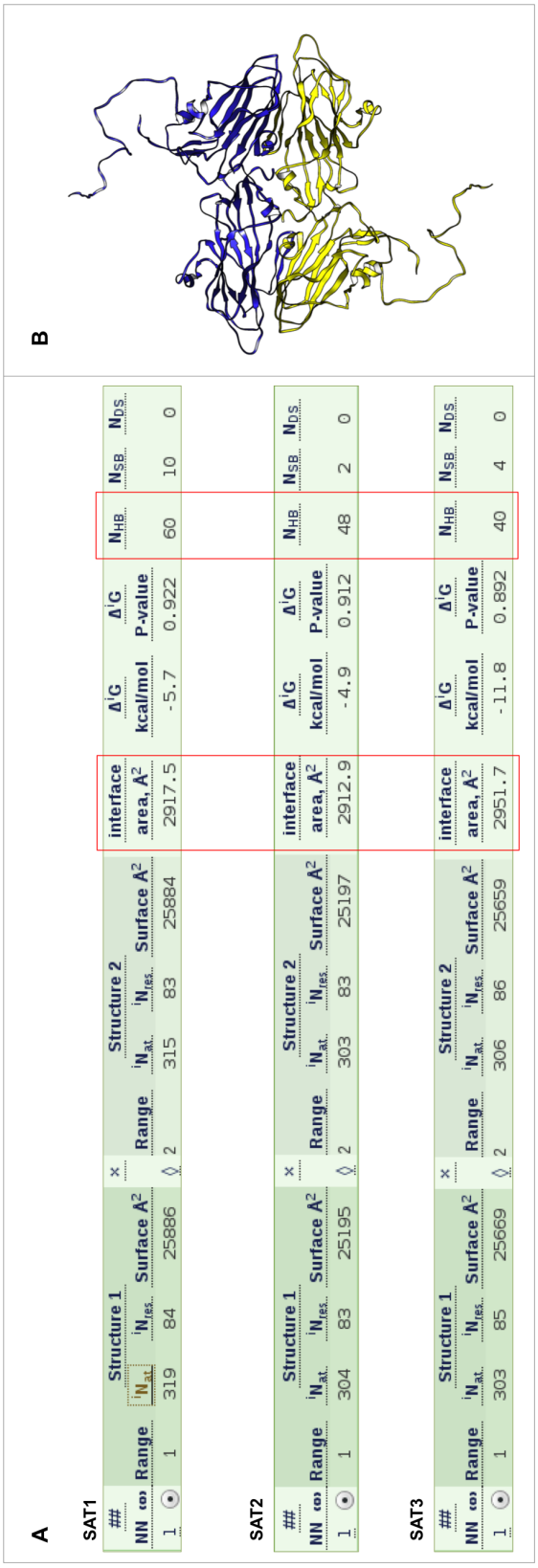


Figure 4.5: PISA analysis of VP2-VP3 interfaces from adjacent pentamers. (A) SAT1, SAT2 and SAT3 inter-protomer interfaces compared. (B) VP2-VP3 were relabelled as a single chain for each promoter and fed into PISA to find interactions between two adjacent promoter interfaces for each serotype.

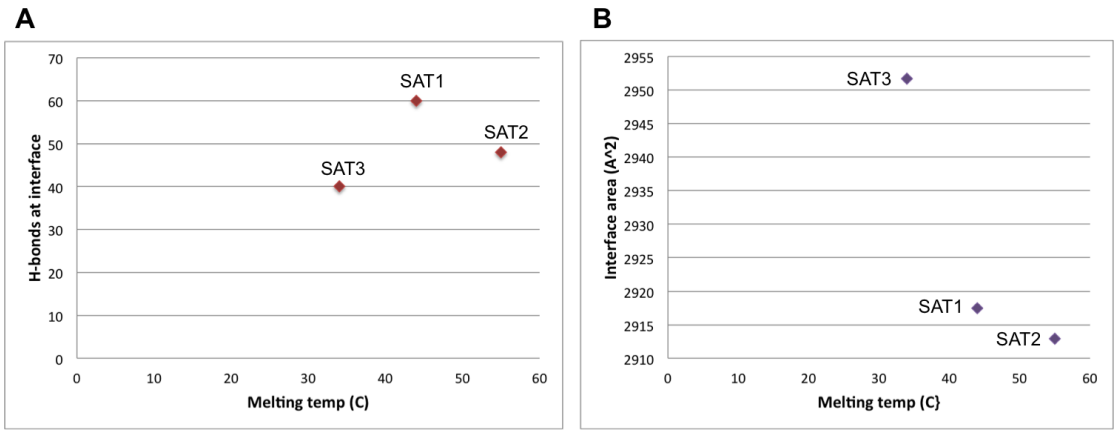


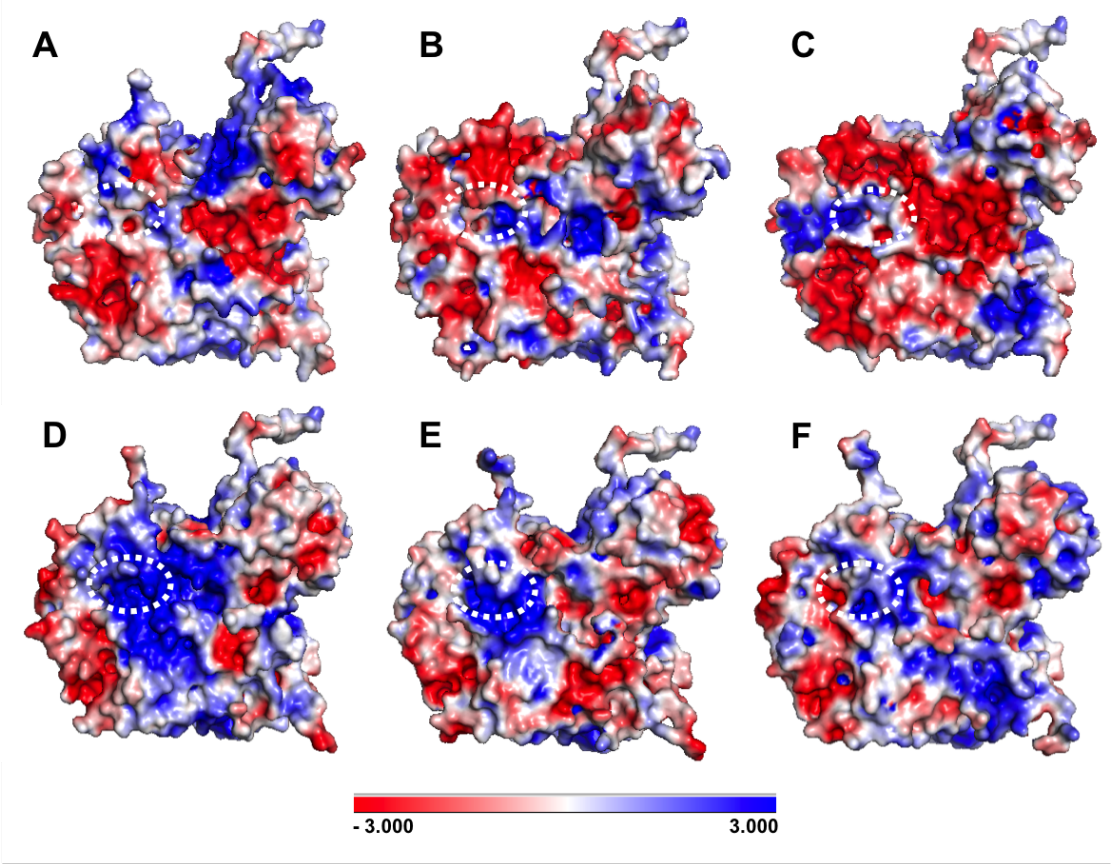
Figure 4.6: (A) Number of hydrogen-bonds and (B) interface area shown in correlation to the melting temperature of each SAT serotype.

This may be explained due to the differences in sequences and thus the interacting side chains at the interface for each structure. Figure 4.6 highlights the correlation between the melting temperature and the number of hydrogen bonds (A) or the interacting interface area (B) for each SAT serotype. A general positive correlation between the extent of hydrogen-bonding and the structural stability indicated by the melting temperature may be seen. However, the lack of correlation between the interface area and the melting temperature was unexpected.

4.2.1.4 Electrostatics

The SAT serotypes have a higher than 65% sequence similarity, and very different structural stability. Structural differences and different charge distribution at the surface may lead to different binding properties to receptors such as Integrin and Heparin Sulfate (HS), and therefore different selection pressure from the host cells' immune system.

Here, Pymol (APBS) was used to perform a comparison of the charged (elec-



FMDV serotype	Passage history	VP3-56
SAT1 (2WZR)	High	D
SAT2 (5ACA)	Low	N
SAT3	Low	D
A10-61 (1ZBA)	High	R
O1BFS (1QQP)	High	R
Cs8c1 (1FMD)	Low	M

Figure 4.7: Electrostatic surface representation of (A) SAT1, (B) SAT2, (C) SAT3, (D) A10-61, (E) O1BFS and (F) Cs8c1 biological protomers. The A10-61 and O1BFS protomers were cell-culture adapted (1ZBA and 1QQP respectively [30,33]), whereas the Cs8c1 protomer was from a low-passage field isolate (1FMD [33]), for comparison against the SATs. The table below shows the residues at VP3-56, the site known to influence Heparan Sulfate binding and the location of this HS-binding site is marked with white ovals.

trostatic) surface of biological protomers from each SAT serotype, as shown in Figure 4.7 (red: most negative, blue: most positive). The charge distribution on the exposed surface of the capsid was quite different between the three SAT serotypes. The distribution of charged residues on the SAT3 surface (C) appeared more similar to that of SAT1 (A) than SAT2 (B), suggesting that its surface properties might also be more similar to SAT1, with which it shares higher sequence similarity than SAT2 (68% vs. 65%).

Figure 4.7 also shows the tissue-culture adapted biological protomers of A10 (1ZBA) and O1BFS (1QQP) (panels D and E respectively), that have been shown to have a strong affinity for HS, a negatively-charged molecule [30, 33]. In comparison, the low-passage SAT3 protomer (Julian Seago, personal communication) was closer to a field isolate. For comparison, the Cs8c1 protomer (1FMD), a low-passage field isolate is also shown. As seen, the tissue-culture adapted protomers had a large positive-charge distribution at the interface of VP1,2 and 3, the site implicated in HS binding, marked by white ovals. The field isolates, like Cs8c1 and SAT3, have a more balanced charge distribution and do not appear to have a large positively-charged surface near the HS-binding site.

The VP3-56 residue is specifically implicated in HS-binding, and is known to mutate from a histidine in the field-isolate to an arginine in the tissue-culture adapted isolate for FMDV serotype O [30, 33]. None of the three SAT serotypes had an arginine residue at VP3-56, as shown by the Table in Figure 4.7, but the general distribution of positive charges on the surface indicated that SAT1 may be adapting to the tissue-culture, by virtue of being a high-passage isolate, whereas

SAT2 and SAT3 have largely negatively-charged surfaces.

4.2.1.5 Surface difference

The different SAT serotypes may also have different antigenic properties owing to differences in the shape of their solvent-exposed surfaces. To compare how different the SAT3 capsid surface was, in comparison to SAT1 or SAT2, it was compared to each of them separately, using a protocol established in the group by Dr. Jingshan Ren [166].

The reference structure, SAT3 protomer, was optimally superposed onto the test structure (in this case SAT1 or the SAT2 protomer) using SHP [167]. Subsequently the solvent-accessible surface atoms were located for each protomer, using *Areaimol* program from the CCP4 suite [168–170]. For each of these atoms in the reference structure, the nearest solvent-accessible atoms of the test structure were located by the *surffdiff* program (courtesy Jingshan Ren). The distance between the two atoms was then stored in the B-factor column of the reference structure's PDB file, which could be coloured by B-factor in Pymol to highlight the variability in the surface-exposed or solvent-accessible surfaces between the two structures in each case, as shown in Figure 4.8.

As observed in Figure 4.8, the SAT3 protomer appeared to have a capsid surface more similar to that of SAT1, than SAT2, in line with the sequence similarity mentioned before.

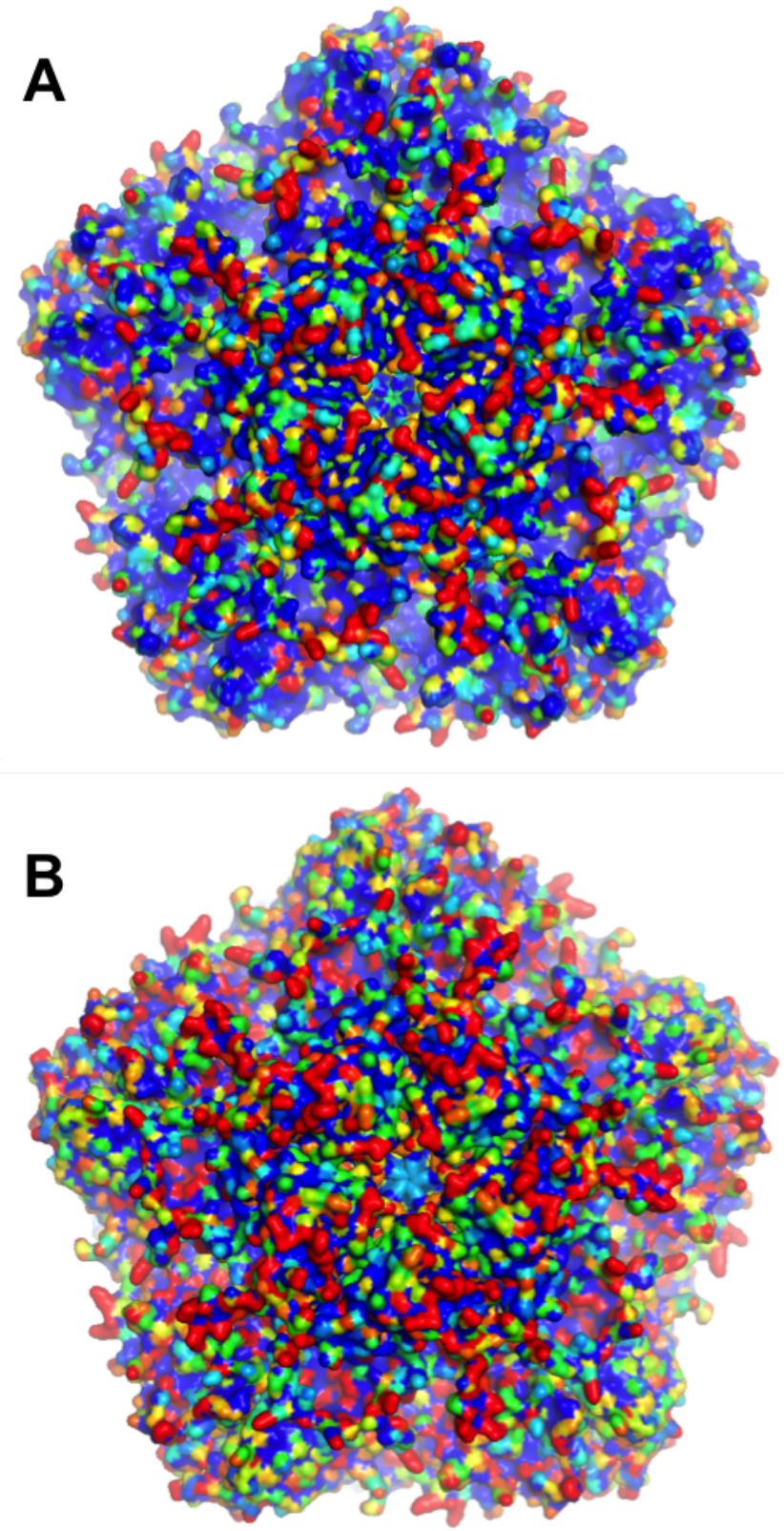


Figure 4.8: Depth-cued surface difference representation between (A) SAT1 and SAT3, and (B) SAT2 and SAT3, highlighted in a blue-red colour scheme in Pymol. Blue areas are the most similar between the two structures and the red areas the most variable. Pentamers shown as seen from outside the capsid.

4.2.2 SAT3 vs. serotypes SAT1, SAT2, A and O

Despite their economic importance in sub-Saharan Africa, the SAT serotypes are not very well-studied FMDV serotypes, structurally or antigenically. Thus far, no experimental studies have elucidated the locations of any antigenic sites on the SAT3 surface. Some information is available on the SAT1 and SAT2 antigenic sites [85, 91]. To make the comparison of the antigenic surfaces more comprehensive, the O and A serotypes were included in this section, as there is more much experimental evidence available for the antigenic sites of these serotypes.

4.2.2.1 Antigenic variation

Using Pymol and the information available from literature, the main antigenic residues and sites were mapped on to the pentamer of SAT3. Figure 4.9 depicts the surface-exposed antigenic sites of O1K (A), A10-A12 (B) and SAT1, SAT2 (C) in white, pink and yellow respectively [85, 86, 89–91]. The last panel (D) depicts all the sites from the four serotypes mapped onto a single pentamer of SAT3 to highlight overlaps, and therefore possibly conserved antigenic sites.

The most well-studied antigenic site (site 1), on the VP1 G-H loop, was common to all the serotypes depicted here. Furthermore, the well-known RGD antigenic sequence was conserved between all three SAT-serotypes. However, this site could not be highlighted on the pentamers shown in Figure 4.8, as in almost all the crystal and cryo-EM FMDV structures, it was too flexible and disordered to be well-resolved. Figure 1.9 in Chapter 1 listed the residues that are known to be antigenic in the serotypes shown in this section, and were used for the annotation

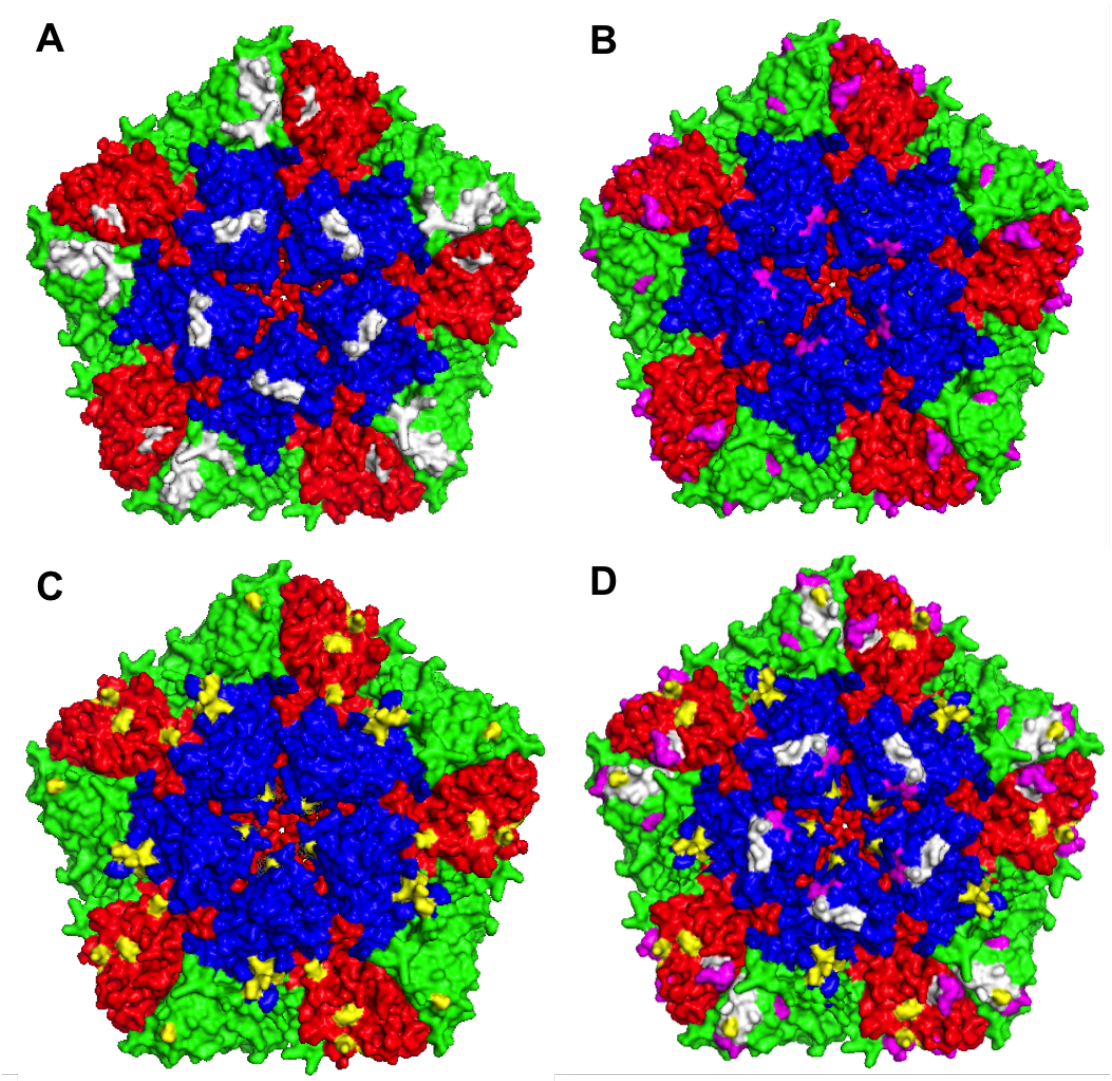


Figure 4.9: Surface representation of a SAT3 pentamer with antigenic sites from (A) O1K [86, 89], (B) A10-A12 [89, 90], (C) SAT1 and SAT2 [85, 91], mapped on in white, pink and yellow respectively. (D) shows all the sites from the other three panels mapped on to the SAT3 pentamer. Pentamers shown as seen from outside the capsid.

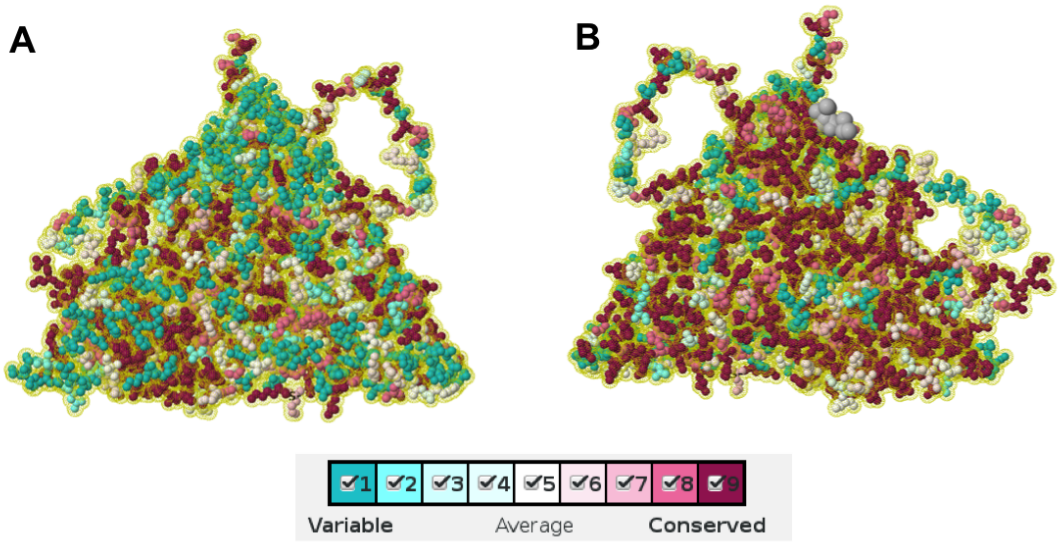


Figure 4.10: Conserved residues between five FMDV sequences from different serotypes (SAT1:2WZR, SAT:5ACA, SAT3, O1K:1BBT and A10:1ZBE), shown on a SAT3 protomer using the ConSurf server [171, 172]. Figure shows the (A) outside and the (B) inside surface of the capsid

in Figure 4.9. Taken together, the antigenic site mapping showed that despite the high variability in the protein sequences between the different FMDV serotypes, there were some antigenic regions in common between all the serotypes. This is shown by the overlap of the three colours (white, pink and yellow), in panel (D) of Figure 4.9, close to the five-fold axis and near the two-fold axis on VP2-VP3 interfaces.

4.2.2.2 ConSurf

ConSurf is an online bioinformatics web-server that calculates the likelihood of the conservation of protein residues in a given structure, based on its homologous sequences and the structural importance of each residue. The conservation scores may provide an insight into the importance of each residue for its struc-

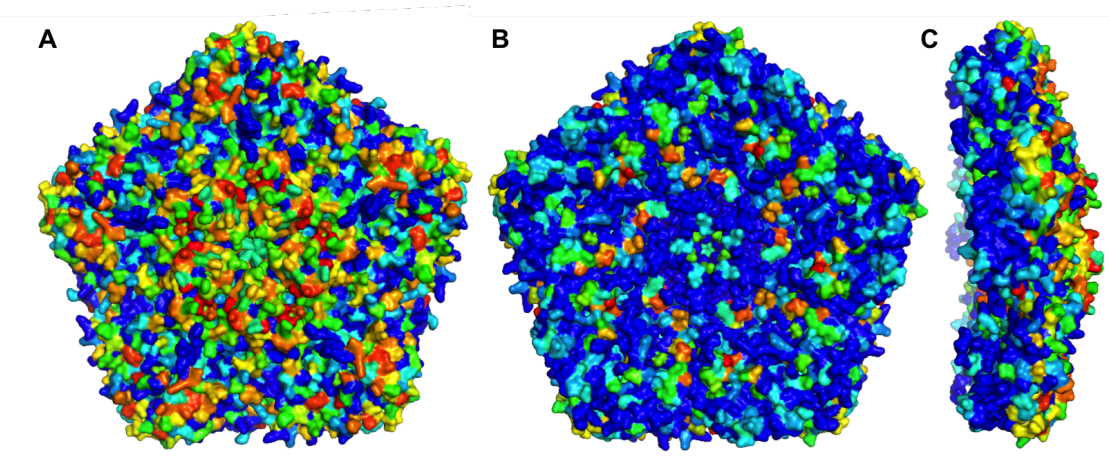


Figure 4.11: Conserved residues on a SAT3 pentamer, shown from the (A) outside and (B) the inside of the capsid. (C) The side view of the pentamer is also shown. Colour coding using conservation score, depicting the least variable regions in blue and the most variable in red.

tural function. It might also help determine how related given structures might be.

Here, ConSurf was used to determine how conserved the structures of the five-serotypes analysed in the antigenic comparison were. A multiple-sequence alignment of the sequences of the five serotypes depicted above (2WZR, 5ACA, SAT3, 1BBT, 1ZBE), generated using MultAlign [173], was input along with the structure of SAT3. The server mapped the sequence conservation information of each residue, by modifying the B-factor in the SAT3 PDB file. The output from the server is graphically depicted in Figure 4.10, where the most variable residues are depicted in cyan, and the most conserved in maroon. As expected, the outer surface of the capsid is far more variable than the inner surface.

To demonstrate in a clear fashion, where the most- and the least-variable regions on the pentamers were, the PDB output file from Consurf with the SAT3 protomer was reconstructed into a pentamer in Chimera and displayed in Pymol, colouring

by the conservation scores in the B-factor column. Figure 4.11 shows the resultant images, where the least variable regions are coloured in blue and the most variable in red.

As expected, the outer surface of the capsid (Figure 4.11 (A)) was generally a lot more variable than the inner surface (B). Furthermore, on the outer surface of the capsid, the residues close to the five-fold axis and at the VP2-VP3 interface near the two-fold axes appeared the most variable, as highlighted in orange and red.

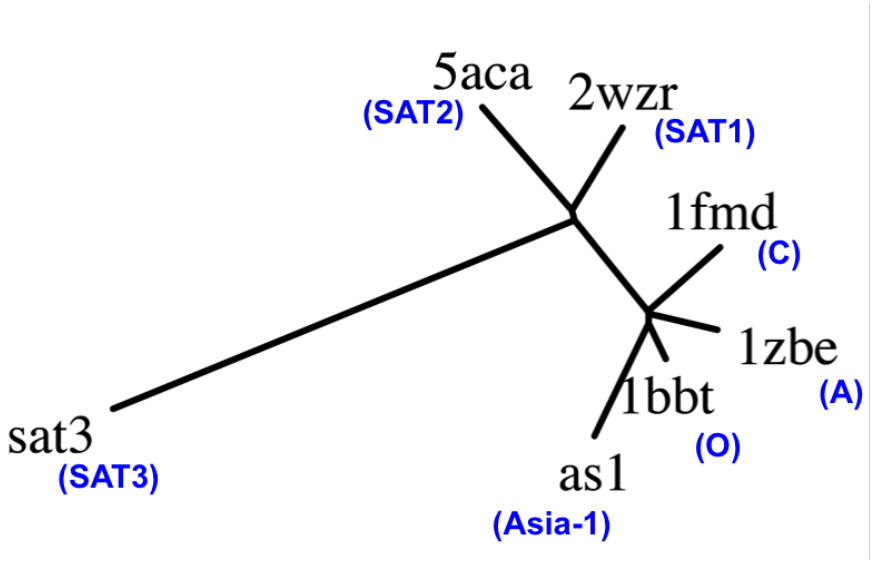


Figure 4.12: A structure-based phylogenetic tree of all the FMDV serotypes, created using Phylip [174] and SHP [167]. The serotypes (blue) and their PDB codes, where available (black), are shown.

4.3 Discussion

The different FMDV serotypes vary in their structure and sequence similarity. Phylip [174] and SHP [167] were used to plot a phylogeny inference tree (Figure 4.12), based on protein structures, for the seven different FMDV serotypes, to show the variation among them and especially highlight the evolutionary difference of SAT3 from other serotypes. The RMSD between SAT3 and the other serotypes was comparatively quite different, compared to the RMSD among the other serotypes. As this was a structure-based phylogenetic analysis, it should be noted that this may also be due to regions of the SAT3 structure not fitting well into the EM density well, due to the low-resolution of the electron density in some loop regions, therefore leading to higher RMSD with other serotypes in those regions. The RMSD scores between the protomers from the different serotypes, and the evolutionary distances derived from that, are included in Appendix D.

Picornavirus	Melting temperature (°C)
FMDV-SAT1	44
FMDV-SAT2	46
FMDV-SAT3	34
FMDV-O	46
FMDV-Asia1	53
FMDV-C	42
FMDV-A22	53
Ljungan virus	60
Poliovirus	45
Equine Rhinitis A Virus	55
Bovine Entero Virus	58
Hepatitis A Virus	80

Figure 4.13: Melting temperatures of different picornaviruses, including the different serotypes of FMDV [32, 163, 175, 176].

4.3.1 Stability

The FMDV SAT serotypes are among the least stable *picornaviruses* (Figure 4.13). The various FMDV serotypes vary in their thermostability as well. Doel et al. [36] had showed early on that among the FMDV serotypes, SATs dissociate the fastest at high temperatures (Figure 1.5), and among the SAT serotypes, SAT3 is the most structurally unstable. Our results confirm these observations. SAT1 dissociates at a temperature of roughly 44 °C, SAT2 at 46 °C and SAT3 being the most unstable, at 34 °C. This poor stability underscores the difficulties in producing stable vaccines for the SAT serotypes, particularly SAT3.

There are specific residues at the inter-protomer interface of the capsids, that interact to determine the stability of the capsid structure. For a close comparison to previous structural studies involving SAT serotypes, the study by Kotecha et al. [103] was referred to. Kotecha and colleagues investigated several residues at the

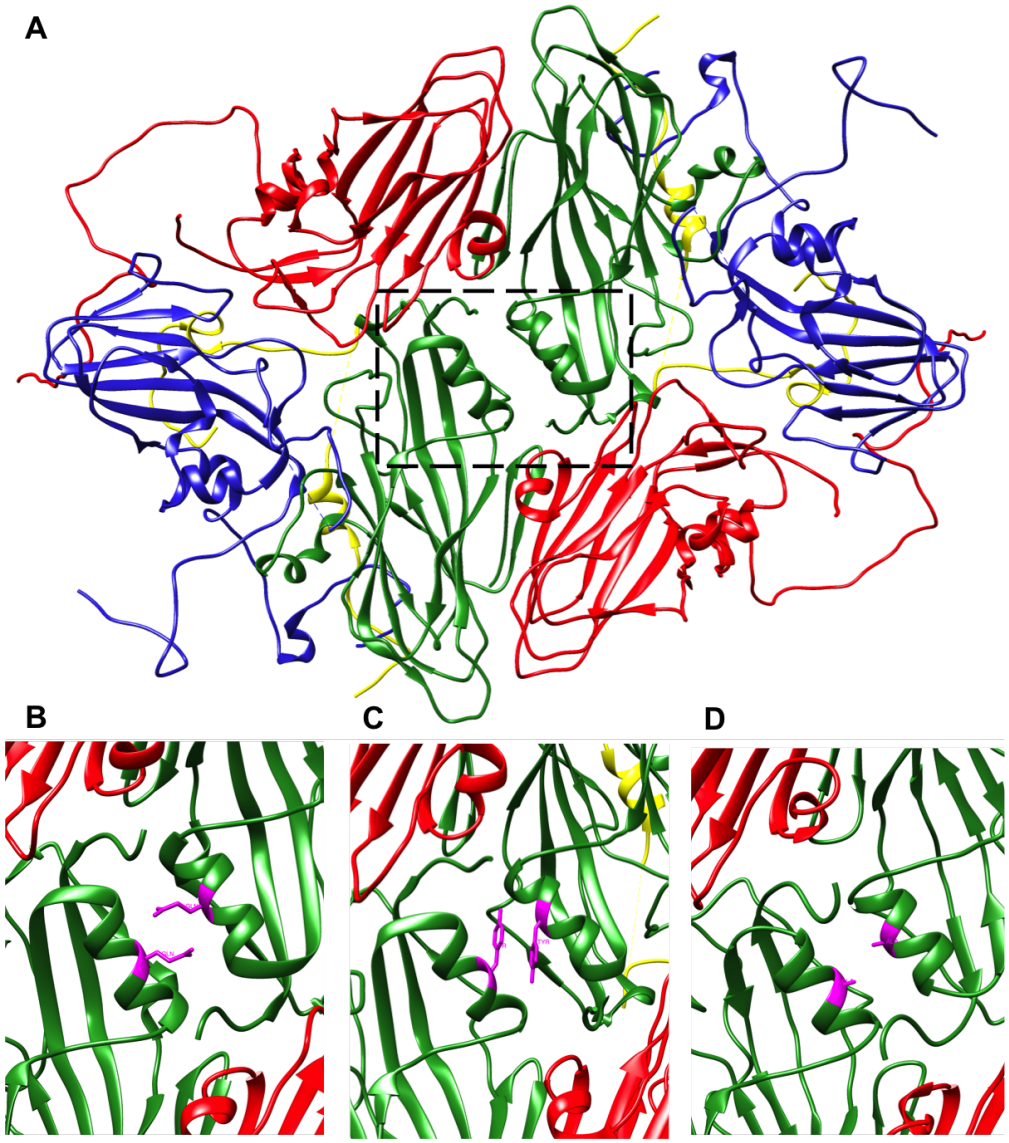


Figure 4.14: (A) Two symmetry related protomers of SAT2 shown; VP1 is shown in blue, VP2 in green, VP3 in red and VP4 in yellow; the black box highlights the location of VP2 residue 93. (B)-(D) Zoomed in views of the highlighted area for SAT1, SAT2 and SAT3 with VP2-93 shown in pink, indicating residues Glutamine, Tyrosine and Alanine respectively, at this position.

protomer-protomer interface of SAT2 through MD simulations, and experimentally tested the most promising candidate mutants, thereby showing that certain mutations did indeed improve structural and thermal stability of the capsids, without compromising the antigenicity of the virus capsid. They showed that residue 93 in VP2 interacted with its symmetry-related counterpart and influenced the capsid stability significantly. The mutant they created, with a stabilised interaction of two tyrosines (instead of two serines) at the VP2-93 position, dissociated at 51 °C instead of 46 °C. Figure 4.14 shows the residues (in pink) present at the VP2-93 symmetry-related positions for the different SAT serotypes. Here, the SAT2 mutant with two stabilising tyrosines at the interface (Figure 4.14 (C)), showed the pi-stacking of the aromatic rings that lead to improved structural stability. Panel (B) shows two glutamines interacting at the SAT1 interface, that stabilised the structure with hydrogen-bond interactions. While these electrostatic interactions lent structural stability to the interface, they were not as strong as the pi-stacking shown for SAT2 (C). SAT3 was the least stable of all the SAT serotypes. This might have been, in part, due to the presence of non-polar amino acids (alanines) at the interface (D), that were unable to participate in hydrogen-bonding or confer significant hydrophobic interactions.

The PISA results alone could also not fully explain why SAT2 was the most stable structure, followed by SAT1 and then SAT3, if the number of hydrogen bonds was the greatest in SAT1. However, as discussed, the stability lent to the SAT2 structure was likely to be a result of the pi-bond stacking of the aromatic rings at the protomer interface (Figure 4.14 (C)). These results might also be explained by the fact that not all hydrogen-bonds are equal in strength. While these results

suggest how more extensive hydrogen-bonding in SAT1 could have helped to make it more stable than SAT3, which had a fewer number of hydrogen bonds at the protomer interface, the far higher stability of SAT2 could not be explained just by the number of hydrogen bonds. It was quite likely that the much stronger pi-bond stacking in SAT2 compensated for fewer number of bonds present in total, thereby making it the most stable structure in this comparison. The correlation between the interfacing area of each serotype and their melting temperature (Figure 4.6, (B)) appeared negatively-correlated, against expectation. This may be because not all the residues at the interface form strong interactions, and therefore the interfacing area is perhaps not a good measure of structural stability. It is therefore perhaps the type of interactions and not necessarily the number of them, that influences structural stability significantly. The resolution of the structures analysed here might also be too low to define the positions of the side chains with certainty, leading to potential errors in the number of hydrogen-bonds calculated by PISA. It should, however, also be noted that PISA results are merely suggestive and not always entirely accurate; they should be considered as insights rather than definitive explanations.

Hydrogen-bonding and inter-protomer interactions at the two-fold axis may influence the stability of the capsid particles. However, another indicator of stability might be the VP4 disorder. SAT3 has a slightly more disordered VP4 of all the FMDV serotypes compared in this thesis. Along with the VP4 N-terminus, which is disordered for all the structures analysed here, SAT3-VP4 also has a region of disorder between residues 39 and 64. This stretch of 25 missing residues is longer than that of SAT1 (24 residues missing), SAT2 (23 missing), A10 (21 missing)

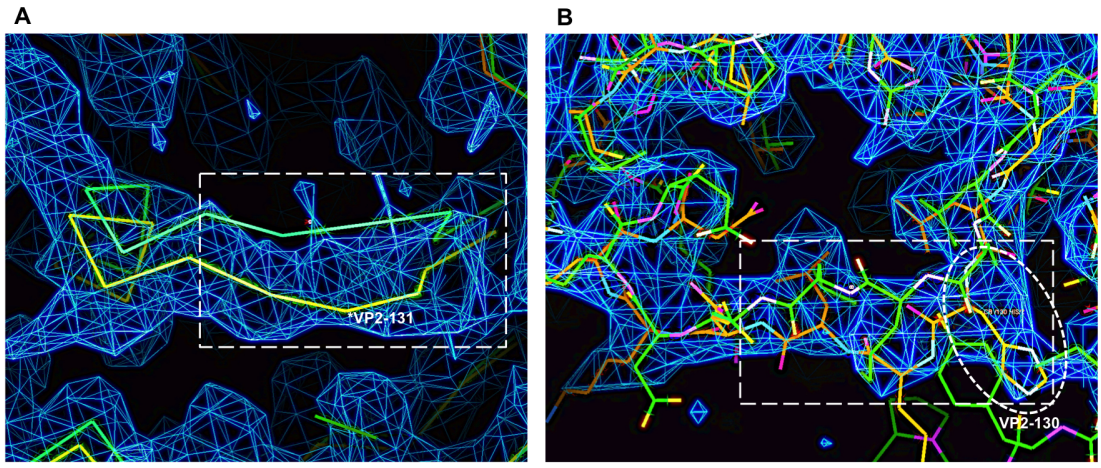


Figure 4.15: Zoomed in views of VP2-131 and neighbouring residues, in (A) backbone and (B) atomic representation. SAT1 (green) and SAT3 (yellow) structures are highlighted in the EM density map of SAT3 (blue mesh, sigma level = 3.4 RMSD) to indicate the region with high RMSD between the two structures. VP2-130 Cysteine is also highlighted in SAT1, and is shown to be absent from the SAT3 structure.

and O (24 missing). As the cleavage of VP0 resulting in the formation of VP2 and VP4 leads to improved stability, required for capsid maturation, the disorder in VP4 might be another contributor to lower capsid stability. The multiple sequence alignment of all the sequences of the serotypes mentioned here is included in Appendix C.

4.3.2 RMSD between SAT serotypes

Most positions with a high RMSD were in the vicinity of disordered (terminal or loop regions) or N-terminal regions and were thus not considered in the analysis of structural difference between the given structures. Some regions with a high pair-wise RMSD were located around antigenic sites (as shown by the asterisks in Figure 4.3) and even if the RMSD values did not exceed 4 Å, this might be an indicator of structural flexibility due to immunogenic pressure from the host cells.

In the RMSD comparison of SAT3 and SAT1, the position that stood out with a high RMSD (around 4 Å) was at the antigenic site around VP2-131 [86]. Figure 4.15 shows two different representations of this region. While the structure fold and the residue (lysine) at VP2-131 were the same in both cases, the RMSD may have resulted from the difference in the sequence among the neighbouring residues. For instance, VP2-130 had a cystine residue in SAT1, whereas SAT3 had a histidine instead. This also indicated that the formation of the di-sulfide bond between VP2-130 and VP1-134 would not be possible in SAT3, but would be in SAT1. This could not be verified in the structure, as the VP1-134 is part of the flexible G-H loop and was missing from the structure, but may be another contributing factor to the lower capsid stability of SAT3. This resulted in a slightly different loop structure in each structure, as shown from the backbone fitting in the EM density map (Figure 4.15 (A)), and thus a high RMSD.

Similarly, the high-RMSD positions for the SAT3 vs. SAT2 comparison were often based around disordered regions or at the loops in VP2 and VP3. Three of these regions coincided with the location of antigenic sites and are shown in Figure 4.16 [86, 90].

Between SAT2 and SAT3, VP2-130 - VP2-131 showed an RMSD around 3.7 Å (Figure 4.16 (A)), and as in the case of the SAT3 vs. SAT1 comparison, may have been due to the sequence difference. Like SAT1, SAT2 also had a cystine residue at VP2-130, whereas SAT3 had histidine, indicating another structural difference that set SAT3 apart from SAT1 and SAT2. This site was also present at a VP2

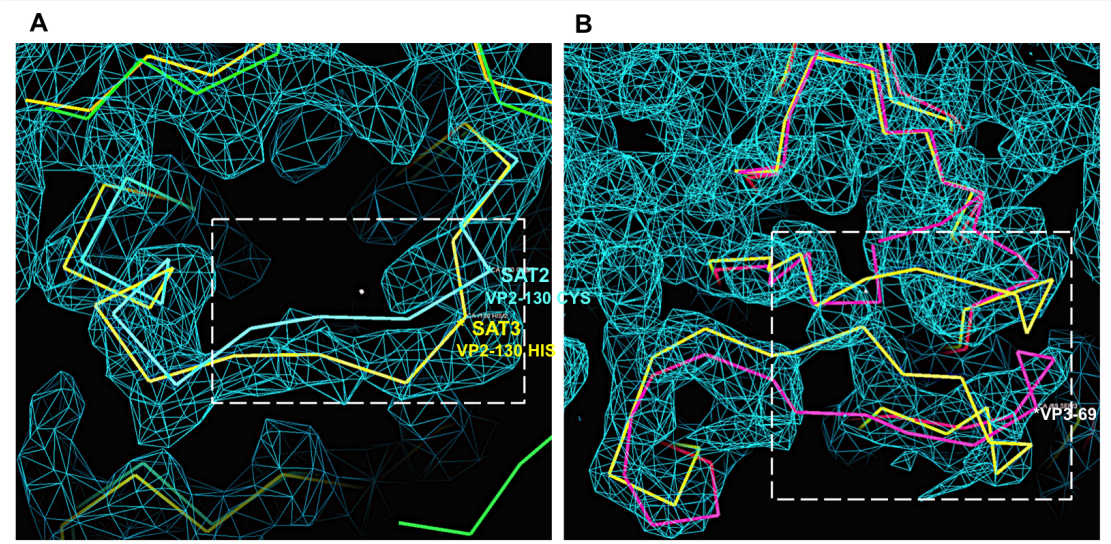


Figure 4.16: Zoomed in views of regions containing (A) VP2-130 and (B) VP3-193 in superposed SAT2 (green in A and yellow in B) and SAT3 (yellow) backbone structures shown in the EM density map of SAT3 (blue mesh). Areas of interest are highlighted by the dashed white box.

loop, but good density was observed. This was expected based on the less than 4 Å RMSD, indicating that the site was not as flexible as the loops in VP3.

The flexibility of the loops in VP3 is shown by the poor density in the regions around VP3-64 - VP3-68 (lower loop) and VP3-192 - VP3-193 (upper loop), as highlighted by the white box in Figure 4.16 (B); both fitted structures corresponded well to their respective EM density. The flexibility of these antigenic loops may be due to selection pressure from the host's immune system, therefore presenting a high RMSD.

4.3.3 Antigenic variation

Taking into account the comparative analyses of the surface structure of the different serotypes, the variability of protein residues on the capsid surface and the

location of antigenic sites from previous studies, a few educated guesses might be made about the antigenic properties of SAT3.

The conservation analysis (Figure 4.11) showed that the outer surface of the capsid is more variable compared to the inner, between the five serotypes compared here. This may have been a result of the selection pressure, as the virus mutated to continue evading the host immune system. Given this continuous evolution of the virus, the antigenic sites and the sequences at the most variable sites differ considerably between the different serotypes. The regions with the antigenic sites and therefore the highest selection pressure are most likely to mutate and therefore vary between the different serotypes. Nonetheless, as shown by the comparison of antigenic sites in serotypes O, A, SAT1 and SAT2 (Figure 4.9), some of the antigenic sites (especially the functional domains within them) may be conserved (for example the conserved RGD sequence in the G-H loop in the antigenic site 1, areas close to the five-fold and at the VP2-VP3 interface near the two-fold axes, etc.).

This comparison may prove useful in designing targeted mutants for these antigenic sites to experimentally validate the findings presented here. We also know from the comparison of SAT3 to SAT1 and SAT2, that the antigenic sites of SAT3 are likely to be more similar to those of SAT1, than of SAT2, owing to their larger shared sequence similarity and surface structure (Figure 4.8).

The various structural differences between SAT3 and the other serotypes discussed here may explain its low structural stability, which in turns leads to the larger RMSD between SAT3 and other FMDV serotypes, and causes it to be an outlier

on the phylogenetic tree (Figure 4.12). A more detailed analysis of the changes between SAT3 and other serotypes, together with the results from subsequent chapters that highlight flexible regions of a dissociated pentamer, may allow the pinpointing of areas that are implicated in capsid uncoating. Stabilising these regions with mutations (as in [103]) may create viable vaccine candidates, effectively circumventing the problem of extremely low thermostability of SAT3, that hinders stable vaccine design.

4.4 Conclusions and future directions

In conclusion, the determination of a high-resolution SAT3 structure has facilitated the comparative analyses of this serotype against other known FMDV structures and their structural properties. We showed that SAT3 is the most thermally unstable of the FMDV serotypes and therefore might present the greatest challenges in vaccine design. Some insights into the antigenic properties of SAT3 were also presented.

It is important to note that the SAT3 sequence fitted into the structure came from SAT/01/06 strain (except VP1), whereas the strain used for structure determination was SAR/02/06. As shown by the results in thesis together with those of Doel et al., the thermal stability of different FMDV strains may vary significantly. Therefore, the minor sequence variation between these two strains may lead to different thermostability and antigenic sites in each case. It would be key to obtain a full sequence of SAR/02/06 for subsequent analyses.

While these analyses may serve as a good starting point in understanding the antigenic properties of SAT3 and why they vary across the serotypes, and therefore eventually lead to the design of a better FMDV vaccine, experimental validation is still required. Furthermore, though some antigenic sites might be shared between the serotypes, there are likely to be completely different sites for each serotype and strain as well, as the viruses evolve to escape detection by the host cells' immune response. This might especially be true for SAT3, a serotype that appears to be quite different from the other FMDV serotypes phylogenetically. Escape-mutant studies may be required to validate the conclusions drawn from the computational approaches used in this study, but we hope that the results presented here offer a good starting insight into the antigenic properties of SAT3.

Chapter 5

A mis-assembled FMDV particle

5.1 Chapter summary

Upon infection, FMDV releases its genome in the host cell in an acidic environment, such as the endosomes, and disassembles into pentamers in the process. This disassembly or uncoating process is poorly understood. While several studies structurally characterising disassembly intermediates of *enteroviruses* are available [59, 60, 64, 66], the *aphthoviruses* are less well-studied. This chapter presents results on the structural characterisation of an FMDV particle that we initially thought might be a disassembly intermediate, and later concluded was a product of the mis-assembly of dissociated pentamers. In this chapter, the possibility of the ERAV structure being a product of re-assembled pentamers is also discussed, and a comparison between the two *aphthovirus* structures is provided.

5.2 Methods

The virus production for the experiments in this section was performed by our collaborators Amin Asfor and Sarah Gold, in Toby Tuthill's group, at the Pirbright Institute. The BEI inactivated samples were then brought to Oxford and treated in accordance with the electron microscopy protocols at the Division of Structural Biology. All subsequent structure determination and data analyses were performed at Oxford. As these samples were obtained from a different lab that worked with a different serotype of FMDV (A10), the results in this chapter focus on A10-61, not the SATs.

5.2.1 Virus growth and harvest

The virus growth and purification protocol was similar to the one described in Chapter 3 for the SAT serotypes. In brief, BHK-21 cells were grown to confluence and infected with FMDV A10-61 in the high-containment laboratories at Pirbright. Upon seeing full cytopathic effect, the cells and the supernatant were harvested. The cells in the mixture were lysed by freeze-thawing at $-20\,^{\circ}\mathrm{C}$ to ensure that all the virus was released into the supernatant. The supernatant was subsequently clarified of the cell debris by low-speed centrifugation at 3500xg and a concentrated virus pellet was obtained by precipitation with ammonium sulphate. This virus pellet was purified through a 30% sucrose cushion and fractionated in a 15 - 45% sucrose gradient to ensure that the virus particles separated from large impurities. The band containing concentrated FMDV particles was treated further to produce intermediate particles.

5.2.2 Low-pH treatment to capture intermediates

Three different treatments were tried, to induce a disassembly intermediate in the FMDV particles. The virus samples had a timed exposure of 125 seconds at room temperature, to low-pH (6.3) 50mM citric acid plus 107mM NaCl buffer, before neutralising with 1M HEPES (4-(2-hydroxyethyl)-1-piperazineethanesulfonic acid), pH 8.0. The exposure was performed either in the presence of 0.2%, 0.5% or no formaldehyde at all. The formaldehyde conditions were used to attempt cross-linking of the virus particles during the uncoating stage, as we predicted that such particles might be quite unstable or transient. The sample without formaldehyde was expected to have only pentamers, produced as a result of rapid dissociation of the virus particles. A sample with untreated purified virus particles was used as a control.

5.2.3 Enzyme Linked Immunosorbent Assay (ELISA)

After the low-pH treatments of each fraction, 50 μL of each was used to coat ELISA (Enzyme Linked ImmunoSorbent Assay) plates (Maxisorp-Nunc) overnight at 4 °C. After washing the plates with Phosphate Buffered Saline (PBS) and blocking with 5% skimmed milk, the plates were washed with PBS containing 0.1% Tween-20 to remove any contaminants, and incubated for an hour with primary antibodies against FMDV A22-Iraq (that cross-react with serotype A10) at 37 °C. After washing the primary antibody away with PBS, a 1:1000 solution of rabbit anti-mouse Horseradish Peroxidase (HRP) conjugated secondary antibody was added to the plates for an hour at 37 °C. At the end, a SigmaFast o-Phenylenediamine dihydrochloride (OPD) (Sigma) solution, a soluble substrate

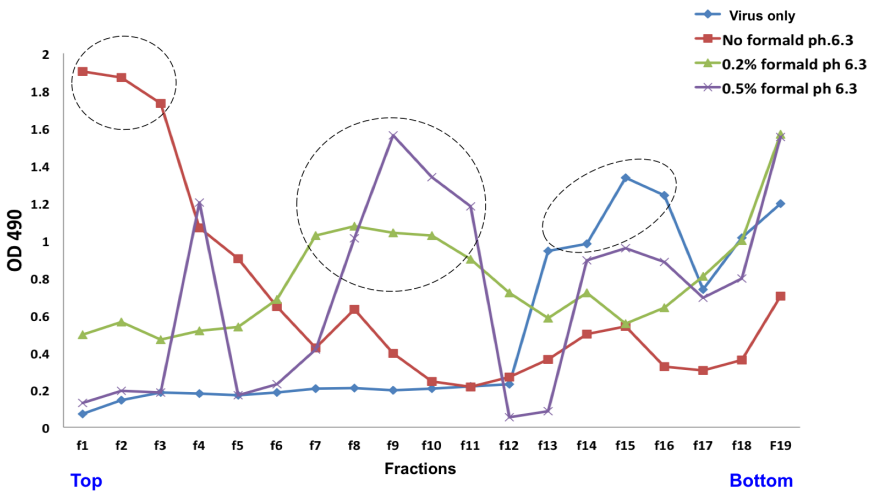


Figure 5.1: Gradient profile (from the top fraction to the bottom of the gradient, as indicated) of the virus samples treated with 0.2% and 0.5% or no Formaldehyde to trap any intermediate particles formed. The control sample with virus only and the three other treatments are shown in the key. Circles highlight the fractions that were pooled (per circle) for subsequent electron microscopy and structure determination. Figure modified from Amin Asfor (personal communications).

to detect peroxidase activity, was added to the well until a colour change was observed (10 minutes), before stopping the reaction using 2.5 M sulphuric acid (Fischer Scientific). The absorbance or OD at 490nm was measured for each sample, using Synergy 2 spectrophotometer (Biotek).

The results are shown in Figure 5.1. It shows the fractions collected going down the gradient. The heavier the particles, the further towards the bottom they travel in the sucrose gradient. The virus-containing sample (blue line) showed a peak in absorbance towards the end of the gradient, indicating the presence of virus particles in fractions 14-17 . The FA treated samples were expected to contain intermediate particles, that would be lighter than full virus particles due to the absence of the genome but heavier than the pentamers, and therefore settle around the middle of

	Batch 1	Batch 2
Virus purification	11.04.2014	25.06.2015
Virus concentration	-	0.35mg/treatment
pH treatment	04.11.2014	02.07.2015
Innocuity testing	14.11.2014	29.07.2015
Samples shipped to Oxford	13.04.2015	06.08.2015
Samples imaged	11.06.2015	29.09.2015

Figure 5.2: A timeline showing the steps and time required for the A10 samples, from preparation to imaging.

the gradient. Thus the peaks detected in 0.2%- (green line) and 0.5%-FA treated samples (purple line), in fractions 7-10 and 8-10 respectively, were consistent with expectations and pooled separately. The low-pH treated sample containing no FA was expected to produce only dissociated pentamers, that do not travel far down the sucrose gradient, and therefore the fractions producing an absorbance peak for these samples (red line) in fractions 1-3 were pooled as a control. The circles in Figure 5.1 indicate the fractions with peak absorbance that were pooled (per treatment condition) and BEI inactivated (as in Chapter 3) to be sent to Oxford for structure determination.

5.2.4 Scale-up and shipment

The virus preparations from Pirbright were sent to Oxford in two batches, separated by several months. In the first batch, the purified virus samples were subjected to a 15 - 30% sucrose gradient after the low-pH treatments, to have a clearer separation of the altered particles from the pentamers and other debris. As these samples were very dilute (shown in the Results section), the next batch was scaled up 10x in terms of virus growth protocols, and also not further purified on a sucrose gradient after the low-pH treatment. These samples appeared much more

concentrated, as shown later. The time line from sample preparation to sample imaging is shown in Figure 5.2. The samples were always kept in dry ice during shipment. They were stored at $-80\,^{\circ}\mathrm{C}$ between reception at Oxford and imaging at the EM.

5.2.5 Desalting and concentration for EM

After receiving the samples at Oxford, they were desalted using 7KDa Molecular Weight Cut-Off (MWCO) 5-mL Zeba spin-desalting columns (ThermoScientific Fischer). The columns were first equilibrated using a 50mM Hepes, 200mM NaCl buffer, by a two-minute centrifugation at 1000xg twice, in an Allegra bench-top centrifuge (Beckman Coulter). The sucrose-containing virus sample was then applied to the columns and centrifuged at 1000xg for two minutes for desalting.

Once desalted, 2 - 3 mL of these samples were concentrated in batches, to a volume of roughly 50 μL. 0.5 mL 100kDa MWCO Amicon concentrators (Merck Millipore Ltd.) were used for this step, at a centrifugation speed of 5000xg for one minute at a time, until the volume was reduced to the desired levels.

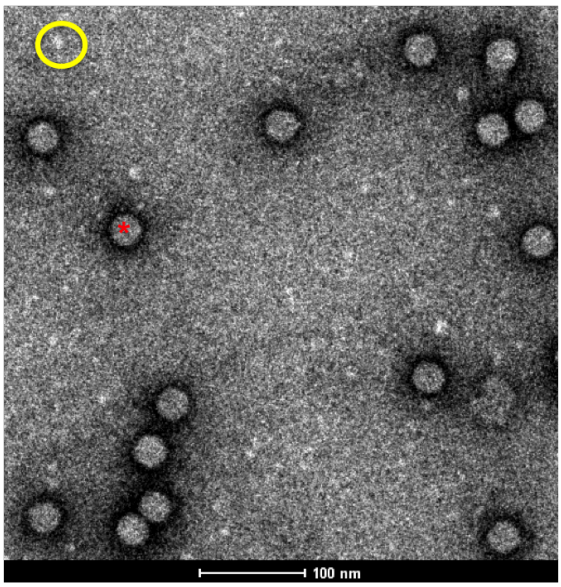


Figure 5.3: Control fraction from the A10 virus preparation. This sample was not subjected to low-pH or formaldehyde treatment. Virus particles (red asterisk) and a few pentamers (yellow circle) can be seen.

5.3 Results

5.3.1 Negative-stain electron microscopy

The samples from Pirbright were received containing high quantities of sucrose, as they were purified on sucrose gradients and sucrose helps in the stabilisation of the virus particles. Initially these samples were tested in negative-stain EM after a desalting step. As those samples proved too dilute and hardly any particles could be observed, the samples were concentrated as explained in the Methods and subsequently checked in negative-stain EM. The results are described in this sub-section.

5.3.1.1 Control fraction with untreated virus

To ensure that the virus preparation protocol had worked and that the samples were not damaged by shipment, storage at −80 °C, and subsequent thawing, the control fraction was tested first for each batch. It was also crucial to check if the desalting and concentration steps introduced any deformities in the virus particles or if there were significant losses of biological material during these steps; therefore the control fraction was checked using negative-stain EM. As seen in Figure 5.3, the virus particles were intact with just a few pentamers indicating virus disassembly. Assured that the sample preparation techniques were consistently functioning as expected, the formaldehyde treated samples were observed for FMDV altered particles next.

5.3.1.2 Low-pH treatment in the presence of Formaldehyde

Concentrated samples were used to prepare negative-stained grids with uranyl acetate, as explained in the protocols described in Chapter 2: Electron microscopy. Figure 5.4 shows the results from the 0.2% and 0.5% formaldehyde-treated samples. As shown by the micrographs, there were quite a few pentamers in the sample (yellow circles), but virus particles were sparse (red squares). These results were consistent for both the batches of samples shipped to Oxford, thereby indicating that this could either be a result of unsuccessful fixation such that all the virus fell apart into pentamers each time, or the altered particles clumping together and sticking to the filters during the desalting and concentration steps. The concentration of the potentially altered particles in these samples was far too low to attempt cryo-EM on them.

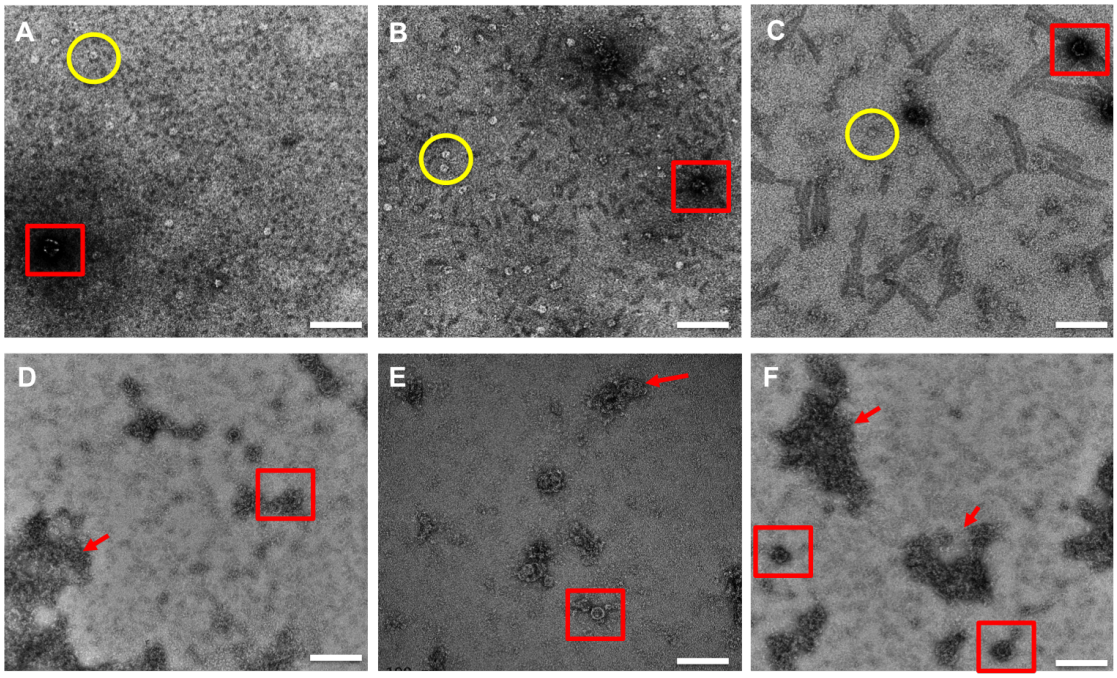


Figure 5.4: Negative-stain electron micrographs showing (A-C) 0.2% or (D-F) 0.5% formaldehyde-treated FMDV samples, followed by desalting and concentration, before grid preparation. Different views show very sparse population of potential altered virus particles (red squares) and top-views of pentamers (yellow circles). Aggregation and debris can also be observed (red arrows). Scale bar = 100nm.

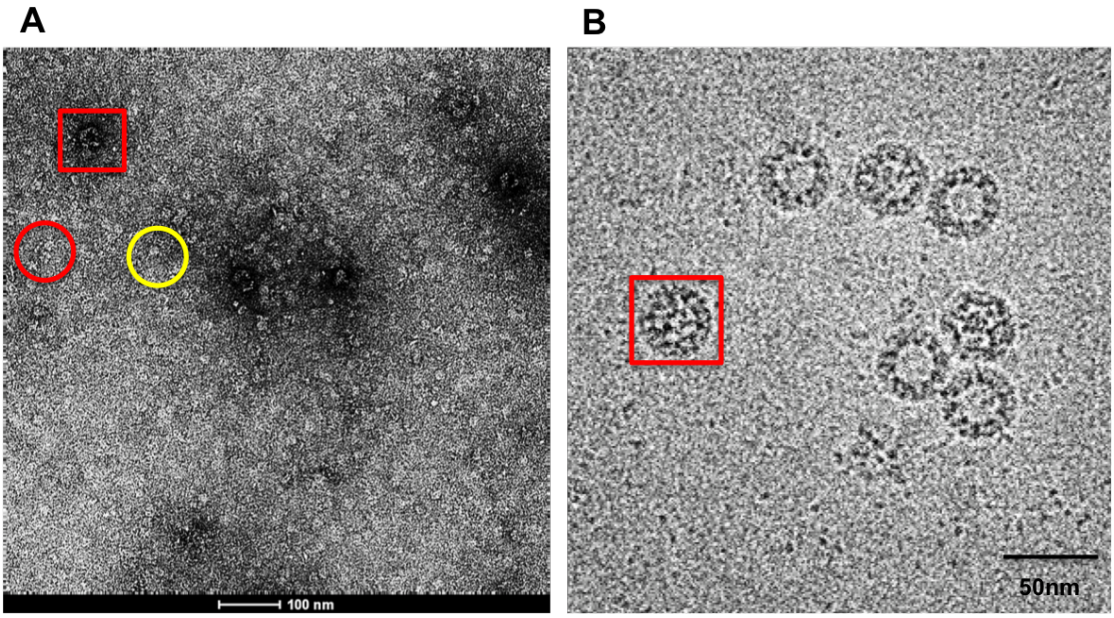


Figure 5.5: (A) Negative-stained and (B) cryo-EM images showing low-pH treated FMDV particles with no formaldehyde treatment, from the first batch. Empty-looking FMDV particles were observed (red square). Pentamers in negative staining appeared predominantly in top-views (yellow circle) but rarely also in side-views (red circles). There were not many pentamers observed in the cryo-EM samples in this batch

5.3.1.3 Low-pH treatment in the absence of Formaldehyde

First batch: We then checked the second control fraction that had no formaldehyde added to it during the low-pH treatment. Figure 5.5 (A) shows the results of negative-stain EM for this sample. Where we were expecting just pentamers, the sample, interestingly, also had some empty-looking, potentially altered particles (red squares) as indicated by the presence of stain inside them. Also present was an abundance of pentamers in top-views (yellow circle), while a few were also seen in side-views (red circle). This sample was plunge-frozen in liquid nitrogen to collect data in cryo-EM; Figure 5.5 (B) shows a typical cryo-EM micrograph from this dataset, collected using a K2 detector (FEI Company) at the Polara microscope. While there were on average 2 - 3 particles per grid hole, there were

not many pentamers seen in this sample and data collection was tedious.

To boost the resolution of the structure solved from this data, a more concentrated sample was arranged from Pirbright.

Second batch: This second batch appeared much more concentrated, as shown in Figure 5.6, and pentamers were visible even in cryo-EM (Figure 5.6 (B)), which would prove useful for the later aspects of the project that are described in the next chapter. Even though the particles did not disperse evenly in the grid holes, the data collection for this sample was slightly easier, as the clusters of larger number of particles could be seen in Search mode at low-magnification a bit more easily.

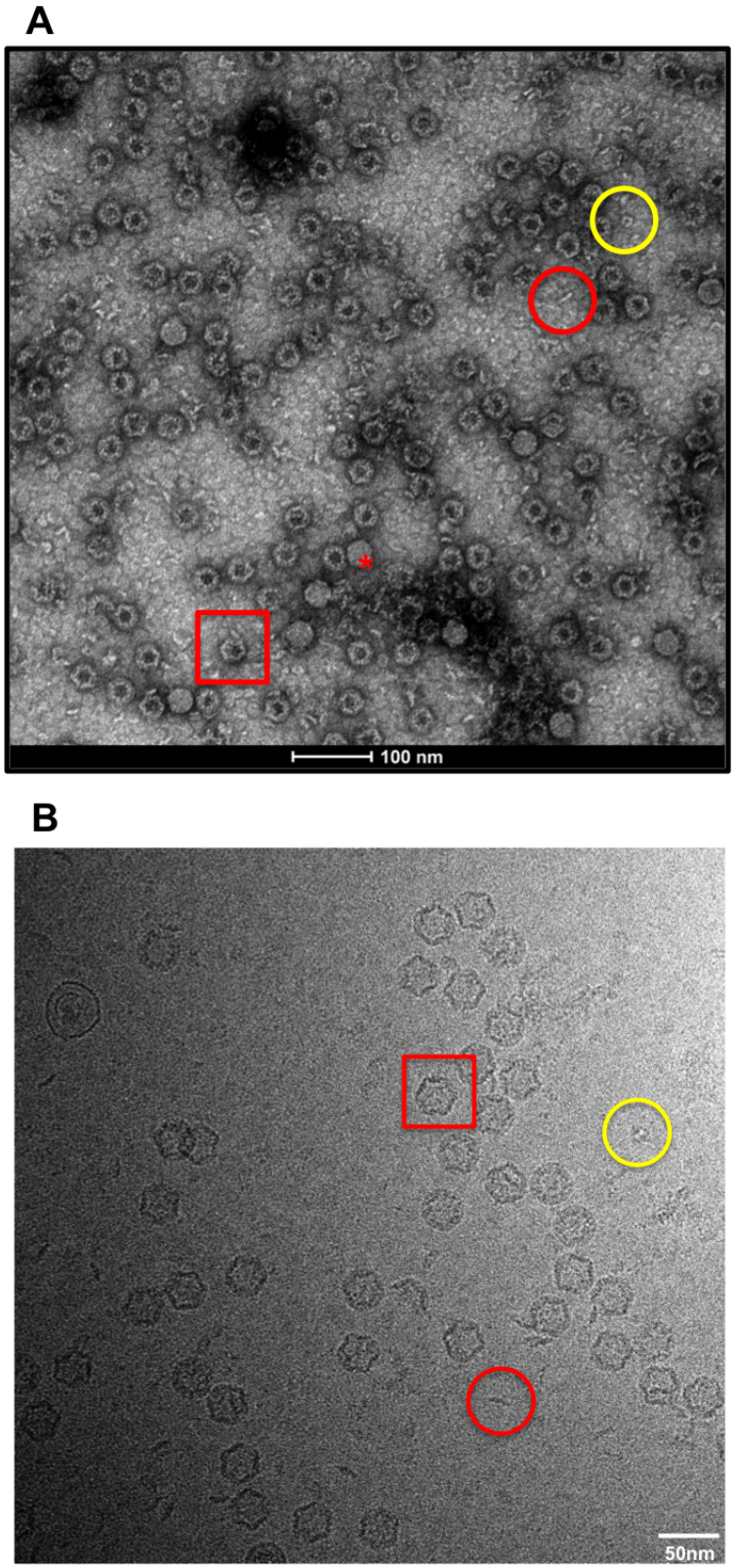


Figure 5.6: (A) Negative-stain and (B) cryo-EM images showing low-pH treated FMDV particles from the second batch. Full (red asterisk) and empty (red square) FMDV particles were observed. Pentamers in negative-staining appeared in predominantly top-views (yellow circle), whereas in cryo-EM most of them were observed in side-views (red circles).

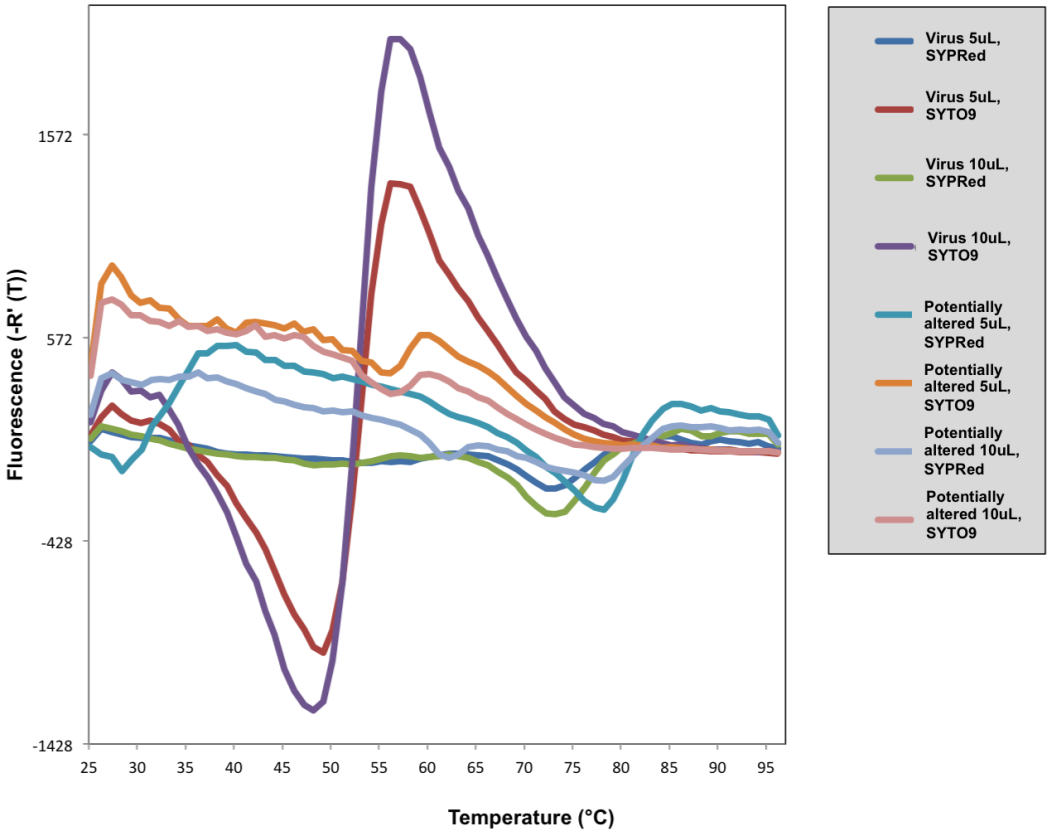


Figure 5.7: PaSTRy assay showing results of the native virus in comparison with the potentially altered particles. An RNA-detection dye, SYTO9, and a protein-melting or denaturation-detection dye, SYPRO red, were used for this assay. Distinct peaks for RNA uncoating using SYTO9 could be seen between 45 °C and 50 °C for the native virus samples (purple and red), whereas no such peaks were observed for the potentially altered particles (orange and pink). All the samples had denaturation peaks in the SYPRO red test, between 70 °C and 80 °C.

5.3.2 Thermofluor assay

As a quick check to confirm that the empty-looking particles were actually devoid of any RNA, they were compared to the native particles in the PaSTRy thermofluor assay [32, 163], as introduced in Chapter 4. Native virus samples were used as a control and two different quantities of the preparation were checked. Either 5 or 10 μL of sample was used for the virus and the potentially altered particles. Two different dyes, SYTO9 and SYPRORed (SYPred) (Molecular Probes,

Invitrogen, final dilution 1:100), were used to check for RNA-binding detection and protein-melting respectively. As before, temperature was increased in 0.5 °C intervals every 10 seconds, in the range of 25 °C to 94 °C. The fluorescence detected at 516 nm for emission (Agilent MX3005 PCR machine) was used to obtain the first negative derivative, and the first minimum was used as the temperature reading for RNA release via uncoating and protein-melting accordingly in each case. The data was visualised in MxPro (Strategene, UK) and is shown in Figure 5.7.

There were clear SYTO9 peaks for the RNA uncoating between 45 °C and 50 °C in case of the native FMDV virus samples (purple and red), whereas no RNA-melting peak was detected for the potentially altered particles samples (orange and pink), confirming that these particles did not contain any RNA and were indeed empty. All the samples denatured between 70 °C and 80 °C, as confirmed using the SYPRed dye.

5.3.3 Cryo-EM data collection and processing

As high-magnification exposure delivers a high dose of electrons to the specimen, the grid holes were always screened in low-magnification, in the Search mode. Only once the object of interest, the potentially altered particles in this case, were found in a specific part of the grid hole, was the high-magnification image acquired. Finding the location of 2 - 3 particles in order to collect a high-magnification image proved extremely difficult and only 572 movies could be acquired over 48 hours of microscope time for the samples from the first batch. Initially, this small dataset

from the first batch was used to determine the structure as a proof-of-principle, making sure the particles seen in the micrographs represented a novel finding. In this case a total of 2372 particles were collected from the initial 572 movies. This resulted in a 3D class with 521 particles producing a 5.9-Å structure that appeared dramatically different from the native FMDV particle. Therefore, more data were collected on the more concentrated samples in the second batch to boost the resolution. The final structure was obtained from 1572 movies collected on the Polara. Some 14,800 particles were collected for this purpose. The further processing was performed as follows.

5.3.3.1 2D classification

Particles were picked manually and 2D classified into 40 classes using Relion [128], to ensure good separation of full or native (Figure 5.8, red asterisk) from potentially altered particles. As particles were manually picked and none of the 2D classes appeared damaged or contaminated by ice all but four classes, with a rotational angular accuracy of worse than 0.7 (marked with yellow asterisks on Figure 5.8), were merged (roughly 12,700 particles) and 3D classified.

5.3.3.2 3D classification

All the picked particles were 3D classified into four classes. A previous structure of FMDV [30] was used as an initial template after a low-pass filter was applied to it to bring it to a resolution of 50 Å, at which no high-resolution features were visible. After one round of 3D classification, the class most resembling an empty particle was chosen as a template, and low-pass filtered, to be used for a second round of 3D classification. The final results of 3D classification are shown in Figure 5.10, where

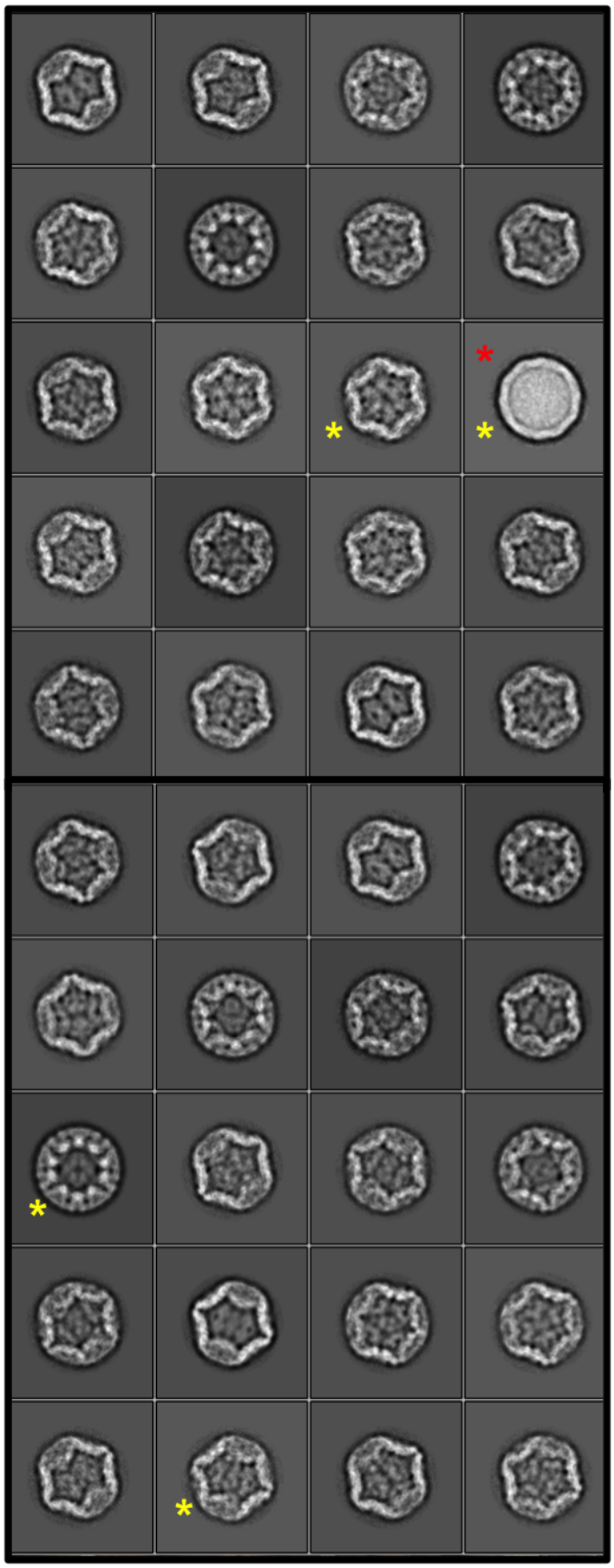


Figure 5.8: Central slices through the 2D classes of the altered particle. Red asterisk indicates what appears to be a class with full particles and yellow asterisks mark the classes that were excluded from subsequent analyses due to poor rotational angular accuracy.

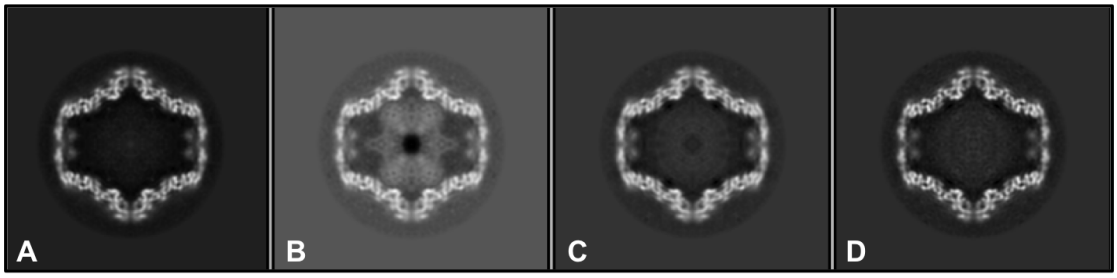


Figure 5.9: 2D projections of the four 3D classes of the potentially altered particle. The number of particles in the classes was (A) 4953, (B) 1053, (C) 4990 and (D) 1731 respectively.

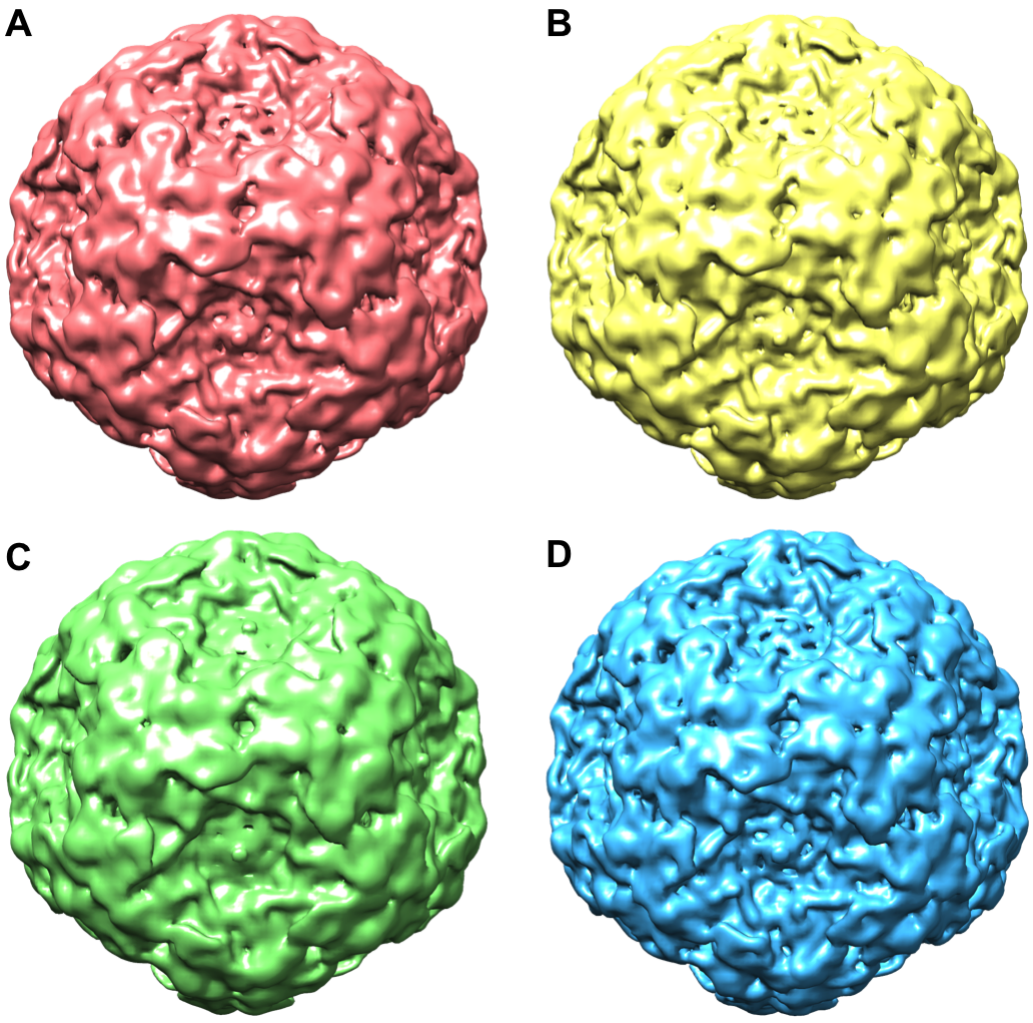


Figure 5.10: 3D rendering of the 3D class averages in Chimera, in the same order as in Figure 5.9.

Class A has 4953, Class B 1053, Class C 4990 and Class D 1731 particles. Based on how the classes appeared in 3D, as seen in Chimera (Figure 5.10), the most similar looking classes with good rotational angular accuracy of sampling (classes A, C and D in this case) were combined for structural refinement in Relion [128].

The final structure (Figure 5.11) had 11,674 particles and was resolved to 5.19 Å. An optional step of re-classifying the particles contributing to the final structure, based on their orientation only, was performed to see if a better separation of the altered particles could be obtained and whether it would result in a better resolution of the EM map. This resulted in a new classification where the majority of the particles (8,077) went into one class. The structure resolved from this class however did not have a higher resolution.

The final structure was thus resolved from 8,077 particles after iterative 3D classification and refinement. The resolution of 5.19 Å was obtained at the FSC of 0.143, the gold-standard in the field. ResMap was then used to highlight the areas with the highest and lowest resolution. As seen in Figure 5.13, most of the structure was between 3 - 4 Å (additional ResMap statistics, Appendix B), and the outer-most parts of the structure went up to 9 Å.

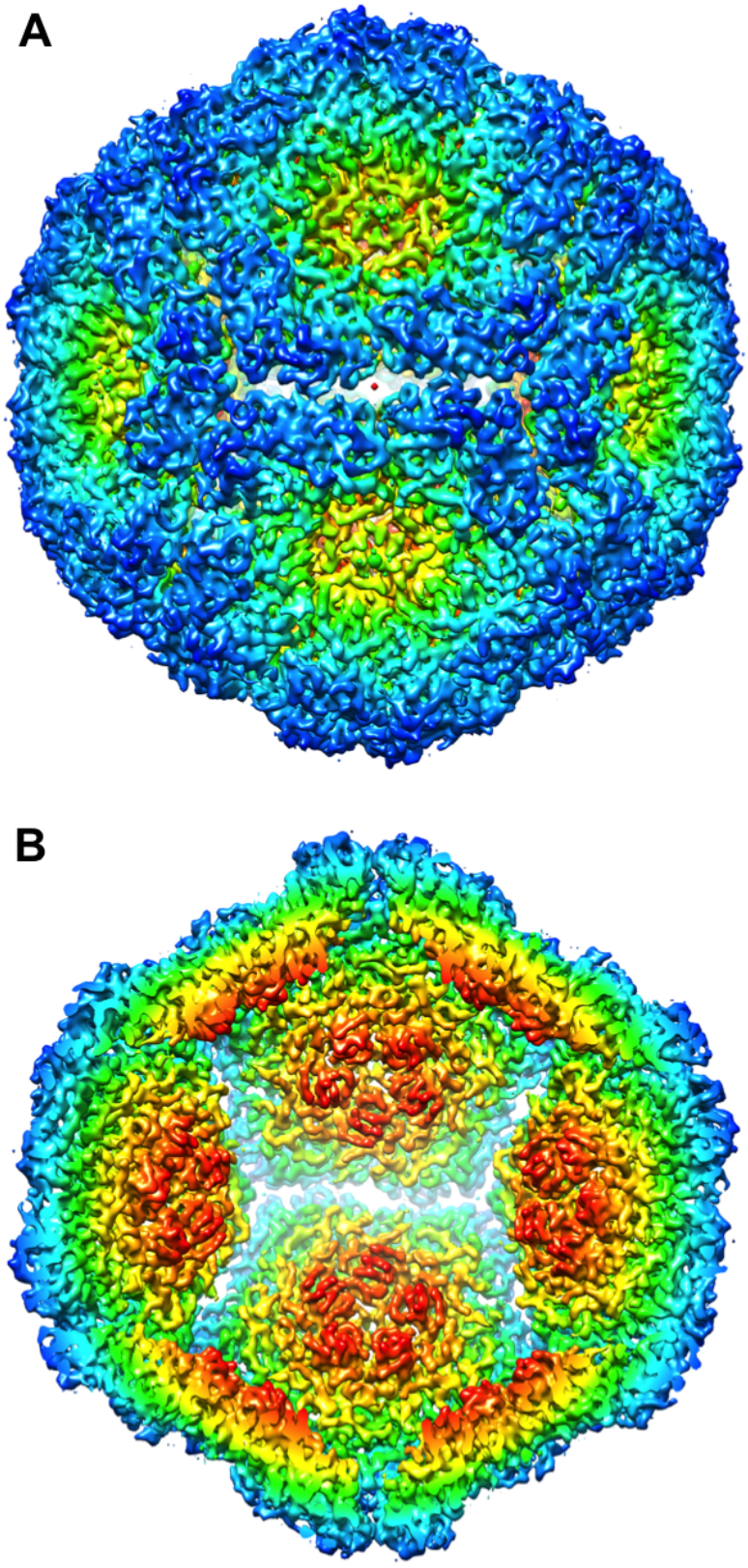


Figure 5.11: The refined 5.19-Å structure of the (A) mis-assembled FMDV capsid and (B) its cross section showing gaps at the pentameric interfaces and a collapsed five-fold axis. Coloured by radial-depth, cueing from red (innermost) to blue (outermost) in Chimera.

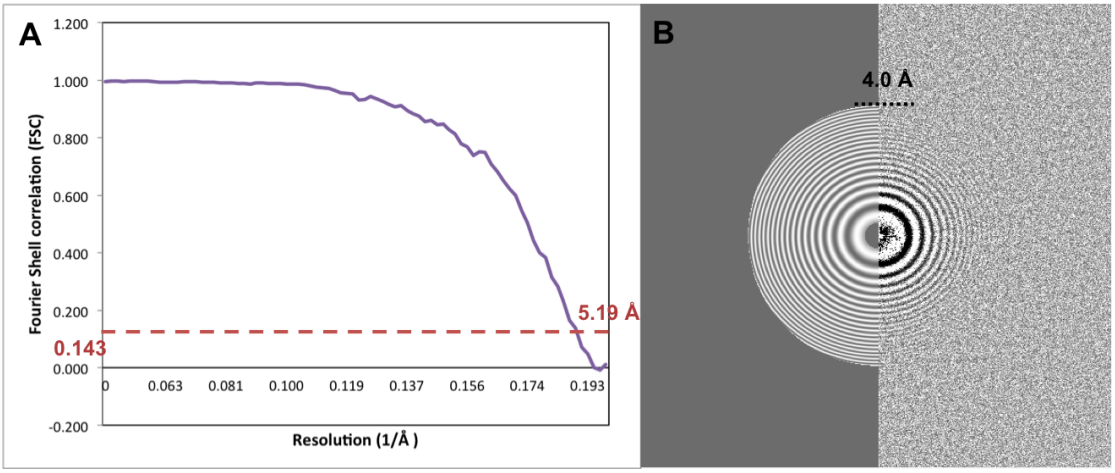


Figure 5.12: (A) Resolution determination to 5.19 Å, using the gold-standard FSC cut-off at 0.143. (B) Thon rings from an example micrograph's CTF showing the extent of useful information up to 4 Å.

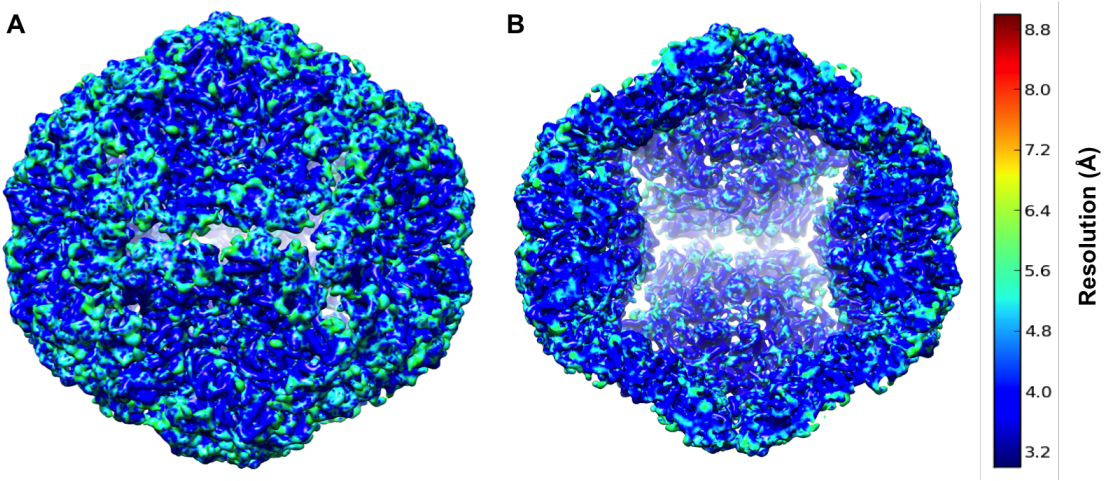


Figure 5.13: Resolution determination of the final FMDV mis-assembled particle structure, on the scale shown, using ResMap.

5.3.3.3 Refinement and model fitting

Once a map was obtained, the crystal structure from the native A10 FMDV particle (PDB 1ZBE [30]) was rigid-body fitted into the density using Coot [146]. The quality of the model fitting into the density is shown in Figures 5.14 and 5.15, in wall-eyed stereo representations and can be viewed in 3D. As the full model of the native virus did not seem to fit well into the density, and it appeared that the proteins had re-arranged in this particle (discussed in later sections), the three capsid proteins were separated and fitted individually. In some regions of the structure, manual fitting of the chains to ensure they were well-fitted into the density was performed. The medium resolution of the map allowed us to do this for the protein backbone with high confidence; the density for the protein side chains could also be identified in some cases as shown in representative areas here. At this stage it became apparent that VP2 and VP3 were switched and that the pentamers were assembled inside-out. In this orientation, the native pentamer fitted into the EM density rather well.

Following this initial fitting, Phenix [147] was used to perform a global minimisation and real-space refinement to ensure that there were no rotamer clashes in the structure. As a result, the model fitted into the map with a high cross-correlation of over 77% in the unit cell, and the cross-correlation around the atoms was higher than 80%. Figure 5.16 shows the final refinement statistics from Phenix real-space refinement, as well as the Ramachandran plot of the final structure.

The regions of the atomic model from 1ZBE, for which no electron density was

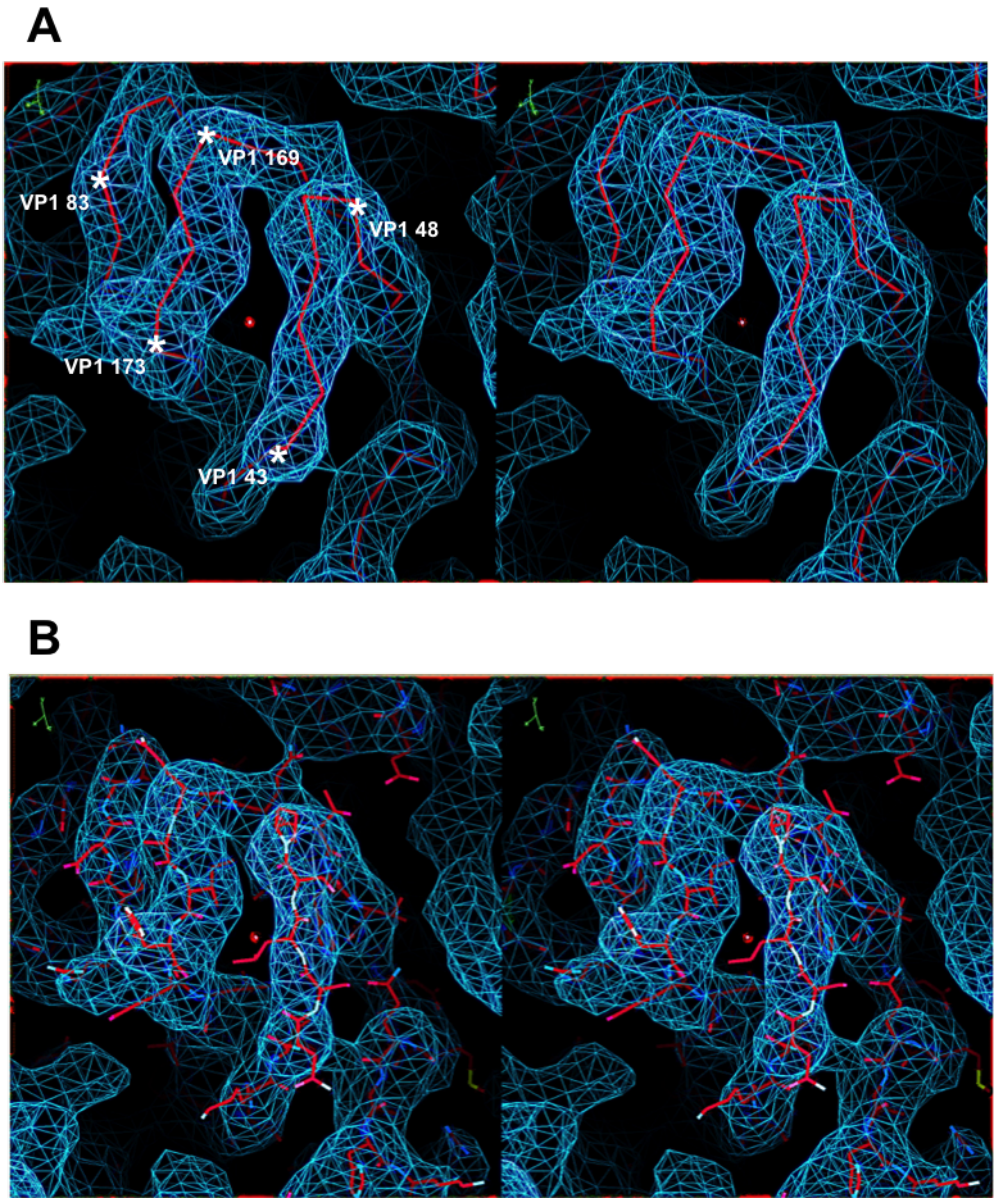


Figure 5.14: Wall-eyed stereo view of the atomic model of native A10 FMDV from a crystal structure (1ZBE [30]) docked into the electron density map obtained from cryo-EM at a resolution of 5.19 Å. (A) Backbone and (B) atomic representations are shown in left and right panels, showing the fitting of the model in the density of the VP1 loops (some residues labelled to provide context). Sigma level = 4.00 RMSD.

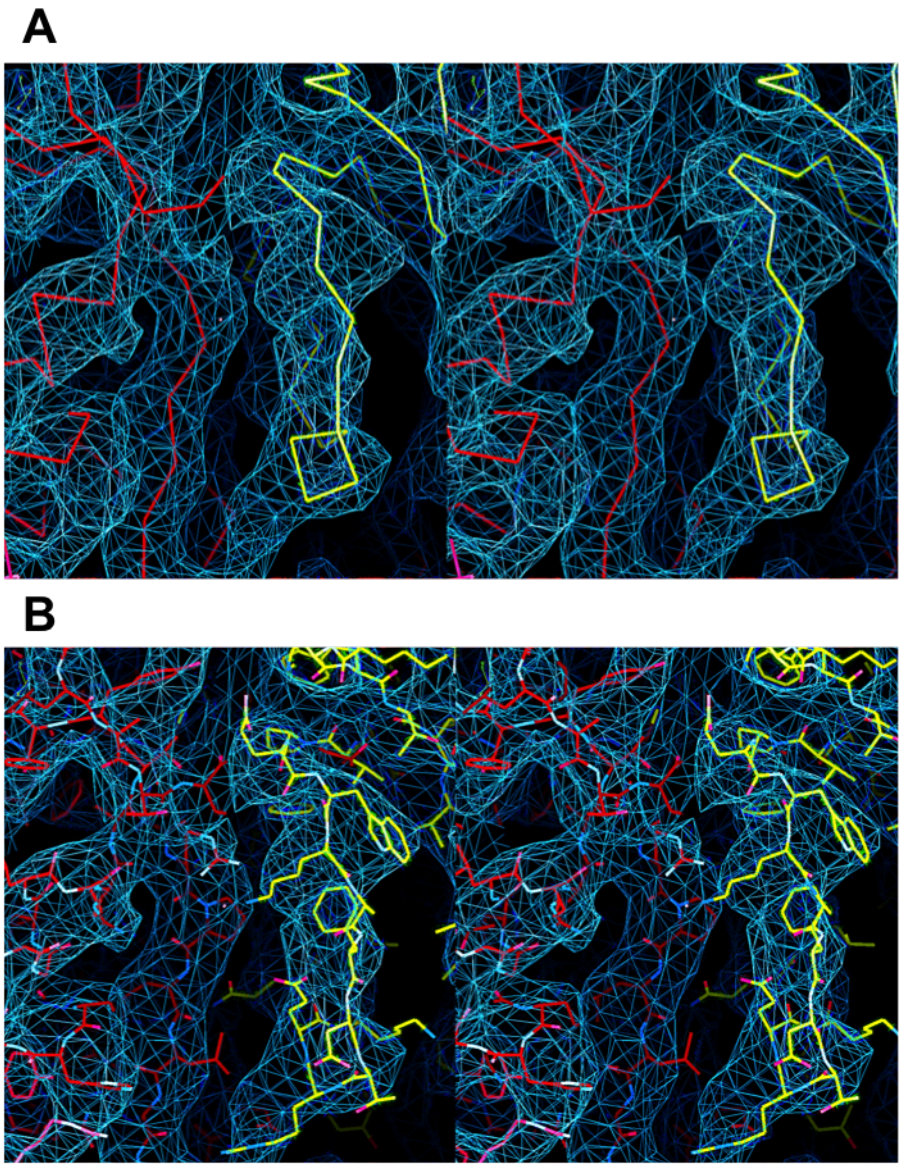


Figure 5.15: Wall-eyed stereo view of the atomic model of native A10 FMDV from a crystal structure (1ZBE [30]) docked into the electron density map obtained from cryo-EM at a resolution of 5.19 Å. (A) Backbone and (B) atomic representations of two different chains (red and yellow) are shown. Sigma level = 4.00 RMSD.

A10 refinement measure	Final figures
Map cross-correlation (whole unit cell)	77.2%
Map cross-correlation (around atoms)	81.1%
All-atom clash score	24.52
Ramachandran outliers	0.00%
Ramachandran allowed	16.37%
Ramachandran preferred	83.63%
Rotamer outliers	0.00%
C-beta deviations	0

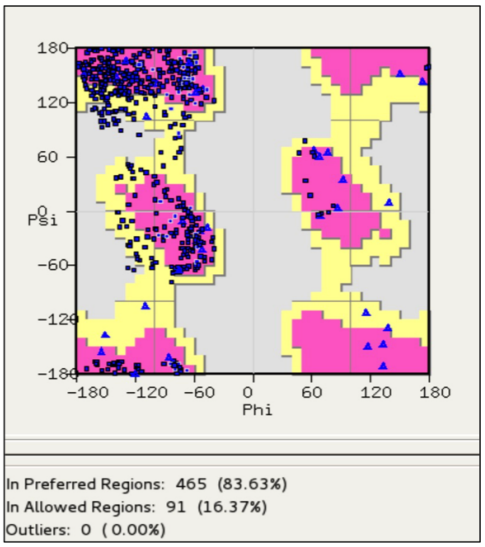


Figure 5.16: Refinement statistics and the Ramachandran plot of the final structure of the FMDV mis-assembled particle.

visible in the altered particle, were removed. The final model comprised residues 27 - 208 of VP1, 29 - 210 of VP2 and 1 - 221 of VP3. VP4 was entirely missing.

5.3.4 Polara vs. Titan Krios

At this stage of the project, the Titan Krios electron microscope (FEI Company) had become available at eBIC (electron Bio-Imaging Centre), at the Diamond Light Source. In an attempt to use automated data collection and make use of the higher stability and the superior electron optics of the Titan Krios to improve the resolution of the structure, three days of data collection time were awarded to us at the Titan Krios. Using automated data collection in EPU (FEI Company), as mentioned in the EM methods chapter earlier, 4451 movies were collected using the K2 direct electron detector (Gatan Inc.). Unfortunately, as the sample was not concentrated or distributed in the grid holes uniformly enough, a lot (1608) of these movies were found empty and thus discarded. As previously, the particles

	Polara, attempt 1	Polara, attempt 2	Titan Krios
Total movies collected	686	1572	4451
Empty movies	14	-	1608
No. of movies	572	1572	2843
Particles in 2D classes	~2300	~14000	~5866
Particles in the final 3D class	521	C1C4 = 6684 C1C3C4 = 11,674 C1C3C4 refined = 8077	C1 = 2079 C1C2 = 4359
Final Resolution	5.9 Å	5.19 Å	C1 = 5.7 Å C1C2 = 5.3 Å

Figure 5.17: Comparison of data collection strategies between the manual collection at the Polara vs. the automated collection at the Titan Krios, both equipped with the a K2 direct electron detector. C1-C4 = classes 1-4.

were 2D and 3D classified. Of the four 3D classes, one or two were picked, with 2079 and 4359 particles respectively, to refine the final structure. These generated structures at 5.7 Å and 5.3 Å respectively.

As the previous structures (both at 5.9 Å and 5.19 Å) were solved using manual data collection, those datasets had fewer unusable movies. On the other hand, those data collections consumed several days and nights of manual work at the microscope. Figure 5.17 summarises the number of movies and particles picked from each dataset and highlights how many of those particles were used to produce a final structure at the shown resolutions in each case. The image processing pipeline was kept consistent. The attempt to obtain a higher resolution structure from the Titan Krios data was unsuccessful due to a much lower number of particles in the collected movie frames. It is interesting to note however, that roughly

the same resolution of the final structure could be achieved using half the number of particles from the Krios dataset. A more homogeneously distributed sample on the grids would therefore dramatically benefit from automated data collection at the Titan Krios.

5.3.5 A novel FMDV mis-assembly structure

The final structure of the potentially altered particle was drastically different from the native (1ZBE) crystal structure (Figure 5.18). The particles appeared slightly expanded compared to the native capsids (312.12 Å in diameter, compared to 296.69 Å). The potentially altered particles contained no RNA, and the pentamers were inverted such that their natural curvature gave rise to the appearance of depressions at the five-fold axis (Figure 5.19). The pentamer structure of the mis-assembled pentamer (B) and curvature was broadly the same as in the native capsid structure (A), but the orientation had reversed (Figure 5.20). VP4 was also missing and the N-termini of VP1 and VP2 were disordered (the first 26 and 28 residues respectively), consistent with previous picornavirus studies of empty particles [59–62,64,66]. VP3 showed large-scale disorder and there were large gaps at the two-fold axes; the distance between the backbone Cαs of the two symmetry-related proteins at the interface being 20 Å at the widest and 9 Å at the narrowest point, as measured in Coot. Consequently, the structure on the whole appeared loosely-held together.

Upon superimposing the individual protein chains from the mis-assembled particle on to those from the native (1ZBE) (Figure 5.21), the largest differences in the

structures were seen at the inter-pentameric loop regions. The core structures of the proteins superimposed well and had not changed dramatically between the native and the mis-assembled particle, but the β-sheets of VP2 near the C-terminus showed a large translation. The N-terminus hairpin structure was also missing, in the mis-assembled particle.

Similarly, β-sheets and loops in VP3 showed some translation, but more notably when the full protomers were superposed only using VP1, to allow maximum difference between the inter-pentameric regions to be visualised, the three loops (BC, HI, and DE) showed a 4.6° rotation with respect to the native (discussed in later sections). The VP1 structure did not appear drastically different between the two particles.

5.3.6 Inter-pentameric interfaces of the mis-assembled particle

Once a well-resolved structure was available, the aim was to study the structural interactions holding the particles together. It was clear that the pentamers were loosely-held together so efforts were made to understand the key interactions responsible for this. PISA [165] was used as an initial analysis tool. VP2 and VP3 from each of the two opposing protomers at the inter-pentameric interface were used, for the native and the altered particle, as shown in Figure 5.22. Even on visual inspection, the interactions at the interface of the altered particle appeared dramatically reduced compared to the native virus. This was confirmed by PISA, which showed 8 hydrogen bonds and no salt bridges at the interface for the altered

particle, whereas there were 38 hydrogen bonds and 6 salt bridges for the native (Figure 5.22 (C)). The predicted interactions in the output, that hold the pentamers together, were between VP2 Lys64 - VP3 Asp70, VP2 Phe65 - VP3 Arg67, VP2 Tyr200 - VP3 Asp69 and VP2 Lys198 - VP3 Glu196 and each interaction was present twice across the interface (Appendix A). The interacting surface area of the interface was also reduced from 2772.9 Å^2 in the native to 927.0 Å^2 in the altered particle.

As the structure was not at a high enough resolution to fit all the side chains unambiguously, PISA results may not be entirely reliable. Therefore, the inter-pentameric interface was also inspected manually in Coot, observing the fitted protein structure backbones in the electron density. Figure 5.23 shows the regions that were observed to be in close proximity to each other in order to form hydrogen bonds. The BC loop (residues 68-73) and the adjacent EF loop (residues 135-136) of VP3 interact with the βB strand of VP2 (residues 62-68) and the CD loop (residues 85-88), of VP2 in the opposing pentamer, to stabilise the assembly (Figure 5.23 (B)). It is hard to accurately predict the interactions between the side chains, but the fitting suggests that there might be stacking hydrophobic interactions between VP3 Arg72 and VP2 His88. VP2 Lys63 also appears likely to form hydrogen bonding with the main chain of VP3 Asp70 or VP3 Thr71.

The three-fold axis also shows the symmetry-related copies of VP2 from three pentamers in close proximity to each other (Figure 5.23 (C)). While the Cαs of VP2 are more than 8 Å apart, there might be some weak Van der Waals interactions between the side chains.

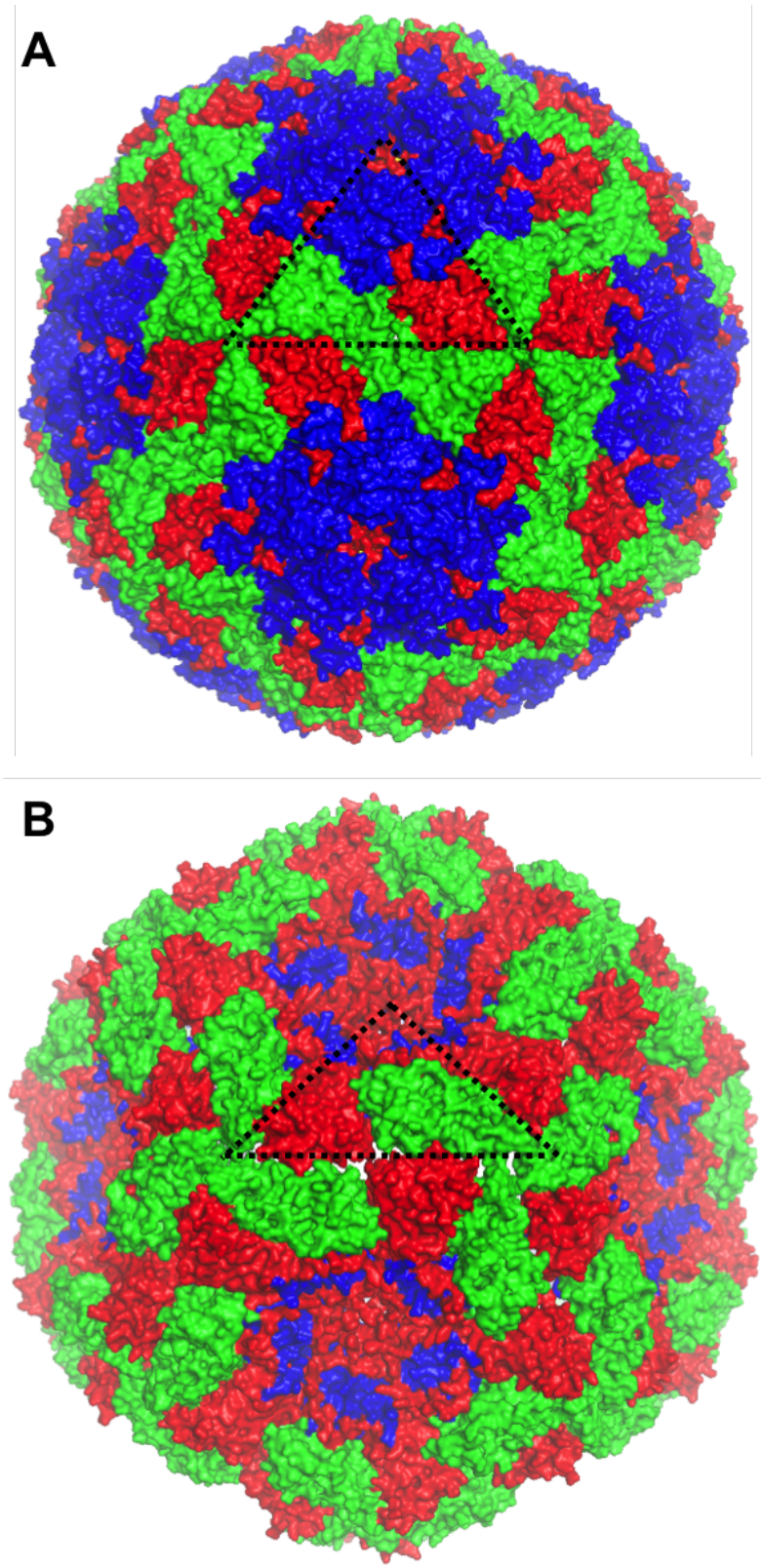


Figure 5.18: A comparison of the structure of the (A) native (1ZBE) and the (B) mis-assembled FMDV particles. An icosahedral protomer with VP1 (blue), VP2 (green) and VP3 (red) is highlighted with a black triangle in each case. Note the gap at the two-fold axis and the reverse arrangement of VP2 and VP3 in the mis-assembled particle, indicating the orientation of pentamers as inside-out.

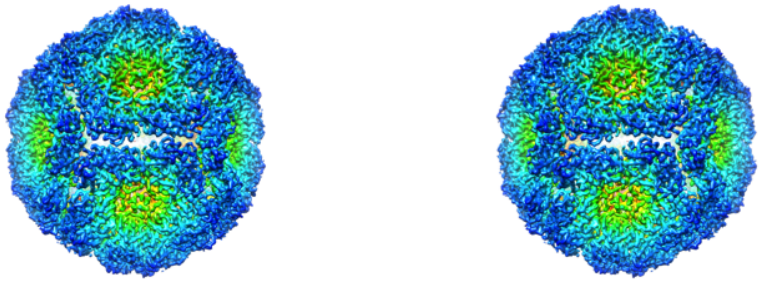


Figure 5.19: A wall-eyed stereo view of the altered particle to highlight the curvature of the pentamers.

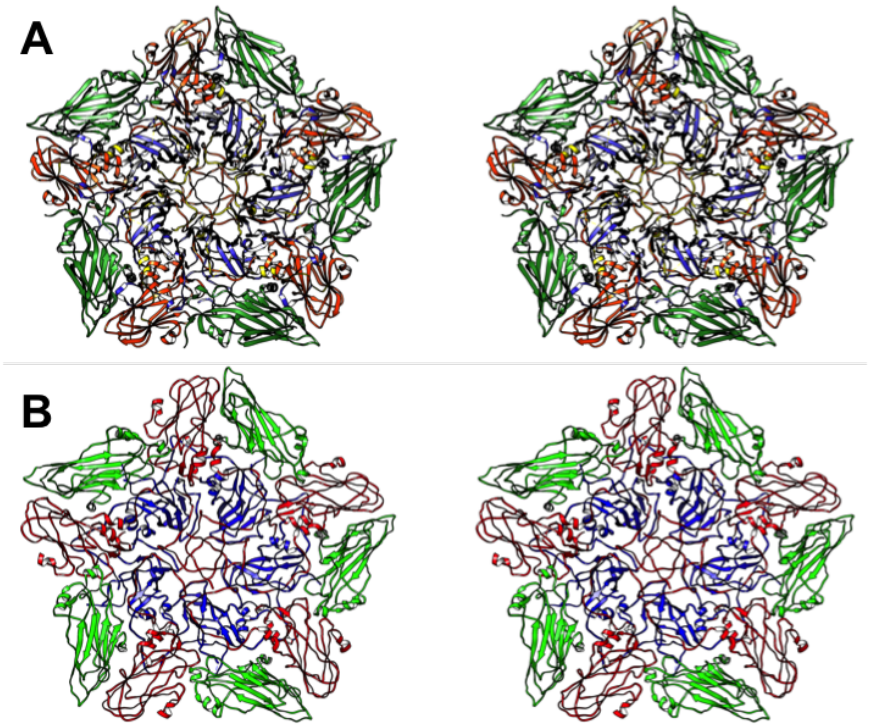


Figure 5.20: A comparison of the structure of the (A) native (1ZBE) and the (B) mis-assembled FMDV pentamers in the same orientation, shown in stereo wall-eye representation. VP1 is shown in blue, VP2 in green, VP3 in red, and VP4 in yellow where it is present.

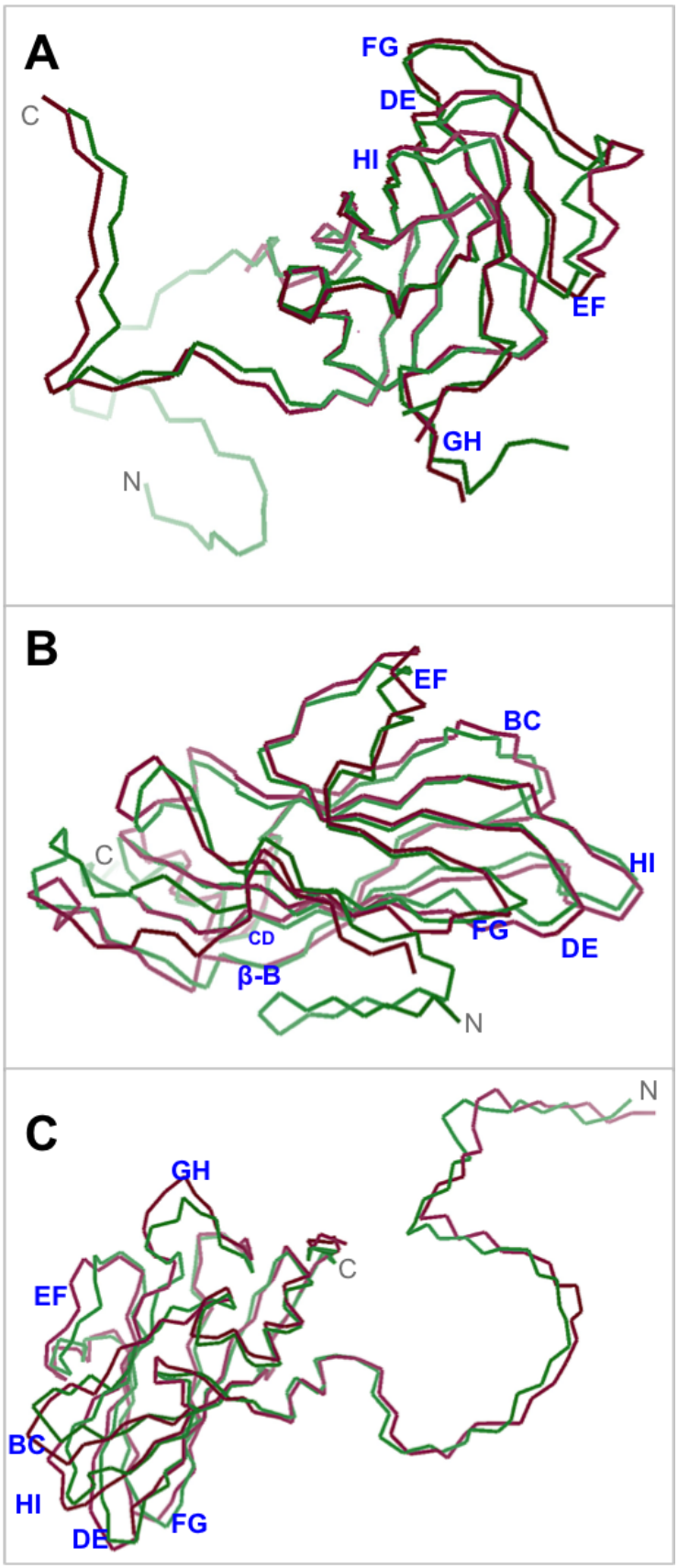
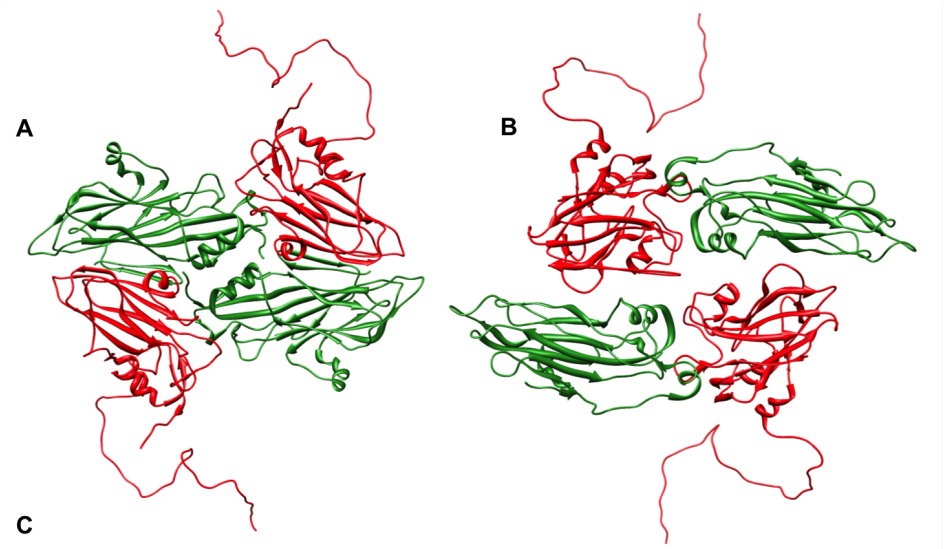


Figure 5.21: Individual protein chains (A) VP1, (B) VP2 and (C) VP3 of the native (green) and the mis-assembled (red) particle superposed for comparison.



VP2-VP3 interface	Interface area (Å^2)	No. of Hydrogen bonds	No. of salt bridges
Native (1ZBE)	2772.9	38	6
Altered particle	927.0	8	0

Figure 5.22: The inter-pentameric interfaces of the (A) native and the (B) altered particles, as viewed from outside the particle, and the (C) PISA interaction statistics for the two interfaces.

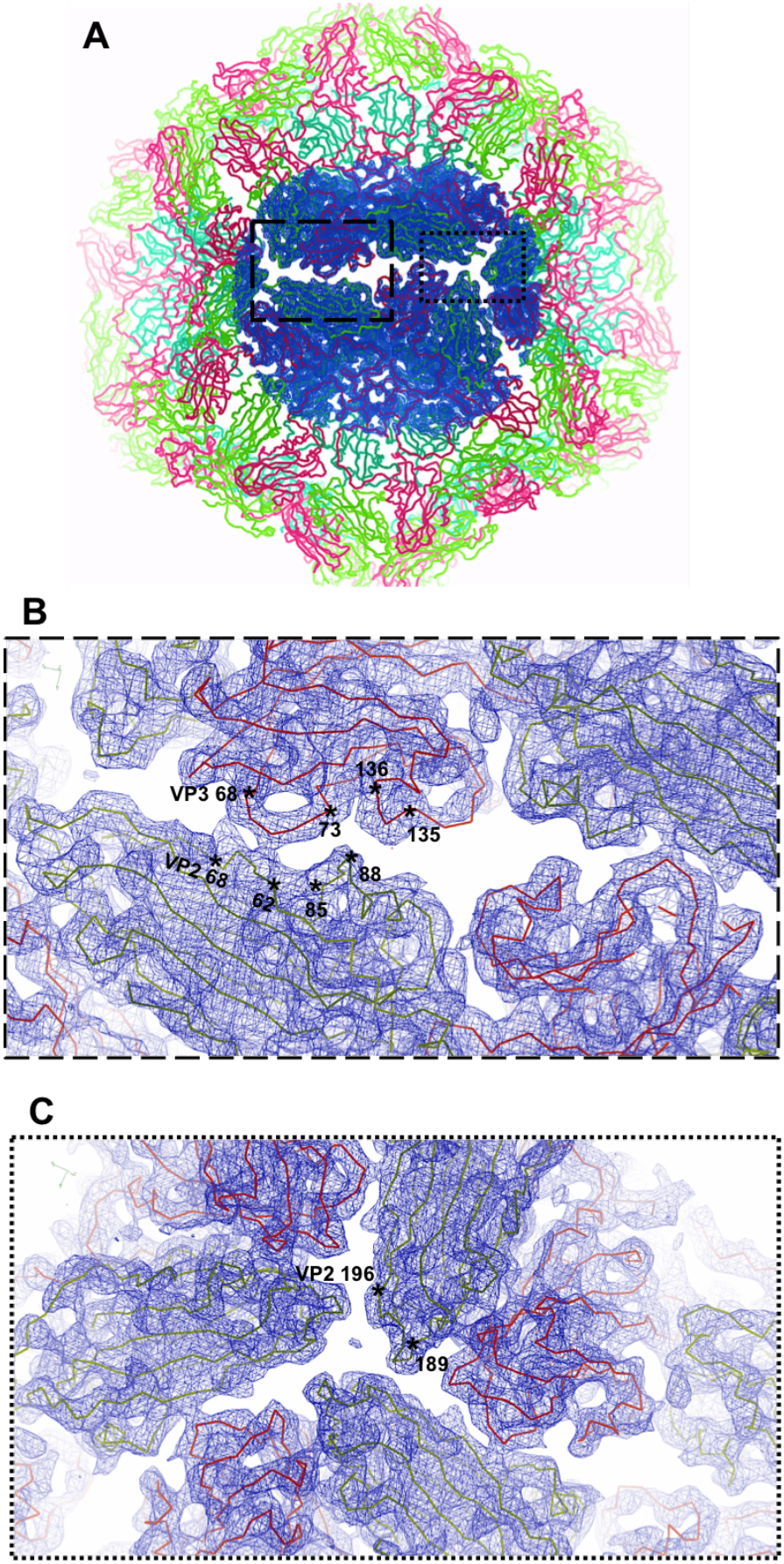


Figure 5.23: Highlighting the stabilising interactions at the inter-pentameric interfaces of the (A) mis-assembled particle at (B) the two-fold and (C) the three-fold axes. VP1 is shown in teal, VP2 in green and VP3 in red.

5.4 Discussion

5.4.1 Native vs. mis-assembled FMDV particles

The mis-assembled particle clearly had inverted pentamers, as shown by the reversed positions of VP2 and VP3 at the interfaces (Figure 5.18). The depressed five-fold axis observed in the electron density (Figure 5.11) was therefore a result of the reversed curvature of the pentamers and not due to any significant conformational changes of VP1. VP1 was however missing density for the N-terminus. There was also no observed electron density for VP4 or the N-terminus of VP2 in the mis-assembled pentamers. Such observations have been reported for the disassembly intermediates from different *picornaviruses* [59–62, 64, 66]. The absence of the N-terminus of VP2 in particular, on top of missing VP4 and VP1 N-terminus, was an indication that the structure might have re-assembled from dissociated pentamers.

5.4.1.1 Structural changes in VP2

Furthermore, when compared to the native crystal structure (1ZBE), large shifts were observed in VP2 and VP3 (Figure 5.21 (B)), the proteins that form inter-pentameric interfaces in the capsids. The VP2 β-sheets showed significant structural conformation changes (Figure 5.24); residues 29 - 52 were shifted in the range of 3 - 7 Å (A), resulting in a relaxation of all the β-sheets (B). It is plausible that the absence of VP4 and the N-terminus of VP1 (yellow and dark blue chains in the Figure 5.24) facilitated this translation. This translation of the β-sheets would not be possible due to steric hindrance from VP4 in the native structure.

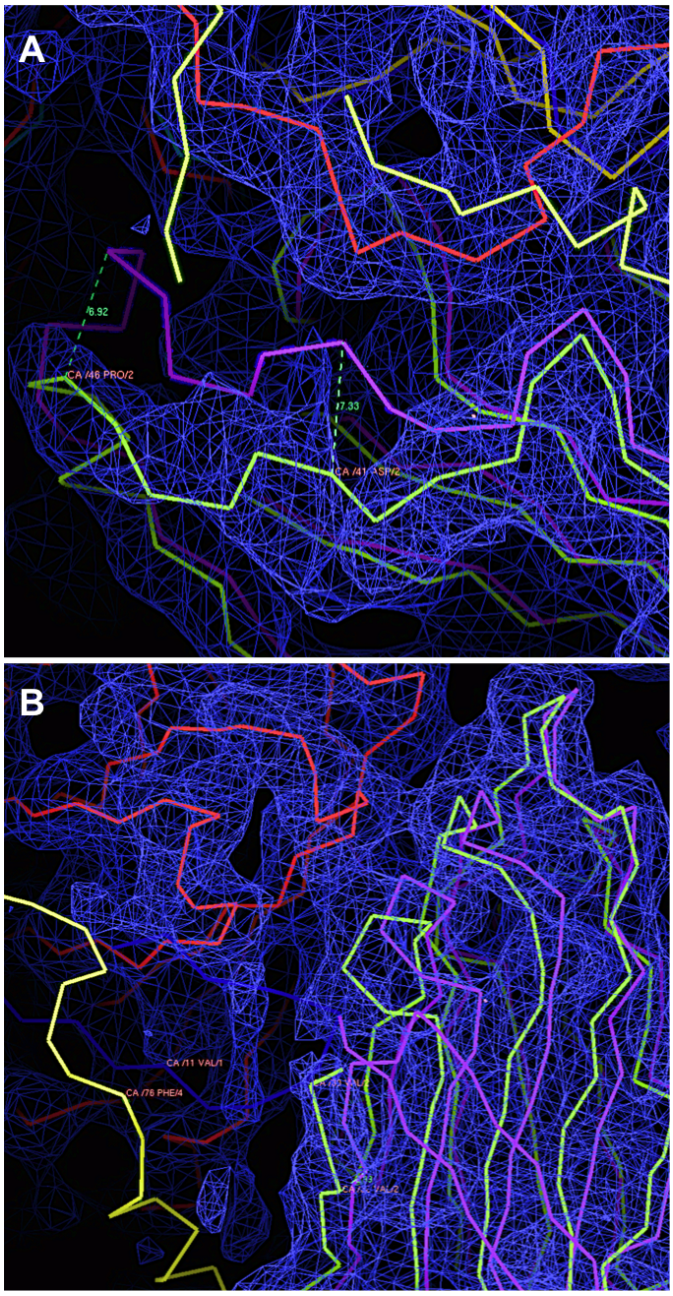


Figure 5.24: Two different views of the VP2 electron density (blue mesh) at the interface, with the atomic structure of the mis-assembled particle and the native particle overlaid. (A) VP2 from the mis-assembled particles (green) is shown shifted down by 3 - 7 Å, in comparison to where it is in the native particle (purple). VP4 (yellow) from the native structure and VP3 (red) from the mis-assembled particle can also be seen. (B) All the β-sheets in case of the mis-assembled particle's VP2 (green) can be seen shifted in comparison to the native's (purple). The electron density for VP4 (yellow) and the VP1 N-terminus (dark blue in the background) from the native structure are missing in the mis-assembled particle.

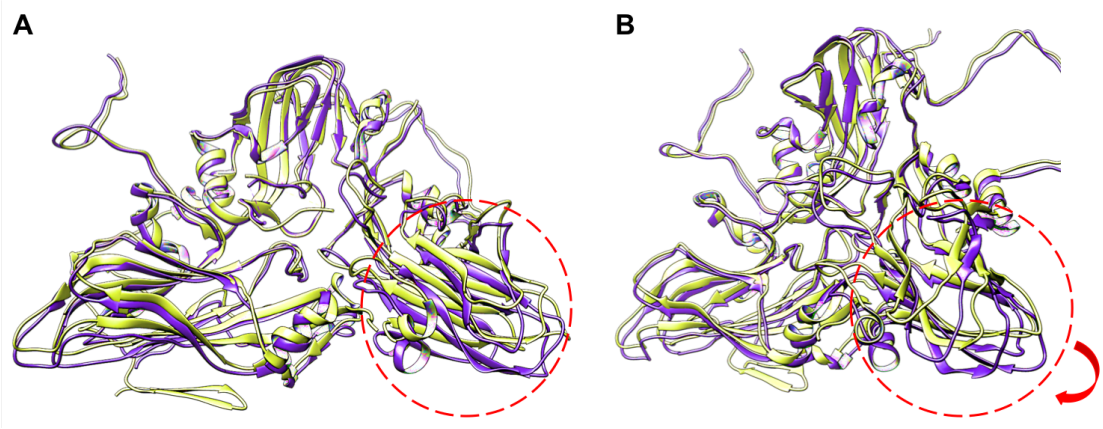


Figure 5.25: Depth-cued structures, after VP1 superposition, of native (yellow) and mis-assembled particle protomers (purple), to highlight the large conformational changes in VP3 (red circles). (A) The large shift in VP3 β-sheets in the mis-assembled particle is highlighted. (B) The 20° y-axis rotated protomers emphasise the 4.6° rotational shift in VP3 (red arrow).

5.4.1.2 Structural changes in VP3

Interestingly, the largest changes in the mis-assembled particle appeared in VP3 (Figure 5.25). Upon superposing the native capsid structure (1ZBE) and the fitted model from the mis-assembled particles in SHP [167], the average RMSD between the two structures was roughly 2 Å. VP3 was rotated by 4.6° and the β-sheets close to the interface had shifted down compared to the native structure by 4 - 9 Å, thereby changing the inter-pentameric interactions significantly. This perhaps explains why the pentamers were unable to re-assemble correctly.

To check this, after the protomer from the mis-assembled particle was superposed on to the one from the native virus, a full-virus capsid was generated in Chimera using the mis-assembled protomer but the symmetry operators of the native protomer. This showed how the pentamers would have appeared, had they tried to assemble in a native-like capsid.

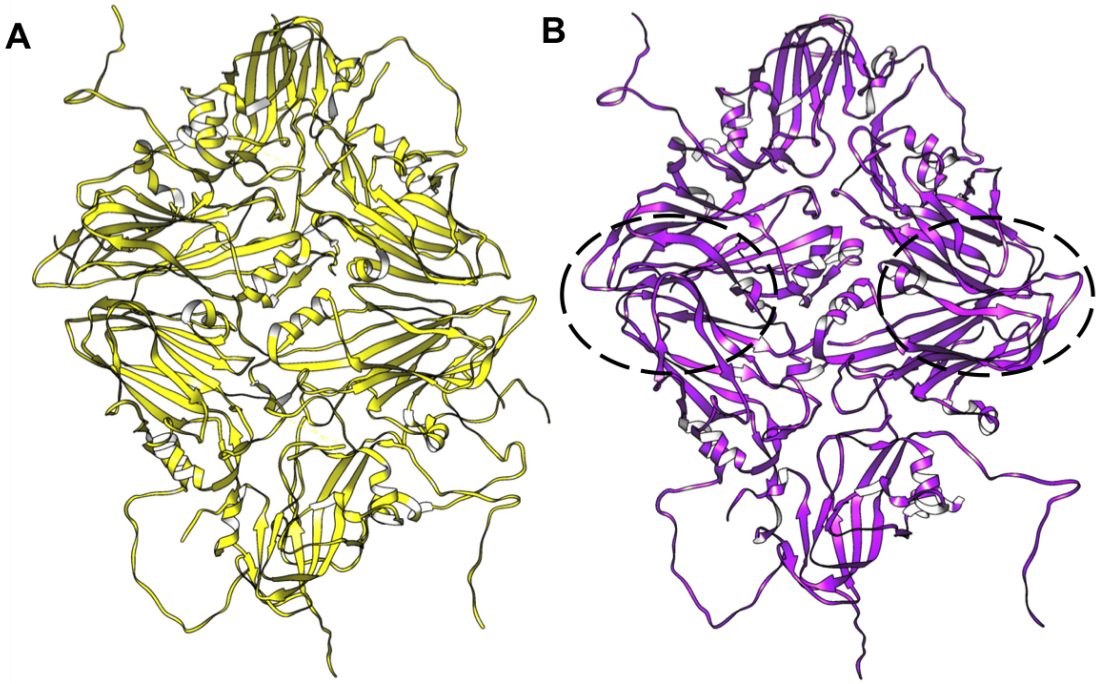


Figure 5.26: Two opposing pentamers showing the arrangement of VP2 and VP3 at the interfaces in the (A) native protomers from 1ZBE (yellow) and the (B) mis-assembled protomers (purple). The structural clashes between the purple protomers at the VP2-VP3 two-fold axis, had they assembled in the same orientation as the native, are highlighted by the black circles.

Figure 5.26 shows two protomers in this virus generated in Chimera, from the interface of two opposing pentamers. A comparison of the native and the mis-assembled particle is shown here to demonstrate the differences. The protomers from the mis-assembled particle were oriented in reverse, as they would be if they were to assemble correctly. The steric clashes between the opposing VP2 and VP3 are marked with black circles on Figure 5.26, panel (B). It is therefore very likely that these clashes prevented the pentamers from assembling correctly, but whether these changes occurred before or after the disassembly of the pentamers is harder to conclude. Either the rotation and translation of VP3 resulted in the destabilisation and consequent disassembly of the whole capsid, or these changes took place once the pentamers had dissociated from each other and had the room to relax due to the absence of VP4 and the VP1 N-terminus, as suggested by Figure 5.24.

In the native capsid formation in-vivo, the cleavage of VP0 results in the formation of VP2 and VP4 for the maturation of the capsid; VP4 is thus likely to play a role in capsid stabilisation. In the case of the mis-assembled particles, the capsids were unable to assemble correctly in the absence of VP4, it may therefore be the case that VP4 or its precursor, VP0, is involved in the correct assembly and genome packaging into the native capsids.

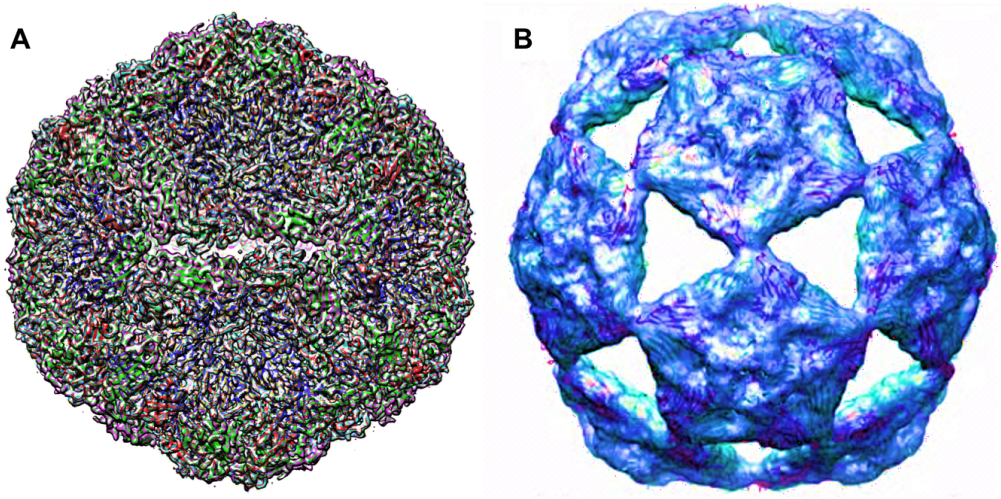


Figure 5.27: A comparison between the (A) FMDV mis-assembled particle at 5.19 Å and (B) the ERAV expanded capsid structure at 17 Å. The atomic structure from the native and the mis-assembled particles are fitted into the electron density in both cases. Adapted from Bakker et al., 2014 [42].

5.4.2 Comparison with other *aphthoviruses*

FMDV belongs to the *aphthovirus* genus and the closest relative, for which this dis-assembly process has been studied, is Equine rhinitis A virus (ERAV) [42]. The low-resolution (about 17 Å) structure mooted to be an intermediate stage of *apthovirus* disassembly was published in 2014 and there have been no higher-resolution structures for *aphthovirus* intermediates since.

Upon discovering the empty-looking particles in the sample and solving their structure, it appeared that they resembled the ERAV expanded particle in several ways. The VP4 density was missing, the particles were slightly expanded and loosely-held together with large holes between pentamers (Figure 5.27) and there was no genome inside them. Had the FMDV particle not been resolved to a high enough resolution to fit in the protein backbone of the atomic structure from the native

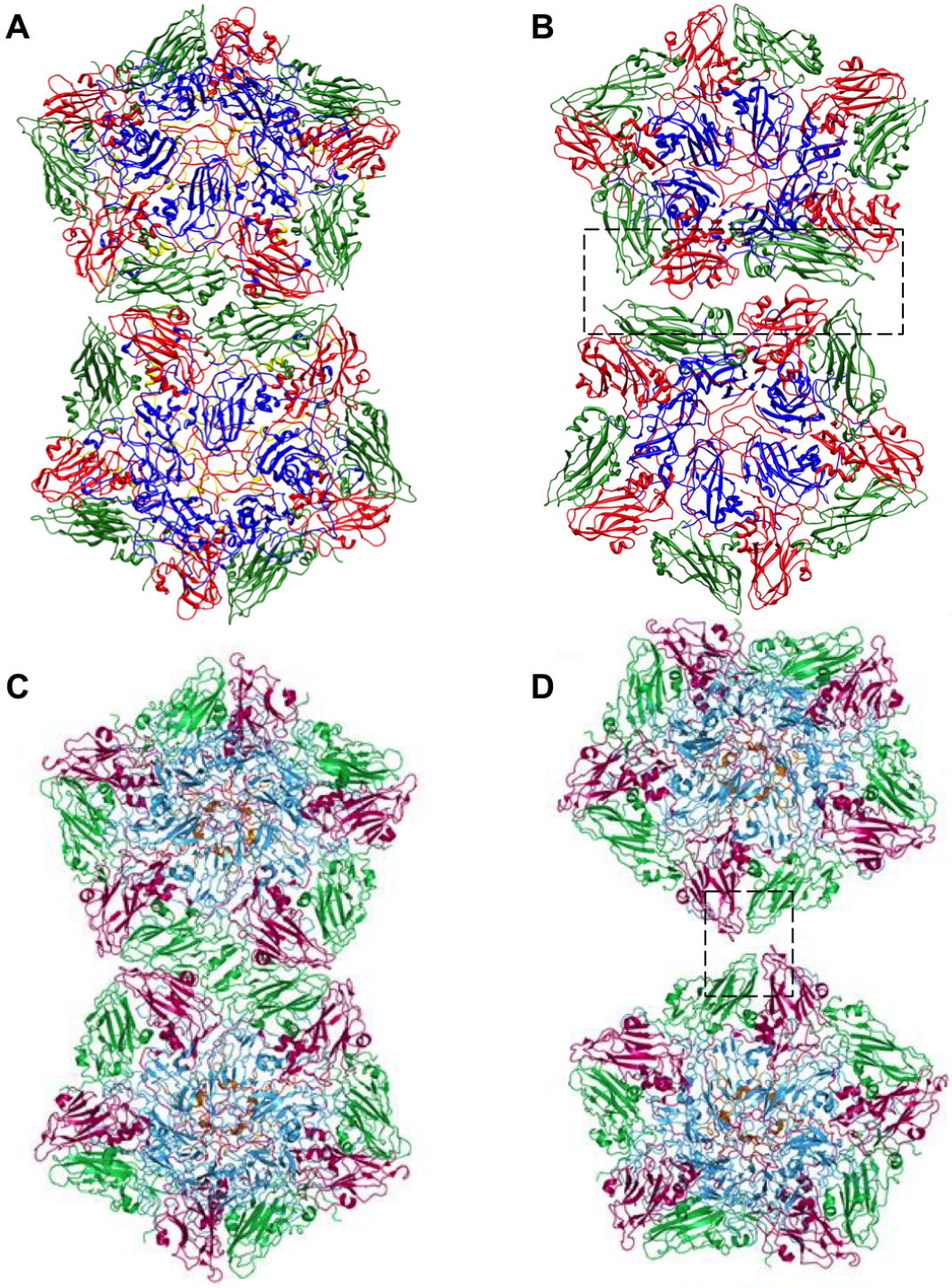


Figure 5.28: A comparison of inter-pentameric interfaces (black rectangles) between the FMDV mis-assembled and the ERAV expanded particle. (A - B) FMDV and (C - D) ERAV pentamers are shown. While the (A) FMDV native pentamer interface resembles the (C) ERAV native pentamer interface quite closely, the (B) FMDV mis-assembled pentamers arrange dramatically differently from the (D) ERAV re-assembled pentamers. Adapted from Bakker et al., 2014 [42].

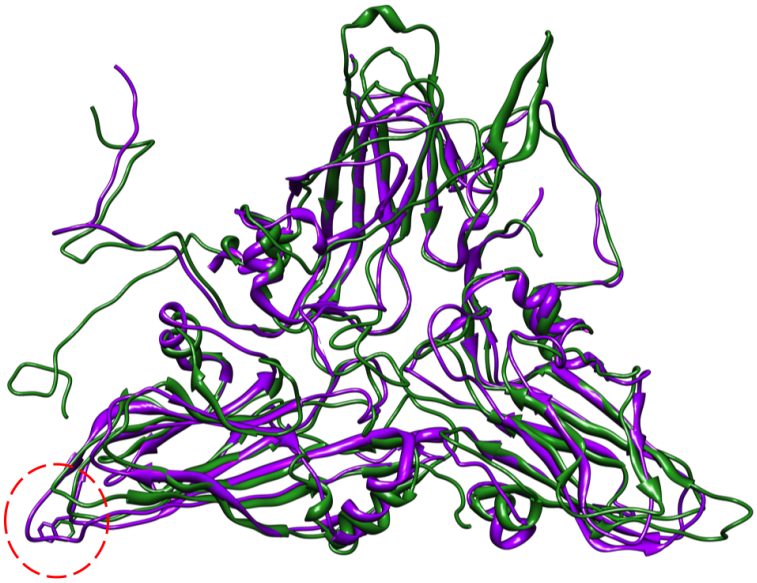


Figure 5.29: A superposition of the FMDV (purple) and ERAV (green) protomers in SHP [167] to show similarities between the two. The red circle highlights the positions of VP2 Phe116 for FMDV and VP2 Phe118 for ERAV, which was presumed to form inter-pentameric interactions in case of the expanded particle for the latter [42].

particle (1ZBE), it would not have been immediately obvious that the particle was indeed a loosely-held re-assembly of the dissociated pentamers.

There were also numerous key differences between the expanded ERAV and the mis-assembled FMDV particle structures. As shown in Figure 5.28, the native pentamers of FMDV (A) and ERAV (C) appear similar. However, assuming that in both cases the pentamers dissociate and re-assemble, they do so in dramatically different conformations. The FMDV mis-assembled particle interface (B) was observed to be larger and have more interactions than that of the ERAV expanded particle (D). The particles were nevertheless not as compactly assembled as the native capsids and formed only a few key interactions that held the pentamers together, hence the expanded size.

Bakker et. al hypothesised that the ERAV expanded particle was formed by key interactions between pentamers, by symmetry-related copies of VP2, in particular Phe118 (highlighted by the black rectangle in Figure 5.28). To investigate whether such interactions might be common between the ERAV and the FMDV mis-assembled capsids, a structural alignment of the ERAV and FMDV protomers was performed in SHP [167]. A sequence similarity of 36.5% and an average RMSD of roughly 2 Å was found between the two protomers. The two superimposed structures are shown in Figure 5.29. As shown by the stick representation, the FMDV protomer also had a Phe residue (VP2 Phe116) in roughly the same region as the ERAV protomer did. The sequence alignment showed that FMDV VP2 Gln115 aligns against ERAV VP2 Phe116. In either case, both these positions were not even close to the inter-pentameric region for the FMDV mis-assembled particle. Figure 5.30 shows the large (around 25 Å) distance between Cαs of the symmetry-related VP2 Phe116 residues in the FMDV mis-assembled capsids; Gln115 is shown next to one of them. It was hard to say if any of the residues were involved in any significant interactions at the three-fold axis for the FMDV particle, as it can be seen that the protein backbones were at least 8 Å apart, even at the narrowest points, at the three-fold axis.

Therefore, it was clear that the FMDV mis-assembled particle had formed in a different way to the ERAV expanded particles. These results were also reproducible and consistent between several sample and grid preparations.

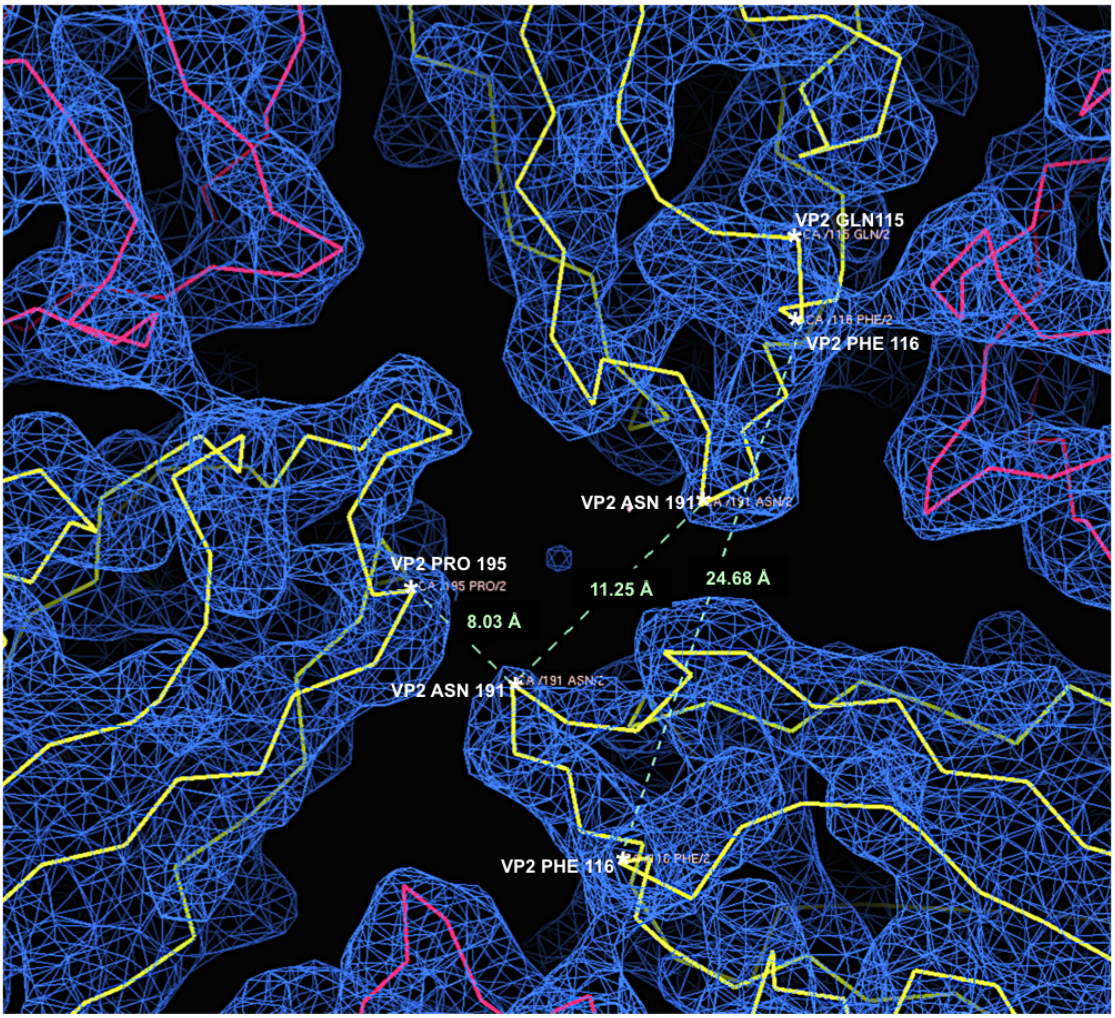


Figure 5.30: EM density (blue mesh) of the FMDV mis-assembled particle at the three-fold axis shown with the backbone of fitted atomic structure, with VP3 in red and VP2 in green. Distances between the VP2 Phe116 residues, that were implicated in ERAV expanded particle inter-pentameric interactions, are shown. Distances between other residues in close proximity to their symmetry-related counterparts at the three-fold axis are also shown.

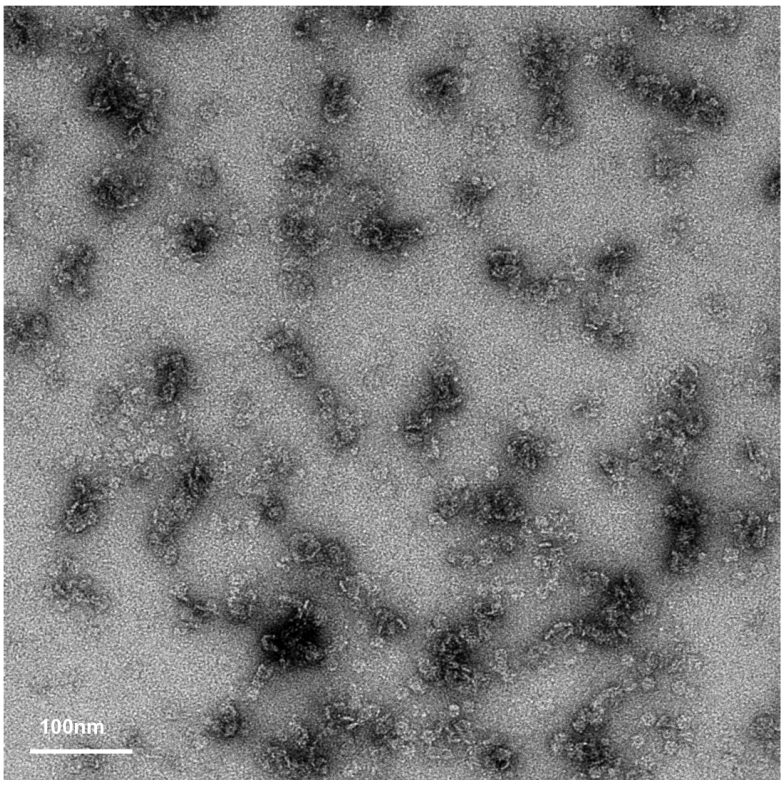


Figure 5.31: Negative-stained EM on purified and inactivated FMDV particles after low-pH exposure. The pH was dropped to 6.3 for one minute before the sample was washed and stained for imaging. The majority of the virus particles appear dissociated into pentamers already.

5.5 Conclusion and future direction

The FMDV mis-assembled particle, which was initially thought to be an uncoating or a disassembly intermediate, was in fact a loosely-arranged product of pentamer re-assembly. The medium-resolution of the structure allowed for unambiguous fitting of the backbone structure, but the side-chains were not always fully visible in the EM density. To improve the resolution, more high-quality data collection would be required. The sample preparation may also benefit from the use of graphene-oxide coated grids, that provide a (almost electron-transparent) support surface for the particles to adhere to, thus allowing more of them to remain in

vitreous ice instead of adhering to the carbon-support surface of the holey-grid. These optimised grids, with homogeneously distributed particles in vitreous ice, may be much more amenable to automatic data-collection at the Titan Krios.

Furthermore, a detailed analysis of the final mis-assembled structure revealed that the dissociated pentamers were quite different from the native (also discussed in the next chapter) and loose interactions at the two-fold axis predominantly, held the particle together. These changes, especially the loss of VP4 and the shifts in VP2 and VP3, are likely to be responsible for the incorrect re-assembly of the pentamers. Whether the shifts in VP2 and VP3 lead to the dissociation of the capsid, or they took place once the pentamers had lost their VP4 and dissociated already, remains unclear. The results further indicate that the ERAV structure, mooted to be an *aphthovirus* disassembly intermediate [42], is likely to also be a result of the re-assembly of dissociated pentamers. If this is the case, then there is thus far no structural evidence supporting the argument that *aphthoviruses* have an intermediate stage, as *enteroviruses* do, in the uncoating process at all. The structure we see is unlikely to have any biological significance.

We have been unable to capture an intermediate particle, if it does indeed exist, by temporary lowering of the pH environment around live, purified capsids. Perhaps if they do exist, the particles in an intermediate stage had exposed charges and thus stuck to filter membranes during concentration or desalting. Alternatively, it is also possible that they dissociated too fast for a two-minute experiment and could thus benefit from a much shorter pulse of low pH in order to be trapped. The transient nature of such intermediates is the more likely explanation in our ex-

perience, as our attempts to treat inactivated capsids with a low-pH buffer shortly before plunging did not produce any altered conformation in virus particles either. Figure 5.31 shows the negative-stained EM results of these experiments. A one-minute exposure to pH 6.3 just before the grid preparation already appeared to be too long, as all the virus particles were observed to have dissociated into pentamers. Thus a faster pH drop for a shorter time, to capture the potentially transient intermediate stages of the disassembly of the particle, might be necessary.

To overcome the two potential obstacles noted above and to test whether an FMDV uncoating intermediate exists at all, an alternative experimental set-up is proposed as follows: Purified FMDV capsids may be applied to a cryo-EM grid in a buffer containing NPE-caged ATP (Sigma Aldrich) that releases protons upon cleavage by a laser pulse of 360 nm. The laser pulse on the sample just before it is plunge-frozen should ensure that the reaction time between steps is minimised and the sample plunged on a sub-second time scale after low-pH exposure, to try to capture the transient intermediate stages. This should reduce the timescale of the experiments required to capture any intermediates and also remove the need to filter and purify any charged particles in the process. The system, however, is still being established in the lab.

Chapter 6

FMDV pentamer structure

6.1 Chapter summary

Each FMDV capsid comprises of twelve pentamers. As introduced in Chapter 1: Introduction, the virus infects the cells and dissociates into its pentamers in an acidic compartment, such as the endosomes. Not only is this dissociation process not well-characterised, there are also no published structures of the dissociated FMDV pentamers, the building units of the virus, which might give an insight into the disassembly process. This chapter aims to provide some understanding of how these dissociated pentamers might differ from the conformation they are in the native virus and how they compare to the structure in the mis-assembled particles described in the previous chapter. These structural studies contribute to our understanding of the virus disassembly and the structures determined here are the first when it comes to the standalone dissociated pentamers of any *picornavirus*.

6.2 Methods

6.2.1 Sample preparation

To obtain a cryo-EM structure of a standalone pentamer, the first step was to prepare a sample for cryo-EM that contained dissociated pentamers. For the vast majority of sample preparation described here, this was performed by heating a sample of purified FMDV capsids in buffer at 55 °C for 10 minutes. The heat treatment disrupted the inter-pentameric interactions in the capsids and lead to the formation of dissociated pentamers. The sample was then throughly mixed using a pipette and initially checked in negative-stain EM for the presence of pentamers. Sample preparation for this was performed as explained in Chapter 2: Electron Microscopy.

6.2.2 Negative-stain electron microscopy

Negative-stain electron microscopy, using uranyl acetate stain, showed that the heat treatment produced well-separated dissociated pentamers. There were no large aggregates observed in the samples and pentamers could be observed predominantly in top- but also in side-views, as shown in Figure 6.1. All samples were checked and subsequently plunge-frozen for data collection in cryo-EM. FMDV Asia-1 or O1K capsids were used (due to sample availability issues) for the initial experiments to optimise the cryo-EM conditions for obtaining well-distributed dissociated pentamers in vitreous ice; however the data collection for final structure determination was performed on A10 capsids (explained later). This was essential for high-resolution structure determination, in order to determine how the

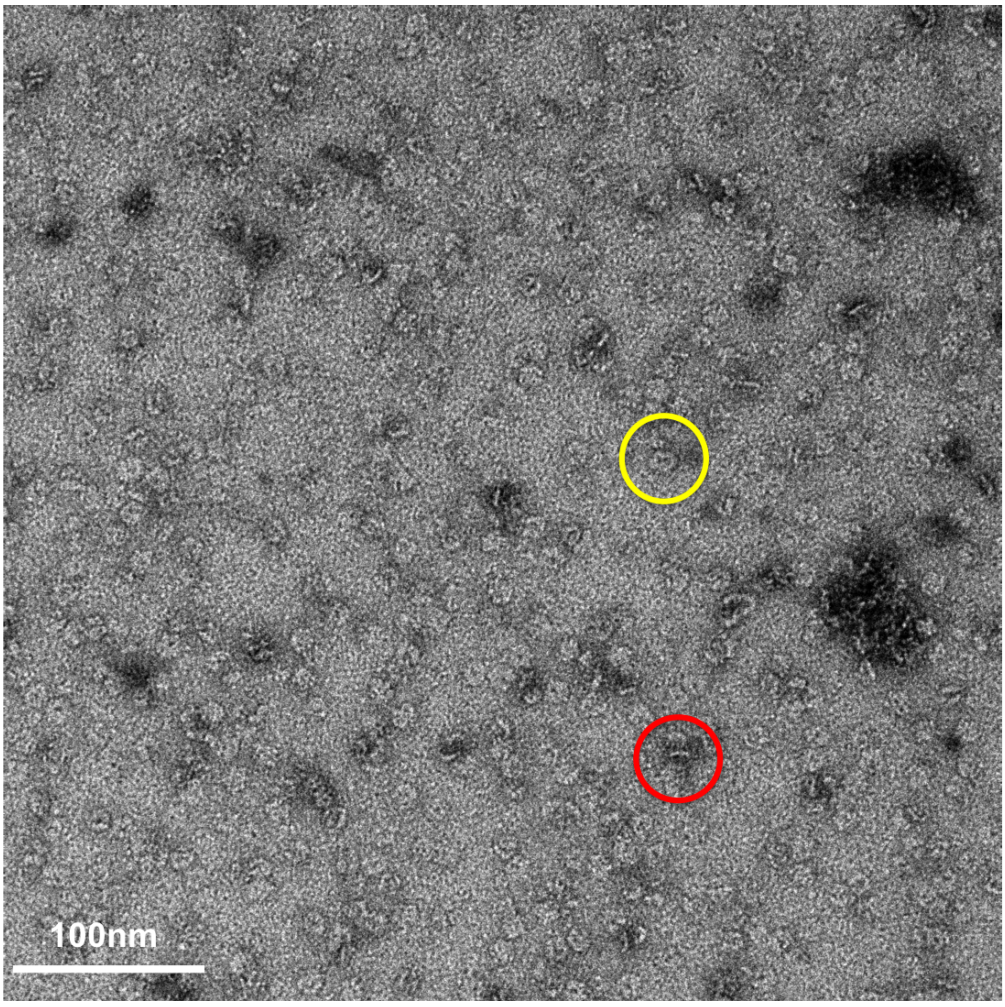


Figure 6.1: Heat treatment to generate dissociated pentamers worked successfully as shown using negative-stain EM. Pentamers were observed mostly in top-views (yellow circle), but some side-views (red circle) could also be seen.

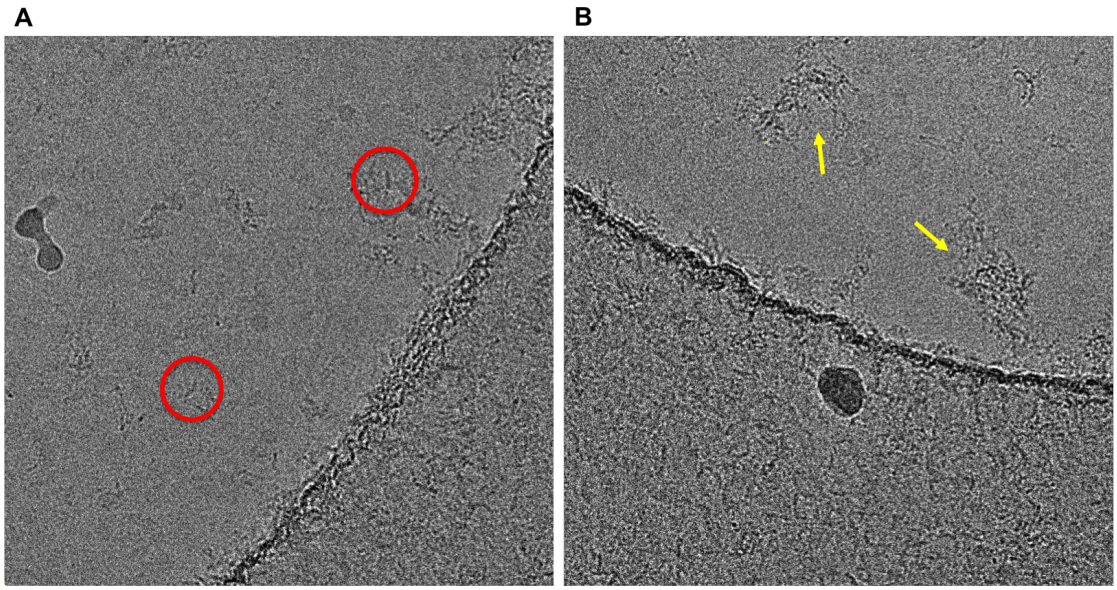


Figure 6.2: A 1:10 dilution of the samples for cryo-EM. Yellow arrows indicate aggregates of pentamers in vitreous ice, while the red circles show the rare, dissociated pentamers nicely separated in ice for imaging.

dissociated pentamers might differ from those in a native capsid.

6.2.3 Attempts at cryo-electron microscopy

While the negative-stain EM did not show any problems with the sample, cryo-EM data collection was faced with a few challenges. The pentamer samples did not seem amenable to vitrification in ice, and were consistently observed aggregated or mostly stuck to the hydrophobic carbon support of the cryo-EM grids, where they could not be imaged. The following sub-sections highlight the different conditions and grid supports that were tried, to force the pentamers into vitreous ice.

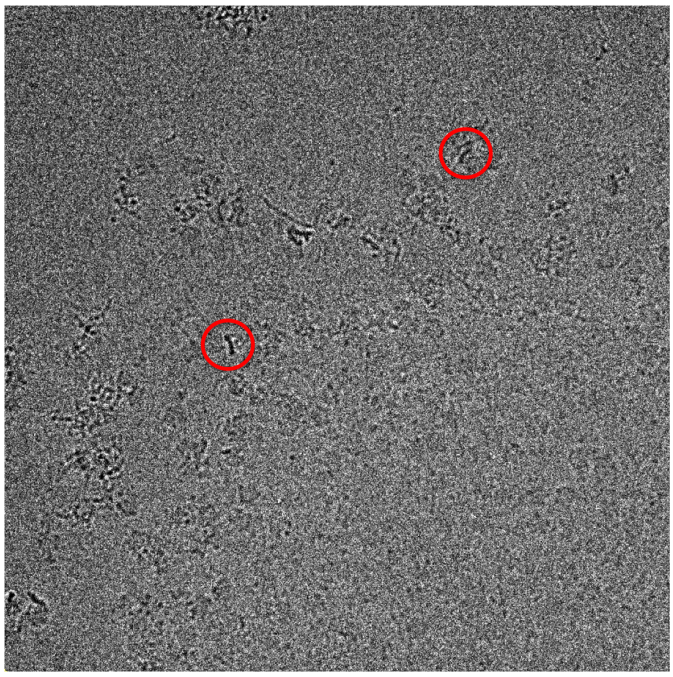


Figure 6.3: A 1:20 dilution of the samples for cryo-EM. Red circles show the dissociated pentamers.

6.2.3.1 1:10 dilution

Initially, different dilutions of the pentamers used for negative-staining were screened in cryo-EM. As per experience, a 1:10 dilution compared to what is used in negative-staining was attempted first; the results are shown in Figure 6.2. All the dilutions were performed in the Hepes buffer (50mM Hepes, 400mM NaCl, pH 8.0) as used for virus capsid purification. As shown, most of the pentamers were present on the carbon grid support. The ones present in vitreous ice had aggregated (yellow arrows). Rarely, a few separate pentamers could also be seen in vitreous ice (red circles).

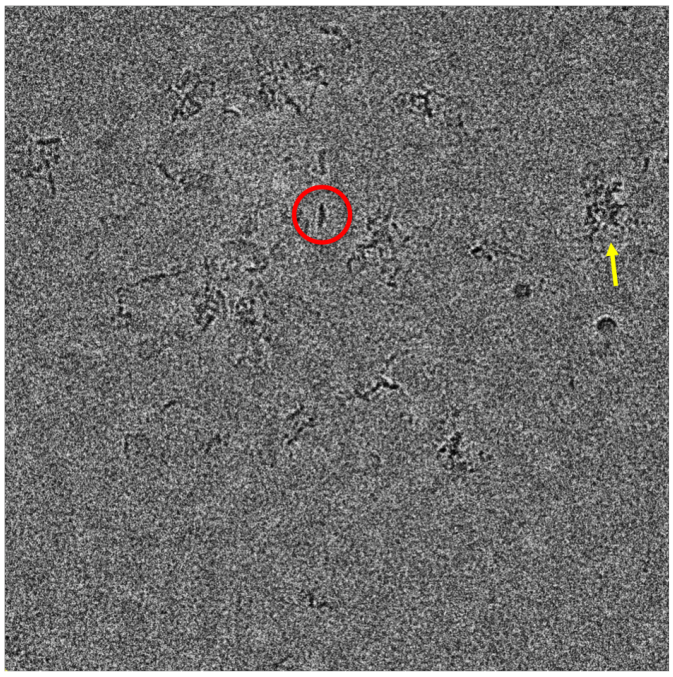


Figure 6.4: A 1:20 dilution of the samples for cryo-EM, applied and blotted away once, before re-applying samples to the same grids and blotting for plunging.

6.2.3.2 1:20 dilution

In an attempt to reduce aggregation, the sample was diluted further to 1:20. This did not appear to get rid of the aggregation problem in the sample preparation, and as before only a few pentamers were seen nicely distributed in vitreous ice (Figure 6.3).

6.2.3.3 1:20 dilution, double-blotted grids

In order to increase the concentration of dissociated pentamers seen in vitreous ice in the 1:20 diluted samples, the double-blotting technique was used before plunging. In this case, a 3 μL aliquot of the 1:20 diluted sample of pentamers was applied to the grids, allowed to incubate for 30 seconds and blotted gently from one side, such that the grids may not dry out. These grids were then used for

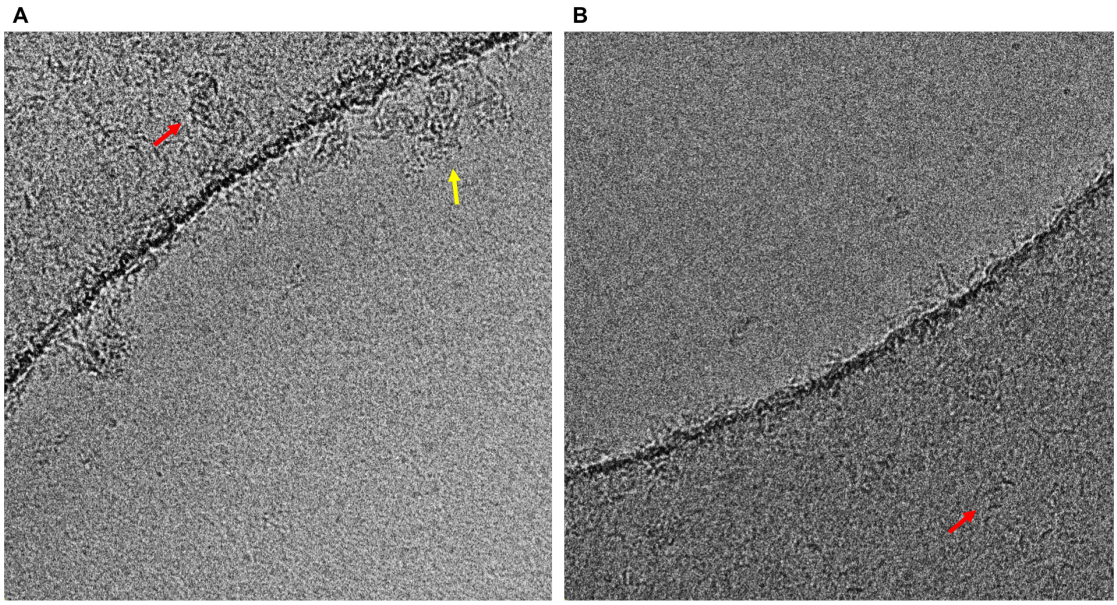


Figure 6.5: A 1:10 dilution of the samples for cryo-EM in the presence of (A) 0.005% or (B) 0.01% TWEEN-20. Arrows indicate aggregates of pentamers on the carbon (red) or in vitreous ice (yellow).

sample loading, blotting and plunging as normal in the Vitrobot (FEI Company). This was an attempt to increase the number of pentamers in the vitreous ice layer suspended between carbon support layer holes to consequently have more particles for imaging. As shown by Figure 6.4, the number of particles in the vitreous ice (red circles) did increase, but not significantly. The aggregates of pentamers (yellow arrow) prevented a good distribution of the sample in ice. These imaging conditions were not considered ideal for large-scale data collection, as there were not enough separated pentamers to solve a high-resolution structure. Thus sample optimisation was continued.

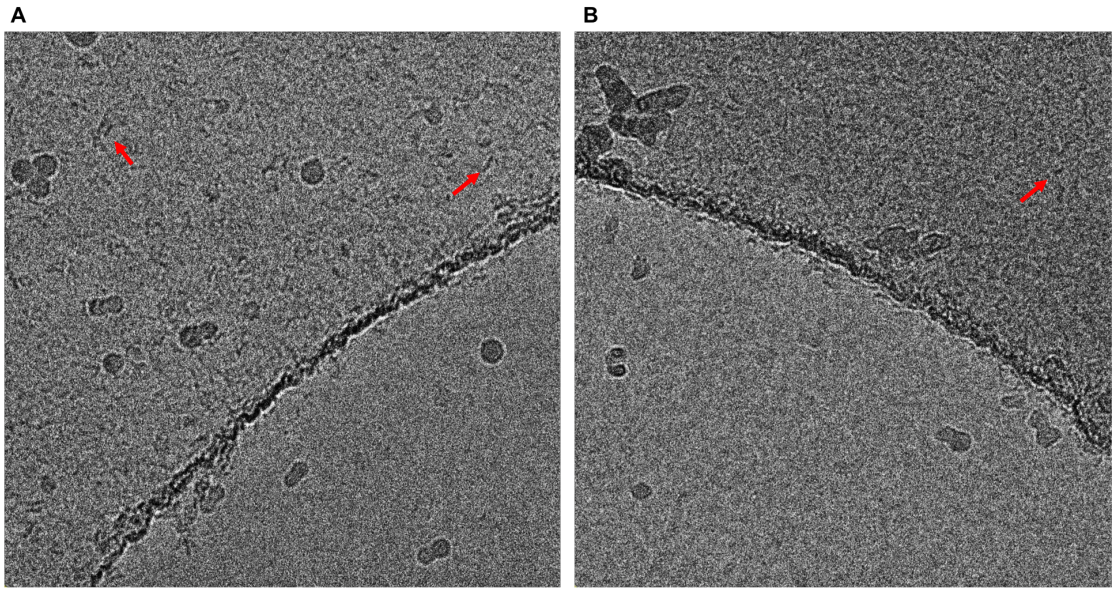


Figure 6.6: A 1:20 dilution of the samples for cryo-EM after soaking in 0.003% DMNG detergent on (A) glow discharged grids, or on (B) grids that were not glow discharged. Almost all the pentamers were seen on the carbon support (red arrows).

6.2.3.4 1:10 dilution with TWEEN-20

A series of detergents was investigated to see if they could prevent the pentamers from forming large aggregates. TWEEN-20 (Sigma Aldrich), a common detergent in most laboratories, was tried first, in two different concentrations: 0.005% and 0.01%. As shown by two representative images in Figure 6.5, these attempts were unsuccessful. Almost all the sample was seen sticking to the carbon grid support (red arrows) and in occasional cases, some pentamers were seen next to the carbon support rim, in ice (yellow arrow), but aggregated nevertheless.

6.2.3.5 1:20 dilution with DMNG

The next detergent attempted in order to prevent sample aggregation, which was suggested by colleagues in Radu Aricescu's group for cryo-EM grid preparation,

was DMNG (Decyl Maltose Neopentyl Glycol) (Generon Ltd. UK). Their group had shown that soaking grids in 0.003% DMNG for 15 minutes before applying the sample to them, introduced a charge on the carbon surfaces and thus prevented samples from attaching to the support film. The concentration of DMNG used was just under its Critical Micelle Concentration. This treatment was thus attempted with the pentamer sample, with and without modifications such as glow-discharging of grids (Figure 6.6 (A)), or the lack thereof (B), before the DMNG soak. Neither of these attempts generated successful grid preparations. In most of the cases, the samples did not adhere to the grids at all. In some good preparations, the pentamers could be seen, but only on the carbon support film, as shown in Figure 6.6. Keeping in mind, that every cryo-EM sample preparation is different and what works for one sample might not always work for another, this was not an uncommon result.

6.2.3.6 1:20 dilution with NP-40

The last attempt to prevent the pentamers from clumping was by the use of the non-ionic detergent NP-40 (Thermo Fischer Scientific). 0.01% NP-40 was used (just under Critical Micelle Concentration) in the sample preparation, with 1:20 dilution of pentamers. As Figure 6.7 shows, this did not improve the sample distribution in the ice at all, and all the pentamers were found to prefer adhering to the carbon support film as before. The detergent screening was abandoned at this point.

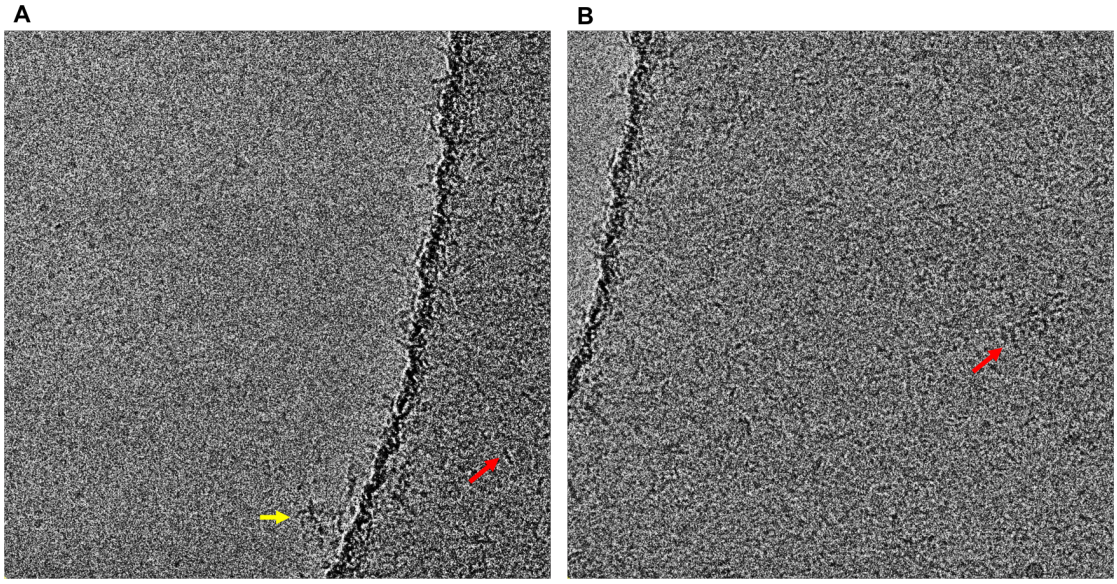


Figure 6.7: A 1:20 dilution of the samples for cryo-EM in the presence of 0.01% NP-40 detergent. Red arrows show the majority of the pentamer sample on the carbon support, and the yellow arrow indicates the occasional aggregate of pentamers near the carbon rim in vitreous ice.

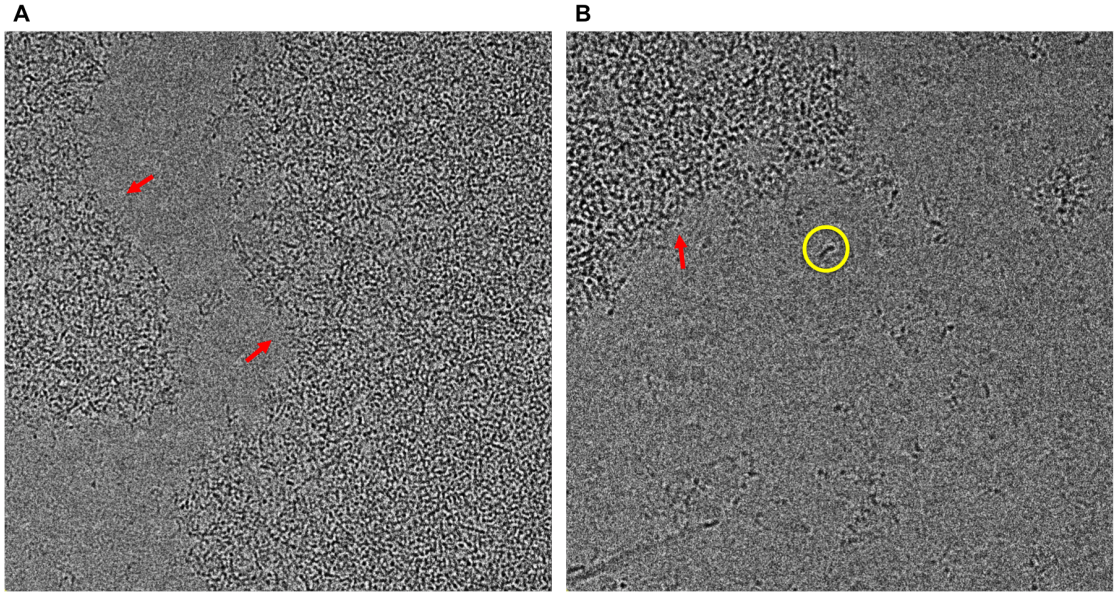


Figure 6.8: A 1:30 dilution of the samples for cryo-EM applied to lacey-carbon support grids. Large aggregates of pentamers were observed in vitreous ice (red arrows) and there were also the occasional standalone pentamers (yellow circle) near them.

6.2.3.7 Lacey-carbon support grids

As most of the conditions showed that the pentamers had a preference for carbon, lacey-carbon support grids (Electron Microscopy Sciences) were tested. The rationale behind this was to reduce the surface area of the carbon support, so that the pentamers would be forced into vitreous ice. A reduced concentration (1:30) of pentamers was applied to the grids in an attempt to prevent large-scale aggregation. This, as shown by Figure 6.8, did not help significantly. The pentamers were almost always seen as large aggregates near the edges, next to the carbon support, leaving most of the holes largely empty. A few dispersed pentamers could sometimes be observed next to the large aggregates, which was nevertheless not enough for large-scale data collection.

In parallel to the screening for a good sample preparation condition, micrographs containing any standalone pentamers were combined and particles picked from them. This was attempted from both the negative-stained and cryo-EM datasets. The outcome from these attempts is detailed in the Results section. Eventually, the FMDV A10-serotype samples from Pirbright containing altered particles and some pentamers were used to determine the final standalone pentamer structure at roughly 8 Å, as explained in the following section.

6.3 Results

6.3.1 Structure determination from negative-stained EM

Roughly 500 micrographs were collected from the negative-stained pentamer samples. About 23,000 particles were picked from these and put through the image processing pipeline for a rough structure determination.

6.3.1.1 2D classification

All the picked particles were classified into 20 classes. There were very few side-views (1076 particles) of the pentamers seen in this dataset. Nonetheless, they were classified into a class (Figure 6.9, yellow asterisk) which was included in subsequent analyses. Some classes appeared to have damaged pentamers (red asterisk) and were removed from the subsequent classification steps.

6.3.1.2 3D classification

The remaining particles (roughly 18,000) were classified into 5 classes, as shown in Figure 6.10. There were 2790 particles in Class A, 1 in Class B, 8228 in Class C, 2495 in Class D and 4695 in Class E respectively. As it was hard to determine which class looked the best based on the 2D projections in Relion, they were examined in Chimera in 3D.

Due to the particles being on a carbon support surface for the negative-stain grid preparations, the particles appeared smeared in the direction of the electron beam, as shown by their side-views in Chimera (Figure 6.11). Based on the 3D representations, Class D appeared to have the least smearing and was therefore

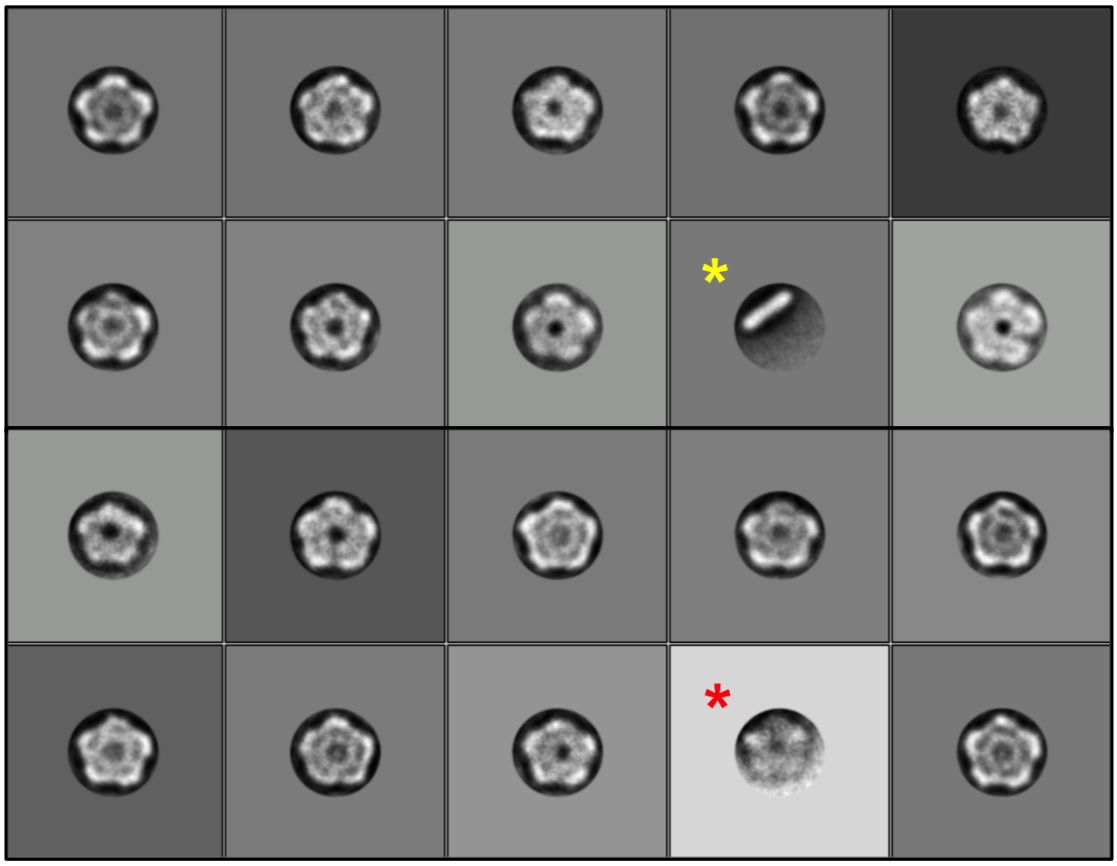


Figure 6.9: 2D classification of the standalone dissociated FMDV pentamers into 20 classes, in a negative-stained EM dataset. The side-views of the pentamers were observed separated into a class of their own (yellow asterisk), and included in subsequent analyses. Some particles appeared damaged (red asterisk) and were separated into a class which was excluded from the analyses.

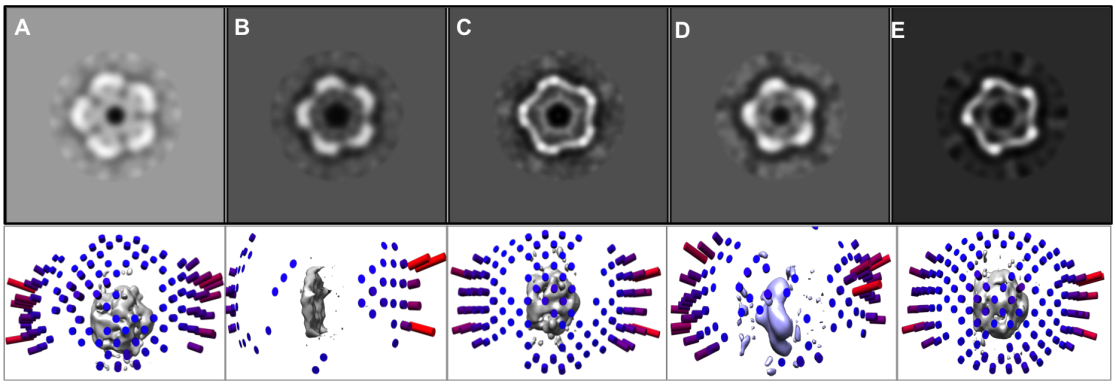


Figure 6.10: 3D classification of about 18,000 FMDV pentamers into 5 classes, in negative-stained EM. Class A had 2790, Class B 1, Class C 8228, Class D 2495 and Class E had 4695 pentamers respectively. The orientation sampling of each class is also shown; the height and density of the blue-red bars represent the frequency and the distribution of the views sampled respectively. As seen, most classes only had top views contributing to them.

picked for subsequent refinement. The other classes had more particles, but the noise from the smearing effect seemed to distort the structure too much in those cases. As this was not an attempt to solve a high-resolution structure but only to get a first rough idea of the structure, the processing was continued with the class with the least amount of noisy data (Class D).

6.3.1.3 Final structure from negative-stained EM

The final structure obtained from the negative-stained dataset was reported to be at 30 Å in Relion (Figure 6.12). This was obtained from roughly 2500 particles and had no high-resolution information. The curvature and the five-fold symmetry could, however, be seen clearly. For negative-stained EM, this number of particles is too low to result in any meaningful high-resolution structural interpretation. The particles from all the classes could have been combined to attempt a better resolution but as the attempts to get a cryo-EM structure were underway in parallel, this was not deemed necessary. The only reliable information obtained out of

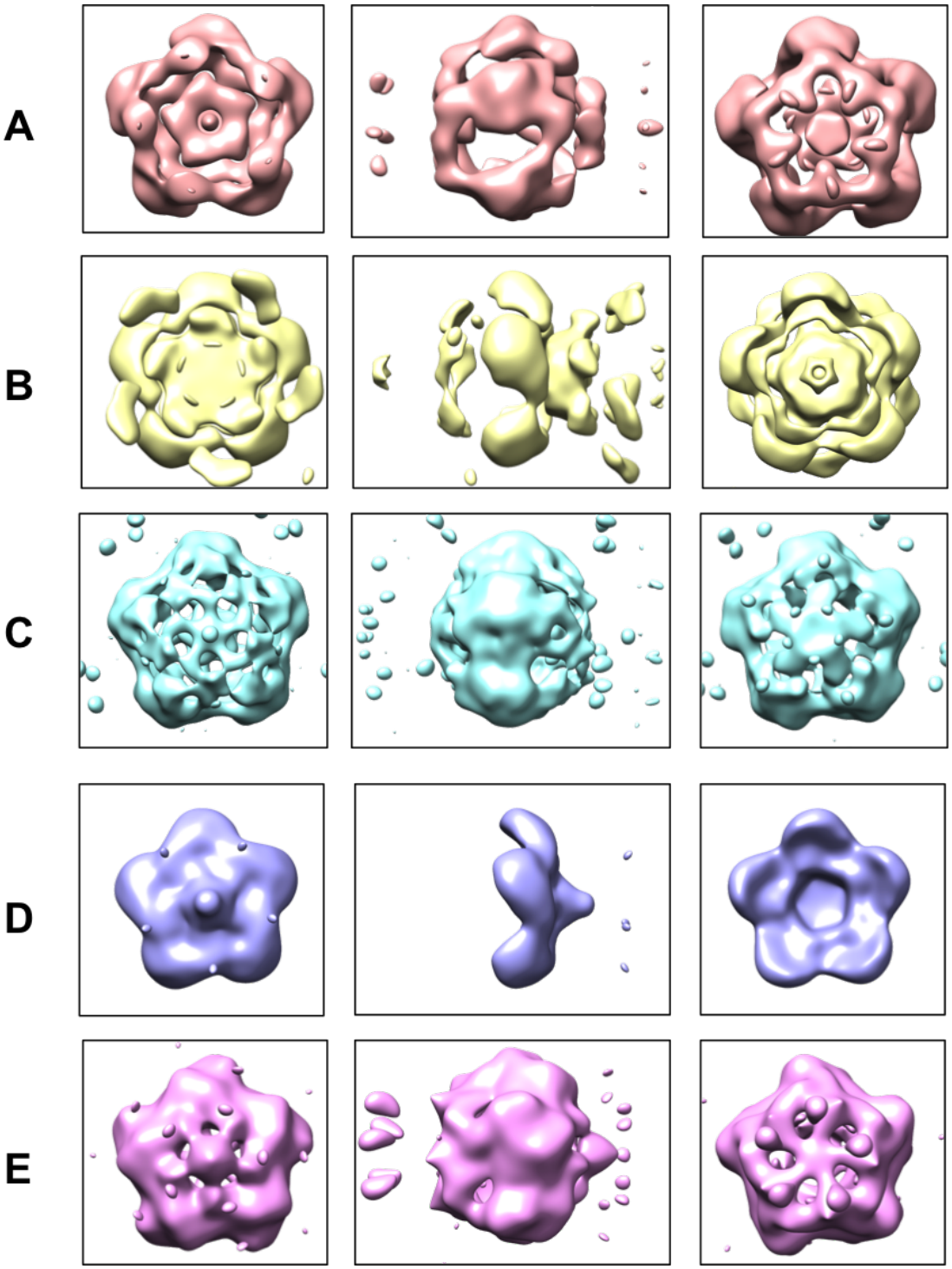


Figure 6.11: The five 3D classes of the negative-stained pentamers rendered in Chimera. The three panels in each row indicate the view of the pentamer from outside a native virus, the side-view of the pentamer and the view from inside a native virus particle respectively. The side-views show how noisy and smeared negative-stained EM data can be.

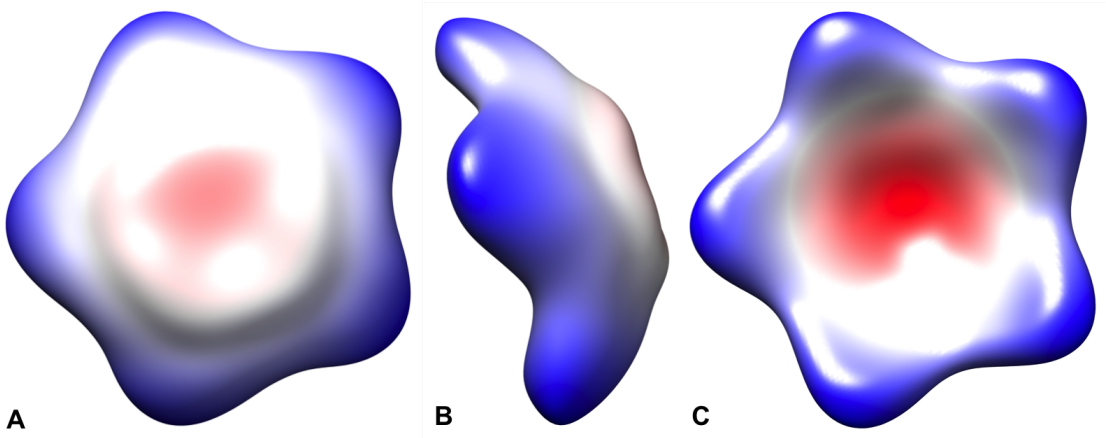


Figure 6.12: The final structure from the negative-stained EM data. Three different views represent the pentamer as might be seen from (A) outside a native virus particle, (B) side-view of the pentamer, (C) view from inside a native virus particle. Here, blue indicates the part of the pentamer closest to the centre of the particle and red indicates the parts furthest away.

this small exercise was a confirmation of the identity of the pentamers seen in the negative-stained EM samples and the general curvature of the pentamer structure.

6.3.2 Structure determination from cryo-EM

The cryo-EM sample optimisation proved difficult initially. In some experimental conditions, isolated pentamers were observed in the micrographs, but these were too few to perform large-scale data collection on said samples. Most of the pentamers in the samples had aggregated or preferred to stick to the carbon support surface. Nevertheless, the micrographs from all the conditions were combined to confirm the identity of these particles in cryo-EM micrographs and to see if enough pentamers could be picked to obtain a low-resolution structure that would serve the purpose of our studies such that we could compare the pentamer assembly discussed in Chapter 5 to the stand-alone dissociated pentamers.

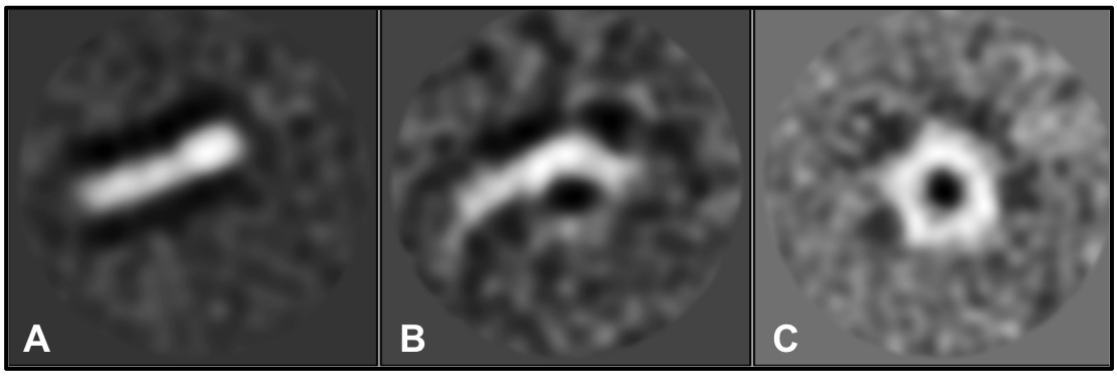


Figure 6.13: 280 particles from the initial cryo-EM data were classified in three 2D classes as a rough attempt to solve a low resolution cryo-EM structure. Class A had 130, Class B 45 and Class C had 109 particles.

6.3.2.1 2D classification: first attempt

The picked pentamers from several hundred movies amounted to roughly 280. These were classified in 2D, as shown in Figure 6.13, and the particles were found in side-views predominantly. Class A had the most particles (130), followed by class C (109) and B (45). The number of particles, even after combining Class A and C, was too low for cryo-EM processing, and this dataset was not processed any further.

Luckily, at this stage, the FMDV samples for the potentially altered particles from Pirbright had arrived. Even though the majority of the pentamers were found on the carbon support in the grid preparation from those samples as well, there were nevertheless quite a few isolated pentamers seen in vitreous ice. Mostly side-views (Figure 6.14, red circles) of the pentamers were observed in the new samples. The altered particle samples were used for large-scale data collection to determine the structure of the potentially altered FMDV particle anyhow; as a positive consequence, the same dataset with 1500 movies could be processed for

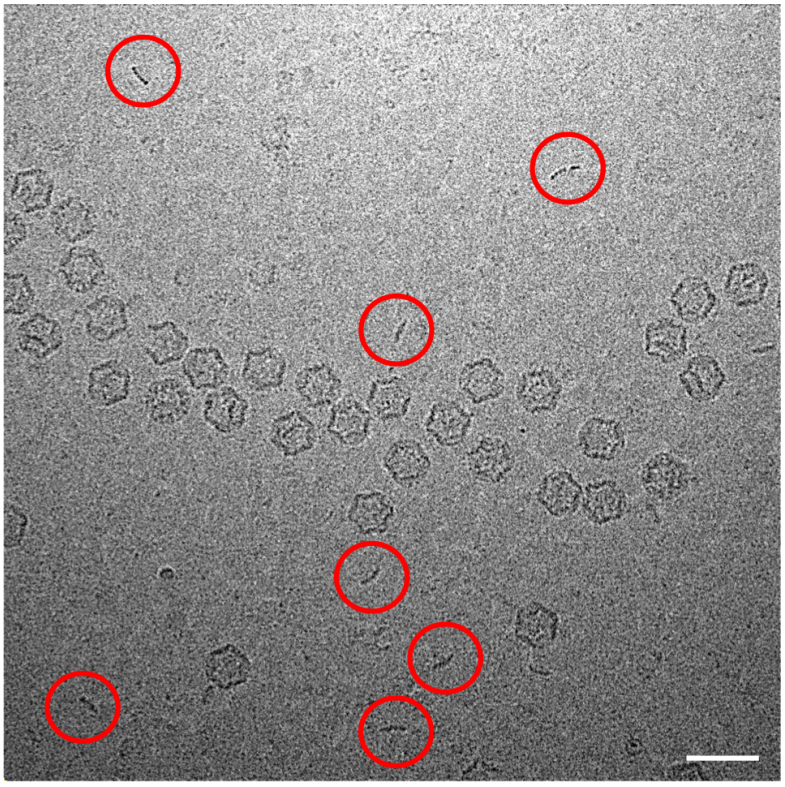


Figure 6.14: A representative micrograph showing the low-pH treated sample with pentamers, received from Pirbright, that was used for the second attempt at cryo-EM structure determination of a dissociated pentamer. Red circles show the pentamers in side-views. Scale bar = 50nm.



Figure 6.15: Roughly 4800 particles were manually picked and 2D-classified into 10 classes. As shown here, most of the particles were in side-views and the top-views were not separated out into any separate classes.

the isolated pentamers as well.

6.3.2.2 2D classification: second attempt

The second attempt at 2D classification, was performed on the pentamers picked from the altered particle grid preparations mentioned above. Roughly 4800 pentamers were manually picked and classified in 2D. These particles were mostly in side-view orientations, as expected from previous cryo-EM screening of the samples. The 2D classes obtained are shown in Figure 6.15. As none of the classes appeared to contain damaged particles, they were all were combined and the particles classified in 3D.

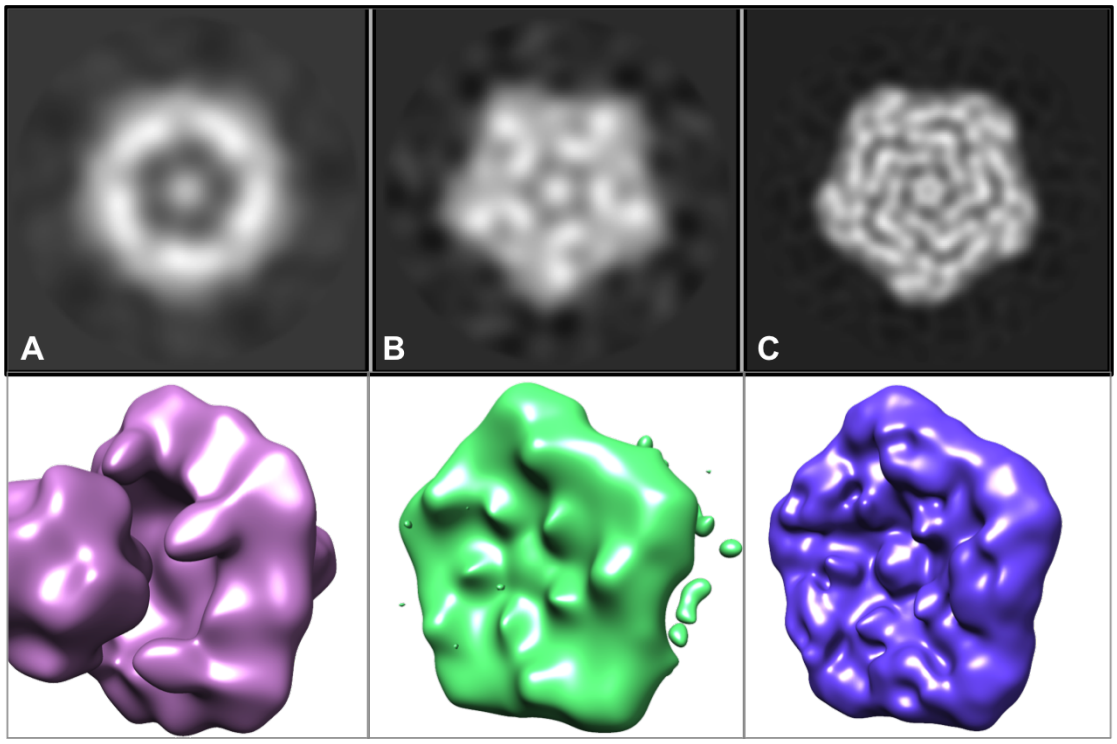


Figure 6.16: 3D classification of roughly 4800 pentamer particles into 3 classes. The 2D projection of each 3D class (top panels) and the 3D rendering in Chimera (at the same threshold for each class) accordingly (bottom panels) are shown here. Class A had 226, Class B 354 and Class C had 4260 particles.

6.3.2.3 3D classification

Using a pentamer cut-out from the native FMDV virus capsid (1ZBE), a low-pass filtered template at 50 Å was generated as described previously in Chapter 2, and used to classify all the picked pentamers into 3 classes. Class A had 226, Class B 354, and Class C had 4260 particles. Figure 6.16 shows the 2D projection of the class average of each 3D class in the top, and the 3D rendering from Chimera in the bottom panels. As most of the particles were clustered in Class C and it appeared to be the least noisy when seen in Chimera, it was selected for the final structural refinement.

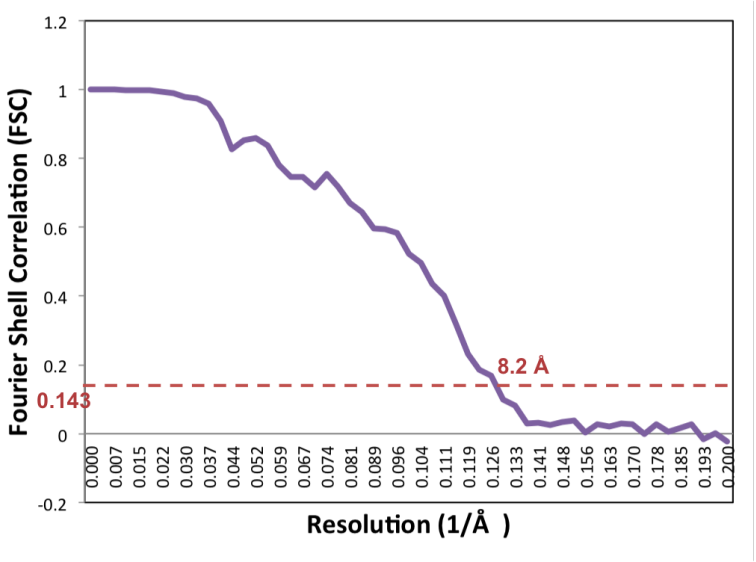


Figure 6.17: The resolution of the final structure was determined using the gold-standard FSC cut-off of 0.143 at 8.2 Å.

6.3.2.4 Final structure from cryo-EM

The final structure of an FMDV dissociated pentamer was thus generated from 4260 particles, at 8.2 Å. The resolution post-refinement was determined at the gold-standard FSC cut-off of 0.143 (Figure 6.17).

Figure 6.18 shows the final structure rendered in 3D in Chimera, where the blue parts of the structure are closest to the centre of the particle and the red the furthest towards the outside, as they would be in the context of a native virus capsid. The curved shape of the pentamer, as expected based on the low-resolution structure from negative-stained EM (Figure 6.12), as well as the density for secondary structural elements could clearly be observed.

Furthermore, ResMap was used to show the varying resolution of the different parts

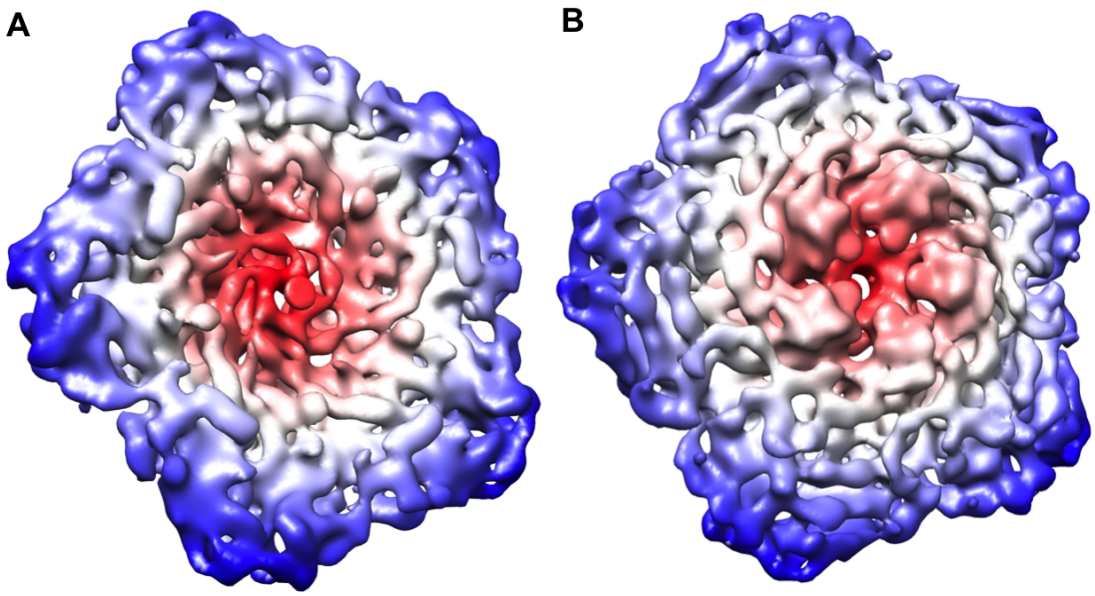


Figure 6.18: The views of the final 8.2Å-structure of the dissociated FMDV pentamer from (A) inside and (B) outside a native virus particle, shown at a slight tilt to highlight the curvature of the structure. The red areas correspond to the outermost and blue the innermost towards the centre of the capsid, in a native arrangement.

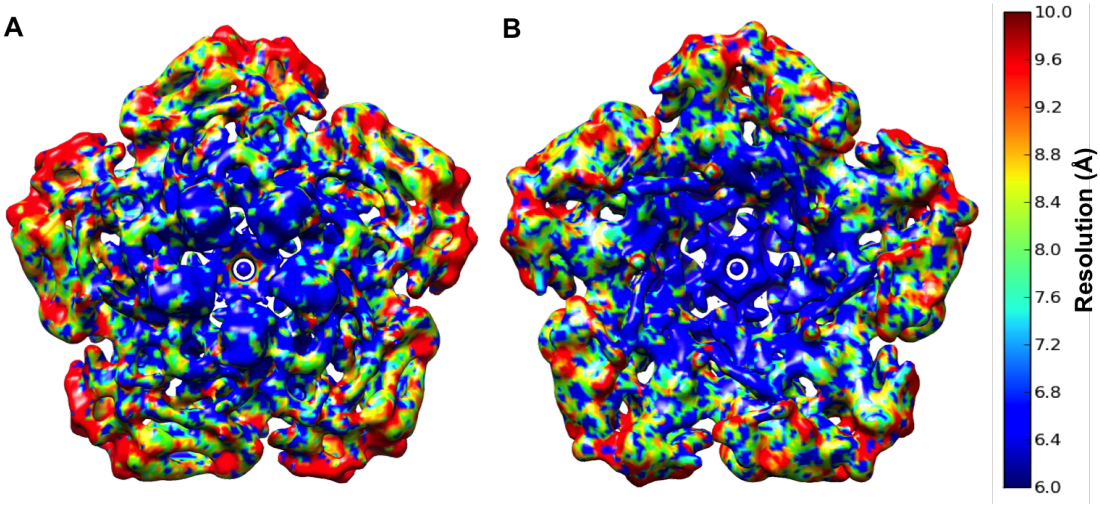


Figure 6.19: Resolution determination of the final pentamer structure in Resmap.

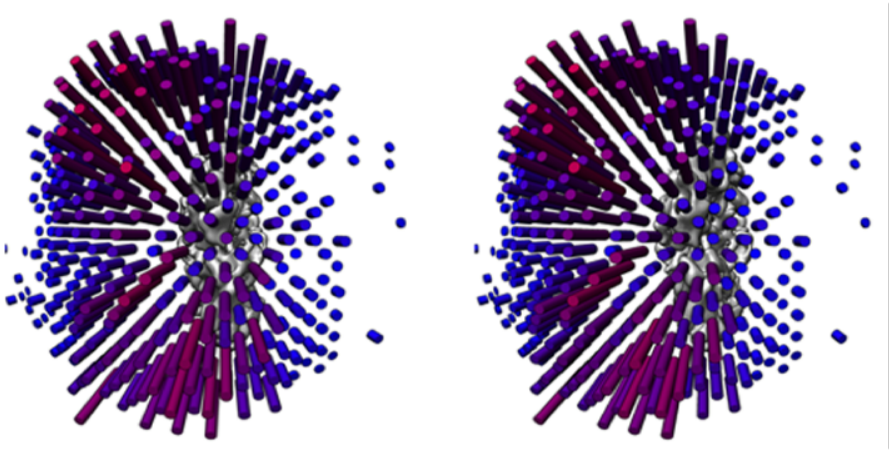


Figure 6.20: Stereo views of the orientations (angular distribution) of the pentamer contributing to the final structure of the dissociated pentamer is shown using the length of the bars, in Chimera. The taller, redder and more densely packed the bars, the higher the contribution from those angles to the final structure. As shown, the side-views contributed the most significantly to the final structure.

of the pentamer structure, as shown on the scale in Figure 6.19. Even though the overall resolution of the pentamer, according to the FSC cut-off was around 8.0 Å, most of the core structure was determined to a resolution of 6 Å, as shown in the ResMap results in Figure 6.19 (additional details: Figure B.4 Appendix B).

The analysis (displaying Relion *angdist.bild* files in Chimera) of the orientation sampling in the final structure of the dissociated pentamer also showed that the side-views of the pentamers contributed the most heavily to the structure (Figure 6.20). This was expected, as most of the pentamers in the cryo-EM preparation were oriented on their sides in vitreous ice. To boost the resolution of the final structure, a larger variety of orientations needs to be sampled.

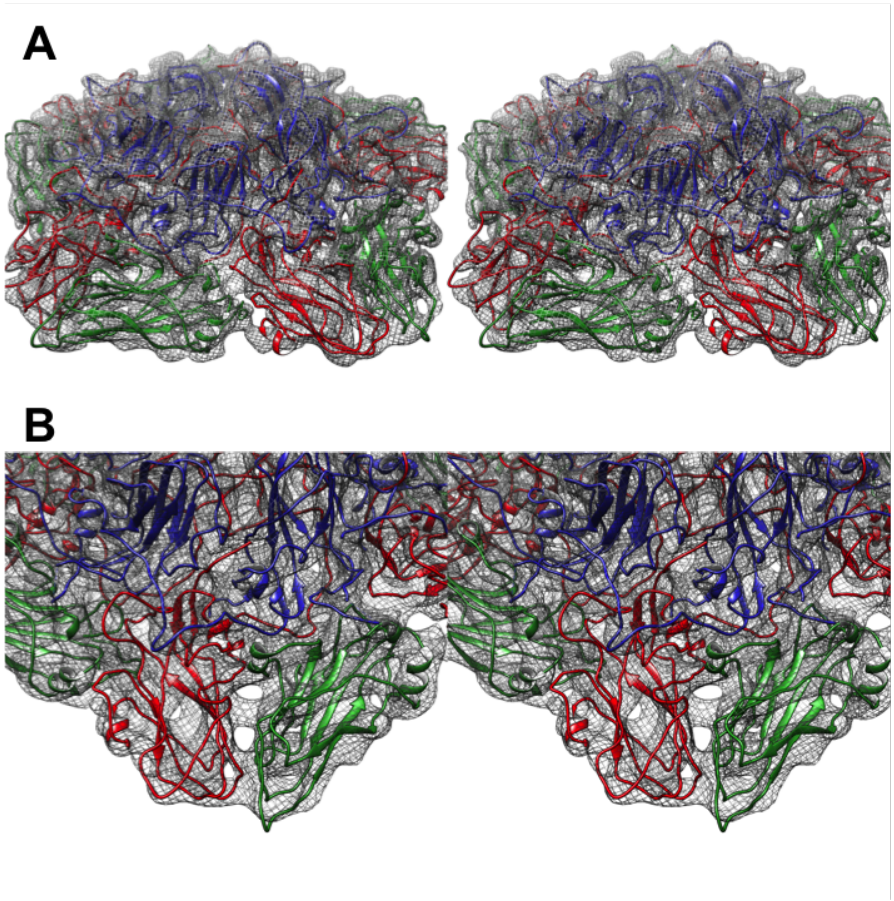


Figure 6.21: Two different wall-eyed stereo views of the EM density of the standalone pentamer shown with the model from the mis-assembled particle fitted in, to demonstrate the quality of the fitting.

6.3.2.5 Atomic-model fitting into the EM structure

The medium resolution of the structure was encouraging for the fitting of the atomic model of a dissociated pentamer obtained from the mis-assembled pentamers introduced in Chapter 5. It was not high enough to refine single atoms, but a rigid-body docking could easily be performed. The structure did not contain any density for VP4, which was therefore removed from the atomic model fitted in the density.

The rigid-body fitting was performed using the Fit-to-Volume program available in Chimera. The atomic structure fitted into the EM density with a cross-correlation (CC) of 88% in Chimera. As shown by Figures 6.21 and 6.22, the fit into the density was especially well observed at the inter-pentameric edges. The helices at the inter VP2-VP3 interface can be seen corresponding especially well to the EM density mesh. The side-view shown in Figure 6.22 (C) showed that the curvature of the atomic model matched that of the density extremely well and that there were no structural components of the atomic model that did not have any electron density to account for them. Also vice versa, no part of the density was unaccounted-for by the atomic model fit. It was therefore confirmed that the atomic model that had been built into the mis-assembled pentamer electron density in Chapter 5 corresponded well with that of the dissociated pentamers. The comparison of the dissociated pentamers against the native ones, is covered in the Discussion section.

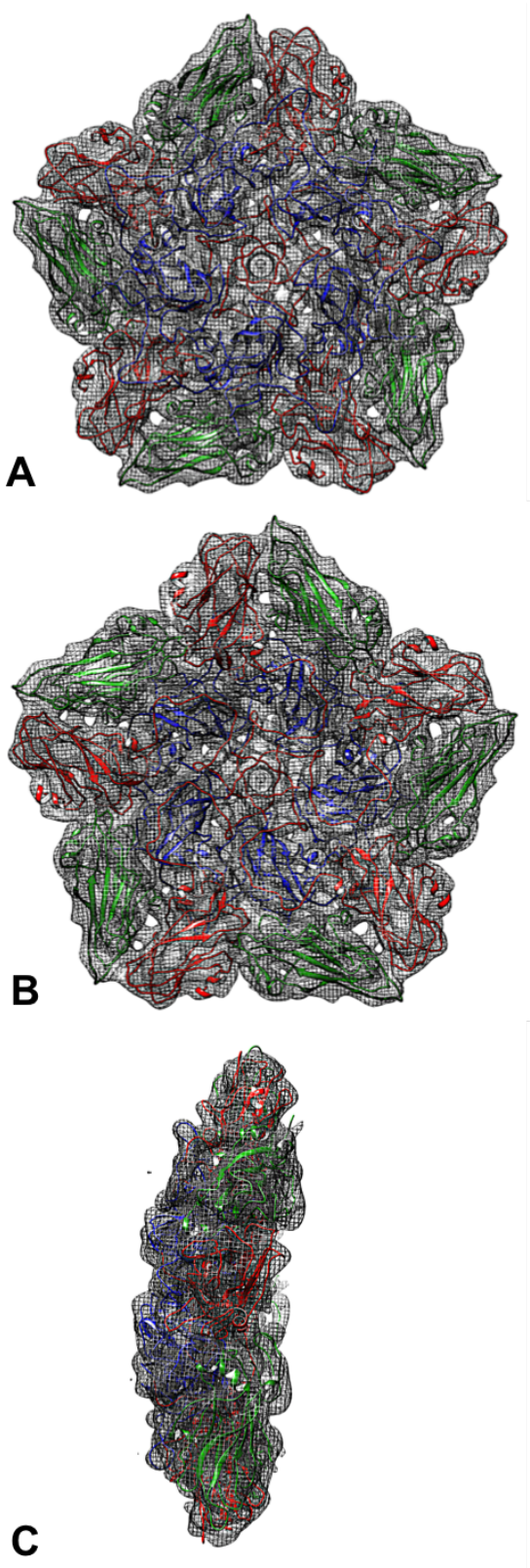


Figure 6.22: The atomic model obtained from the mis-assembled particles (Chapter 5) shown fitted into the EM density (mesh) of the standalone pentamer. The views of the pentamer as seen from (A) outside and (B) inside a native virus are shown, along with the (C) side-view of the dissociated pentamer, to show the arrangement of the atomic structure and its curvature. VP1 is shown in blue, VP2 in green and VP3 in red. No density for VP4 was observed.

6.4 Discussion

6.4.1 Difficulties with sample preparation for pentamers

Obtaining a homogeneously-distributed pentamer sample in vitreous ice proved challenging at the outset of this part of the project. The difficulties mentioned here are commonly encountered in cryo-EM preparations and the reasons are not always obvious. In this case, comparing the samples that did and did not have pentamers in vitreous ice, it was tempting to speculate that the hydrophobic air-water interface was not amenable to the distribution of the pentamers in the water film in holes in the carbon support. In the samples from Pirbright, with the mis-assembled capsids, the thickness of the vitreous ice film was thicker than in our initial samples with just pentamers. This increased distance between the air-water interfaces on both sides of the vitreous ice may have allowed more pentamers to go into the water layer during grid preparation. Additionally, the samples from Pirbright contained FMDV serotype A10, whereas the pentamer sample optimisation attempts, as previously mentioned, were performed using serotypes O1K (cryo-EM attempts) and Asia-1 (negative-stained EM). Different structural properties of different serotypes may also influence the sample distribution on the grids.

Another potential reason for the difference in the quality of grid preparations could have been due to the different methods of producing the pentamers: low-pH treatment in one case versus high-temperature exposure in the other. The protonation of Histidine residues at the edges of the dissociated pentamers in the former might have lead to different electrostatic properties compared to the pentamers that were formed by the dissociation of the capsids at a high temperature. These

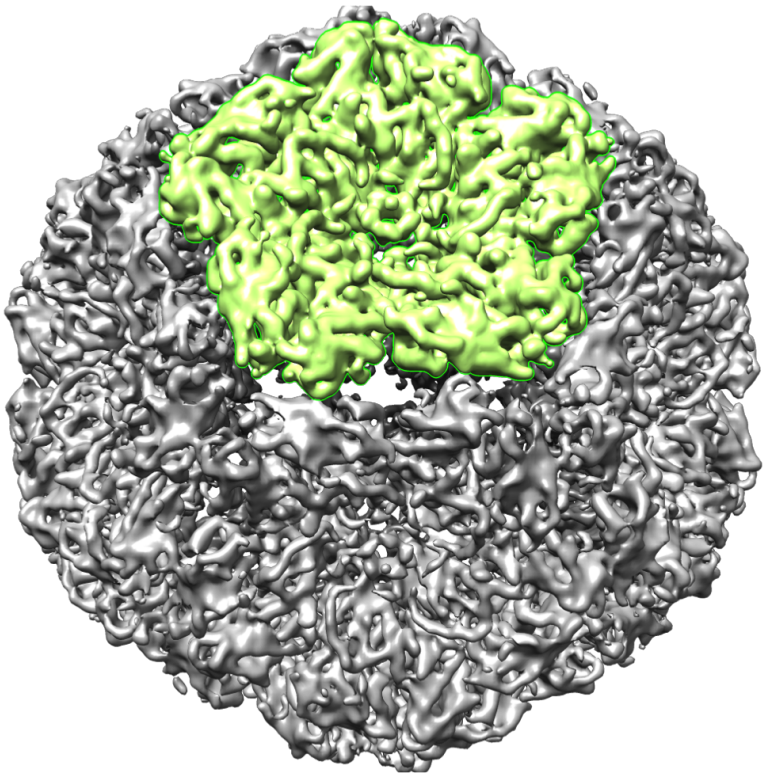


Figure 6.23: Segmentation of a pentamer (green density) out of the electron density for the mis-assembled FMDV particle (gray), performed using Chimera.

differences were not thoroughly tested in this case, due to lack of time, and could be investigated further in the future.

6.4.2 Pentamer from the mis-assembled particle

Ultimately, once the electron density for a standalone pentamer was obtained from the low-pH treated samples, the next question to address was whether the native, or the altered structure from the mis-assembled particles from Chapter 5, would fit better into the electron density. As shown in the Results, the atomic model from the mis-assembled particle pentamer did fit well into the electron density of the standalone pentamer. But when the structure of the mis-assembled particle

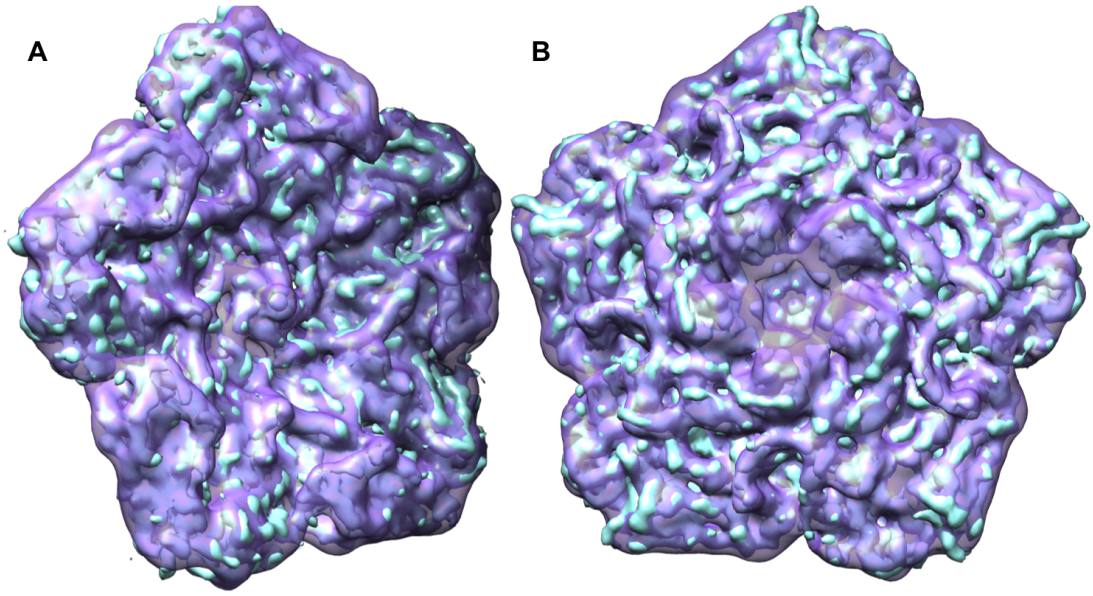


Figure 6.24: Two different views showing the fitting of the 5.19 Å pentamer density (cyan) from the mis-assembled particle into the observed density of a standalone, dissociated pentamer at 8.2 Å (purple) for comparison in Chimera.

was being resolved, the fitting of the atomic model into the particle density had proved extremely challenging. It had not been obvious at first, as the structure was not high-resolution, that the pentamers were flipped inside out and therefore it took a while to get the fitting right.

While waiting for an accurate atomic model fitting in the mis-assembled particles, an initial comparison was performed between the standalone and the mis-assembled pentamers, based only on the EM density. To this end, the Segmentation tool in Chimera was used to select the density corresponding to an individual pentamer from the mis-assembled particles, as shown in Figure 6.23.

Both the structures were brought to a contour level where the most structural features were visible, just before noisy data appeared at the edges. The segmented

density at 5.19 Å showed more features than the pentamer map at 8.2 Å and when docked into the EM map of the standalone pentamer, a good fit could be observed. The curvature of both the structures was almost exactly the same and the high-resolution density docked into the pentamer density well enough at the edges that no empty spaces or extra density could be observed at the edges of the pentamers. Figure 6.24 shows the fitting of the 5.19 Å density into the 8.2 Å density shown from the two different sides of the pentamers. It was therefore considered likely that the atomic model from the mis-assembled pentamers would fit well into the standalone pentamer density. To compare the two structures in atomic detail, the atomic models from the native and from the fitted mis-assembled particle pentamer were compared next.

6.4.3 Dissociated vs. pentamers from the native particle

Once a good atomic model fitting into the mis-assembled particle was obtained, the structure of one of the pentamers was cut out of the model for comparison against the native structure, in Chimera. Figure 6.25 shows this model, where VP1 in shown in blue, VP2 in green, and VP3 in red. For the comparison, the structure of the native pentamer from 1ZBE (yellow) was overlaid onto our structure, in the electron density. As there was no density for VP4 observed in the EM map for the standalone pentamer, it was removed from the models and the three capsid proteins were fitted into the EM density map.

The pentamer from the mis-assembled particle fit into the pentamer density with a cross-correlation of 88%, higher than that of the native pentamer structure fitting

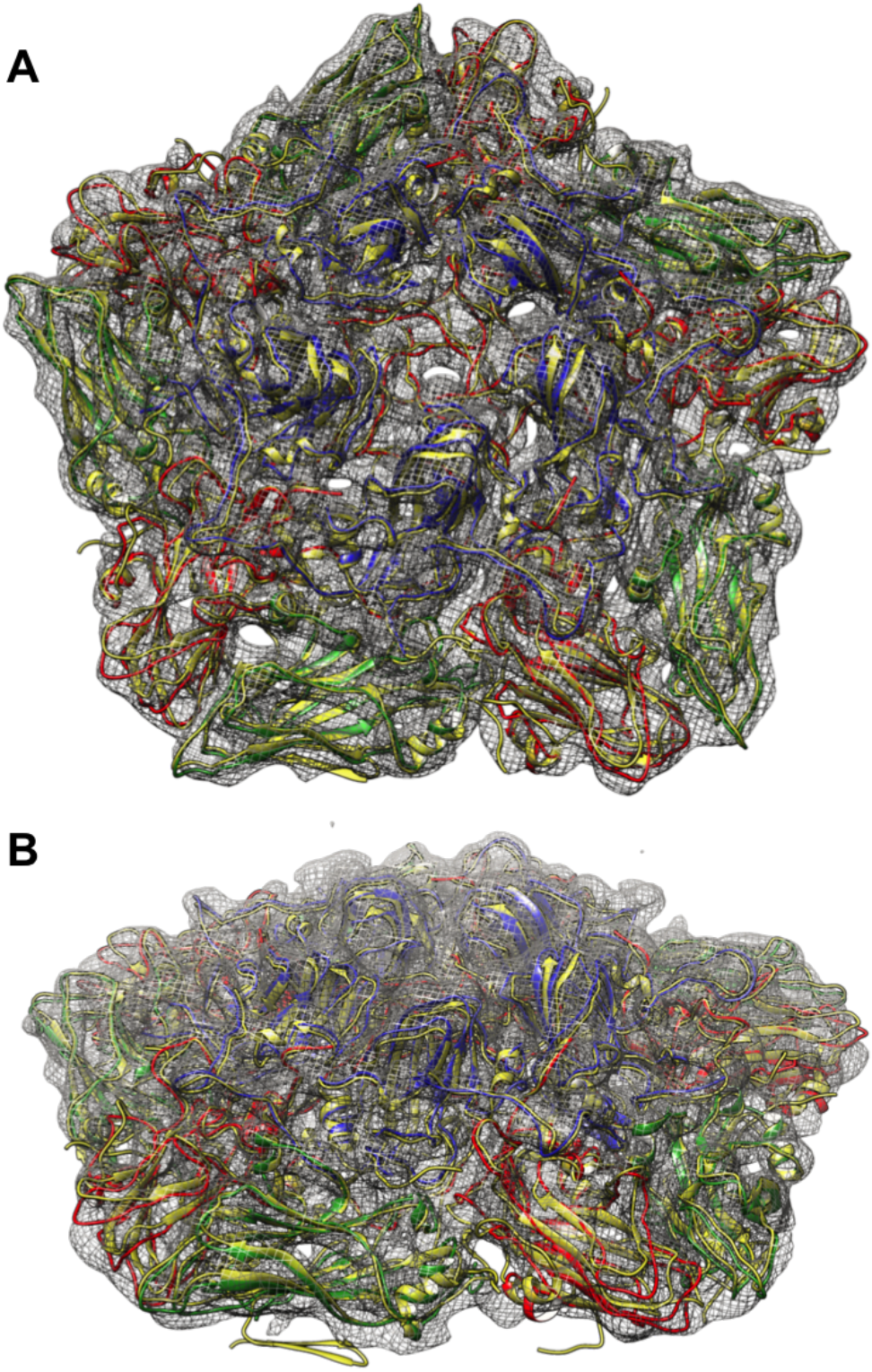


Figure 6.25: Native pentamer atomic model (yellow) in comparison to the fitted structure from the mis-assembled particle which shows VP1 (blue), VP2 (green) and VP3 (red). (A) View of the pentamer as from outside the native virus particle. (B) Structure from (A) tilted by 45°.

(81%). It was clear, on manual inspection, that the density corresponded to the former structure much better than to that of the latter, as shown in Figure 6.25. None of the structural elements in the density were unaccounted for when the pentamer from the mis-assembled particle, with a removed VP4, was fitted into the electron density. However, in comparison, the native structure did not fit as well. VP3 from the mis-assembled pentamer model fitted much better into the density of the standalone pentamer; it was seen rotated and translated by several degrees, which allowed a visibly better fitting into the EM density. Furthermore, there was no density for VP4, which is known to be lost during *picornavirus* disassembly, or for the VP2 N-terminal hairpin loop (Figure 6.25 (B)). This is consistent with what is previously known about *picornavirus* disassembly intermediates [59–62, 64, 66]. The structural changes in VP2 and VP3 were conclusive evidence for the confirmation that the structure of the pentamers in the mis-assembled particles, was that of dissociated pentamers that had re-assembled in the wrong orientation.

6.5 Conclusion and future direction

With the results in this chapter, a novel structure of a standalone FMDV pentamer was presented at a resolution of 8.2 Å. The resolution could be improved by acquiring more data, but for the purpose of this study, a medium resolution was enough. These results were used to confirm that the mis-assembled particle was in fact an assembly of dissociated pentamers. These pentamers differed from the native significantly, as explained in the previous chapter, and the fitting of the structure into the pentamer map, in comparison to the native, showed that the density was unambiguously that of a dissociated and not a native pentamer.

Chapter 7

Contributions and prospects

This main contributions of the projects in this thesis to the area of structural biology of *picornaviruses* are highlighted in this concluding chapter. Some areas that have a scope for further studies are also discussed here.

7.1 A complete SAT structural repository

With the high-resolution (3.1 Å) cryo-EM structure of FMDV SAT3 now determined, the repository of sub-nm structures for FMDV SAT serotypes is now complete. The SAT serotypes are prevalent in sub-Saharan African FMDV outbreaks and there is a dire need for thermostable and cross-protective vaccines for such warm climates, in countries with often inadequate cold-chains. The cryo-EM structure of SAT1 at 3.8 Å also ensured that there are now cryo-EM structures available for all SAT serotypes, as previously only a crystal structure was available for it. These high-resolution structures are crucial to the structural studies of thermostable vaccines for FMDV being actively researched and developed at

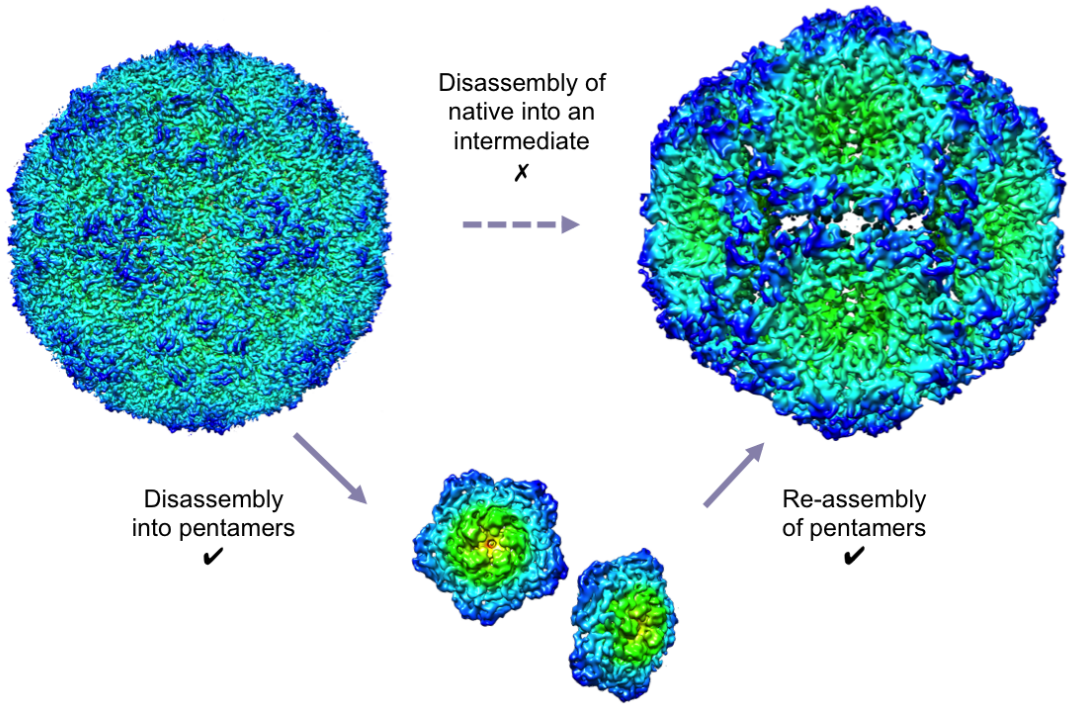


Figure 7.1: Illustrating the overview of the FMDV disassembly process.

the moment. There is a scope for in-depth analyses and comparison of the three SAT structures now available, such as escape-mutant studies complemented by MD simulations, to compare the different antigenicities and structurally stable mutants of FMDV SAT serotypes. The structural comparison between SAT3 and other serotypes (SAT1, SAT2, O1K and A10) in terms of antigenic properties and the high-resolution structures presented here may help with the design of such experiments and offer a good starting point.

7.2 Insights into FMDV disassembly

The question of FMDV disassembly has been an elusive area of research so far. Studies of other closely-related (*aphthoviruses* [42]) or distantly-related *picor-*

naviruses (*enteroviruses* [59–62]) have not shed any light on the FMDV disassembly process thus far. In this study, by solving the structure of a mis-assembled FMDV particle and comparing it to the native FMDV capsids, some insights into the disassembly process were presented. VP3 was shown to play a potential role in the disassembly process, by possible structural destabilisation of the capsid. The missing VP4 and the translation of the beta-sheets of VP2 and VP3 were implicated in the relaxation of the general capsid structure, as shown by the structure of the dissociated pentamers. The same changes indeed prevented a normal re-assembly of the capsids into a native-like capsid structure (Figure 7.1) and therefore indicated that all four viral proteins might play a role in the correct assembly of the pentamers into mature capsids.

In future studies, a comparison of the pentamers (containing VP0) from naturally empty capsids produced during an FMDV infection, the pentamers in the mature particles, and the standalone pentamers after disassembly may provide further insight into the FMDV assembly and disassembly mechanisms.

7.3 Questions about *aphthovirus* intermediates

The methods used in this thesis did not succeed in capturing a true FMDV disassembly intermediate, but they did indicate that if an *aphthovirus* intermediate does exist, it is likely to be very transient or charged, or perhaps both. It is, on the other hand, also possible that *aphthoviruses* disassemble into pentamers directly and such an intermediate does not exist. The results here further showed that the expanded ERAV particle structure previously published is likely to be

a result of pentamer mis-assembly rather than a true intermediate, as suggested by the results shown in Chapters 5 and 6. While these structures certainly contribute to our understanding of how *aphthoviruses* disassemble, the search for a true intermediate is not yet over. Experimental set-ups that allow quicker lowering of the pH in the surrounding of the purified FMDV capsids are needed. A potential way of doing this was discussed at the conclusion of Chapter 5, i.e the use of caged-protons that are released by a laser pulse shortly before the sample is plunge-frozen, and is an avenue worth exploring. It might also be worthwhile to repeat the experiments producing the altered particles with a range of pH values, in case the uncoating in the endosomes takes place at a slightly different pH value.

7.4 The first high-resolution standalone pentamer

FMDV is a well-studied *picornavirus*; even so, the building blocks of the virus capsid, the standalone pentamers, had thus far not been structurally characterised. Here, the first cryo-EM structure of a standalone, dissociated FMDV pentamer was presented. The comparison of these pentamers to the native FMDV structure allowed for some conclusive insights into the disassembly process.

As the structure of the standalone pentamer presented here is at a medium-resolution of roughly 8 Å, there is room for improvement of the resolution to uncover finer details of the structural differences between the dissociated and the native pentamers. For further attempts to prepare cryo-EM samples with standalone pentamers in the future, several conditions could be tried, based on the lessons learnt from this study. The use of EM grids coated with a layer of (al-

most electron-transparent) graphene-oxide might provide a support surface for the pentamers to adhere to. This might help with the collection of more top-views in cryo-EM and help improve the resolution of the final structure.

As the pentamers appear to avoid the air-water interface and more of them appear in vitreous ice if the thickness of the ice is increased, further samples could be attempted with a mixture of purified capsids and the dissociated pentamers, such that the layer of water containing the sample, in the holey-carbon support, is thicker before the grid is plunge-frozen. This might allow for a higher concentration of the pentamers in vitreous ice and consequently more particles for imaging and structure determination.

Furthermore, dissociated pentamers produced by the low-pH treatment, instead of high-temperature exposure, were used for the structure determination in this case. This is a closer-to-native treatment of the sample, as the pentamers in infected host cells are produced in the endosomes in an acidic pH at a physiological temperature. Therefore, further experiments with standalone pentamers might benefit from low-pH treatment to produce pentamers and it might also be helpful in preventing aggregation due to exposed charges. RNase treatment may also facilitate a better dispersion of the pentamers in vitreous ice, to prevent any RNA released during capsid disassembly sticking to the pentamers and causing them to clump together.

7.5 Concluding remarks

Overall, the different parts of this thesis highlight the importance of structural biology in contributing to the understanding of the functional aspects of biological assemblies, such as viruses. It also demonstrates the increasing power of cryo-EM as a structural biology tool, in combination with other biological assays, and shows the long way the technique has come due to the advancement of detector technology and computational capabilities.

I immensely enjoyed working on these projects and hope they were equally interesting for the readers of this thesis to learn about.

Appendix A

PISA: FMDV mis-assembled particle interface

The results from the PISA server [165] for the FMDV mis-assembled particle inter-pentameric interface are included here. Below is the table with a summary of the interface statics, followed by the interaction prediction between individual residues of VP2 and VP3 at the interface and the images from Coot showing the said residues.

Interface Summary XML

	Structure 1		Structure 2	
Selection range	2		1	
class	Protein		Protein	
symmetry operation	x,y,z		x,y,z	
symmetry ID	1_555		0_555	
Number of atoms				
interface	104	3.4%	105	3.4%
surface	2445	80.2%	2457	80.6%
total	3047	100.0%	3047	100.0%
Number of residues				
interface	30	7.8%	29	7.5%
surface	387	100.0%	387	100.0%
total	387	100.0%	387	100.0%
Solvent-accessible area, Å				
interface	931.0	3.4%	923.1	3.3%
total	27570.3	100.0%	27793.5	100.0%
Solvation energy, kcal/mol				
isolated structure	-305.2	100.0%	-303.8	100.0%
gain on complex formation	1.5	-0.5%	1.0	-0.3%
average gain	-5.0	1.7%	-5.1	1.7%
P-value	0.975		0.968	

Hydrogen bonds XML

##	Structure 1	Dist. [Å]	Structure 2
1	2:LYS 64[N]	3.21	1:ASP 70[OD2]
2	2:LYS 198[NZ]	3.52	1:GLU 196[O]
3	2:TYR 200[OH]	3.35	1:ASP 69[OD1]
4	2:ARG 67[NH2]	3.60	1:PHE 65[O]
5	2:PHE 65[O]	3.60	1:ARG 67[NH2]
6	2:ASP 70[OD2]	3.21	1:LYS 64[N]
7	2:GLU 196[O]	3.51	1:LYS 198[NZ]
8	2:ASP 69[OD1]	3.35	1:TYR 200[OH]

Figure A.1: A summary of the PISA statistics for the inter-pentameric interface of the FMDV mis-assembled particles.

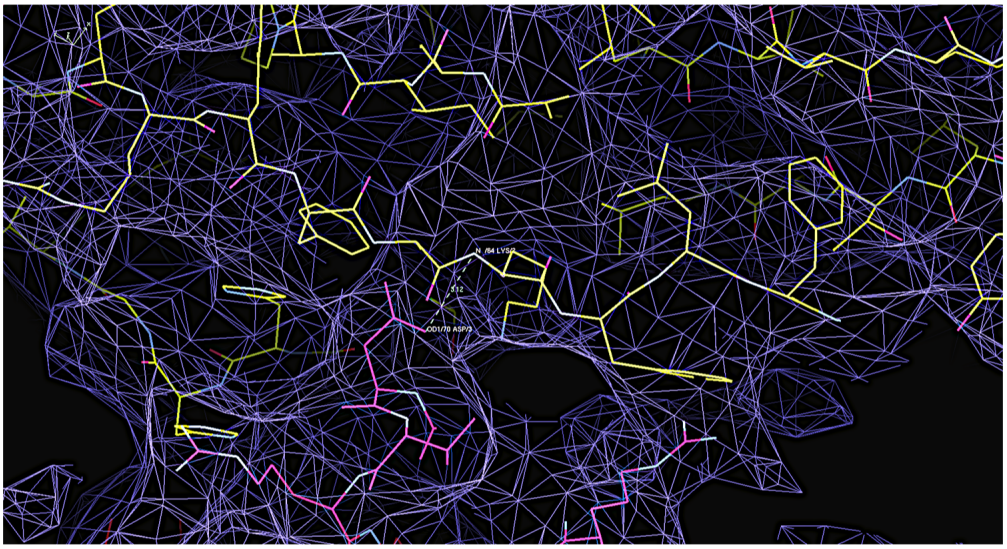


Figure A.2: Inter-pentameric interactions between VP2 Lys64 and VP3 Asp70 as predicted by PISA.

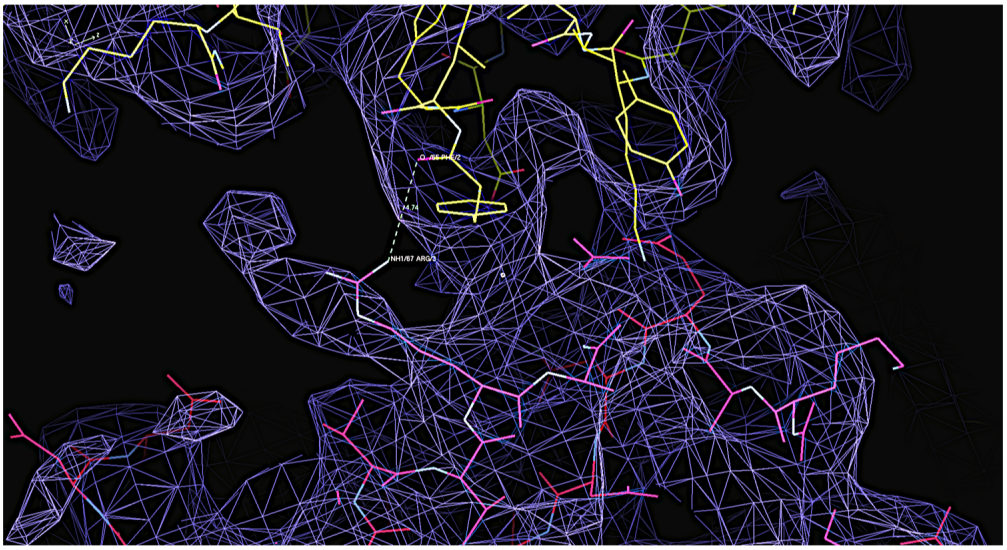


Figure A.3: Inter-pentameric interactions between VP2 Phe65 and VP3 Arg67 as predicted by PISA.

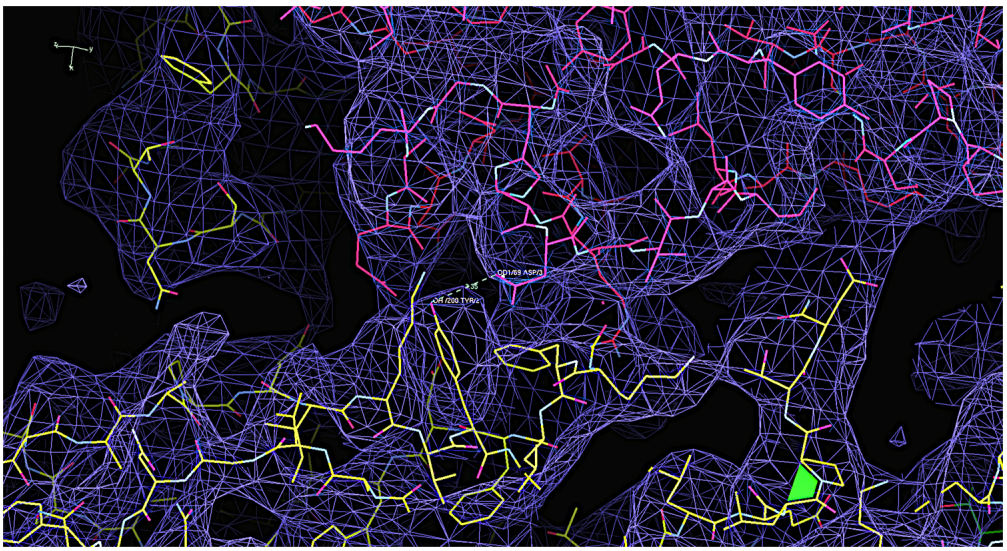


Figure A.4: Inter-pentameric interactions between VP2 Tyr200 and VP3 Asp69 as predicted by PISA.

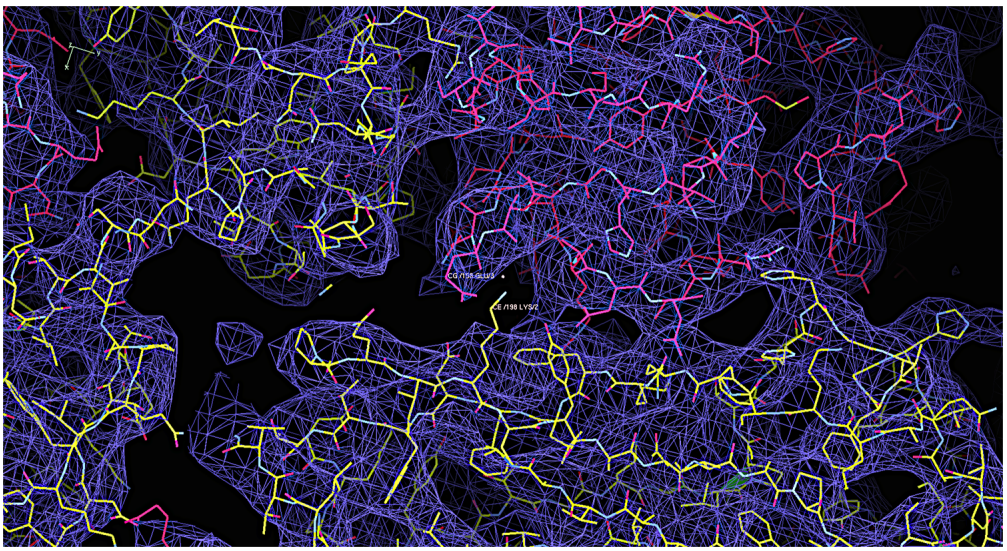


Figure A.5: Inter-pentameric interactions between VP2 Lys198 and VP3 Glu196 as predicted by PISA.

Appendix B

ResMap stats

The additional statistics and figures generated by ResMap, by calculation of resolution per voxel, for all the structures (SAT1, SAT3, A10 mis-assembled particle and the dissociated pentamer) included in this thesis are presented in this Appendix.

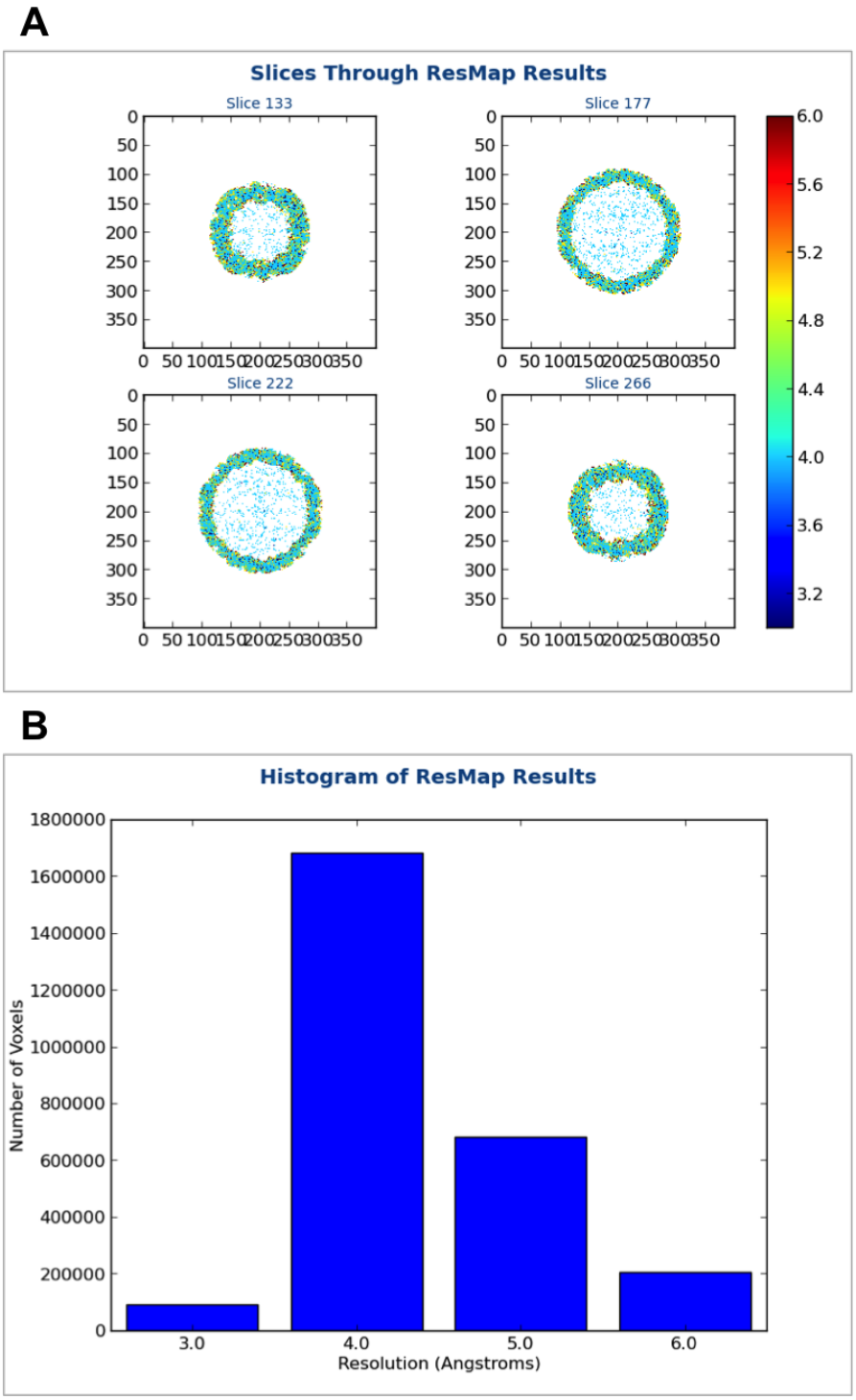


Figure B.1: Figures and additional statistics for the SAT1 structure, generated using ResMap.

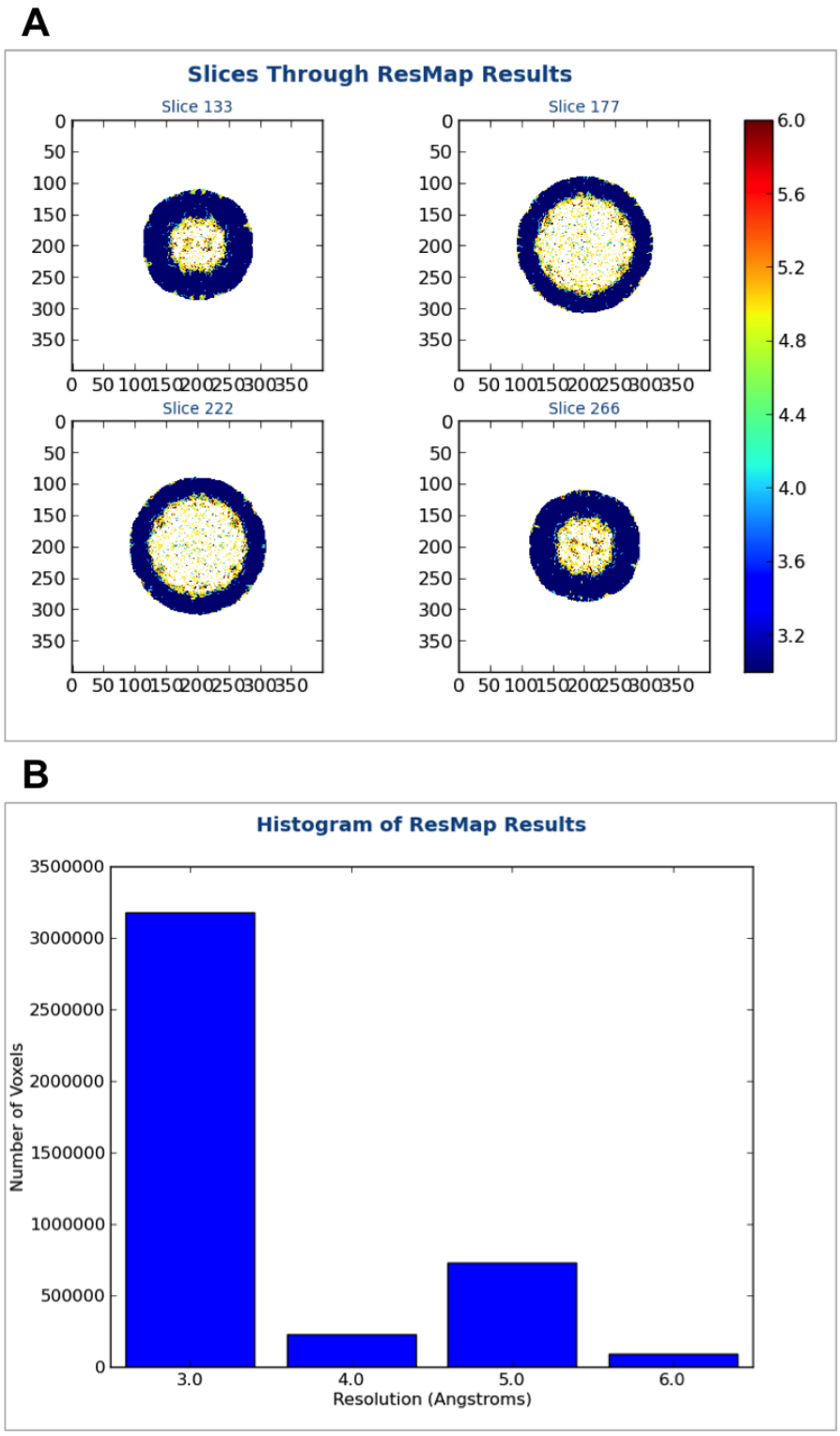


Figure B.2: Figures and additional statistics for the SAT3 structure, generated using ResMap.

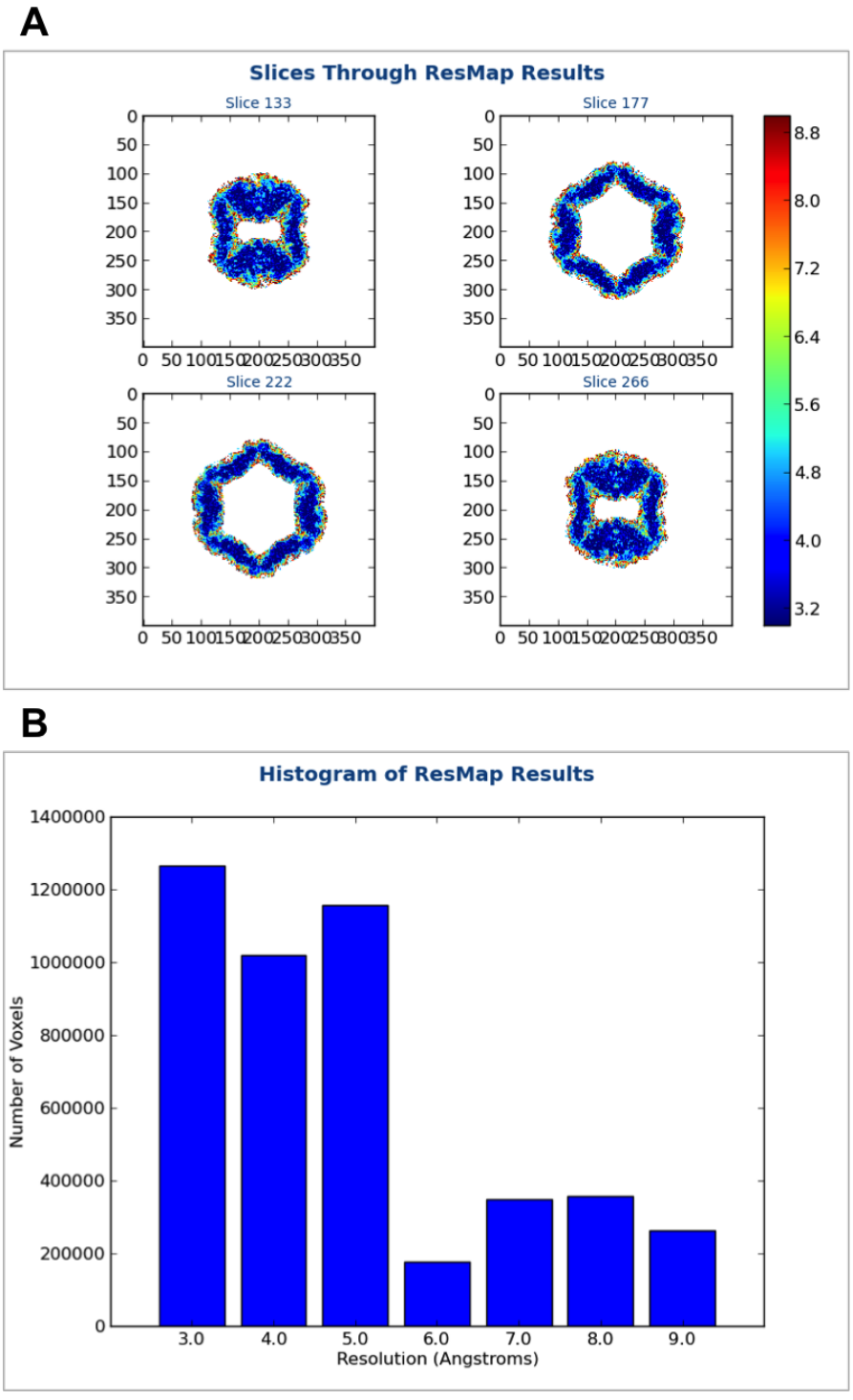


Figure B.3: Figures and additional statistics for the FMDV mis-assembled structure, generated using ResMap.

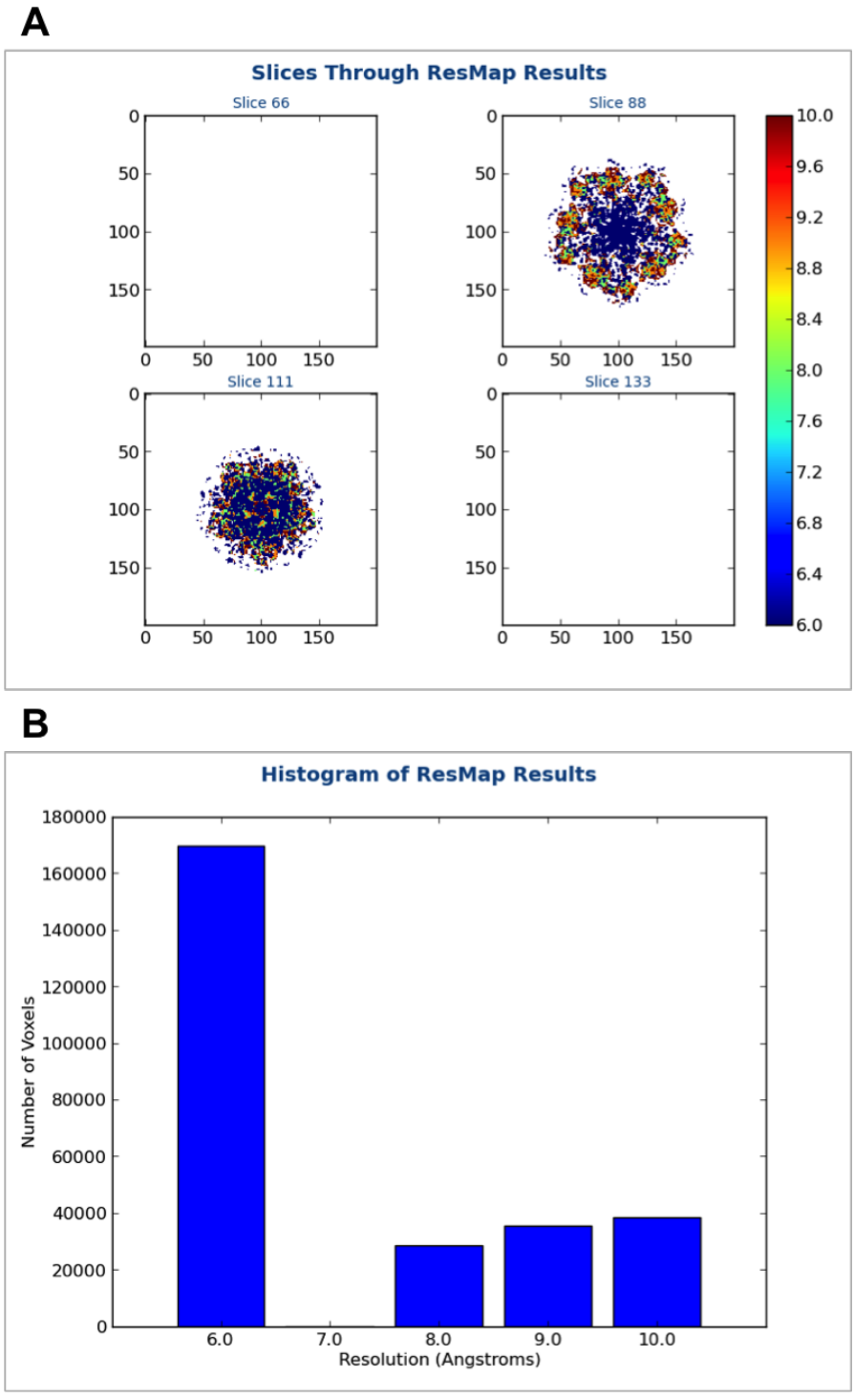
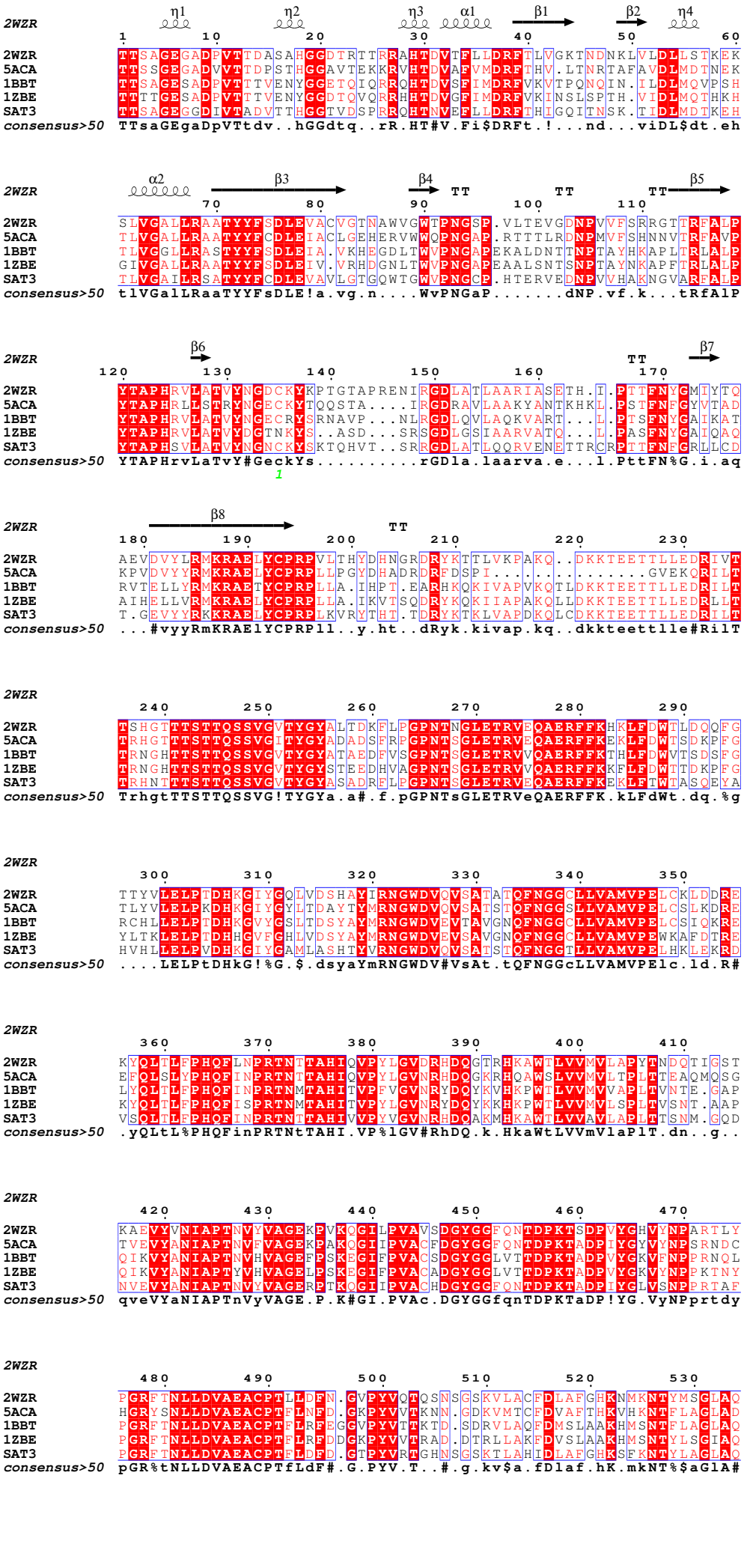


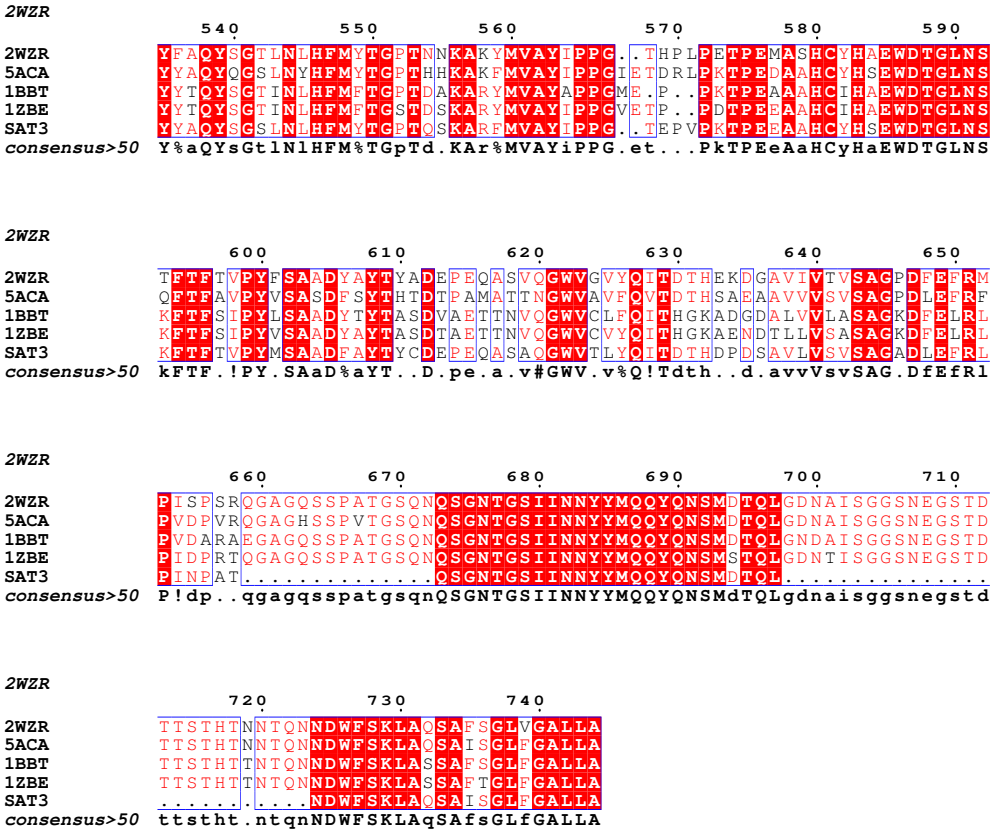
Figure B.4: Figures and additional statistics for the FMDV standalone pentamer, generated using ResMap.

Appendix C

Multiple sequence alignment

Multiple sequence alignment of VP1-4 of SAT3 against those of serotypes O (1BBT), A (1ZBE), SAT1 (2WZR) and SAT2 (5ACA). Mean sequence identity was shown to be 44%.


2WZR
η1 η2 η3 α1 β1 β2 η4
1 10 20 30 40 50 60
2WZR TTSAGEGADPVTTDASAHGGDTRTTRRAHTDVTFLLDRFTLVGKTNDNKLVLDLLSTKEK
5ACA TTSSGEGADVVTTDPSTHGGAVTEKKRVHTDVAFVMDRFTHV.LTNRTAFAVDLMDTNEK
1BBT TTSAGESADPVTTTVENYGGETQIQRRQHTDVSFIMDRFVKVTPQNQIN.ILDLMQVPSH
1ZBE TTTTGESADPVTTTVENYGGDTQVQRRHHTDVGFIMDRFVKINSLSPTH.VIDLMQTHKH
SAT3 TTSAGEGGDIVTADVTTHGGTVDSPRRQHTNVEFLLDRFTHIGQITNSK.TIDLMDTKEH
consensus>50 TTsaGEgaDpVTtdv..hGGdtq..rR.HT#V.Fi$DRFt.!...nd...viDL$dt.eh
2WZR
α2 β3 β4 TT TT TT β5
70 80 90 100 110
2WZR SLVGALLRAATYYFSDLEVACVGTNAWVGWTPNGSP.VLTEVGDNPVVFSRRGTTRFALP
5ACA TLVGALLRAATYYFCDLEIACLGEHERVWWQPNGAP.RTTTLRDNPMVFSHNNVTRFAVP
1BBT TLVGGLLRASTYYFSDLEIA.VKHEGDLTWVPNGAPEKALDNTTNPTAYHKAPLTRLALP
1ZBE GIVGALLRAATYYFSDLEIV.VRHDGNLTWVPNGAPEAALSNTSNPTAYNKAPFTRLALP
SAT3 TLVGAILRSATYYFCDLEVAVLGTGQWTGWVPNGCP.HTERVEDNPVVHAKNGVARFALP
consensus>50 tlVGalLRaaTYYFsDLE!a.vg.n....WvPNGaP.......dNP.vf.k...tRfAlP
2WZR
β6 β7
120 130 140 150 160 170
2WZR YTAPHRVLATVYNGDCKYKPTGTAPRENIRGDLATLAARIASETH.I.PTTFNYGMIYTQ
5ACA YTAPHRLLSTRYNGECKYTQQSTA....IRGDRAVLAAKYANTKHKL.PSTFNFGYVTAD
1BBT YTAPHRVLATVYNGECRYSRNAVP...NLRGDLQVLAQKVART...L.PTSFNYGAIKAT
1ZBE YTAPHRVLATVYDGTNKYS..ASD...SRSGDLGSIAARVATQ...L.PASFNYGAIQAQ
SAT3 YTAPHSVLATVYNGNCKYSKTQHVT..SRRGDLATLQQRVENETTRCRPTTFNFGRLLCD
consensus>50 YTAPHrvLaTvY#GeckYs.........rGDla.laarva.e...l.PttFN%G.i.aq
1
2WZR
β8 TT
180 190 200 210 220 230
2WZR AEVDVYLRMKRAELYCPRPVLTHYDHNGRDRYKTTLVKPAKQ..DKKTEETTLLEDRIVT
5ACA KPVDVYYRMKRAELYCPRPLLPGYDHADRDRFDSPI.....GVEKQRILT
1BBT RVTELLYRMKRAETYCPRPLLA.IHPT.EARHKQKIVAPVKQTLDKKTEETTLLEDRILT
1ZBE AIHELLVRMKRAELYCPRPLLA.IKVTSQDRYKQKIIAPAKQLLDKKTEETTLLEDRLLT
SAT3 T.GEVYYRKKRAELYCPRPLKVRYTHT.TDRYKTKLVAPDKQLCDKKTEETTLLEDRILT
consensus>50 ...#vyyRmKRAElYCPRPll..y.ht..dRyk.kivap.kq..dkkteettlle#RilT
2WZR
240 250 260 270 280 290
2WZR TSHGTTTSTTQSSVGVTYGYALTDKFLPGPNTNGLETRVEQAERFFKHKLFDWTLDQQFG
5ACA TRHGTTTSTTQSSVGITYGYADADSFRPGPNTSGLETRVEQAERFFKEKLFDWTSDKPFG
1BBT TRNGHTTSTTQSSVGVTYGYATAEDFVSGPNTSGLETRVVQAERFFKTHLFDWVTSDSFG
1ZBE TRNGHTTSTTQSSVGVTYGYSTEEDHVAGPNTSGLETRVVQAERFFKKFLFDWTTDKPFG
SAT3 TRHNTTTSTTQSSVGVTYGYASADRFLPGPNTSGLETRVEQAERFFKEKLFTWTASQEYA
consensus>50 TrhgtTTSTTQSSVG!TYGYa.a#.f.pGPNTsGLETRVeQAERFFK.kLFdWt.dq.%g
2WZR
300 310 320 330 340 350
2WZR TTYVLELPTDHKGIYGQLVDSHAYIRNGWDVQVSATATQFNGGCLLVAMVPELCKLDDRE
5ACA TLYVLELPKDHKGIYGYLTDAYTYMRNGWDVQVSATSTQFNGGSLLVAMVPELCSLKDRE
1BBT RCHLLELPTDHKGVYGSLTDSYAYMRNGWDVEVTAVGNQFNGGCLLVAMVPELCSIQKRE
1ZBE YLTKLELPTDHHGVFGHLVDSYAYMRNGWDVEVSAVGNQFNGGCLLVAMVPEWKAFDTRE
SAT3 HVHLLELPVDHKGIYGAMLASHTYVRNGWDVQVSATSTQFNGGTLLVAMVPELHKLEKRD
consensus>50 ....LELPtDHkG!%G.$.dsyaYmRNGWDV#VsAt.tQFNGGcLLVAMVPElc.ld.R#
2WZR
360 370 380 390 400 410
2WZR KYQLTLFPHQFLNPRTNTTAHIQVPYLGVDRHDQGTRHKAWTLVVMVLAPYTNDQTIGST
5ACA EFQLSLYPHQFINPRTNTTAHIQVPYLGVNRHDQGKRHQAWSLVVMVLTPLTTEAQMQSG
1BBT LYQLTLFPHQFINPRTNMTAHITVPFVGVNRYDQYKVHKPWTLVVMVVAPLTVNTE.GAP
1ZBE KYQLTLFPHQFISPRTNMTAHITVPYLGVNRYDQYKKHKPWTLVVMVLSPLTVSNT.AAP
SAT3 VSQLTLFPHQFINPRTNTTAHIVVPYVGVNRHDQAKMHKAWTLVVAVLAPLTTSNM.GQD
consensus>50 .yQLtL%PHQFinPRTNtTAHI.VP%lGV#RhDQ.k.HkaWtLVVmVlaPlT.dn..g..
2WZR
420 430 440 450 460 470
2WZR KAEVYVNIAPTNVYVAGEKPVKQGILPVAVSDGYGGFQNTDPKTSDPVYGHVYNPARTLY
5ACA TVEVYANIAPTNVFVAGEKPAKQGIIPVACFDGYGGFQNTDPKTADPIYGYVYNPSRNDC
1BBT QIKVYANIAPTNVHVAGEFPSKEGIFPVACSDGYGGLVTTDPKTADPVYGKVFNPPRNQL
1ZBE QIKVYANIAPTYVHVAGELPSKEGIFPVACADGYGGLVTTDPKTADPVYGKVYNPPKTNY
SAT3 NVEVYANIAPTNVYVAGERPTKQGIIPVACHDGYGGFQNTDPKTADPIYGLVSNPPRTAF
consensus>50 qveVYaNIAPTnVyVAGE.P.K#GI.PVAc.DGYGGfqnTDPKTaDP!YG.VyNPprtdy
2WZR
480 490 500 510 520 530
2WZR PGRFTNLLDVAEACPTLLDFN.GVPYVQTQSNSGSKVLACFDLAFGHKNMKNTYMSGLAQ
5ACA HGRYSNLLDVAEACPTFLNFD.GKPYVVTKNN.GDKVMTCFDVAFTHKVHKNTFLAGLAD
1BBT PGRFTNLLDVAEACPTFLRFEGGVPYVTTKTD.SDRVLAQFDMSLAAKHMSNTFLAGLAQ
1ZBE PGRFTNLLDVAEACPTFLRFDDGKPYVVTRAD.DTRLLAKFDVSLAAKHMSNTYLSGIAQ
SAT3 PGRFTNLLDVAEACPTFLDFD.GTPYVRTGHNSGSKTLAHIDLAFGHKSFKNTYLAGLAQ
consensus>50 pGR%tNLLDVAEACPTfLdF#.G.PYV.T..#.g.kv$a.fDlaf.hK.mkNT%$aGlA#


2WZR
540 550 560 570 580 590
2WZR YFAQYSGTLNLHFMYTGPTNNKAKYMVAYIPPG.THPLPETPEMASHCYHAEWDTGLNS
5ACA YYAQYQGSLNYHFMYTGPTHHKAKFMVAYIPPGIETDRLPKTPEDAAHCYHSEWDTGLNS
1BBT YYTQYSGTINLHFMFTGPTDAKARYMVAYAPPGME.P..PKTPEAAAHCIHAEWDTGLNS
1ZBE YYTQYSGTINLHFMFTGSTDSKARYMVAYIPPGVETP..PDTPEEAAHCIHAEWDTGLNS
SAT3 YYAQYSGSLNLHFMYTGPTQSKARFMVAYIPPG.TEPVPKTPEEAAHCYHSEWDTGLNS
consensus>50 Y%aQYsGtlNlHFM%TGpTd.KAr%MVAYiPPG.et...PkTPEeAaHCyHaEWDTGLNS
2WZR
600 610 620 630 640 650
2WZR TFTFTVPYFSAADYAYTYADEPEQASVQGWVGVYQITDTHEKDGAVIVTVSAGPDFEFRM
5ACA QFTFAVPYVSASDFSYTHTDTPAMATTNGWVAVFQVTDTHSAEAAVVVSVSAGPDLEFRF
1BBT KFTFSIPYLSAADYTYTASDVAETTNVQGWVCLFQITHGKADGDALVVLASAGKDFELRL
1ZBE KFTFSIPYVSAADYAYTASDTAETTNVQGWVCVYQITHGKAENDTLLVSASAGKDFELRL
SAT3 KFTFTVPYMSAADFAYTYCDEPEQASAQGWVTLYQITDTHDPDSAVLVSVSAGADLEFRL
consensus>50 kFTF.!PY.SAaD%aYT..D.pe.a.v#GWV.v%Q!Tdth..d.avvVsvSAG.DfEfRl
2WZR
660 670 680 690 700 710
2WZR PISPSRQGAGQSSPATGSQNQSGNTGSIINNYYMQQYQNSMDTQLGDNAISGGSNEGSTD
5ACA PVDPVRQGAGHSSPVTGSQNQSGNTGSIINNYYMQQYQNSMDTQLGDNAISGGSNEGSTD
1BBT PVDARAEGAGQSSPATGSQNQSGNTGSIINNYYMQQYQNSMDTQLGNDAISGGSNEGSTD
1ZBE PIDPRTQGAGQSSPATGSQNQSGNTGSIINNYYMQQYQNSMSTQLGDNTISGGSNEGSTD
SAT3 PINPAT.............QSGNTGSIINNYYMQQYQNSMDTQL.............
consensus>50 P!dp..qgagqsspatgsqnQSGNTGSIINNYYMQQYQNSMdTQLgdnaisggsnegstd
2WZR
720 730 740
2WZR TTSTHTNNTQNNDWFSKLAQSAFSGLVGALLA
5ACA TTSTHTNNTQNNDWFSKLAQSAISGLFGALLA
1BBT TTSTHTTNTQNNDWFSKLASSAFSGLFGALLA
1ZBE TTSTHTTNTQNNDWFSKLASSAFTGLFGALLA
SAT3 ...._....NDWFSKLAQSAISGLFGALLA
consensus>50 ttstht.ntqnNDWFSKLAqSAfsGLfGALLA

Appendix D

RMSD between FMDV serotypes

The output from Phylip [174] and SHP [167], in phylogeny determination, showing the RMSD and the structure-based evolutionary distances between the different FMDV serotypes is included here.

	1BBT	1FMD	1ZBE	2WZR	5ACA	AS-1	SAT3
1BBT	0.00	0.50	0.43	0.73	0.76	0.64	1.24
1FMD	0.50	0.00	0.53	0.76	0.80	0.68	1.29
1ZBE	0.44	0.53	0.00	0.72	0.80	0.69	1.27
2WZR	0.71	0.76	0.71	0.00	0.70	0.89	1.19
5ACA	0.77	0.79	0.79	0.70	0.00	0.84	1.23
AS-1	0.64	0.68	0.68	0.89	0.83	0.00	1.32
SAT3	1.25	1.29	1.27	1.20	1.24	1.31	0.00

Figure D.1: Phylip/SHP output showing the RMSD, in Å, between the different FMDV serotypes.

	1BBT	1FMD	1ZBE	2WZR	5ACA	AS-1	SAT3
1BBT	0.0000	0.1060	0.0840	0.1970	0.2350	0.1170	0.4710
1FMD	0.1060	0.0000	0.1180	0.2220	0.2630	0.1680	0.5120
1ZBE	0.0840	0.1180	0.0000	0.2110	0.2460	0.1530	0.5050
2WZR	0.1970	0.2220	0.2110	0.0000	0.1660	0.2630	0.4240
5ACA	0.2350	0.2630	0.2460	0.1660	0.0000	0.2590	0.4710
AS-1	0.1170	0.1680	0.1530	0.2630	0.2590	0.0000	0.5270
SAT3	0.4710	0.5120	0.5050	0.4240	0.4710	0.5270	0.0000

Figure D.2: Phylip/SHP output showing the structure-based evolutionary distances between the different FMDV serotypes.

Bibliography

[1] Chris Lauber and Alexander E Gorbalenya. Toward genetics-based virus taxonomy: comparative analysis of a genetics-based classification and the taxonomy of picornaviruses. *Journal of virology*, 86(7):3905–3915, April 2012.

[2] N J Knowles, T Hovi, AMQ King, and G Stanway. Overview of taxonomy. In Ehrenfeld E, E Domingo, and Roos R P, editors, *The picornaviruses*, pages 19–32. 2010.

[3] Alexander E Gorbalenya and Chris Lauber. Origin and evolution of the picornaviridae proteome. In Ehrenfeld E, Domingo E, and Roos R P, editors, *The picornaviruses*, pages 253–270. 2010.

[4] J Lindsay Whitton, Christopher T Cornell, and Ralph Feuer. Host and virus determinants of picornavirus pathogenesis and tropism. *Nature Reviews Microbiology*, 3(10):765–776, October 2005.

[5] E Martinez-Salas and M D Ryan. Translation and protein processing. In Ehrenfeld E, Domingo E, and Roos R P, editors, *The picornaviruses*, pages 141–161. 2010.

[6] Marvin J Grubman, Betty H Robertson, Donald O Morgan, Douglas M Moore, and Donald Dowbenko. Biochemical Map of Polypeptides Specified by Foot-and-Mouth Disease Virus. *Journal of virology*, pages 1–8, August 1984.

[7] Betty H Robertson, Marvin J Grubman, Greg N Weddell, Douglas M Moore, J Douglas Welsh, Thomas Fischer, Donald J Downbenko, Daniel G Yansura, Barbara Small, and Dennis G Kleid. Nucleotide and Amino Acid Sequence Coding for Polypeptides of Foot-and-Mouth Diease Virus Type A12. *Journal of virology*, pages 651–660, July 1985.

[8] Roland R Ruekert and Eckard Wimmer. Systematic Nomenclature of Picornavirus Proteins. *Journal of virology*, pages 957–959, October 1984.

[9] P W Mason, S V Bezborodova, and T M Henry. Identification and Characterization of a cis-Acting Replication Element (cre) Adjacent to the Internal Ribosome Entry Site of Foot-and-Mouth Disease Virus. *Journal of virology*, 76(19):9686–9694, October 2002.

[10] Akio Nomoto, Barbara Morgan Detjen, Pozzati R, and Eckard Wimmer. The location of the polio genome in viral RNAs and its implication for RNA synthesis. *Nature*, 268:208–213, 1977.

[11] Yuan Fon Lee, Akio Nomoto, Barbara Morgan Detjen, and Eckard Wimmer. A protein covalently linked to poliovirus genome RNA. 74(1):59–63, 1977.

[12] J B Flanegan, R F Petterson, V Ambros, N J Hewlett, and D Baltimore. Covalent linkage of a protein to a defined nucleotide sequence at the 5'-terminus of virion and replicative intermediate RNAs of poliovirus. *Proceedings of the National Academy of Sciences*, 74(3):961–965, March 1977.

[13] E Wimmer and Paul A. Making of a picornavirus genome. In Ehrenfeld E, E Domingo, and Roos R P, editors, *The picornaviruses*, pages 33–55. 2010.

[14] Evgeny V Pilipenko, Svetlana V Maslova, Alexander N Sinyakov, and Vadim I Agol. Towards identification of cis-acting elements involved in the replication of enterovirus and rhinovirus RNAs: a proposal for the existence of tRNA-like terminal structures. *Nucleic Acids Research*, 20(7):1739–1745, 1992.

[15] Karoline Dorsch-Hasler, Yoshiaki Yogo, and Eckard Wimmer. Replication of Picornaviruses. *Journal of virology*, pages 1512–1527, July 1975.

[16] Jing-Yi Lin, Tzu-Chun Chen, Kuo-Feng Weng, Shih-Cheng Chang, Li-Lien Chen, and Shin-Ru Shih. Viral and host proteins involved in picornavirus life cycle. *Journal of Biomedical Science*, 16(1):103–14, 2009.

[17] Yoshiaki Yogo and Eckard Wimmer. Polyadenylic Acid. *Proceedings of the National Academy of Sciences*, 69(7):1877–1882, July 1972.

[18] P Serrano. The 3' end of the foot-and-mouth disease virus genome establishes two distinct long-range RNA-RNA interactions with the 5' end region. *Journal of General Virology*, 87(10):3013–3022, October 2006.

[19] D V Sangar, S E Newton, D J Rowlands, and B E Clarke. All foot and mouth disease virys serotypes initiate protein synthesis at two separate AUGs. *Nucleic Acids Research*, pages 1–11, March 1987.

[20] K M Cowan and J H Graves. A third antigenic component associated with Foot-and-Mouth Disease infection. *Virology*, pages 1–13, November 1966.

[21] J F E Newman, B CARTWRIGHT, T R Doel, and F Brown. Purification and Identification of the RNA-dependent RNA Polymerase of Foot-and-Mouth Disease Virus. *Journal of General Virology*, pages 497–507, 1979.

[22] Jerome Polatnick. Isolation of a foot-and-mouth disease polyuridic acid polymerase and its inhibition by antibody. *Journal of virology*, pages 1–6, February 1980.

[23] Loeffler F and Frosch P. Summarischer Bericht über die Ergebnisse der Untersuchungen zur Erforschung der Maul- und Klauenseuche. *Parasitenkd Abt.*, (22):257–259, 1897.

[24] Howard L Bachrach. Foot-and-Mouth Disease. *Annu. Rev. Microbiol.*, pages 1–44, June 1968.

[25] J B Condy, R S Hedger, C Hamblin, and I T Barnett. The duration of the foot-and-mouth disease virus carrier state in African buffalo (i) in the individual animal and (ii) in a free-living herd. *Comparative immunology, microbiology and infectious diseases*, 8(3-4):259–265, 1985.

[26] M J Grubman and B Baxt. Foot-and-Mouth Disease. *Clinical Microbiology Reviews*, 17(2):465–493, April 2004.

[27] Yves Leforban. Prevention measures against foot-and-mouth disease in Europe in recent years. *Vaccine*, pages 1–5, February 1999.

[28] N J Knowles, A R Samuel, P R Davies, R P Kitching, and A I Donaldson. Outbreak of foot-and-mouth disease virus serotype O in the UK caused by a pandemic strain. *The Veterinary record*, 148(9):258–259, March 2001.

[29] J M Scudamore and D M Harris. Control of foot and mouth disease: lessons from the experience of the outbreak in Great Britain in 2001. *Revue scientifique et technique (International Office of Epizootics)*, 21(3):699–710, December 2002.

[30] E E Fry. Structure of Foot-and-mouth disease virus serotype A1061 alone and complexed with oligosaccharide receptor: receptor conservation in the face of antigenic variation. *Journal of General Virology*, 86(7):1909–1920, July 2005.

[31] R Acharya, E Fry, D Stuart, G Fox, D Rowlands, and F Brown. The three-dimensional structure of foot-and-mouth disease virus at 2.9 A resolution. *Nature*, 337(6209):709–716, February 1989.

[32] Abhay Kotecha, Furquan Zhang, Nicholas Juleff, Terry Jackson, Eva Perez, Dave Stuart, Elizabeth Fry, Bryan Charleston, and Julian Seago. Application of the thermofluor PaSTRy technique for improving Foot-and-Mouth Disease Virus vaccine design. *Journal of General Virology*, 9(3):e1003255–26, 2016.

[33] Elizabeth Fry, Susan M Lea, Terry Jackson, John W I Newman, Fiona M Ellard, Wendy E Blakemore, Robin Abu-Ghazaleh, Alan Samuel, Andrew M Q King, and David I Stuart. The structure and function of a foot-and-mouth disease virus–oligosaccharide receptor complex. *The EMBO journal*, 18(3):543–554, 1999.

[34] S Lea, R Abu-Ghazaleh, W Blakemore, S Curry, E Fry, T Jackson, A King, D Logan, J Newman, and D Stuart. Structural comparison of two strains of foot-and-mouth disease virus subtype O1 and a laboratory antigenic variant, G67. *Structure*, 3(6):571–580, June 1995.

[35] S Lea, J Hernandez, W Blakemore, E Brocchi, S Curry, E Domingo, E Fry, R Abu-Ghazaleh, A King, and J Newman. The structure and antigenicity of a type C foot-and-mouth disease virus. *Structure*, 2(2):123–139, February 1994.

[36] T R Doel and P J Baccarini. Thermal stability of Foot-and-Mouth Disease Virus. *Archives of Virology*, 70:21–32, 1981.

[37] Barry Baxt. Effect of lysosomotropic compounds on early events in foot- and- mouth disease virus replication. *Virus Research*, 7:257–271, 1987.

[38] F Brown and B CARTWRIGHT. Dissociation of foot-and-mouth disease virus into its nucleic acid and protein components. *Nature*, 192:1163–1164, December 1961.

[39] Stephen Curry, Charles C Abrams, Elizabeth Fry, John C Crowther, Graham J Belsham, David I Stuart, and Andrew M Q King. Viral RNA Modulates the Acid Sensitivity of Foot-and-Mouth Disease Virus Capsids. *Journal of virology*, 69(1):430–438, 1995.

[40] Fiona M Ellard, Jeff Drew, Wendy E Blakemore, David Stuart, and Andrew M Q King. Evidence for the role of His-142 of protein 1C in the acid- induced disassembly of foot-and-mouth disease virus capsids. *Journal of General Virology*, pages 1–8, September 1999.

[41] James M Hogle. Poliovirus Cell Entry: Common stuctural themes in viral cell entry. *Annu. Rev. Microbiol.*, 56:677–702, 2002.

[42] S E Bakker, E Groppelli, A R Pearson, P G Stockley, D J Rowlands, and N A Ranson. Limits of Structural Plasticity in a Picornavirus Capsid Revealed by a Massively Expanded Equine Rhinitis A Virus Particle. *Journal of virology*, 88(11):6093–6099, May 2014.

[43] Graham Fox, Nigel R Parry, Paul V Bartnett, Brian McGinn, David J Rowlands, and Fred Brown. The cell attachment site on Foot-and-Mouth Disease Virus includes the amino acid sequence RGD (Arginine-Glycine-Aspartic Acid). *Journal of General Virology*, 70:625–637, 1989.

[44] Martina Leippert, Ewald Beck, Frank Weiland, and Eberhard Pfaff. Point Mutations within the G-H Loop of Foot-and-Mouth Disease Virus O. *Journal of virology*, 71(2):1046–1051, February 1997.

[45] Terry Jackson, Andrew M Q King, David I Stuart, and Elizabeth Fry. Structure and receptor binding. *Virus Research*, 91:33–46, December 2003.

[46] A Berinstein, M Roivainen, T Hovi, P W Mason, and B Baxt. Antibodies to the vitronectin receptor (integrin alphav-beta3) inhibit binding and infection of Foot-and-Mouth Disease Virus to cultured cells. *Journal of virology*, 69(4):2664–2666, 1995.

[47] Terry Jackson, Dean Sheppard, Michael Denyer, Wendy E Blakemore, and Andrew M Q King. The epithelial integrin alphav-beta6 is a receptor for Foot-and-Mouth Disease Virus. *Journal of virology*, 74(11):4949–4956, 2000.

[48] T Jackson, A P Mould, D Sheppard, and A M Q King. Integrin alphav-beta1 is a receptor for Foot-and-Mouth Disease Virus. *Journal of virology*, 76(3):935–941, 2002.

[49] T Jackson, S Clark, S Berryman, A Burman, S Cambier, D Mu, S Nishimura, and A M Q King. Integrin alphav-beta8 functions as a receptor for Foot-and-Mouth Disease Virus: Role of the beta-chain cytodomain in integrin-mediated Infection. *Journal of virology*, 78(9):4533–4540, April 2004.

[50] P Monaghan. The alphav-beta6 integrin receptor for Foot-and-mouth disease virus is expressed constitutively on the epithelial cells targeted in cattle. *Journal of General Virology*, 86(10):2769–2780, October 2005.

[51] A Burman, S Clark, N G A Abrescia, E E Fry, D I Stuart, and T Jackson. Specificity of the VP1 GH Loop of Foot-and-Mouth Disease Virus for alphav Integrins. *Journal of virology*, 80(19):9798–9810, 2006.

[52] Martina Leippert, Ewald Beck, Frank Weiland, and Eberhard Pfaff. Point Mutations within the G-H Loop of Foot-and-Mouth Disease Virus O. *Journal of virology*, pages 1–6, December 1997.

[53] Peter W Mason, Elizabeth Rieder, and Barry Baxt. RGD sequence of foot-and-mouth disease virus is essential for infecting cells via the natural receptor but can be by passed by an antibody-dependent enhancement pathway. *Proceedings of the National Academy of Sciences*, 91:1932–1936, February 1994.

[54] Thomas S C McKenna, Juan Lubroth, Elizabeth Rieder, Barry Baxt, and Peter W Mason. Receptor Binding Site-Deleted Foot-and-Mouth Disease (FMD) Virus Protects Cattle from FMD. *Journal of virology*, pages 1–4, August 1995.

[55] Terry Jackson, Fiona M Ellard, Robin Abu-Ghazaleh, Sharon M Brookes, Wendy E Blakemore, Amanda H Corteyn, David I Stuart, John W I Newman, and Andrew M Q King. Efficient Infection of Cells in Culture by Type O Foot-and-Mouth Disease Virus Requires Binding to Cell Surface Heparan Sulfate. *Journal of virology*, 70(8):5282–5287, July 1996.

[56] Eric Baranowski, Carmen M Ruiz-Jarabo, Filip Lim, and Esteban Domingo. Foot-and-Mouth Disease Virus Lacking the VP1 G-H Loop: The Mutant Spectrum Uncovers In-

teractions among Antigenic Sites for Fitness Gain. *Virology*, 288(2):192–202, September 2001.

[57] E C Carrillo, C Giachetti, and R H Campos. Effect of lysosomotropic agents on the foot-and-mouth disease virus replication. *Virology*, 135(2):542–545, June 1984.

[58] E C Carrillo, C Giachetti, and R Campos. Early steps in FMDV replication: further analysis on the effects of chloroquine. *Virology*, 147(1):118–125, November 1985.

[59] Xiangxi Wang, Wei Peng, Jingshan Ren, Zhongyu Hu, Jiwei Xu, Zhiyong Lou, Xumei Li, Weidong Yin, Xinliang Shen, Claudine Porta, Thomas S Walter, Gwyndaf Evans, Danny Axford, Robin Owen, David J Rowlands, Junzhi Wang, David I Stuart, Elizabeth E Fry, and Zihe Rao. A sensor-adaptor mechanism for enterovirus uncoating from structures of EV71. *Nature Structural & Molecular Biology*, 19(4):424–429, March 2012.

[60] D Bubeck, D J Filman, N Cheng, A C Steven, J M Hogle, and D M Belnap. The Structure of the Poliovirus 135S Cell Entry Intermediate at 10-Angstrom Resolution Reveals the Location of an Externalized Polypeptide That Binds to Membranes. *Journal of virology*, 79(12):7745–7755, May 2005.

[61] K Lyu, J Ding, J F Han, Y Zhang, X Y Wu, Y L He, C F Qin, and R Chen. Human Enterovirus 71 Uncoating Captured at Atomic Resolution. *Journal of virology*, 88(6):3114–3126, February 2014.

[62] Kristin L Shingler, Jennifer L Yoder, Michael S Carnegie, Robert E Ashley, Alexander M Makhov, James F Conway, and Susan Hafenstein. The Enterovirus 71 A-particle Forms a Gateway to Allow Genome Release: A CryoEM Study of Picornavirus Uncoating. *Journal of General Virology*, 9(3):e1003240–10, March 2013.

[63] Tobias J Tuthill, Karl Harlos, Thomas S Walter, Nick J Knowles, Elisabetta Groppelli, David J Rowlands, David I Stuart, and Elizabeth E Fry. Equine Rhinitis A Virus and Its Low pH Empty Particle: Clues Towards an Aphthovirus Entry Mechanism? *Journal of General Virology*, 5(10):e1000620–11, October 2009.

[64] Jingshan Ren, Xiangxi Wang, Zhongyu Hu, Qiang Gao, Yao Sun, Xuemei Li, Claudine Porta, Thomas S Walter, Robert J Gilbert, Yuguang Zhao, Danny Axford, Mark Williams,

Katherine McAuley, David J Rowlands, Weidong Yin, Junzhi Wang, David I Stuart, Zihe Rao, and Elizabeth E Fry. Picornavirus uncoating intermediate captured in atomic detail. *Nature Communications*, 4:1–7, June 2013.

[65] H C Levy, M Bostina, D J Filman, and J M Hogle. Catching a Virus in the Act of RNA Release: a Novel Poliovirus Uncoating Intermediate Characterized by Cryo-Electron Microscopy. *Journal of virology*, 84(9):4426–4441, April 2010.

[66] C Butan, D J Filman, and J M Hogle. Cryo-Electron Microscopy Reconstruction Shows Poliovirus 135S Particles Poised for Membrane Interaction and RNA Release. *Journal of virology*, 88(3):1758–1770, January 2014.

[67] Jingshan Ren, Xiangxi Wang, Ling Zhu, Zhongyu Hu, Qiang Gao, Pan Yang, Xuemei Li, Junzhi Wang, Xinliang Shen, Elizabeth E Fry, Zihe Rao, and David I Stuart. Structures of Coxsackievirus A16 Capsids with Native Antigenicity: Implications for Particle Expansion, Receptor Binding, and Immunogenicity. *Journal of virology*, 89(20):10500–10511, September 2015.

[68] Marvin J Grubman, Marla Zellner, Gayne Bablanian, Peter W Mason, and Maria E Piccone. Identification of the Active-Site Residues of the 3C Proteinase of Foot-and-Mouth Disease Virus. *Virology*, pages 1–9, January 1995.

[69] Martin D Ryan, Andrew M Q King, and G Paul Thomas. Cleavage of foot-and-mouth disease virus polyprotein is mediated by residues located within a 19 amino acid sequence. *Journal of General Virology*, pages 1–6, January 1991.

[70] Vikram N Vakharia, Margaret A Devaney, Douglas M Moore, John J Dunn, and Marvin Grubman. Proteolytic Processing of Foot-and-Mouth Disease Virus Polyproteins Expressed in a Cell-Free System From Clone-Derived Transcripts. *Journal of virology*, pages 3199–3207, December 1987.

[71] Gayne M Bablanian and Marvin J Grubman. Characterization of Foot-and-Mouth Disease Virus 3C Protease Expressed in E. Coli. *Virology*, February 1993.

[72] B E Clarke and D V Sangar. Processing and Assembly of Foot-and-Mouth Disease Virus Proteins Using Subgenomic RNA. *Journal of General Virology*, pages 2313–2325, January 1988.

[73] Ann C Palmenberg. Proteolytic processing of picornaviral polyprotein. *Annu. Rev. Microbiol.*, pages 1–21, July 1990.

[74] Janet E Novak and Karla Kirkegaard. Improved Method for Detecting Poliovirus Negative Strands Used To Demonstrate Specificity of Positive-Strand Encapsidation and the Ratio of Positive to Negative Strands in Infected Cells. *Journal of virology*, pages 3384–3387, June 1991.

[75] R Basavappa, R Syed, O Flore, J P Icenogle, D J Filman, and J M Hogle. Role and mechanism of the maturation cleavage of VP0 in poliovirus assembly: Structure of the empty capsid assembly intermediate at 2.9A resolution. *Protein Science*, pages 1651–1669, January 1994.

[76] Stephen Curry, Elizabeth Fry, Wendy Blakemore, Robin Abu-Ghazaleh, Terry Jackson, Andrew King, Susan Lea, John Newman, and David Stuart. Dissecting the Roles of VP0 Cleavage and RNA Packaging in Picornavirus Capsid Stabilization: the Structure of Empty Capsids of Foot-and-Mouth Disease Virus. *Journal of virology*, pages 1–10, November 1997.

[77] Musa Hindiyeh, Qi-Han Li, Ravi Basavappa, James M Hogle, and Marie Chow. Poliovirus Mutants at Histidine 195 of VP2 Do Not Cleave VP0 into VP2 and VP4. *Journal of virology*, pages 1–8, September 1999.

[78] James J Harber, Johnathan Bradley, Carl W Anderson, and Eckard Wimmer. Catalysis of Poliovirus VPO Maturation Cleavage. *Journal of virology*, pages 1–9, February 1991.

[79] Tina Knipe, Elizabeth Rieder, Barry Baxt, Gordon Ward, and Peter W Mason. Characterization of Synthetic Foot-and-Mouth Disease Virus Provirions Separates Acid-Mediated Disassembly from Infectivity. *Journal of virology*, pages 2851–2856, March 1997.

[80] Wai-Ming Lee, Stephan S Monroe, and Roland R Ruekert. Role of Maturation Cleavage in Infectivity of Picornaviruses: Activation of an Infectosome. *Virology*, pages 1–13, June 1993.

[81] Elida M Bautista, Geoffrey S Ferman, and William T Golde. Induction of lymphopenia and inhibition of T cell function during acute infection of swine with foot and mouth disease virus (FMDV). *Veterinary Immunology and Immunopathology*, 92(1-2):61–73, March 2003.

[82] John Holland, Katherine Spindler, Frank Horodyski, Elizabeth Grabau, Stuart Nichol, and Scott VandePol. Rapid Evolution of RNA Genomes. *Science*, 215(4540):1577–1585, March 1982.

[83] E Domingo and J J Holland. RNA VIRUS MUTATIONS AND FITNESS FOR SURVIVAL. *Annu. Rev. Microbiol.*, 51:151–178, October 1997.

[84] D T Haydon, A R Samuel, and N J Knowles. The generation and persistence of genetic variation in foot-and-mouth disease virus. *Preventive Veterinary Medicine*, 51:111–124, 2001.

[85] Mark Rweyemamu, Francois Maree, Christopher Kasanga, Katherine Scott, Pamela Opperman, Melanie Chitray, Abraham Sangula, Raphael Sallu, Yona Sinkala, Philemon Wambura, Donald King, and David Paton. Challenges and prospects for the control of foot-and-mouth disease: an African perspective. *Veterinary Medicine: Research and Reports*, pages 119–20, October 2014.

[86] J D Kitson, D McCahon, and G J Belsham. Sequence analysis of monoclonal antibody resistant mutants of type O foot and mouth disease virus: evidence for the involvement of the three surface exposed capsid proteins in four antigenic sites. *Virology*, 179(1):26–34, November 1990.

[87] Mauricio G Mateu. Antibody recognition of picronaviruses and escape from neutralisation: a structural view. *Virus Research*, 38:1–24, 1995.

[88] P J Klasse and Q J Sattentau. Occupancy and mechanism in antibody-mediated neutralization of animal viruses. *Journal of General Virology*, 83:2091–2108, 2002.

[89] D McCahon, J R Crowther, G J Belsham, J D A Kitson, M Duchesne, P Have, R H Meloen, D O Morgan, and F De Simone. Evidence for at least four antigenic sites on Type O Foot-and-Mouth Disease Virus involved in neutralisation; Identification by single and multiple site monoclonal antibody-resistant mutants. *J. Gen. Virology*, 70:639–645, 1989.

[90] A A M Thomas, R J Woormeijer, W Puijk, and S J Barteling. Antigenic Sites on Foot-and-Mouth Disease Virus Type A10. *Journal of virology*, pages 2728–2789, October 1988.

[91] Santina Grazioli, Marcella Moretti, Ilaria Barbieri, Marialuisa Crosatti, and Emiliana Brocchi. Use of monoclonal antibodies to identify and map new antigenic determinants involved in neutralisation on FMD viruses type SAT1 and SAT2. *European Commission for the Control of Foot-and-Mouth Disease International control of Foot-and-Mouth disease Tools, Trends and perspectives. Paphos, Cyprus: Food and Agriculture Organization.*, pages 287–297, 2006.

[92] M G Mateu, J Hernandez, M A Martinez, D Feigelstock, S Lea, J J Perez, E Giralt, D Stuart, E L Palma, and E Domingo. Antigenic heterogeneity of a Foot-and-Mouth Disease Virus serotype in the field is mediated by very limited sequence variation at several antigenic sites. *Journal of virology*, 68(3):1407–1417, 1994.

[93] J B Brooksby. Portraits of viruses: foot-and-mouth disease virus. *Intervirology*, 18(1-2):1–23, 1982.

[94] H S Frenkel. La culture de virus de la fievre aphteuse sur l'epithelium de la langue des bovides. *Bull. Off. Int. Epiz.*, pages 155–162, 1947.

[95] F Brown. New approaches to vaccination against foot-and-mouth disease. *Vaccine*, 10(14):1022–1026, 1992.

[96] M M Rweyemamu and Y Leforban. Foot-and-mouth disease and international development. *Advances in virus research*, 53:111–126, 1999.

[97] P C Yang, R M Chu, W B Chung, and H T Sung. Epidemiological characteristics and financial costs of the 1997 foot-and-mouth disease epidemic in Taiwan. *The Veterinary record*, 145(25):731–734, December 1999.

[98] N P Ferris, A I Donaldson, I T R Barnett, and R W Osborne. Inactivation, purification and stability of 146S antigens of foot and mouth disease virus for use as reagents in the complement fixation test. *Rev. sci. tech. Off. int. Epiz.*, 3(2):339–350, 1984.

[99] Ian Anderson. Foot and Mouth Disease 2007: A Review and Lessons Learned. pages 1–141, March 2008.

[100] Satya Parida. Vaccination against foot-and-mouth disease virus: strategies and effectiveness. *Expert Review of Vaccines*, 8(3):347–365, 2009.

[101] Verónica Rincón, Alicia Rodríguez-Huete, Silvia López-Argüello, Beatriz Ibarra-Molero, Jose M Sanchez-Ruiz, Michiel M Harmsen, and Mauricio G Mateu. Identification of the Structural Basis of Thermal Lability of a Virus Provides a Rationale for Improved Vaccines. *Structure*, 22(11):1560–1570, November 2014.

[102] Claudine Porta, Abhay Kotecha, Alison Burman, Terry Jackson, Jingshan Ren, Silvia Loureiro, Ian M Jones, Elizabeth E Fry, David I Stuart, and Bryan Charleston. Rational engineering of recombinant picornavirus capsids to produce safe, protective vaccine antigen. *Journal of General Virology*, 9(3):e1003255, March 2013.

[103] Abhay Kotecha, Julian Seago, Katherine Scott, Alison Burman, Silvia Loureiro, Jingshan Ren, Claudine Porta, Helen M Ginn, Terry Jackson, Eva Perez-Martin, C Alistair Siebert, Guntram Paul, Juha T Huiskonen, Ian M Jones, Robert M Esnouf, Elizabeth E Fry, Francois F Maree, Bryan Charleston, and David I Stuart. Structure-based energetics of protein interfaces guides foot-and-mouth disease virus vaccine design. *Nature Publishing Group*, 22(10):788–794, September 2015.

[104] Arthur L Robinson. Electron Microscope Inventors Share Nobel Physics Prize. *Science*, 234, November 1986.

[105] Rasmus R Schroder, Waltraud Hofmann, and Jean-Francois Menetret. Zero-Loss Energy Filtering as Improved Imaging Mode in Cryoelectronmicroscopy of Frozen-Hydrated Specimens. *Journal of Structural Biology*, 105:28–34, 1990.

[106] John Trinick and John Berriman. Zero-loss electron microscopy with Zeiss EM902. *Ultramicroscopy*, 21:393–398, 1987.

[107] Kenneth H Downing and Felicia M Hendrickson. Performance of a 2k CCD camera designed for electron crystallography at 400 kV. *Ultramicroscopy*, pages 215–233, 1999.

[108] W S Boyle and G E Smith. Charge coupled semiconductor devices. *B.S.T.J Briefs*, pages 587–593, 1970.

[109] Andreas Hoenger. High-resolution cryo-electron microscopy on macromolecular complexes and cell organelles. *Protoplasma*, 251(2):417–427, January 2014.

[110] Yifan Cheng. Single-Particle Cryo-EM at Crystallographic Resolution. *Cell*, 161(3):450–457, April 2015.

[111] A R Faruqi. Principles and prospects of direct high resolution electron image acquisition with CMOS detectors at low energies. *Journal of Physics: Condensed Matter*, 21(31):314004–10, July 2009.

[112] Anna-Clare Milazzo, Grigore Moldovan, Jason Lanman, Liang Jin, James C Bouwer, Stuart Klienfelder, Steven T Peltier, Mark H Ellisman, Angus I Kirkland, and Nguyen-Huu Xuong. Characterization of a direct detection device imaging camera for transmission electron microscopy. *Ultramicroscopy*, 110(7):741–744, June 2010.

[113] Axel F Brilot, James Z Chen, Anchi Cheng, Junhua Pan, Stephen C Harrison, Clinton S Potter, Bridget Carragher, Richard Henderson, and Nikolaus Grigorieff. Beam-induced motion of vitrified specimen on holey carbon film. *Journal of Structural Biology*, 177(3):630–637, March 2012.

[114] J C Dainty and R Shaw. Detective quantum efficiency, signal to noise ratio, and the noise-equivalent number of quanta . *Image Science*, pages 152–188, 1974.

[115] G McMullan, A R Faruqi, D Clare, and R Henderson. Comparison of optimal performance at 300keV of three direct electron detectors for use in low dose electron microscopy. *Ultramicroscopy*, 147(C):156–163, December 2014.

[116] Rachel S Ruskin, Zhiheng Yu, and Nikolaus Grigorieff. Quantitative characterization of electron detectors for transmission electron microscopy. *Journal of Structural Biology*, 184(3):385–393, December 2013.

[117] G Jensen. Cryo-EM Part A: Sample Preparation and Data Collection: Sample Preparation and Data Collection, 2010.

[118] Helen R Saibil. Macromolecular structure determination by cryo-electron microscopy. *Acta Crystallographica Section D Biological Crystallography*, 56:1215–1222, 2000.

[119] Jacques Dubochet, Marc Adrian, Jiin-Ju Chang, Jean-Claude Homo, Jean Lepault, Alasdair W McDowall, and Patrick Schultz. Cryo-electron microscopy of vitrified specimens. *Quarterly Review of Biophysics*, 21(2):129–228, 1988.

[120] Ashraf A-Amoudi, Jiin-Ju Chang, Amelie Leforestier, Alasdair McDowall, Lauree Michel Salamin, Lars PO Norlen, Karsten Richter, Nathalie Sartori Blanc, Daniel Studer, and Jacques Dubochet. Cryo-electron microscopy of vitreous sections. *The EMBO journal*, 23:358303588, 2004.

[121] Megan J Dobro, Linda A Melanson, Grant J Jensen, and Alasdair W McDowall. *Plunge Freezing for Electron Cryomicroscopy*, volume 481. Elsevier Masson SAS, January 2010.

[122] David N Mastronarde. Automated electron microscope tomography using robust prediction of specimen movements. *Journal of Structural Biology*, 152(1):36–51, October 2005.

[123] Xueming Li, Paul Mooney, Shawn Zheng, Christopher R Booth, Michael B Braunfeld, Sander Gubbens, David A Agard, and Yifan Cheng. Electron counting and beam-induced motion correction enable near-atomic-resolution single-particle cryo-EM. *Nature Methods*, 10(6):584–590, May 2013.

[124] E V Orlova and H R Saibil. Structural Analysis of Macromolecular Assemblies by Electron Microscopy. *Chemical Reviews*, 111(12):7710–7748, December 2011.

[125] P A Thuman-Commike and W Chiu. Reconstruction principles of icosahedral virus structure determination using electron cryomicroscopy. *micron*, 31:687–711, 2000.

[126] H P Erickson and A Klug. Measurement and compensation of defocusing and aberrations by Fourier processing of electron micrographs. *Phil. Trans. Roy. Soc. Lond.*, 261:105–118, 1971.

[127] Wah Chiu and R M Glaeser. Factors affecting high resolution fixed-beam transmission electron microscopy. *Ultramicroscopy*, 2:207–217, 1977.

[128] Sjors H W Scheres. RELION: Implementation of a Bayesian approach to cryo-EM structure determination. *Journal of Structural Biology*, 180(3):519–530, December 2012.

[129] Joseph A Mindell and Nikolaus Grigorieff. Accurate determination of local defocus and specimen tilt in electron microscopy. *Journal of Structural Biology*, 142(3):334–347, June 2003.

[130] Guang Tang, Liwei Peng, Philip R Baldwin, Deepinder S Mann, Wen Jiang, Ian Rees, and Steven J Ludtke. EMAN2: An extensible image processing suite for electron microscopy. *Journal of Structural Biology*, 157(1):38–46, January 2007.

[131] Yuanxin Zhu, B Carragher, F Mouche, and C S Potter. Automatic particle detection through efficient hough transforms. *IEEE Transactions on Medical Imaging*, 22(9):1053–1062, September 2003.

[132] Helen E White, Elena V Orlova, Shaoxia Chen, Luchun Wang, Athanasios Ignatiou, Brent Gowen, Thusnelda Stromer, Titus M Franzmann, Martin Haslbeck, Johannes Buchner, and Helen R Saibil. Multiple Distinct Assemblies Reveal Conformational Flexibility in the Small Heat Shock Protein Hsp26. *Structure*, 14(7):1197–1204, July 2006.

[133] Mikel Valle, Andrey Zavialov, Jayati Sengupta, Urmila Rawat, Måns Ehrenberg, and Joachim Frank. Locking and Unlocking of Ribosomal Motions. *Cell*, 114(1):123–134, July 2003.

[134] Elena V Orlova and Helen R Saibil. *Chapter 12 - Methods for Three-Dimensional Reconstruction of Heterogeneous Assemblies*, volume 482. Elsevier Inc., 1 edition, 2010.

[135] Laurent Joyeux and Pawel A Penczek. Efficiency of 2D alignment methods. *Ultramicroscopy*, 92:33–46, 2002.

[136] Grant Jensen. *Cryo-EM, Part B: 3-D Reconstruction.* Elsevier, 2010.

[137] R A Crowther. Procedures for three-dimensional reconstruction of spherical viruses by Fourier synthesis from electron micrographs. *Phil. Trans. Roy. Soc. Lond.*, 261:221–230, 1971.

[138] Pawel A Penczek, Robert A Grassucci, and Joachim Frank. The ribosome at improved resolution: new techniques for merging and orientation refinement in 3D cryo-electron microscopy of biological particles. *Ultramicroscopy*, 52:251–270, 1994.

[139] N A Kiselev, D J De Rosier, and A Klug. Structure of the Tubes of Catalase: Analysis of Electron Micrographs by Optical Filtering. *Journal of molecular biology*, 35:561–566, 1968.

[140] Marin van Heel and Michael Schatz. Fourier shell correlation threshold criteria. *Journal of Structural Biology*, 151(3):250–262, September 2005.

[141] Sjors H W Scheres and Shaoxia Chen. Prevention of overfitting in cryo-EM structure determination. *Nature Methods*, 9(9):853–854, September 2012.

[142] Richard Henderson, Andrej Sali, Matthew L Baker, Bridget Carragher, Batsal Devkota, Kenneth H Downing, Edward H Egelman, Zukang Feng, Joachim Frank, Nikolaus Grigorieff, Wen Jiang, Steven J Ludtke, Ohad Medalia, Pawel A Penczek, Peter B Rosenthal, Michael G Rossmann, Michael F Schmid, Gunnar F Schröder, Alasdair C Steven, David L Stokes, John D Westbrook, Willy Wriggers, Huanwang Yang, Jasmine Young, Helen M Berman, Wah Chiu, Gerard J Kleywegt, and Catherine L Lawson. Outcome of the First Electron Microscopy Validation Task Force Meeting. *Structure*, 20(2):205–214, February 2012.

[143] Schrodinger, LLC. The PyMOL Molecular Graphics System, Version 1.8 .

[144] Michael G Rossmann. Fitting atomic models in electron-microscopy maps. *Acta Crystallographica Section D Biological Crystallography*, D56:1341–1349, 2000.

[145] Pablo Chacon and Willy Wriggers. Multi-resolution Contour-based Fitting of Macromolecular Structures. *Journal of molecular biology*, 317:375–384, 2002.

[146] P Emsley, B Lohkamp, W G Scott, and K Cowtan. Features and development of Coot. *Acta Crystallographica Section D Biological Crystallography*, 66(4):486–501, March 2010.

[147] Paul D Adams, Pavel V Afonine, Gábor Bunkóczi, Vincent B Chen, Ian W Davis, Nathaniel Echols, Jeffrey J Headd, Li-Wei Hung, Gary J Kapral, Ralf W Grosse-Kunstleve, Airlie J McCoy, Nigel W Moriarty, Robert Oeffner, Randy J Read, David C Richardson, Jane S Richardson, Thomas C Terwilliger, and Peter H Zwart. PHENIX: a comprehensive Python-based system for macromolecular structure solution. *Acta Crystallographica Section D Biological Crystallography*, 66(2):213–221, January 2010.

[148] J Dubochet, J Lepault, R Freeman, J A Berriman, and J C Homo. Electron microscopy of frozen water and aqueous solutions. *Journal of Microscopy*, 128(3):219–237, December 1982.

[149] Nicolas Boisset, Pawel A Penczek, Jean-Christophe Taveau, Valerie You, Felix de Haas, and Jean Lamy. Overabundant single-particle electron microscope views induce a three-dimensional reconstruction artifact. *Ultramicroscopy*, 74:201–207, 1998.

[150] Vladan Lučić, Friedrich Förster, and Wolfgang Baumeister. STRUCTURAL STUDIES BY ELECTRON TOMOGRAPHY: From Cells to Molecules. *Annual Review of Biochemistry*, 74(1):833–865, June 2005.

[151] Kay Grünewald, Ohad Medalia, Ariane Gross, Alasdair C Steven, and Wolfgang Baumeister. Prospects of electron cryotomography to visualize macromolecular complexes inside cellular compartments: implications of crowding. *Biophysical chemistry*, 100(1-3):577–591, January 2003.

[152] S Curry, E Fry, W Blakemore, R Abu-Ghazaleh, T Jackson, A King, S Lea, J Newman, D Rowlands, and D Stuart. Perturbations in the surface structure of A22 Iraq foot-and-mouth disease virus accompanying coupled changes in host cell specificity and antigenicity. *Structure*, 4(2):135–145, February 1996.

[153] S Lea, J Hernandez, W Blakemore, E Brocchi, S Curry, E Domingo, E Fry, R Abu-Ghazaleh, A King, and J Newman. The structure and antigenicity of a type C foot-and-mouth disease virus. *Structure*, 2(2):123–139, February 1994.

[154] M Chow, J F Newman, D Filman, J M Hogle, D J Rowlands, and F Brown. Myristylation of picornavirus capsid protein VP4 and its structural significance. *Nature*, 327(6122):482–486, June 1987.

[155] Shi-Chong Han, Hui-Chen Guo, and Shi-Qi Sun. Three-dimensional structure of foot-and-mouth disease virus and its biological functions. *Archives of Virology*, 160(1):1–16, November 2014.

[156] P B Capstick, A J Garland, W G Chapman, and R C Masters. Production of Foot-and-mouth Disease Virus antigen from BHK 21clone 13 cells growns and infected in deep suspension cultures. *Nature*, 205:1135–1136, March 1965.

[157] D Aarthi, K Ananda Rao, R Robinson, and V A Srinivasan. Validation of binary ethyleneimine (BEI) used as an inactivant for foot and mouth disease tissue culture vaccine. *Biologicals*, 32(3):153–156, September 2004.

[158] J Bernard Heymann. Bsoft: Image and Molecular Processing in Electron Microscopy. *Journal of Structural Biology*, 133(2-3):156–169, February 2001.

[159] Eric F Pettersen, Thomas D Goddard, Conrad C Huang, Gregory S Couch, Daniel M Greenblatt, Elaine C Meng, and Thomas E Ferrin. UCSF Chimera - A visualization system for exploratory research and analysis. *Journal of Computational Chemistry*, 25(13):1605–1612, 2004.

[160] Alp Kucukelbir, Fred J Sigworth, and Hemant D Tagare. Quantifying the local resolution of cryo-EM density maps. *Nature Methods*, 11(1):63–65, 2014.

[161] Dexiang Chen and Debra Kristensen. Opportunities and challenges of developing thermostable vaccines. *Expert Review of Vaccines*, 8(5):547–557, 2009.

[162] T R Doel and Deborah J David. The stability and potency of vaccines prepared from inactivated foot-and-mouth disease virus concentrates*. *Journal of Biological Standardization*, 12:241–255, 1984.

[163] Thomas S Walter, Jingshan Ren, Tobias J Tuthill, David J Rowlands, David I Stuart, and Elizabeth E Fry. A plate-based high-throughput assay for virus stability and vaccine formulation. *Journal of Virological Methods*, 185(1):166–170, October 2012.

[164] M A Larkin, G Blackshields, N P Brown, R Chenna, P A McGettigan, H McWilliam, F Valentin, I M Wallace, A Wilm, R Lopez, J D Thompson, T J Gibson, and D G Higgins. Clustal W and Clustal X version 2.0. *Bioinformatics*, 23(21):2947–2948, November 2007.

[165] Evgeny Krissinel and Kim Henrick. Inference of Macromolecular Assemblies from Crystalline State. *Journal of molecular biology*, 372(3):774–797, September 2007.

[166] Jingshan Ren, Xiangxi Wang, Ling Zhu, Zhongyu Hu, Qiang Gao, Pan Yang, Xuemei Li, Junzhi Wang, Xinliang Shen, Elizabeth E Fry, Zihe Rao, and David I Stuart. Structures of Coxsackievirus A16 Capsids with Native Antigenicity: Implications for Particle Expansion, Receptor Binding, and Immunogenicity. *Journal of virology*, 89(20):10500–10511, September 2015.

[167] David I Stuart, Michael Levine, Hilary Muirhead, and David K Stammers. Crystal structure of cat muscle pyruvate kinase at a resolution of 2.6 A. *Journal of molecular biology*, 134:100–142, 1979.

[168] Martyn D Winn, Charles C Ballard, Kevin D Cowtan, Eleanor J Dodson, Paul Emsley, Phil R Evans, Ronan M Keegan, Eugene B Krissinel, Andrew G W Leslie, Airlie McCoy, Stuart J McNicholas, Garib N Murshudov, Navraj S Pannu, Elizabeth A Potterton, Harold R Powell, Randy J Read, Alexei Vagin, and Keith S Wilson. Overview of the CCP4 suite and current developments. *Acta Crystallographica Section D Biological Crystallography*, 67(4):235–242, 2011.

[169] B Lee and F M Richards. The interpretation of protein structures: Estimation of static accessibility. *Journal of molecular biology*, 55:379–400, 1971.

[170] E B Saff and A B J Kuijlaars. Distributing many points on a sphere. *The mathematical intelligencer*, 19(1):5–11, 1997.

[171] O Goldenberg, E Erez, G Nimrod, and N Ben-Tal. The ConSurf-DB: pre-calculated evolutionary conservation profiles of protein structures. *Nucleic Acids Research*, 37(Database):D323–D327, 2009.

[172] Gershon Celniker, Guy Nimrod, Haim Ashkenazy, Fabian Glaser, Eric Martz, Itay Mayrose, Tal Pupko, and Nir Ben-Tal. ConSurf: Using Evolutionary Data to Raise Testable Hypotheses about Protein Function. *Israel Journal of Chemistry*, 53(3-4):199–206, 2013.

[173] Florence Corpet. Multiple sequence alignment with hierarchical clustering. *Nucleic Acids Research*, 16(11):10881–10890, 1988.

[174] Felsenstein J. Phylip - Phylogeny inference package (version (3.2). *cladistics*, 5(2):163–166, June 1989.

[175] Xiangxi Wang, Jingshan Ren, Qiang Gao, Zhongyu Hu, Yao Sun, Xuemei Li, David J Rowlands, Weidong Yin, Junzhi Wang, David I Stuart, Zihe Rao, and Elizabeth E Fry. Hepatitis A virus and the origins of picornaviruses. *Nature*, 517:85–89, 2015.

[176] Ling Zhu, Xiangxi Wang, Jingshan Ren, Claudine Porta, Hannah Wenham, Jens-Ola Ekstr ouml m, Anusha Panjwani, Nick J Knowles, Abhay Kotecha, C Alistair Siebert, A Michael Lindberg, Elizabeth E Fry, Zihe Rao, Tobias J Tuthill, and David I Stuart. Structure of Ljungan virus provides insight into genome packaging of this picornavirus. *Nature Communications*, 6:1–9, 2015.